Petrology and Geochemistry of Olivine-Bearing Diogenites and a Group of Paired Howardites

A Dissertation Presented for the
Doctor or Philosophy Degree
The University of Tennessee, Knoxville

Andrew William Beck
August, 2011

Dedication

To mom and dad.

Acknowledgements

First and foremost, I would like to thank my advisor, Dr. Harry Y McSween Jr., for giving me this great opportunity. Over the past five years, Hap has made it possible for me to conduct research that both interests and challenges me, and he has given me the flexibility to pursue different research avenues I enjoy. I have been fortunate to attend meetings and conduct research in various locations around the world thanks to Hap. I also wish to thank the members of my committee, Dr.'s Lawrence A. Taylor, David W. Mittlefehldt, Theodore C. Labotka, and Michael Sepaniak for their tutelage in geochemistry, petrology and meteoritics, and for all of their encouragement along the way. I would also like to thank the rest of the faculty and staff in the Earth and Planetary Sciences Department for their generous support. Part of the funding for this work was made possible by NASA cosmochemistry grant NNG06GG36G to Hap McSween.

I wish to thank my parents, who encouraged me to pursue my interests from an early start, and who have supplied me with wonderful opportunities throughout my life. I also wish to thank the late Jim Bibee, a Tennessee Geology alum, who played a major role in me going to Tennessee for graduate school. A very special thank you to Christina Viviano, whose tireless support and willingness to read drafts of papers, and hear versions of presentations, has helped me significantly.

Last but not least, I would like to thank the Albion College Geology Department. Without their support when I was both an undergraduate and a technician in their department, I would not have been able to get to where I am today.

Abstract

Asteroid 4 Vesta, the largest differentiated body in the asteroid belt, is a protoplanet, much like those that accreted to form the Earth. Understanding the geology of Vesta furthers understanding of early differentiation processes that occurred on Earth and helps define igneous processes occurring on other differentiated bodies in the early solar system. Howardite, eucrite and diogenite (HED) meteorites, which are thought to have originated from Vesta, can be analyzed to better understand the geology of that asteroid. Here my colleagues and I investigate the petrology and geochemistry of two groups of HEDs. This work is timely, in that the insights gained from these studies can be used to interpret data from the Dawn spacecraft, which has just been placed into orbit around Vesta. In the first four parts of this dissertation we investigate the origin of olivine in diogenites, which are ultramafic cumulates from Vesta. We discover that the majority of these samples are dimict (two-component) breccias, composed of harzburgitic and orthopyroxenitic lithologies. This is contrary to the traditional belief that all diogenites are orthopyroxenites with small amounts of cumulus olivine. Using bulk and in situ trace element chemistries, along with mineral major/minor element compositions, we demonstrate that these two lithologies were likely related through fractional crystallization. We also examine an anomalous achondritic dunite, and use geochemistry and petrology to demonstrate that it is the first recognized dunite belonging to the HED group. This sample likely also fractionated from a melt prior to the fractionation of harzburgitic and orthopyroxenitic diogenites. In the final part of this dissertation, we investigate compositional and textural heterogeneity in a large group of paired howardites, Vestan regolith breccias composed of diogenite and eucrite. We find

significant compositional and textural variation within the group, and a preferential distribution of eucritic material in the finer grain sizes. This suggests an immature regolith, and has implications for interpretation of spectral data to be collected by the Dawn orbiter at Vesta.

Table of Contents

Part 1: Introduction…….....……..1

1.0 Diogenites……3

2.0 Howardites……..4

3.0 Authorship……..5

References……..6

Part 2: Diogenites as polymict breccias…….10

Abstract……11

1.0 Introduction……..12

2.0 Methods…….14

3.0 Results……...16

4.0 Discussion……..23

5.0 Conclusions……...33

References……36

Appendix A……..…44

Part 3: MIL 03443, a dunite from the asteroid 4 Vesta……67

Abstract……68

1.0 Introduction……..69

2.0 Methods…….71

3.0 Results……...75

4.0 Discussion……..81

5.0 Conclusions……...……95

References……....97

Appendix B…….115

Part 4: In situ trace elements concentrations in dimict diogenites……127

Abstract……..128

1.0 Introduction……...…….129

2.0 Methods……...130

3.0 Results……..…133

4.0 Discussion…….…..137

5.0 Conclusions……...……...…144

References……...…146

Appendix C……...150

Part 5: Compositional constraints on the genesis of diogenites……159

Abstract……..160

1.0 Introduction……...……..……...162

2.0 Methods…….…..….164

3.0 Results…….……170

4.0 Discussion……....175

5.0 Conclusions……..……...190

References……..……193

Appendix D……..…..204

Part 6: Petrologic and textural diversity in one of the largest pieces of the Vestan regolith……..……..……225

Abstract……...…….....226

1.0 Introduction……...……..……...227

2.0 Methods……..……228

3.0 Results…….……230

4.0 Discussion……..……..238

5.0 Conclusions……...……..……245

References……..247

Appendix E…….254

Appendix F…….258

Part 7: Conclusion……..270

VITAE…….....275

List of Tables

Part 2

Table A1. Modal mineralogy……..……45

Table A2. Average pyroxene compositions..……..……46

Table A3. Average olivine compositions……48

Table A4. Representative chromite compositions...……49

Table A5. Representative plagioclase compositions...……50

Table A6. Representative metal and sulfide compositions...……..……51

Table A7. New classification of samples in this study…....……..……52

Part 3

Table B1. Representative mineral compositions grouped by textural setting.……116

Table B2. Bulk composition of MIL 03443,14 and control samples determined by ICP-MS…….....117

Part 4

Table C1. Average orthopyroxene compositions…….……..……151

Table C2. Representative olivine and plagioclase trace element compositions…….....152

Part 5.

Table D1. ICP-MS Details of diogenite samples studied**.**……..……205

Table D2. Representative pyroxene grain compositions for diogenites..……206

Table D3. Representative oxide grain compositions for diogenites..……..……209

Table D4. Representative olivine grain compositions for diogenites ….....……211

Table D5. Representative plagioclase grain compositions for diogenites...……...212

Table D6. Bulk major and minor element concentrations determined by LA-ICP-MS on fused glass beads……..……..……..……213

Table D7. INAA data on diogenite samples...……..……..……214

Table D8. ICP-MS analyses of duplicate splits of diogenites.……216

List of Figures

Part 2

Figure A1. Histograms showing modal abundances of (a) orthopyroxene and olivine, with the remaining minerals being grouped into "other", and (b) breakdown of the "other" group…….……..…….……53

Figure A2. Histograms showing orthopyroxene Fe# (molar Fe/Fe+Mg *100) in diogenites…….……...…….……54

Figure A3. Backscattered electron (BSE) composite images and representative phase distribution maps of LEW 88679 and MET 01084. ..…….……55

Figure A4. BSE images highlighting assemblages of olivine and magnesian pyroxene with non-brecciated (igneous) grain contacts…..……56

Figure A5. Representative BSE images of two olivine diogenites displaying non-brecciated grain contacts between olivine and orthopyroxene, and Al-rich chromite at those grain boundaries...…..……..……57

Figure A6. BSE images of chromite/clinopyroxene inclusions in the olivine (MIL 03443) and chromite at olivine/orthopyroxene grain boundaries (LAP 03979).…….…58

Figure A7. Ternary plots showing relative abundances of Cr, Al and Ti(X2) in chromite……59

Figure A8. Average olivine Fe# versus both the average magnesian orthopyroxene and ferroan orthopyroxene for each meteorite…….....…60

Figure A9. Illustration of a mixing model where harzburgitic and orthopyroxenitic diogenite fragments are mixed to produce polymict diogenites.……..…..…61

Figure A10. Two transects across a zoned orthopyroxene grain showing Mg/Fe zonation away from an adjacent olivine.……..……62

Figure A11. Average molar Fe/Mn and Fe/Mg ratios in magnesian and ferroan orthopyroxenes in diogenites…….....63

Figure A12. Minor element variation vs. Fe# diagram for orthopyroxenes in the harzburgitic diogenites……..……64

Figure A13. Trend 1 in minor element variation vs. Fe# for orthopyroxenes in polymict diogenites……...……65

Figure A14. Trend 2 in minor element variation vs. Fe# for orthopyroxenes in polymict diogenites……...……66

Part 3

Figure B1. (a) BSE map of MIL 03443,17 showing its fragmental texture comprised mainly of olivine (ol) with smaller amounts of orthopyroxene (opx), chromite (cm) and troilite (tr)…….118

Figure B2. Comparison of pyroxene and olivine compositions in MIL 03443 with those in diogenites……119

Figure B3. MIL 03443 orthopyroxene (a) Al_2O_3 vs. TiO_2 and (b) Yb vs. TiO_2 concentrations compared to diogenite orthopyroxene……120

Figure B4. FeO/MnO wt. ratios in MIL 03443 (a) olivine and (b) pyroxene compared to diogenites……..…...…….……..……...121

Figure B5. A diopside (cpx)+chromite (cm) inclusion in olivine observed in diogenite LAP 03979……..122

Figure B6. Comparison of chromite compositions in MIL 03443 and diogenites…….123

Figure B7. Comparison of element-element diagrams for MIL 03443 and diogenites..124

Figure B8. Comparison of oxygen isotope compositions of MIL 03443 to the HED $D^{17}O$ average and individual eucrite and diogenite analyses……..…….....125

Figure B9. BSE images showing the systematic distributions of melt inclusions in MIL 03443 olivine……...……126

Part 4

Figure C1. Orthopyroxene Yb vs. Fe# (molar Fe/(Fe+Mg)*100) in (a) five dimict diogenites and (b) samples from the Ultramafic Zone of the Stillwater Complex……..153

Figure C2. Orthopyroxene Y vs. Fe# in (a) five dimict diogenites and (b) samples from the Ultramafic Zone of the Stillwater Complex……..154

Figure C3. Orthopyroxene REE/CI for (a) three dimict diogenites and (b) samples from the Ultramafic Zone of the Stillwater Complex……..155

Figure C4. Orthopyroxene REE/CI for two dimict diogenites……...156

Figure C5. Plagioclase REE/CI in the orthopyroxenite fraction of three dimict diogenites.....157

Figure C6. (a) Expected orthopyroxene REE/CI for the two lithologies in LEW 88008, calculated after [a]Jones (1995), and (b) expected orthopyroxene REE/CI vs. actual (measured) REE/CI for LEW 88008...……...…..…158

Part 5

Figure D1. Histogram of orthopyroxene mg# for diogenites……..….218

Figure D2. Al_2O_3 vs. mg# for chromites…….219

Figure D3. Major element compositions of diogenites determined by LA-ICP-MS of fused beads in this work compared to literature data on diogenites……220

Figure D4. La vs. Yb and Hf vs. Yb for the diogenites studied here and literature analyses……...221

Figure D5. REE diagram for GRA 98108 and LEW 88679 compared to two orthopyroxene/melt distribution coefficient sets; J calculated after Jones (1995) and SM from Schwandt and McKay (1998)……...222

Figure D6. Eu vs. Gd for acid leached diogenites from Barrat et al. (2010) and (untreated) GRA 98108 from this study…….223

Figure D7. Eu/Eu* vs. Gd/Lu and Eu/Eu* vs. La/Sm for leached diogenites from Barrat et al. (2010) compared to unleached GRA 98108 and LEW 88679 from this study……224

Part 6

Figure F1. (a)Cross-polarized image of howardite PCA 02015, (b) typical composite x-ray map of 4 elements, (c) composite x-ray map of 8 elements, where minerals belonging to specific HED lithologies have been grouped, and denoted by different colors..…...……..……..…….……..259

Figure F2. Pyroxene and olivine compositions in the PCA02 howardites…….260

Figure F3. Plagioclase end member compositions for six paired howardites……261

Figure F4. BSE image of K-rich (K_2O = 10.1 wt.%) glass in howardite PCA 02014...262

Figure F5. BSE image of a lithified regolith clast in PCA 02019,4…..……...……..263

Figure F6. Impact melt breccia clast in PCA 02015……..264

Figure F7. BSE images of an impact melt breccia clast in the howardite PCA 02014..265

Figure F8. . A possible type IIB chondrule in PCA 02014……...……..…266

Figure F9. False color lithologic distribution maps of two howardites…….....267

Figure F10. False color lithologic distribution maps of the remaining howardites……268

Figure F11. Bulk composition of matrix in PCA 02 impact melt breccia clasts vs. bulk eucrite/diogenite, modified after Usui and McSween (2007)…….……269

Part 1
Introduction

Asteroid 4 Vesta is the largest surviving differentiated asteroid (Keil 2005). Early in solar system history, radiogenic heating caused Vesta to segregate minerals into a crust, mantle, and core (Ghosh and McSween 1998). Subsequent cooling, combined with a lack of tectonic activity on Vesta, has preserved an unparalleled picture of protoplanetary evolution in the early solar system. The differentiated layers of Vesta hold the key to understanding bodies that may have accreted to form the terrestrial planets.

Visible/near-infrared reflectance spectra of Vesta collected by the ground-based telescopes (McCord et al. 1970) closely match the spectra of a group of petrogenetically linked achondrites, known as the HEDs (Howardite, Eucrite, and Diogenite) (Mason 1962, Stolper 1977), suggesting they might have been derived from Vesta. This is supported by the discovery of many smaller asteroids ("vestoids") with similar spectra to Vesta near the 3:1 resonance, which functions as an escape hatch (Binzel and Xu 1993). Eucrites represent the fine-grained basaltic volcanic outer crust of Vesta, whereas diogenites are coarser-grained, orthopyroxene and olivine-orthopyroxene cumulates of the lower crust or upper mantle. Howardites are regolith breccias composed mostly of coarse eucrite and diogenite clasts derived from surficial impact excavation (McSween et al. 2011). Theories for HED petrogenesis commonly employ either partial melting (Stolper 1977) or fractional crystallization (Ikeda and Takeda 1985), with the latter sometimes modeled as a magma ocean (Righter and Drake 1997; Ruzicka et al. 1997). HED meteorites are hand samples that can be analyzed in a laboratory setting to elucidate the intricacies of differentiation on Vesta. Laboratory analyses of these meteorites, coupled with remote sensing of the units on Vesta, would help confirm differentiation

theories. Identifying geochemical and petrographic variations of differentiated layers will also allow for the improved interpretation of spacecraft observations, like those from the Dawn mission, which began mapping the surface compositions of Vesta in mid-2011 (Russell et al. 2004).

1.0 DIOGENITES

Diogenites are mostly orthopyroxene (84-100% by volume), with minor amounts olivine, accessory chromite, FeNi metal, and troilite, along with rare plagioclase and phosphate (Bowman et al. 1997). Diogenite orthopyroxene compositions vary on slightly, ranging from En_{69-76} (Fowler et al. 1994, Berkley and Boynton 1992). Similarly, olivine compositions in diogenites span a very narrow range, from Fo_{70-73} (McSween et al. 2011).

While most diogenites are almost entirely orthopyroxene, a few diogenites have been found to have greater amounts of olivine (>10% modal olivine) and have been dubbed “olivine diogenites” (Sack et al. 1991). The high olivine/pyroxene modal ratio, and lack of plagioclase in these samples, are consistent with residual materials predicted for partial melting on Vesta (Sack et al. 1991). However, subsequent modal analysis of different sections from these two meteorites resulted in <10% modal olivine and contradicts the notion that "olivine diogenites" are a separate group of meteorites from the diogenites. Mittlefehldt (1994) and Bowman (1997) measured the abundance of olivine in these meteorites to be 1/3 the volume reported by Sack et al. (1991). They suggest that the high abundance of olivine in the sections analyzed by Sack et al. (1991) is due to sampling bias.

In part 2 we conduct an investigation into the occurrence of olivine in both brecciated and unbrecciated diogenites. In the course of that investigation, we test the hypothesis that the brecciated samples may be composed of multiple lithologies. We also examine mineral major and minor element chemistries of phases in these samples in an effort to detect how these lithologies might have formed on Vesta. In part 3 we conduct a comprehensive study of an anomalous achondritic dunite, testing the hypothesis that it belongs with the HED group. We also examine its possible petrogenetic relationship between it and the diogenite group, discerning if it is a cumulate like the diogenites, or a piece of the Vestan sample. Part 4 further tests the hypothesis that the diogenite breccias examined in part 2 are in fact dimict, i.e. composed of two distinct lithologies. To test this hypothesis, we conduct in situ trace elements on the different lithologic clasts in five samples. This will also aid in constraining the igneous processes that separated the two lithologies. We measure bulk compositional variation among a large group of diogenites in part 5 in an effort to further constrain the genesis of this group as a whole. This work also investigates a few samples which have anomalously high trace incompatible element concentrations, and tests a hypothesis, proposed by Barrat et al. (2010), that very low Eu concentrations in diogenite bulk chemistries are due to anatexis of eucritic material.

2.0 HOWARDITES

Howardites are fragmental and regolith breccias that primarily consist of eucrite and diogenite clasts. These breccias are formed by impact and local mixing on or near the surface of Vesta (Bunch 1975). Howardites typically contain coarse fragments embedded in a fine-grained matrix (e.g. Delaney et al. 1984; Bunch 1975). Impact-

generated features (i.e. glass and impact-melt rocks) can also be found in howardites due to their formation mechanism. Ground-based observation suggests that much of the Vestan surface is covered in howardite-like material (Gaffey 1997). Understanding the petrologic variation in these samples will be essential in data interpretation for the Dawn mission.

Collectively, the Pecora Escarpment Icefield (PCA) howardites, recovered in 2002, represent a $\geq$ 1m (diameter) piece of the Vestan surface (Welten et al. 2008). This is one of the largest pieces yet identified in the meteorite collection. In part 6 we investigate the petrologic and textural variation within the PCA02 group of howardites. Constraining this variation will be valuable not only in data interpretation from Dawn, but also further our understanding of regolith maturity on Vesta.

3.0 AUTHORSHIP

Parts of this dissertation have multiple authors, and before relevant parts those authors are identified. In most cases, coauthors were added in agreement with the use of their analytical facilities. Andrew Beck wrote the entirety of parts 2, 4 and 6, and he wrote all but three sections of part 3. David W. Mittlefehldt, an expert in diogenite bulk chemistry, was the primary author of part 5. Andrew wrote three sections of that part, and is the second author. Andrew collected the nearly all of the data reported in this dissertation. Any data he did not collect is noted prior to each part.

REFERENCES

Barrat J. A., Yamaguchi A., Zanda B., Bollinger C., and Bohn M. (2010) Relative chronology of crust formation on asteroid Vesta: Insights from the geochemistry of diogenites. *Geochimica et Cosmochimica Acta* **74**:6218–6231.

Berkley J. L. and Boynton N. J. (1992) Minor/major element variation within and among diogenite and howardite orthopyroxenite groups. *Meteoritics* **27**:387-394.

Binzel R. P. and Xu S. (1993) Chips off of asteroid 4 Vesta: Evidence for the parent body of basaltic achondrite meteorites. *Science* **260:**186-191.

Bowman L. E., Spilde M. N. and Papike J. J. (1997) Automated energy dispersive spectrometer modal analysis applied to the diogenites. *Meteoritics and Planetary Science*. **32**:869-875.

Bunch T. E. (1975). Petrography and petrology of basaltic achondrite polymict breccias (howardites). Proceedings of the Lunar and Planetary Science Conference VI, **1**:469-492.

Delaney J. S., Prinz M., and Takeda H. (1984) The polymict eucrites. Proceedings of the Lunar and Planetary Science Conference XV, **89**:C251-C288

Fowler G. W., Papike J. J., Spilde M. N. and Shearer C. K. (1994) Diogenites as asteroidal cumulates: Insights from orthopyroxene major and minor element chemistry. *Geochimica et Cosmochimica Acta* **58**:3921-3929.

Gaffey M. J. (1997) Surface lithologic heterogeneity of asteroid 4Vesta. *Icarus* **127**:130-157.

Ghosh A. and McSween H. Y. (1998) A Thermal Model for the Differentiation of Asteroid 4 Vesta, Based on Radiogenic Heating. *Icarus* **134**:187-206.

Ikeda Y. and Takeda H. (1985). A model for the origin of basaltic achondrites based on the yamato 7309 meteorite. *Journal of Geophysical Research* **90**:C649-C663.

Keil K. (2005) Geological history of asteroid 4 Vesta: The smallest terrestrial planet. In *Asteroids III*, edited by Bottke W., Cellino A., Paolicchi P., and Binzel R. University of Arizona Press, Tucson, AZ.

Mason B. H. (1962) The Achondrites. In *Meteorites*, J. Wiley & Sons, New York, NY.

Mittlefehldt D. W. (1994) The genesis of diogenites and HED parent body petrogenesis. *Geochimica et Cosmochimica Acta* **58**:1537-1552.

McSween H. Y., Mittlefehldt D. W., Beck A. W., Mayne R. G., and McCoy T. J. (2011)

HED meteorites and their relationship to the geology of Vesta and the Dawn mission. *Space Science Reviews*, doi: 10.1007/s11214-010-9637-z.

Righter K. and Drake M. (1997) A magma ocean on Vesta: Core formation and petrogenesis of eucrites and diogenites. *Meteoritics and Planetary Science* **32**:929-944.

Russell C., Coradini A., Christensen U., De Sanctis M., Feldman W., Jaumann R., Keller H., Konopliv A., McCord T., McFadden L., McSween H., Mottola S., Neukum G., Pieters C., Prettyman T., Raymond C., Smith D., Sykes M., Williams B., Wise J., and Zuber M. (2004) Dawn: A journey in space and time. *Planetary and Space Science* **52**:465-489.

Ruzicka A., Synder G. A., and Taylor L. A. (1997) Vesta as the howardite, eucrite, and diogenite parent body: Implications for the size of a core and for large scale differentiation. *Meteoritics and Planetary Science* **32**:825-840.

Sack R. O., Azeredo W. J. and Lipschutz M. E. (1991) Olivine diogenites: The mantle of the eucrite parent body. *Geochimica et Cosmochimica Acta* **55**:1111-1120.

Stolper E. (1977) Experimental petrology of eucrite meteorites. *Geochimica et Cosmochimica Acta* **41**:587-611.

Usui T. and McSween H. Y. (2007) Geochemistry of 4 Vesta based on HED meteorites: Prospective study for interpretation of gamma ray and neutron spectra for the Dawn mission. *Meteoritics and Planetary Science* **42**:455-269.

Welten K.C., Caffee M.W., and Beck A.W. (2009) Cosmogenic radionuclides in three paired howardites and a polymict diogenites from Pecora Escarpment Icefield, Antarctica (abstract). Meteoritics and Planetary Science **44**:A216.

Part 2
Diogenites as polymict breccias composed of harzburgite and orthopyroxenite

This part is a reformatted version of a paper of the same name published in Meteoritics and Planetary Science in 2010. Andrew Beck and Hap McSween wrote this paper. Andrew preformed all data analyses.

Beck A. W. and McSween H. Y. (2010) Diogenites as polymict breccias composed of orthopyroxenite and harzburgite. *Meteoritics and Planetary Science* **45**:850-872.

Abstract

A few relatively unbrecciated olivine-rich diogenites consist of an equilibrium assemblage of olivine and magnesian orthopyroxene (harzburgite). More common diogenites with smaller amounts of olivine are breccias containing two distinct orthopyroxenes – one magnesian and one ferroan. These diogenites are mixtures of a harzburgite lithology that is more magnesian, with the 'normal' orthopyroxenite lithology that is ferroan and may contain small amounts of plagioclase. Both lithologies likely formed by fractional crystallization in multiple plutons emplaced within the crust of asteroid 4Vesta. Minor element trends in orthopyroxenes indicate that these plutons exhibited a range of compositions. We propose a revised taxonomy for the HED suite where all ultramafic samples are referred to as *diogenites*. Within this group, the prefixes *dunitic*, *harzburgitic*, and *orthopyroxenitic* are used to distinguish diogenites consisting of ≥90% olivine, olivine + orthopyroxene, and ≥90% orthopyroxene, respectively. The prefix *polymict* is used to describe brecciated mixtures of any of these rock types. The recognition that olivine is a significant phase in some diogenites is consistent with spectral interpretations of olivine in a deeply excavated crater on Vesta, and has important implications for the bulk composition and petrogenesis of that body.

1.0 INTRODUCTION

Diogenites are orthopyroxenite cumulate rocks that are linked with the eucrites and howardites. Together, these three meteorite classes constitute the most voluminous group of achondrites, the HEDs (Mittlefehldt et al. 1998). Asteroid 4Vesta is thought to be the parent body for most HEDs, based on spectral similarities (McCord et al. 1970; Binzel et al. 1997). Most diogenites are composed primarily of orthopyroxene (85-100%) with small amounts of other minerals, including chromite, olivine, exsolved clinopyroxene, plagioclase, and accessory troilite, FeNi metal and phosphate (Mittlefehldt 1994; Bowman et al. 1997). The nearly monomineralic nature of the diogenites and their uniform bulk compositions have made them relatively easy to account for in Vestan petrogenetic models, compared to the wide variations among the eucrites (Mittlefehldt et al. 1998). However, significant variations do exist in orthopyroxene minor and trace element concentrations (Fowler et al. 1994,1995; Mittlefehldt 1994), spinel compositions (Bowman et al. 1999), and bulk rare earth element (REE) concentrations (Mittlefehldt et al. 2009; Barrat et al. 2008). These findings suggest that there is more to the petrogenesis of the diogenites than has been commonly appreciated.

Almost all diogenites are breccias, comprised of crystals up to 5 cm in diameter (Mason 1963). The brecciated nature of these samples can lead to difficulties in determining primary phase relationships and thus their petrogenesis. For example, olivine occurs exclusively as brecciated fragments in the matrix and is reported in less than one-third of the samples recovered from Antarctica. Only a few reports exist describing olivine in non-brecciated contact with adjacent pyroxene grains (Barrat et al.

2006; Mittlefehldt 1994, 2000). However, traditional petrogenetic models for Vesta invoke widespread crystallization of olivine (Righter and Drake 1997; Grove and Bartels 1992) because of the high abundance of that phase in chondritic precursors (Jones 1984). While it seems logical for olivine to be a primary phase in diogenites, the textural ambiguity and lack of olivine in a majority of the samples prompts a reassessment of olivine occurrence in these meteorites.

Although the vast majority of diogenites are dominated by orthopyroxene, a few unusually olivine-rich (up to 68 vol. %) diogenites exist (Bowman et al. 1997; Irving et al. 2009). Initially it was proposed that these samples, dubbed "olivine diogenites", were pieces of depleted peridotite mantle residue after melts had been extracted (Sack et al. 1991). This would place them in a separate category from 'normal' diogenites, which are thought to have crystallized from magmas in the lower crust of Vesta. Subsequent modal analyses of other thin sections of the olivine diogenites, however, revealed significantly less to no olivine present (Bowman et al. 1997). This observation, coupled with the realization that orthopyroxene compositions in the olivine diogenites are very similar to those in 'normal' diogenites (Mittlefehldt 1994; Fowler et al. 1995), suggests that they are not mantle residues but likely crustal cumulates as well. Their petrologic relationship to the rest of the diogenites, though, remains undetermined. The heterogeneity in olivine abundance also presents a challenge in distinguishing olivine diogenites from normal diogenites with accessory olivine. For example, section 115 of EETA79002 contains 68% olivine and would be classified as an olivine diogenite, whereas section #145 contains no olivine and would thus have a diogenite classification (Bowman et al. 1997). Understanding the petrologic relationship of olivine in the diogenite group and

determining an appropriate classification scheme have become more pressing with the recovery of additional olivine-rich samples (Righter 2001; Irving et al. 2003).

The scarce abundance of olivine in most HEDs is even more perplexing considering the discovery of purported olivine-rich material at the south pole of Vesta (Binzel et al. 1997). This region is heavily cratered, exposing parts of the lower crust and possibly the mantle (Thomas et al. 1997). Excavation of this huge crater is thought to have provided the Vestoid family (small asteroids spectrally similar to Vesta), which may in turn have been sources for many HEDs (Binzel and Xu 1993).

In this study we will constrain the occurrence of olivine in 'normal' diogenites and address the question of why olivine is not ubiquitous in that group. Second, we will explore the nature of the olivine-rich diogenites and their relationship to the rest of the HEDs. Beyond this, our observations could alleviate the problematic and confusing classification scheme that currently exists.

2.0 METHODS

Thirteen diogenites having a range in olivine abundance were selected for this study. Ten are classified strictly as diogenites, with between 0-10% olivine, two of the samples are "olivine diogenites" (>10% olivine) and one is a dunite (>90% olivine), which has been tentatively tied to the HED group based on similarities in silicate compositions and phase abundances (Krawczynski et al. 2008; Mittlefehldt 2008). At the time of selection, we chose all of the available olivine diogenites recovered from Antarctica except EETA79002, which is already well characterized (Mittlefehldt 2000). Selection of the other samples was based primarily on degree of alteration and sample

size. Observations of multiple thin sections at NASA-JSC were also used to aid in sample selection.

Chemical analyses were made using a Cameca SX-100 electron microprobe (EMP) at the University of Tennessee. Analytical conditions were: 20 kV, 30 nA, 2 μm beam for pyroxene, olivine, chromite, metal and troilite; 15 kV, 10-20 nA, 8-10 μm beam for plagioclase, glass and phosphate. Backscatter electron (BSE) images were collected at 20 kV and 30 nA. Counting times for major elements ranged from 20-40 s, while minor elements had counting times of 60-80 s. Approximately 140 analyses were conducted for each sample. Only analyses that had significant oxide totals (98.5-101 wt.%) and acceptable stoichiometry were used. Sodium was measured in all pyroxenes; however it was below the detection limit and will not be reported.

Modal abundances were determined using an energy dispersive spectrometer on a Cameca SX-50 EMP. A grid of approximately 75,000 points across the entire section was used, as described in Bowman et al. (1997) and Taylor et al. (1996). Analytical conditions were: 15 kV, 4 nA and 70 ms per phase. Quantitative analyses were used to determine appropriate phase filter conditions for each sample. MIL 03443 was not available at the beginning of this study when the SX-50 EMP was used. As a result, its phase abundances were estimated using optical point counting.

The compositions of both cores and rims of grains were measured and are reported where appropriate. However, only core analyses were used when comparing adjacent grains thought to be from the same parent lithology (see section 4.1). Rim analyses of adjoining grains were not used because of the widespread secondary equilibration that has affected the diogenites (Fowler et al. 1995; Mittlefehldt 1994).

Using such analyses may in fact show that the two phases are in equilibrium, but the equilibration may not be due to the two phases co-crystallizing from a melt, but from metamorphic effects.

Finally, before reporting the average composition and standard deviation for a particular mineral, the data were tested for normality using SAS/SAT® software. If the mineral compositions from a sample did not have a normal distribution, or the data volume was too small to calculate a meaningful average, then a "representative" analysis is reported. If the data were normally distributed, the average, standard deviation and number of analyses are given. In the case of orthopyroxene, many of the samples showed a bimodal distribution in composition. In such a case, the data were separated into two groups, and each group was then re-tested for normality. A subsequent pass of the normality test resulted in the reporting of two compositional averages, with respective standard deviations and numbers of analyses.

3.0 RESULTS

3.1 Modal Mineralogy

Modal mineralogy results are displayed in Figure A1 and Table A1. Orthopyroxene and olivine abundances are similar to those in other diogenites (Bowman et al. 1997). Excluding the dunite breccia MIL 03443, three samples contain >10% olivine, eight samples have between 1-10%, and one sample has no measurable olivine in the thin section studied. QUE 99050,4 and LEW 88679,8 have olivine abundances that are significantly different from those previously reported in Antarctic Meteorite

Newsletters (AMN-24 and AMN-15 respectively), suggesting they are heterogeneous breccias.

Plagioclase + clinopyroxene comprise >8% of PCA 02008, ALH 85015, EET 83246 and MIL 03368. The clinopyroxenes in EET 83246 and MIL 03368 occur as small exsolution lamellae in orthopyroxene as well as smaller fragments in the matrix. However, in PCA 02008 and ALH 85015 all of the clinopyroxene and plagioclase occur in small basaltic fragments localized in veins between the dominant, and much larger, clasts of orthopyroxene and olivine. This suggests that the incorporation of clinopyroxene and plagioclase arises from the brecciation and admixture of eucritic material. The pairing of PCA 02008 to the PCA 02' group of howardites based on cosmogenic nuclide data (Welten et al. 2009) and the interpretation that other sections of ALH 85015 appear more howardite-like (Berkley and Boynton 1992) support this hypothesis.

3.2 Mineral Compositions and Textures

Pyroxene

Two distinct orthopyroxene compositions were observed in nine samples. This distinction in pyroxene Fe# [molar Fe/(Mg+Fe)*100] can be seen in the bimodal distribution of the first nine plots in Figure A2. Three of the samples contain only one composition of pyroxene, and are shown at the bottom of Figure A2. The bimodal distributions in orthopyroxenes are in contrast to the traditional findings in diogenites, that orthopyroxenes are homogeneous in composition (Fowler et al. 1994; Mittlefehldt 1994). The main chemical distinction between the two phases is in Fe#, although the ferroan pyroxene tends to be slightly more calcic. The terms magnesian and ferroan are

relative and the compositions differ from sample to sample. Average compositions for the ferroan and magnesian orthopyroxene phases are listed in Table A2. In the samples with bimodal distribution, the relative abundance of the magnesian pyroxene phase roughly correlates with the abundance of olivine. In figure A2, samples with bimodal pyroxene distributions are listed in order of increasing olivine abundance to highlight this point. This correlation is less than ideal, likely due to the comparison between modal abundances and a distribution of points selected by an EMP operator. The samples with only one composition of pyroxene contain either 0 or >10% olivine.

Minor element concentrations differ between magnesian and ferroan pyroxenes as well. LEW 88679, LAP 03979, LAP 02216, and PCA 02008 have ferroan orthopyroxenes with higher concentrations of Al_2O_3, Cr_2O_3 and TiO_2 than magnesian orthopyroxenes. The largest variation is in LAP 03979, which ranges from 0.45 Al_2O_3 (wt.%), 0.52 Cr_2O_3, 0.05 TiO_2 in magnesian orthopyroxene to 1.05 Al_2O_3, 0.68 Cr_2O_3, 0.15 TiO_2 in ferroan orthopyroxene (Table A2). ALH 85015 shows a similar pattern in minor elements to those samples listed above, but Cr_2O_3 decreases from magnesian to ferroan orthopyroxenes in this sample. The above described trend in minor elements (increase in Al_2O_3, Cr_2O_3 and TiO_2 from magnesian to ferroan) will be referred to as 'trend 1' in a later section of this paper. LEW 88008, MET 01084 and MIL 03368 show a different pattern. These samples have slightly lower Al_2O_3 and Cr_2O_3 in ferroan orthopyroxene relative to magnesian orthopyroxene, while TiO_2 remains about the same or increases slightly. The largest variation in this subset occurs in MET 01084, which ranges from (wt.%) 1.01 Al_2O_3, 0.51 Cr_2O_3, 0.16 TiO_2 in magnesian orthopyroxene to 0.66 Al_2O_3, 0.37 Cr_2O_3, 0.21 TiO_2 in ferroan orthopyroxene (Table A2). The common

trend in minor elements for these samples (decreases in Al_2O_3 and Cr_2O_3 from magnesian to ferroan, with a minor increase in TiO_2) will be referred to as 'trend 2' in a later section.

ALHA77256 and GRA 98108, the "olivine diogenites", have only one composition of orthopyroxene, which tends to be more magnesian than average diogenites (Mittlefehldt et al. 1998). The minor element concentrations in these pyroxenes are more homogenized and typical of the diogenite group. However, ALHA77256 does contain very Al-rich orthopyroxene, with an average of 1.11 wt.% Al_2O_3 (Table A2). This is higher then most diogenites and has been documented before (Fowler et al. 1994). MIL 03443, the dunite breccia, contains two distinct pyroxene phases, but in this case the distinction is between a clinopyroxene (Ca-rich) and orthopyroxene (Ca-poor), not between two orthopyroxenes with varied Fe#s.

There are also textural differences that correspond to compositions. In the case of diogenites containing two different Fe# orthopyroxene populations, the magnesian phase is always found in close proximity to fragments of olivine. Conversely, ferroan orthopyroxene does not occur near olivine but in some cases, is located near plagioclase grains (Fig. A3). This plagioclase is not the phase in basaltic eucrite clasts mentioned in section 3.1. These grains appear in clasts with ferroan orthopyroxene, not clinopyroxene. The textural relationship between magnesian orthopyroxene and olivine suggests that they were both sampled from a lithology that is separate from the ferroan orthopyroxene +/- plagioclase. It is important to note that these are brecciated fragments of magnesian orthopyroxene and olivine in close proximity. Therefore, although the localization of these mineral fragments may suggest a common lithologic origin, it does not necessitate one. However, there are some grains of magnesian orthopyroxene and olivine in non-

brecciated contact (Fig. A4). We interpret these contacts as primary (igneous) due the absence of fractures at grain boundaries. The occurrence of these pristine clasts of magnesian orthopyroxene and olivine strongly buttresses the interpretation that they are from the same parent lithology. The olivine diogenite sections only contain grains of olivine and orthopyroxene which appear to be in non-brecciated contact (Fig. A5). The similarities in textures between the brecciated clasts of magnesian orthopyroxene and olivine to the relatively unbrecciated olivine diogenites suggests that the later may represent the lithology from which these clasts were derived.

The textural distinction between the two pyroxene phases in the dunite MIL 03443 is quite different. In this meteorite, clinopyroxene occurs as small (≤10 μm), euhedral inclusions in olivine, as previously documented by Mittlefehldt (2008) and Krawczynski et al. (2008). These inclusions are always associated with an opaque assemblage, typically chromite with small amounts of troilite, and rarely FeNi metal (Fig. A6, MIL 03443). The orthopyroxene in this sample occurs as larger, subhedral grains in the matrix and resembles orthopyroxene in diogenites, both texturally and chemically.

Olivine

Average olivine compositions for each sample are listed in Table A3. There is little compositional variation among analyses for a given sample, as seen by the small deviations from the mean. With the exception of two samples, the compositional averages reported here are similar to the typical Fo_{69-73} range reported for other diogenites (Floran et al. 1981; Mittlefehldt 1994; Sack et al. 1991). LEW 88008 and ALH 85015, with $Fo_{61.7}$ and $Fo_{65.5}$ olivine respectively, are both more Fe-rich than

olivine previously reported. Dunite MIL 03443 has $Fo_{73.7}$ olivine, which is not unusually Mg-rich, as might be expected from a residue sample from the Vestan mantle.

Chromite

Due to the non-normal distribution of chromite compositions, and the paucity of this mineral, representative compositions are listed in Table A4. Chromite compositional data are plotted in Figure A7, where samples are grouped based on their classification (Fig. A7a-c) and chromite textures (large and euhedral, small and at grain boundaries, inclusions in olivine). Compositional variations between all the samples fall within the previously reported low-Al/high-Cr to high-Al/low-Cr compositional spectrum (Bowman et al. 1999). Intra-sample variation, however, exists in LAP 03979 where an Al-poor chromite occurs as larger grains in the matrix and a smaller Al-rich phase exists as coronas surrounding olivine grains (Fig. A6, LAP 03979). Based on previous models of chromite crystallization in diogenites, the Al-poor phase should crystallize prior to the Al-rich phase (Bowman et al. 1999). This is consistent with the textures of the two phases (large euhedral grains versus partial coronas). This sequence is further supported by the work of Barrat et al. (2006) who found Al-rich chromites forming through post-crystallization reaction with adjacent olivine grains in other diogenites. The section of LEW 88679 used in this study contains relatively Al-rich chromite that is localized to pyroxene/olivine grain boundaries and intergrown with adjacent silicates (Fig. A3, LEW 88679). These chromites may have formed late through a reaction with adjacent olivine as well. All of the chromites in GRA 98108, and ~90% of those in ALHA77256, both of which are olivine diogenites, occur at grain boundaries between olivine and magnesian orthopyroxene (Fig. A5). Similar to chromites occurring at grain boundaries in LEW

88679 and LAP 03979, these inter-grain chromites are also Al-rich (Fig. A7b). No Al-poor chromites were observed in GRA 98108. ALHA77256 contains only a few Al-poor chromites, which are larger, euhedral grains occurring in the matrix or as inclusions in orthopyroxene. No Al-poor chromites were found in the non-brecciated clasts of olivine + magnesian pyroxene in the normal diogenites. This suggests that the Al-rich chromites occurring at grain boundaries in LAP 03979 and LEW 88679 originated from an olivine diogenite-like parent lithology, whereas the more Al-poor chromites found in the matrix likely come from a normal diogenite lithology.

MIL 03443, the dunite breccia, also contains two compositionally distinct chromites. Al-rich chromite in this sample occurs as fragments in the matrix, not at orthopyroxene/olivine boundaries, and the Al-poor phase is found as inclusions within olivine and in association with the rare clinopyroxene grains (Fig. A6, MIL 03443). Chemically, it seems appropriate for Cr-rich chromites to have crystallized early from the melt (Bowman et al. 1999), and thus occur as inclusions within olivine. However, their exact origin (melt inclusions, trapped melt, etc.) and relationship to surrounding clinopyroxene and troilite grains is unclear and requires further investigation.

Accessory Phases

Plagioclase compositions measured range from $An_{84.1}$ in MET 01084 to $An_{96.5}$ in LEW 88008 (Table A5). The textural relationship of plagioclase to the other phases is difficult to determine due to brecciation and the small amounts of plagioclase. However, as mentioned above, in some cases plagioclase seems to be localized in areas near ferroan orthopyroxene (Fig. A3). The sulfide in all of the samples is troilite, although some had higher concentrations of Ni (Table A6). Most FeNi metal has 0.1-3.0 wt.% Ni and <0.8

wt.% Co (Table A6). ALH 85015 contains a few metal grains with up to 2.28 wt.% Co and 3.27 wt.% Ni. One fluoroapatite grain was found in QUE 99050. Its composition is 41.9 P_2O_5 (wt.%), 0.05 MgO, 54.7 CaO, 0.43 FeO, 0.04 Na_2O, 3.7 F, and 0.08 Cl.

4.0 DISCUSSION

4.1 Equilibrium Between Orthopyroxene and Olivine

As described above, textural and compositional evidence indicates that two separate ultramafic lithologies have been sampled in varying amounts to produce the diogenites: one consists of olivine + magnesian orthopyroxene, and the other consists of ferroan orthopyroxene. To evaluate this hypothesis further, we will examine equilibrium between olivine and the two orthopyroxene phases in each sample. Our observations predict that olivine should be in equilibrium with magnesian orthopyroxene. The average magnesian and ferroan orthopyroxene Fe#s for each meteorite are plotted versus that sample's olivine Fe#. In Figure A8 the large open circles represent Fe-Opx while large closed circles represent Mg-Opx. An open and closed circle pair thus represents each meteorite containing two pyroxene populations. Each pair is plotted over the same x-axis value (the sample's average olivine Fe#). These have been superimposed on a regression line representing previously documented equilibrium assemblages of olivine and orthopyroxene in H, L and LL chondrites (Brearley and Jones 1998), along with main group pallasites (Mittlefehldt 2000) and other diogenites (Mittlefehldt 1994). This regression line closely matches the ratio of Fe#s in low-Ca pyroxene and olivine assemblages derived from eucrite melting experiments (Stolper 1977). The lack of calibration data for more Fe-rich olivine + orthopyroxene assemblages in equilibrium

precludes extension of this line beyond the limits shown. However, experimental data suggests that this line would remain relatively constant into the Fe-rich fields, although a drop in temperature could create a slight decrease in slope (Seckendorff and O'Neill 1993). Also plotted in Figure A8 are data from the olivine diogenites and dunite, along with individual clasts of olivine and orthopyroxene, which are interpreted as having igneous contacts (see Fig. A4). Where the equilibrium line is constrained, magnesian orthopyroxene and olivine appear to be in equilibrium in each sample. We cannot say the same for the two outlying samples (ALH 85015, LEW 88008). The clasts displaying textural evidence of magnesian orthopyroxene and olivine co-crystallization are useful indicators of how this regression line might behave in more Fe-rich fields. The pattern of non-brecciated clasts into the Fe-rich region suggests that an equilibrium regression line for diogenites at these compositions may have a shallower slope, possibly caused by a decrease in temperature. Even with a slight decrease in slope though, a projected regression line through the non-brecciated clasts would still remain above magnesian orthopyroxene averages for ALH 85015 and LEW 88008. This may be due to these samples incorporating orthopyroxene and olivine with a wide variety of compositions from multiple, unrelated sources. The large variations in those mineral compositions are reflected in the x- and y- error bars respectively. With an admixture of pyroxene and olivine from unrelated sources, we would not expect that the average of those values would be anywhere near equilibrium. Other sections of ALH 85015 appearing howardite-like, support this hypothesis (Berkley and Boynton 1992).

Based on equilibrium information and the textural evidence, we conclude that olivine formed concurrently with magnesian pyroxene in a separate lithology from the

ferroan pyroxene in the brecciated diogenite samples. We have calculated a temperature of ~1100°C of olivine-magnesian orthopyroxene assemblages crystallizing with these compositions using the QUILF program (Anderson et al. 1993).

The orthopyroxenes in the olivine diogenites also lie along the equilibrium line. These are the only samples in which all of the pyroxene and olivine are in non-brecciated contact and have very little chemical variation. Thus we interpret this material as representing the lithology from which fragments of olivine and magnesian orthopyroxene were derived and incorporated into the brecciated samples discussed above. Conversely, the ferroan orthopyroxene in the brecciated samples is clearly not in equilibrium with olivine and was likely derived from normal diogenite (orthopyroxenite with no olivine, but perhaps some minor plagioclase). We propose that these two lithologies have been brecciated and mixed together to produce the diogenites containing olivine and two pyroxenes, as depicted in Figure A9.

4.2 Taxonomy

The discovery of two distinct ultramafic lithologies in many members of the diogenite suite indicates that an adjustment to the classification scheme is needed. A similar observation in one meteorite (EETA79002) was made by Mittlefehldt (2000), and we will build upon his work here.

The IUGS classification scheme used for terrestrial ultramafic rocks would categorize these two lithologies as *harzburgite* (magnesian orthopyroxene + olivine) and *orthopyroxenite* (ferroan orthopyroxene +/- minor plagioclase) (Streckeisen, 1976). We propose a new taxonomy for the ultramafic (olivine + pyroxene $\geq$ 90 vol.%) members of the HED meteorite group, drawing on precedents provided by eucrites and shergottites.

When new types of eucrites were distinguished, the prefixes *basaltic*, *cumulate*, and *polymict* were added (e.g. Delaney et al. 1983; Miyamoto et al. 1978). Similarly, new types of shergottites were distinguished by adding the prefixes *basaltic*, *olivine-phyric*, and *lherzolitic* (e.g. Goodrich 2002).

Diogenites are usually described as orthopyroxenites, which is correct in most cases. However, in this paper we recognize diogenites that contain sufficient modal olivine to be classified as harzburgites, as well as a dunite that is apparently related to the HEDs. Previously, uncommonly olivine-rich diogenites have been referred to as olivine diogenites (Sack et al. 1991). To avoid the proliferation of more meteorite names with obscure or imprecise meanings, we propose that *all* ultramafic rocks (having modal olivine + pyroxene ≥ 90 vol. %) of the HED suite be called diogenites. Appropriate prefixes should be added to distinguish the various ultramafic lithologies unambiguously. Thus, the diogenite nomenclature would be:

orthopyroxenitic diogenites, with ≥90 vol. % orthopyroxene,

harzburgitic diogenites, composed of orthopyroxene with >10 to <90 vol. % olivine,

dunitic diogenites, with ≥90 vol. % olivine.

If other types of ultramafic rocks belonging to the HED suite are discovered, they can be named diogenites with an appropriate lithologic modifier, based on IUGS nomenclature (Streckeisen 1976). This scheme has the advantage of not requiring additions to the acronym HED (i.e. addition of "H" for harzburgite or a second "D" for dunite).

Diogenite breccias can be monomict (as are most of the orthopyroxenites), or polymict (as are the majority of the samples described in this paper). *Polymict diogenites* contain clasts or mineral fragments derived from more than one of the diogenite types

above, or diogenite clasts mixed with small quantities (<10%) of eucrite material (Delaney et al. 1983). It is conceivable that through trace element and isotopic analyses it may be demonstrated that all of the clasts in a polymict diogenite are from the same magmatic fractionation sequence. In such a scenario, it would be appropriate to classify that sample as a *genomict diogenite* (Wasson 1974).

We recommend against continued use of the term olivine diogenite. Sack et al. (1991) used this term to describe diogenites with "unusually high olivine concentrations" without indicating what level of olivine content would qualify. Sack et al. (1991) recognized that their olivine diogenites were the "equivalent of terrestrial harzburgites" in tacit agreement with the taxonomy proposed here.

The variability of olivine abundance and its heterogeneous distribution in diogenites present a potential difficulty in utilizing this classification scheme. For example, different thin-sections of EETA79002 contain a range in olivine abundance from 0-68.6% (Bowman et al. 1997). However, some samples of this meteorite contain magnesian and ferroan orthopyroxenes from harzburgite and orthopyroxenite lithologies (Mittlefehldt 2000), and thus it is clearly a *polymict diogenite.* A check for dual pyroxene compositions should be applied to other diogenite breccias of problematic classification. If a sample contains >10% olivine, but also contains >10% of a pyroxene phase not in equilibrium with olivine, it is a *polymict diogenite*. A dual pyroxene check is also needed to correctly classify LEW 88679 as a polymict diogenite (see Table A7).

4.3 Petrogenesis

Harzburgites are found in ophiolites and layered mafic intrusive complexes on Earth. In ophiolites the harzburgites are mainly residues from partial melting and contain

no plagioclase, have polygonal grains with abundant triple junctions and heterogeneous distributions of olivine and are not normally associated with orthopyroxenites (Nicolas et al. 1980). In contrast, layered mafic intrusions formed through fractional crystallization produce cumulate harzburgites and orthopyroxenites with minor amounts of intercumulus plagioclase and heterogeneous olivine distributions (Jackson 1961). Plagioclase occurs in some harzburgitic diogenites (Table A1), olivine is very heterogeneously distributed (Bowman et al. 1997), and there is no evidence of triple junctions. Although the above comparison is somewhat simplified, we believe the most probable process accounting for both lithologies on Vesta is fractional crystallization in magma chambers. We note that Berkley and Boynton (1992) described "well developed triple junctions" in ALHA77256, one of the harzburgitic diogenites. These may be attributable to later metamorphism, not primary processes.

The range of orthopyroxene Fe#s in harzburgite and orthopyroxenite clasts among all the polymict diogenites suggests that a simple (magma ocean) model of fractionation to produce a single diogenite layer is improbable (Ruzicka et al. 1997). Problems arise when trying to reconcile why pyroxenes from some orthopyroxenite clasts from one meteorite are more Mg-rich than pyroxenes from olivine-rich, harzburgite clasts in another meteorite. For example, QUE 99050, an orthopyroxenite, contains no olivine but has some of the most Mg-rich orthopyroxene analyzed (Fig. A2). This problem can be alleviated if diogenites come from multiple plutons, each undergoing fractional crystallization and possibly producing both harzburgite and orthopyroxenite lithologies. Invoking a model whereby multiple batches of magma are injected at different times, similar to that of the Stillwater Complex (Jackson, 1961), might also solve this problem,

but such a scenario is not consistent with a magma ocean. The multiple pluton hypothesis seems more plausible and is supported by trace element analyses of these samples (Mittlefehldt et al. 2009) and of other diogenites (Barrat 2004; Barrat et al. 2008). Dunite formation could also be easily accommodated in the fractional crystallization model, if olivine crystallized and segregated from the melt prior to harzburgite. This model is supported by the extremely Cr-rich chromites found in the dunitic diogenite MIL 03443. It is also possible that this dunite represents depleted mantle from Vesta and is not directly associated with the diogenites, but this seems unlikely (Mittlefehldt 2008). We also note that a magma ocean model, producing a single diogenite layer, might be viable if later re-melting occurred to produce multiple plutons, but such a model seems unnecessarily complicated for an asteroid with a relatively short geologic history.

4.4 Other Possible Formation Scenarios

An alternative interpretation of the textural and chemical evidence linking olivine and magnesian orthopyroxene is that this assemblage equilibrated during thermal metamorphism. A hot ejecta blanket has previously been advocated to explain complex cooling histories in diogenites (Zema et al. 1997). In this scenario, all the orthopyroxenes in an olivine-bearing breccia would initially have come from a single lithology and have the same Fe#s. Post-brecciation equilibration between adjacent pyroxene and olivine grains would lead to the formation of magnesian orthopyroxene, relative to the pyroxene grains not associated with olivine. If this were the case, however, larger pyroxene grains adjacent to olivine would likely display Fe/Mg zonation towards the contacts with olivine, due to incomplete equilibration. We have seen this pattern in only one sample,

and in a very limited area (Fig. A10). Moreover, we see a distinct bimodal distribution in minor element concentrations between ferroan and magnesian orthopyroxene groups in most samples. Even with the variation in minor elements for pyroxenes with homogeneous Fe#s seen in some diogenites (Berkley and Boynton 1992), a more uniform distribution in minor element concentrations would be expected if the two phases were from the same lithology and simply the result of metamorphic equilibration with olivine. This model also ignores the igneous textures in harzburgite clasts. Thus, we reject this explanation.

We also considered the possibility that the harzburgite lithology is not native to Vesta, but was part of a foreign body that impacted and was mixed with the native diogenite lithology. The similar Fe/Mn ratios in orthopyroxenes (Fig. A11), thought to be diagnostic of this parent body (Papike et al. 2003), of the harzburgite and orthopyroxenite clasts, however, argue that both lithologies originated on the HED parent body. Olivine and pyroxene Fe/Mn ratios in these samples are also distinct from those in mesosiderites (Mittlefehldt et al. 1998).

4.5 Minor Element Trends in Pyroxene

The decoupling of major and minor elements in diogenites impedes interpretation of a standard pyroxene Fe# versus minor element variation plot. This decoupling is likely the result of post-crystallization equilibration which homogenized orthopyroxene Fe and Mg concentrations, while preserving the patterns of minor elements having slower diffusivities (Fowler et al. 1994; Mittlefehldt 1994). The same situation has been noted in the pyroxenes of unbrecciated eucrites (Mayne et al. 2009). The harzburgitic diogenites, GRA 98108 and ALHA77256, display this phenomenon (Fig. A12). As

stated before, these samples contain only one lithology and lack extensive brecciation. Thus, all the orthopyroxene in these samples was equilibrated, resulting in the concentration of data points over a very limited Fe# range. The same situation occurs in QUE 99050, which has no olivine or harzburgite component, and thus the section used in this study is considered to represent only the orthopyroxenite lithology. However, the majority of the samples in this study contain fragments of pyroxene from two lithologies, so we see variations between them when looking at minor element variations. If the two lithologies in a sample come from a common igneous source, the relative difference may then be used to further constrain the processes occurring on Vesta. Relative variations that are difficult to explain using igneous processes are likely indicative of a breccia with components from multiple unrelated plutons. Note that correlations seen in pyroxene minor element concentrations cannot definitively tie components in a breccia to a single fractionation sequence, and hence will not be used to determine a genomict versus polymict diogenite classification.

The following is a description of minor element trends seen in the polymict diogenites. Regression analyses were not applied to these data due to the aforementioned bimodal clumping of pyroxene Fe#s. Because of this clumping, applying a regression to these data would result in a misleading correlation coefficient. Instead, interpreted trendlines are used, and are shown in each plot.

As described in section 3.2, the polymict diogenites display two trends in minor elements. Trend 1 is an increase in Al_2O_3, Cr_2O_3 and TiO_2 from magnesian to ferroan orthopyroxenes (Fig. A13). Both aluminum and titanium are incompatible elements in diogenitic orthopyroxene and thus should increase in concentration in a melt where

orthopyroxene is the dominant crystallizing phase (Fowler et al. 1994), as observed in trend 1. Chromium is compatible in orthopyroxene and thus should decrease from harzburgite to orthopyroxenite. However, all the samples in trend 1, with the exception of ALH 85015, show an increase in Cr_2O_3. This phenomenon is difficult to explain and cannot be rationalized based on the crystallization of other phases or other igneous processes. Post-crystallization equilibration may have adjusted Cr_2O_3 concentrations in the form of the Cr-Al tschermak substitutional couple. Evidence supporting this includes the similar pattern seen between Al_2O_3 and Cr_2O_3 in trend 1, the abundance of ^{IV}Al in these pyroxenes (Table 2), and the dominance of the ^{VI}Cr–^{IV}Al substitutional couple in low-Al diogenite pyroxenes (Fowler et al. 1994). Unrelated source plutons for the harzburgite and orthopyroxenite components, however, may offer an easier explanation for the variations in minor elements for trend 1 samples.

Trend 2 samples are shown in Figure A14. These samples show an overall increase in TiO_2 from harzburgite to orthopyroxenite and either 1) slight increases in both Al_2O_3 and Cr_2O_3 within the harzburgite and then an overall decrease to orthopyroxenite (Fig.A14, MET 01084, MIL 03368), or 2) overall decreases in Al_2O_3 and Cr_2O_3 from harzburgite to orthopyroxenite (Fig. A14, LEW 88008). The decrease of Al_2O_3 in LEW 88008 is less distinct, but this sample does show a decrease in Cr_2O_3. Trend 2 samples do not follow a scenario where orthopyroxene is the only crystallizing phase. Instead, this pattern is suggestive of plagioclase beginning to crystallize between harzburgite and orthopyroxenite. Aluminum initially is incompatible in harzburgite orthopyroxene and thus increases slightly, but then the onset of plagioclase crystallization removes aluminum from the melt so that subsequent crystallizing pyroxenes are relatively

depleted in Al_2O_3. This scenario is supported by significant amounts of plagioclase localized near orthopyroxenite fragments in MET 01084 and LEW 88008 (as seen in Fig. A2 MET 01084). Titanium and chromium are not affected by plagioclase crystallization and behave as expected during orthopyroxene crystallization. Similar minor element trends have been observed in Pasamonte (eucrite) and attributed to plagioclase crystallization as well (Ruzicka and Schepker 2008).

The implications of trends 1 and 2 may suggest a modification to the fractional crystallization in plutons model proposed above. The relatively low abundances of Al_2O_3 and the patterns in trend 1 suggest that there was a less primitive source for the plutons producing these samples. Trend 2, on the other hand, displays higher concentrations of Al_2O_3 in harzburgite fragments, and shows evidence both in minor element trends and in textures that plagioclase became a primary phase later in the crystallization sequence. This suggests that trend 2 samples were derived from a relatively more primitive source than those in trend 1. This evidence for multiple sources with varied compositions for diogenitic plutons has also been previously proposed to explain diogenite bulk REE data (Barrat et al. 2008).

5.0 CONCLUSIONS

Diogenites containing olivine are breccias with two distinct compositions of orthopyroxene (magnesian and ferroan). In these samples, olivine is exclusively found in close proximity to, and occasionally in non-brecciated contact with, the magnesian orthopyroxene. The compositions of olivine and magnesian orthopyroxene are in apparent chemical equilibrium. A few olivine-rich diogenites contain only magnesian

orthopyroxene that displays both textural and chemical equilibrium with olivine. From this evidence we propose that the diogenites with olivine are polymict breccias sampling both an olivine + magnesian orthopyroxene lithology and a ferroan orthopyroxene-only lithology. The former are represented by the olivine-rich diogenites, and the latter represent 'normal' orthopyroxenite diogenites. Both lithologies likely originated in multiple plutons through fractional crystallization. Minor element patterns suggest these plutons had varying source compositions. A single dunite sample may have originated in these plutons as well, but might also represent a piece of the Vestan mantle.

We propose a new classification scheme in which *all* ultramafic (olivine + orthopyroxene ≥ 90%) HEDs are called "diogenites". These are subdivided into *dunitic diogenites, harzburgitic diogenites,* and *orthopyroxenitic diogenites,* following the IUGS-approved taxonomy for terrestrial ultramafic rocks. Impact mixing of any of these lithologies has produced *polymict diogenites,* which can be recognized by the occurrence of olivine and two distinct orthopyroxene compositions.

Results from this study have broad implications for interpreting the reported variations in diogenite bulk-rock and mineral geochemistry, petrogenetic models for Vesta, and eventually analysis of spectroscopic data of Vesta from the Dawn spacecraft. Trace element variations in the diogenites likely reflect multiple source plutons, but variations may be enhanced by the dominance of one lithology over another in polymict breccias and possibly in sample splits. No study has yet conducted detailed geochemical analyses on separated harzburgite and orthopyroxenite components from a polymict diogenite. The presence of harzburgite fragments in many of the brecciated diogenites also provides evidence that olivine may be abundant on Vesta. This alleviates

uncertainties in some petrogenetic models for Vesta where the lack of olivine-rich lithologies in the HEDs was problematic. The discovery of a harzburgitic diogenite lithology also suggests interesting possibilities for Dawn mission spectroscopy and mapping. We surmise that larger craters exposing diogenitic plutons could potentially display stratigraphic variations from orthopyroxenitic to harzburgitic and even dunitic diogenite with depth.

ACKNOWLEDGEMENTS

We thank Alex Ruzicka, Tim McCoy and Jean-Alix Barrat for their formal reviews, which considerably improved this manuscript. David Mittlefehldt provided thoughtful comments on our proposed classification scheme. We also thank Cecilia Satterwhite (JSC) for assistance with thin-section observations prior to sample selection. This work was partly supported by NASA cosmochemistry grant NNG06GG36G to HYM.

REFERENCES

Anderson, D. J., Lindsley, D. H. and Davidson, P. M. (1993) QUILF: a PASCAL program to assess equilibria among Fe-Mg-Mn-Ti oxides, pyroxenes, olivine and quartz. *Computers and Geosciences* **19**:1333-1350.

Barrat J. A. (2004) Determination of the parental magmas of HED cumulates: The effects of interstitial melts. *Meteoritics and Planetary Science* **39**:1767-1779.

Barrat J. A., Beck P., Bohn M., Cotten J., Gillet P., Greenwood R. C. and Franchi I. A. (2006) Petrology and geochemistry of the fine-grained, unbrecciated diogenite Northwest Africa 4215. *Meteoritics and Planetary Science* **41**:1045-1057.

Barrat J. A., Yamaguchi A., Greenwood R. C., Benoit M., Cotten J., Bohn M. and Franchi I. A. (2008) Geochemistry of diogenites; still more diversity in their parental melts. *Meteoritics and Planetary Science* **43**:1759-1775.

Berkley J. L. and Boynton N. J. (1992) Minor/major elment variation within and among diogenite and howardite orthopyroxenite groups. *Meteoritics* **27**:387-394.

Brearley A. J. and Jones R. H. (1998) Chondritic meteorites. In Planetary Materials, edited by J. J. Papike, Mineralogical Society of America, *Reviews in Mineralogy* **36**:3.1-3.398,

Binzel R. P., Gaffey M. J., Thomas P. C., Zellner B. H., Storrs A. D. and Wells E. N. (1997) Geologic mapping of Vesta from 1994 Hubble Space Telescope images. *Icarus* **128**:95-103.

Binzel R. P. and Xu S. (1993) Chips off of Asteroid 4Vesta; evidence for the parent body of basaltic achondrite meteorites. *Science* **260**:186-191.

Bowman L. E., Papike J. J. and Spilde M. N. (1999) Diogenites as asteroidal cumulates: Insights from spinel chemistry. *American Mineralogist* **84**:1020-1026.

Bowman L. E., Spilde M. N. and Papike J. J. (1997) Automated energy dispersive spectrometer modal analysis applied to the diogenites. *Meteoritics and Planetary Science* **32**:869-875.

Delaney J. S., Takeda H., Prinz M., Nehru C. E. and Harlow G. E. (1983) The nomenclature of polymict basaltic achondrites. *Meteoritics* **18**:103-111.

Floran R. J., Prinz M., Hlava P. F., Keil K., Spettel B. and Wanke H. (1981) Mineralogy, petrology, and trace element geochemistry of the Johnstown Meteorite: A brecciated orthopyroxenite with siderophile and REE-rich components. *Geochimicia et Cosmochimica Acta* **45**:2385-2391.

Fowler G. W., Papike J. J., Spilde M. N. and Shearer C. K. (1994) Diogenites as asteroidal cumulates: Insights from orthopyroxene major and minor element chemistry. *Geochimicia et Cosmochimica Acta* **58**:3921-3929.

Fowler G. W., Shearer C. K. and Papike J. J. (1995) Diogenites as asteroidal cumulates: Insights from orthopyroxene trace element chemistry. *Geochimicia et Cosmochimica Acta* **59**:3071-3084.

Goodrich C. A. (2002) Olivine-phyric Martian basalts: A new type of shergottite. *Meteoritics and Planetary Science* **37**:B31-B34.

Grove T. L. and Bartels K. S. (1992) The relation between diogenite cumulates and eucrite magmas. *Procedings of the Lunar and Planetary Science Conference* **22**:437-445.

Irving A. J., Bunch T. E., Kuehner S. M., Wittke J. H. and Rumble D. (2009) Peridotites related to 4Vesta: Deep crustal igneous cumulates and mantle samples. *40th Lunar and Planetary Science Conference* **#2466.**

Irving A. J., Kuehner S. M., Rumble D., Hupe A. C. and Hupe G. M. (2003) Olivine diogenite NWA 1459: Plumbing the depths of 4Vesta. *34th Lunar and Planetary Science Conference* **#1502**.

Jackson E. D. (1961) Primary Textures and Mineral Associations in the Ultramafic Zone of the Stillwater Complex. *U. S. Geological Survey Professional Paper*. **#358.**

Jones J. H. (1984) The composition of the mantle of the eucrite parent body and the origin of eucrites. *Geochimicia et Cosmochimica Acta* **48**:641-648.

Krawczynski M. J., Elkins-Tanton L. T. and Grove T. L. (2008) Petrology of mesosiderite(?) MIL 03443,9; constraints on eucrite parent body bulk composition and magmatic processes. *39th Lunar and Planetary Science Conference* **#1229**.

Mason B. (1963) The Hypersthene Achondrites. *American Museum Novitates* **2155**.

Mayne R. G., McSween H. Y., McCoy T. J. and Gale A. (2009) Petrology of the unbrecciated eucrites. *Geochimicia et Cosmochimica Acta* **73**:794-819.

McBride K., McCoy T. and Welzenbach L. (2001) *Antarctic Meteorite Newsletter* **24**, no. 1.

McCord T. B., Adams J. B. and Johnson T. V. (1970) Asteroid Vesta: Spectral reflectivity and compositional implications. *Science* **168**:1445-1447.

Mittlefehldt D. W. (1994) The genesis of diogenites and HED parent body petrogenesis. *Geochimicia et Cosmochimica Acta* **58**:1537-1552.

Mittlefehldt D. W. (2000) Petrology and geochemistry of the Elephant Moraine A79002 diogenite: A genomict breccia containing a magnesian harzburgite component. *Meteoritics and Planetary Science* **35**:901-912.

Mittlefehldt D. W. (2008) Meteorite dunite breccia MIL 03443: A probable crustal cumulate closely related to diogenites from the HED parent asteroid. *39th Lunar and Planetary Science Conference* **#1919**.

Mittlefehldt D. W., Beck A. W., Lee C.-T. A. and McSween H. Y. (2009) Chemistry of diogenites and evolution of their parent asteroid. *40th Lunar an Planetary Science Conference* **#1038**.

Mittlefehldt D. W., McCoy T. J., Goodrich C. A. and Kracher A. (1998) Non-chondritic meteorites from asteroidal bodies. In Planetary Materials, J. J. Papike, ed., *Reviews in Mineralogy and Geochemistry* **36**, 4.1-4.195, Mineral. Soc. Am.

Miyamoto M., Takeda H. and Tanai K. (1978) Yamato achondrite polymict breccias. *National Institute of Polar Research Special Issue* **8**:185-197.

Nicolas A., Boudier F. and Bouchez J.-L. (1980) Interpretation of peridotite structires from opiolitic and oceanic environments. *American Journal of Science.* **280**:192-210.

Papike J. J., Karner J. M. and Shearer C. K. (2001) Mn-Fe systematics in pyroxene from planetary basalts: an indicator of planetary parentage. *32nd Lunar and Planetary Science Conference* **#1009.**

Papike J. J., Karner J. M. and Shearer C. K. (2003) Determination of planetary basalt parentage: A simple technique using the electron microprobe. *American Mineralogist* **88**, 469-472.

Righter K. (2001) Petrography, mineralogy and petrology of two new HED meteorites; diogenite GRA98108 and howardite GRA98030. *32nd Lunar and Planetary Science Conference* **#1765**.

Righter K. and Drake M. J. (1997) A magma ocean on Vesta: Core formation and petrogenesis of eucrites and diogenites. *Meteoritics and Planetary Science* **32**:929-944.

Ruzicka A. and Schepker T. J. (2008) Trace-element analyses of pyroxene and plagioclase in three HED meteorites. *Meteoritics and Planetary Science* **43**:#5310.

Ruzicka A., Snyder G. A. and Lawrence L. A. (1997) Vesta as the howardite, eucrite and diogenite parent body: Implications for the size of a core and for large-scale differentiation. *Meteoritics and Planetary Science* **32**:825-840.

Sack R. O., Azeredo W. J. and Lipschutz M. E. (1991) Olivine diogenites: The mantle of the eucrite parent body. *Geochimica et Cosmochimica Acta* **55**:1111-1120.

Satterwhite C. and Mason B. (1992) *Antarctic Meteorite Newsletter* **15**, no. 1.

Seckendorff V. V. and O'Neill H. St.C. (1993) An experimental study of Fe-Mg partitioning between olivine and orthopyroxene at 1173, 1273 and 1423 K and 1.6 GPa. *Contributions to Mineralogy and Petrology* **113**:196-207.

Stolper E. (1977) Experimental petrology of eucritic meteorites. *Geochimica et Cosmochimica Acta* **41**:587-611.

Streckeisen A. L. (1976) To each plutonic rock its proper name. *Earth Science Reviews* **12**:1-33.

Taylor L. A., Patchen A., Taylor D. S., Chambers J. G. and McKay, D. S. (1996) X-ray digital imaging petrography of lunar mare soils: Modal analyses of minerals and glasses. *Icarus* **124**:500-512.

Thomas P. C., Binzel R. P., Gaffey M. J., Storrs A. D., Wells E. N. and Zellner B. H. (1997) Impact excavation on Asteroid 4Vesta: Hubble Space Telescope results. *Science* **277**:1492-1495.

Wasson J. T. (1974) *Meteorites: Classification and properties,* 1st ed. New York: Springer-Verlag. 316 p.

Welten K. C., Vaffee M. W. and Beck A. W. (2009) Cosmogenic radionuclides in three paired howardites and a polymict diogenite from Pescora Escarpment Icefield, Antarctica. In *72nd Meteoritical Society Meeting*.

Zema M., Domeneghetti M. C., Molin G. M. and Tazzoli V. (1997) Cooling rates of diogenites; a study of Fe (super 2+) -Mg ordering in orthopyroxene by single-crystal X-ray diffraction. *Meteoritics and Planetary Science* **32**:855-862.

Appendix A

Table A1. Modal mineralogy.

Sample, section#	QUE 99050,4	EET 83246,4	LEW 88008,1	LAP 02216,15	MIL 03368,7	PCA 02008,8	LAP 03979,5	ALH 85015,3	MET 01084,5	ALHA77256,128	LEW 88679,8	GRA 98108,16	MIL03443,17*
Orthopyroxene	97.8	89.6	93.8	96.7	83.5	86.8	89.0	84.1	88.6	85.2	81.5	79.4	5.0
Olivine	0.0	1.3	1.6	2.0	2.2	3.7	4.6	4.6	6.1	10.6	14.6	18.5	91.0
Chromite	0.6	0.1	0.2	0.2	1.8	0.3	0.2	0.6	0.1	0.8	0.1	0.2	1.0
Clinopyroxene	0.7	8.7	1.8	0.3	12.1	7.3	1.9	4.9	1.4	3.2	1.8	1.0	0.7
Plagioclase	0.0	0.0	2.2	0.0	0.0	1.3	3.9	5.0	3.6	0.1	0.4	0.3	0.0
FeNi Metal	0.0	0.0	0.0	0.2	0.1	0.1	0.1	0.0	0.0	0.0	0.1	0.2	0.3
Troilite	0.0	0.1	0.3	0.6	0.1	0.2	0.3	0.7	0.1	0.1	1.5	0.4	2.0
Silica	0.0	0.2	0.0	0.0	0.2	0.3	0.0	0.1	0.0	0.0	0.0	0.1	0.0
Phosphate	0.9	0.0	0.0	0.0	0.0	0.0	0.0	0.0	0.0	0.0	0.0	0.0	0.0

* Determined using optical point counting. All other modes determined using an EMP.

Table A2. Average pyroxene compositions.

Sample	EET 83246		LEW 88008		LAP 02216		MIL 03368		PCA 02008		LAP 03979	
	Magnesian	Ferroan	Magnesian	Ferroan	Magnesian	Ferroan	Magnesian	Ferroan	Magnesian	Ferroan	Magnesian	Ferroan
N	**11**	**66**	**30**	**33**	**20**	**75**	**29**	**51**	**18**	**47**	**21**	**27**
						Oxide wt.%						
SiO2	54.4(4)[a]	54.0(2)	54.3(5)	53.2(3)	55.0(3)	54.6(2)	54.4(4)	53.9(3)	55.1(3)	54.4(2)	54.6(4)	53.7(3)
TiO2	0.08(2)	0.09(1)	0.13(3)	0.14(4)	0.08(1)	0.09(1)	0.10(1)	0.09(1)	0.11(2)	0.12(2)	0.05(2)	0.15(4)
Al2O3	0.72(11)	0.84(10)	1.09(10)	1.04(10)	0.51(7)	0.66(9)	0.79(10)	0.74(4)	0.63(16)	0.86(13)	0.45(17)	1.05(23)
Cr2O3	0.67(11)	0.78(11)	0.76(12)	0.68(6)	0.38(6)	0.52(8)	0.46(12)	0.54(8)	0.34(5)	0.53(5)	0.52(10)	0.68(13)
FeO	15.5(3)	16.4(3)	15.8(9)	19.5(5)	13.8(6)	15.5(2)	16.0(4)	17.7(3)	14.1(2)	15.5(2)	16.4(4)	16.9(2)
MnO	0.53(1)	0.54(1)	0.49(2)	0.66(1)	0.49(3)	0.50(1)	0.55(2)	0.60(2)	0.49(3)	0.50(1)	0.51(2)	0.56(2)
MgO	27.2(4)	26.1(3)	26.6(8)	23.0(3)	28.8(5)	27.2(2)	26.8(5)	25.6(5)	28.4(3)	27.2(5)	27.0(5)	25.4(3)
CaO	1.32(11)	1.48(12)	1.40(13)	2.25(10)	1.05(13)	1.13(12)	1.42(14)	1.64(16)	1.24(8)	1.26(9)	0.84(18)	1.71(22)
Total	100.3	100.3	100.58	100.5	100.08	100.46	100.5	100.8	100.5	100.32	100.32	100.19
						Cation Formula Based on 6 Oxygens						
Si	1.96	1.96	1.96	1.96	1.96	1.97	1.96	1.95	1.97	1.96	1.97	1.95
(IV) Al	0.04	0.04	0.04	0.04	0.04	0.03	0.04	0.05	0.03	0.04	0.03	0.05
(VI) Al	0.00	0.00	0.00	0.01	0.00	0.00	0.00	0.00	0.00	0.00	0.00	0.00
Ti	0.00	0.00	0.00	0.00	0.00	0.00	0.00	0.00	0.00	0.00	0.00	0.00
Cr	0.02	0.02	0.02	0.02	0.01	0.02	0.01	0.02	0.01	0.01	0.01	0.02
Fe	0.47	0.50	0.47	0.60	0.41	0.47	0.48	0.54	0.42	0.47	0.49	0.51
Mn	0.02	0.02	0.02	0.02	0.01	0.02	0.02	0.02	0.01	0.02	0.02	0.02
Mg	1.46	1.41	1.43	1.26	1.53	1.46	1.44	1.38	1.51	1.46	1.45	1.38
Ca	0.05	0.06	0.05	0.09	0.04	0.04	0.06	0.06	0.05	0.05	0.03	0.07
Total	4.01	4.01	4.00	4.00	4.01	4.01	4.01	4.02	4.01	4.00	4.01	4.00
						End Member Compositions, Fe/Mn and Fe#						
Wo	2.5	2.9	2.8	4.6	2.0	2.0	3.0	3.0	2.4	2.5	1.6	3.4
En	73.9	71.7	73.0	64.7	77.3	74.1	72.7	69.7	76.3	73.9	73.5	70.4
Fs	23.6	25.3	24.3	30.7	20.7	23.9	24.3	27.3	21.3	23.6	24.8	26.2
Fe/Mn	29.1	29.8	31.5	29.0	27.6	28.8	30.1	29.6	28.5	30.6	31.3	29.9
Fe#	24.2	26.1	25.0	32.2	21.1	24.4	25.0	28.1	21.8	24.2	25.2	27.1

[a] Numbers in ( ) correspond to 1σ from the mean in terms of least units cited.

Table A2. (cont.)

Sample	ALH 85015		MET 01084		LEW 88679		GRA 98108	ALHA 77256	QUE 99050	MIL 03443	
	Magnesian	Ferroan	Magnesian	Ferroan	Magnesian	Ferroan				Low-Ca	High-Ca
N	**15**	**45**	**50**	**27**	**35**	**29**	**67**	**76**	**54**	**11**	**5**
						Oxide wt%					
SiO2	54.5(4)	53.9(4)	54.6(4)	53.8(2)	54.1(5)	53.4(3)	54.7(2)	54.6(2)	54.6(3)	55.1(1)	54.1(4)
TiO2	0.07(1)	0.10(3)	0.16(2)	0.21(3)	0.14(3)	0.17(1)	0.16(2)	0.14(1)	0.06(1)	0.07(1)	0.04(2)
Al2O3	0.48(6)	0.66(16)	1.01(16)	0.66(9)	0.89(19)	1.08(6)	0.85(7)	1.11(16)	0.75(5)	0.56(9)	0.23(9)
Cr2O3	0.58(9)	0.44(12)	0.51(12)	0.37(8)	0.40(12)	0.54(4)	0.28(5)	0.29(3)	0.40(5)	0.53(7)	0.43(5)
FeO	15.6(9)	18.0(13)	14.7(5)	18.5(6)	16.3(5)	17.5(4)	14.9(1)	15.3(1)	14.4(1)	14.6(1)	5.99(27)
MnO	0.51(4)	0.59(7)	0.47(1)	0.61(2)	0.56(2)	0.58(1)	0.52(1)	0.53(1)	0.47(1)	0.52(2)	0.27(4)
MgO	27.2(8)	25.2(10)	27.7(5)	25.01(3)	26.3(8)	25.0(3)	28.0(2)	27.6(2)	28.0(2)	27.6(2)	17.4(6)
CaO	1.01(19)	1.36(18)	1.28(23)	1.44(30)	1.61(32)	1.95(30)	1.00(20)	0.91(13)	0.91(3)	1.67(19)	22.1(9)
Total	100.0	100.2	100.5	100.5	100.3	100.2	100.5	100.5	99.6	100.7	100.6
						Cation Formula Based on 6 Oxygens					
Si	1.97	1.97	1.95	1.96	1.96	1.95	1.96	1.96	1.97	1.97	1.98
(IV) Al	0.03	0.03	0.05	0.04	0.04	0.05	0.04	0.04	0.03	0.03	0.02
(VI) Al	0.00	0.00	0.00	0.00	0.00	0.00	0.00	0.00	0.00	0.00	0.00
Ti	0.00	0.00	0.00	0.01	0.00	0.00	0.00	0.00	0.00	0.00	0.00
Cr	0.02	0.01	0.01	0.01	0.01	0.02	0.01	0.01	0.01	0.01	0.01
Fe	0.47	0.55	0.44	0.56	0.49	0.53	0.45	0.46	0.43	0.44	0.18
Mn	0.02	0.02	0.01	0.02	0.02	0.02	0.02	0.02	0.01	0.02	0.01
Mg	1.46	1.37	1.48	1.36	1.42	1.36	1.49	1.48	1.51	1.47	0.95
Ca	0.04	0.05	0.05	0.06	0.06	0.08	0.04	0.04	0.03	0.06	0.87
Total	4.01	4.00	4.00	4.01	4.01	4.01	4.01	4.00	4.00	4.01	4.01
						End Member Compositions, Fe/Mn and Fe#					
Wo	2.0	2.7	2.5	2.8	3.2	3.9	1.9	1.8	1.8	3.2	43.4
En	74.1	69.5	75.1	68.7	71.8	69.0	75.5	74.9	76.2	74.6	47.4
Fs	23.9	27.8	22.4	28.4	25.0	27.1	22.6	23.3	22.0	22.1	9.2
Fe/Mn	30.4	29.9	30.7	29.7	28.8	29.9	28.3	28.6	30.3	28.0	21.9
Fe#	24.4	28.6	23.0	29.3	25.8	28.2	23.0	23.7	22.4	22.9	16.2

[a] Numbers in ( ) correspond to 1σ from the mean in terms of least units cited.

Table A3. Average olivine compositions.

Sample	EET 83246	LEW 88008	LAP 02216	MIL 03368	PCA 02008	LAP 03979	ALH 85015	LEW 88679	MET 01084	GRA 98108	ALHA 77256	MIL 03443
N	**10**	**26**	**18**	**21**	**22**	**16**	**21**	**31**	**27**	**33**	**24**	**59**
						Oxide wt.%						
SiO2	38.0(2)[a]	36.3(6)	38.1(2)	37.9(2)	38.2(3)	37.5(3)	36.6(4)	37.8(2)	37.8(5)	37.7(4)	37.7(4)	38.3(2)
Al2O3	<0.03	0.05(4)	<0.03	<0.03	<0.03	<0.03	0.06(1)	<0.03	0.07(2)	<0.03	0.02(5)	<0.03
Cr2O3	0.09(8)	0.05(5)	0.03(1)	0.05(4)	0.04(3)	0.05(2)	0.05(3)	<0.03	<0.03	0.03(1)	<0.03	<0.03
FeO	24.7(3)	33.4(9)	23.5(8)	25.9(3)	23.9(7)	27.9(5)	29.6(13)	25.8(5)	26.0(7)	24.9(2)	26.3(5)	24.1(2)
MnO	0.44(1)	0.65(5)	0.51(3)	0.53(1)	0.52(2)	0.62(3)	0.55(3)	0.50(2)	0.47(2)	0.52(2)	0.53(1)	0.52(1)
MgO	37.6(6)	30.2(11)	38.5(7)	36.3(3)	38.2(6)	34.6(4)	33.0(16)	36.6(5)	36.1(6)	37.3(4)	36.5(6)	38.0(3)
CaO	<0.03	0.05(3)	0.04(2)	0.03(1)	0.07(3)	0.05(1)	0.05(3)	0.03(2)	<0.03	0.05(1)	0.05(1)	0.06(4)
Total	100.9	100.6	100.7	100.7	100.9	100.7	100.0	100.9	100.4	100.6	101.0	101.0
						Cation Formula Based on 4 Oxygens						
Si	1.00	0.99	0.99	1.00	0.99	1.00	0.99	0.99	1.00	0.99	0.99	1.00
Al	-	0.00	-	-	-	-	0.00	-	0.00	-	0.00	-
Cr	0.00	0.00	0.00	0.00	0.00	0.00	0.00	-	-	0.00	-	-
Fe	0.54	0.76	0.51	0.57	0.52	0.62	0.67	0.57	0.57	0.55	0.58	0.52
Mn	0.01	0.02	0.01	0.01	0.01	0.01	0.01	0.01	0.01	0.01	0.01	0.01
Mg	1.46	1.23	1.49	1.42	1.48	1.37	1.33	1.43	1.42	1.46	1.43	1.47
Ca	0.00	0.00	0.00	0.00	0.00	0.00	0.00	0.00	0.00	0.00	0.00	0.00
Total	3.00	3.01	3.01	3.00	3.01	3.01	3.01	3.01	3.00	3.01	3.01	3.00
						End Member Compositions and Fe/Mn						
Fo	73.0	61.7	74.5	71.4	74.1	68.8	66.5	71.7	71.2	72.7	71.2	73.7
Fa	27.0	38.3	25.5	28.6	25.9	31.2	33.5	28.4	28.8	27.3	28.8	26.3
Fe/Mn	53.9	50.9	46.5	47.5	45.4	44.3	52.8	51.5	52.1	49.7	48.1	43.7

[a] Numbers in ( ) correspond to 1σ from the mean in terms of least units cited.

Table A4. Representative chromite compositions.

Sample	EET 83246	LEW 88008	LAP 02216	MIL 03368	PCA 02008	ALH 85015	LEW 88679	QUE 99050	MET 01084	GRA 98108	ALHA 77256	LAP 03979		MIL 03343	
												Low-Al	High-Al	Low-Al	High-Al
								Oxide wt%							
SiO2	0.04	0.06	0.04	0.18	0.08	0.07	<0.03	<0.03	0.07	0.03	<0.03	0.10	0.39	0.08	0.09
Al2O3	11.9	16.6	8.99	12.5	11.0	11.2	13.1	9.82	9.86	15.6	21.8	11.2	14.1	3.95	10.6
TiO2	0.79	1.30	0.72	0.91	0.82	1.01	0.89	0.34	1.73	1.24	0.79	0.87	1.14	0.31	0.91
Cr2O3	52.8	46.5	56.9	53.2	54.0	53.8	51.3	56.4	53.2	49.8	43.4	55.0	49.8	61.8	54.2
MgO	2.91	2.59	3.71	3.89	4.10	2.87	2.81	3.26	2.34	4.68	6.72	4.91	4.17	1.90	2.70
FeO	29.3	31.4	28.0	28.5	27.7	29.9	30.5	28.2	31.2	28.2	26.0	26.6	28.9	29.4	29.4
MnO	0.47	0.55	0.48	0.53	0.48	0.53	0.60	0.46	0.57	0.53	0.44	0.47	0.53	0.68	0.64
CaO	<0.03	0.03	<0.03	<0.03	0.03	<0.03	<0.03	<0.03	0.09	0.09	0.30	<0.03	0.16	<0.03	<0.03
V2O3	0.52	0.48	0.52	0.58	0.39	0.52	0.46	0.45	0.53	0.69	0.46	0.59	0.40	0.57	0.48
Total	98.7	99.5	99.3	100.4	98.6	99.9	99.7	98.9	99.6	100.9	99.9	99.7	99.5	98.7	99.1
								Cation Formula Based on 4 Oxygens							
Si	0.00	0.00	0.00	0.01	0.00	0.00	-	-	0.00	0.00	-	0.02	0.01	0.00	0.00
Al	0.49	0.67	0.37	0.50	0.45	0.46	0.53	0.41	0.41	0.61	0.83	0.45	0.56	0.13	0.44
Ti	0.02	0.03	0.02	0.02	0.02	0.03	0.02	0.01	0.05	0.03	0.02	0.02	0.03	0.01	0.02
Cr	1.45	1.25	1.57	1.43	1.48	1.47	1.40	1.56	1.48	1.31	1.11	1.48	1.34	1.81	1.50
Mg	0.15	0.13	0.19	0.20	0.21	0.15	0.14	0.17	0.12	0.23	0.32	0.25	0.21	0.10	0.14
Fe	0.85	0.89	0.82	0.81	0.81	0.87	0.88	0.83	0.91	0.78	0.70	0.76	0.82	0.91	0.86
Mn	0.01	0.02	0.01	0.02	0.01	0.02	0.02	0.01	0.02	0.01	0.01	0.01	0.02	0.02	0.02
Ca	-	0.00	-	-	0.00	-	-	-	0.00	0.00	0.00	-	0.01	-	-
V	0.01	0.01	0.01	0.02	0.01	0.01	0.01	0.01	0.01	0.02	0.01	0.02	0.01	0.03	0.01
Total	3.00	3.00	3.00	3.00	3.00	3.00	3.00	3.00	3.00	3.00	3.01	3.02	3.00	3.01	3.00

Table A5. Representative plagioclase compositions.

Sample	LEW 88008	PCA 02008	LAP 03979	ALH 85015	LEW 88679	MET 01084	GRA 98108	ALHA 77256
				Oxide wt.%				
SiO2	44.0	46.7	47.9	44.3	44.4	44.5	45.7	44.8
Al2O3	35.6	33.8	33.1	35.3	35.2	35.6	34.9	35.3
FeO	0.42	0.59	0.36	0.27	0.11	0.10	0.13	0.29
MgO	0.11	0.07	0.13	0.05	0.03	0.03	0.05	<0.03
CaO	19.9	16.8	16.6	19.4	18.8	19.2	18.8	18.7
Na2O	0.40	1.62	1.78	0.48	0.81	0.75	0.97	0.92
K2O	<0.03	0.13	0.19	<0.03	<0.03	<0.03	0.07	0.05
Total	100.47	99.74	100.06	99.39	99.30	100.23	100.57	100.08
				Cation Formula Based on 8 Oxygens				
Si	2.03	2.16	2.20	2.05	2.06	2.05	2.10	2.07
Al	1.94	1.84	1.79	1.93	1.93	1.94	1.89	1.92
Fe	0.02	0.02	0.01	0.01	0.00	0.00	0.01	0.01
Mg	0.01	0.01	0.01	0.00	0.00	0.00	0.00	-
Ca	0.98	0.83	0.82	0.96	0.94	0.95	0.92	0.92
Na	0.04	0.15	0.16	0.04	0.07	0.07	0.09	0.08
K	-	0.01	0.01	-	-	-	0.00	0.00
Total	5.02	5.00	4.99	5.00	5.01	5.01	5.01	5.01
				End Member Compositions				
An	96.5	84.6	82.8	95.7	92.8	93.4	91.0	91.6
Ab	3.5	14.7	16.1	4.3	7.2	6.6	8.6	8.1
Or	-	0.7	1.1	-	-	-	0.4	0.3

Table A6. Representative metal and sulfide compositions.

Sample	LEW 88008		PCA 02008		LAP 03979		ALH 85015		LEW 88679		GRA 98108		ALHA 77256		LAP 02216		MIL 03368		MIL 03443		MET 01084	EET 83246
	Metal	Sulfide	Metal	Sulfide	Metal	Sulfide	Metal	Sulfide	Metal	Sulfide	Metal*	Sulfide	Metal	Sulfide	Metal	Sulfide	Metal	Sulfide	Metal	Sulfide	Sulfide	Sulfide
S	-	36.9	-	36.4	-	36.3	-	34.9	-	36.2	-	36.4	-	36.3	-	36.8	-	35.8	-	36.2	36.2	36.4
Fe	96.3	63.0	96.1	62.6	95.9	62.1	95.9	63.8	97.6	62.6	96.5	62.6	98.0	63.4	96.7	63.1	99.2	62.8	97.4	62.9	62.2	62.5
Ni	2.54	<0.03	2.11	<0.03	1.92	0.12	2.48	<0.03	0.60	<0.03	1.46	<0.03	0.81	<0.03	1.85	<0.03	0.24	<0.03	0.74	<0.03	0.21	0.06
Co	0.87	-	0.69	-	0.69	-	0.77	-	0.26	-	0.56	-	0.82	-	0.64	-	0.45	-	0.96	-		
Total	99.8	100.0	99.7	99.0	98.5	98.5	99.3	98.7	98.5	99.7	98.6	99.0	99.8	99.8	99.4	100.1	99.9	98.6	99.1	99.1	98.5	98.9

*GRA 98108 metal contains up to 0.05 wt.% P. It was the only sample with measurable P.

Table A7. New classification of samples in this study.

Sample	QUE 99050	EET 83246	LEW 88008	LAP 02216	MIL 03368	PCA 02008	LAP 03979	ALH 85015	MET 01084	LEW 88679	ALHA77256	GRA 98108	MIL 03443
> 0% olivine	✗	✓	✓	✓	✓	✓	✓	✓	✓	✓	✓	✓	✓
1-10% olivine		✓	✓	✓	✓	✓	✓	✓	✓	✓	✓	✓	✓
>10 % olivine		✗	✗	✗	✗	✗	✗	✗	✗	✓	✓	✓	✓
contains only pyroxene in equilibrium with olivine										✗	✓	✓	✓
≥ 90% olivine											✗	✗	✓
Classification	**O**	**P**	**P**	**P**	**P**	**P**	**P**	**P**	**P**	**P**	**H**	**H**	**D**

O - orthopyroxenitic diogenite, **P** - polymict diogenite, **H** - harzburgitic diogenite, **D** - dunitic diogenite.

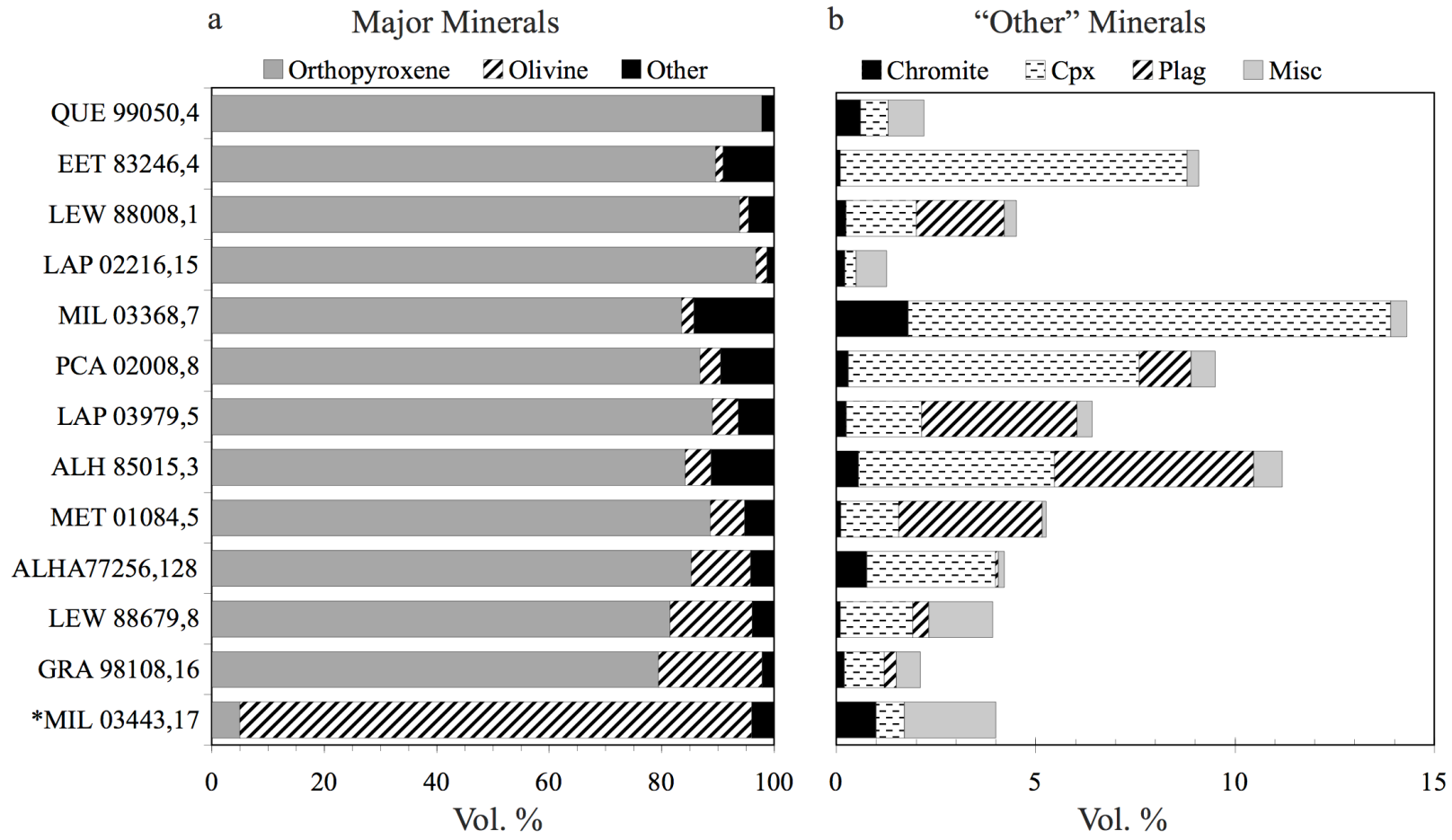


Figure A1. Histograms showing modal abundances of (a) orthopyroxene and olivine, with the remaining minerals being grouped into "other", and (b) breakdown of the "other" group. *mineral abundances were estimated by point counting, all others determined on an EMP.

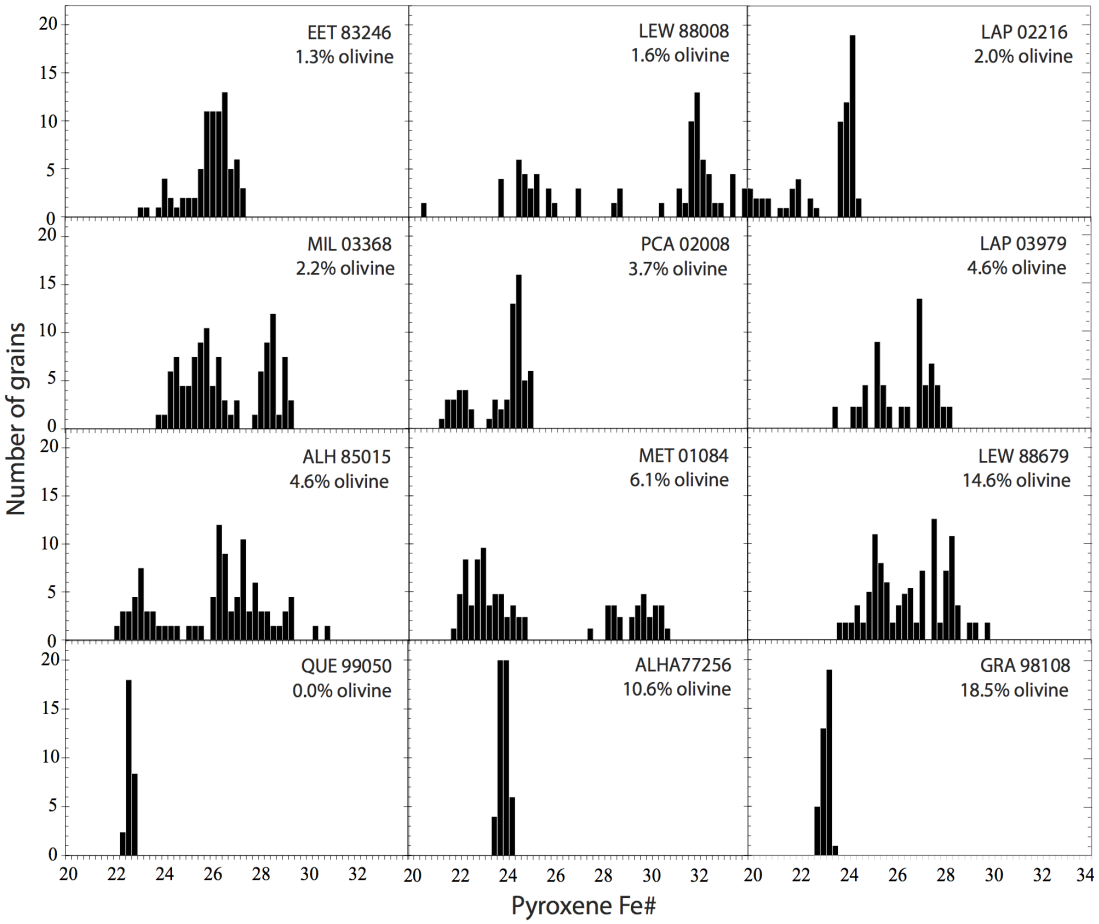


Figure A2. Histograms showing orthopyroxene Fe# (molar Fe/Fe+Mg *100) in diogenites. The first nine samples have bimodal distributions. They are listed in order of increasing olivine abundance, which roughly correlates to the strength of the Mg-Opx peak. The three samples at the bottom of the figure contain only one composition of orthopyroxene

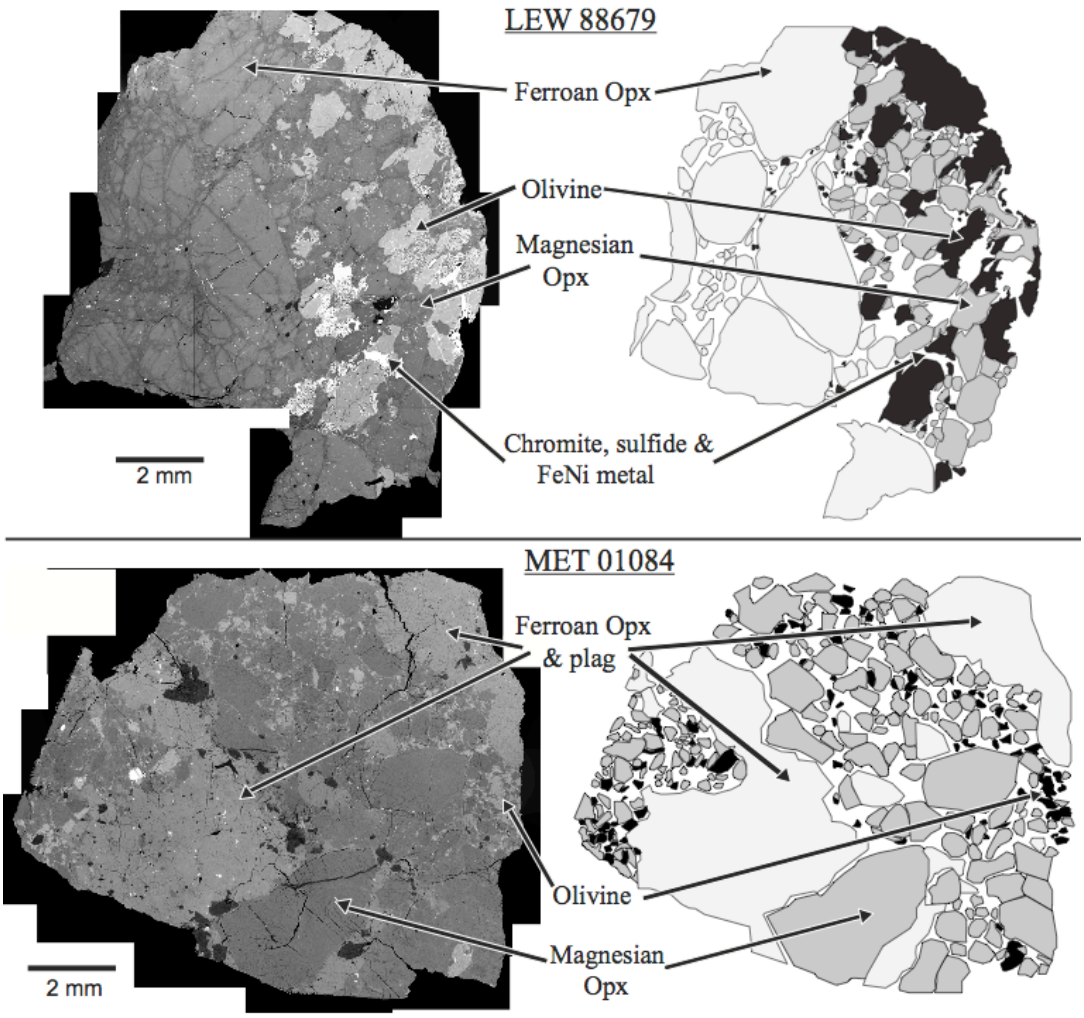


Figure A3. Backscattered electron (BSE) composite images and representative phase distribution maps of LEW 88679 and MET 01084. Phases have been highlighted to distinguish the presence of two compositions of pyroxene and the localized occurrence of olivine with magnesian orthopyroxene. Plagioclase is localized near ferroan orthopyroxenes in MET 01084

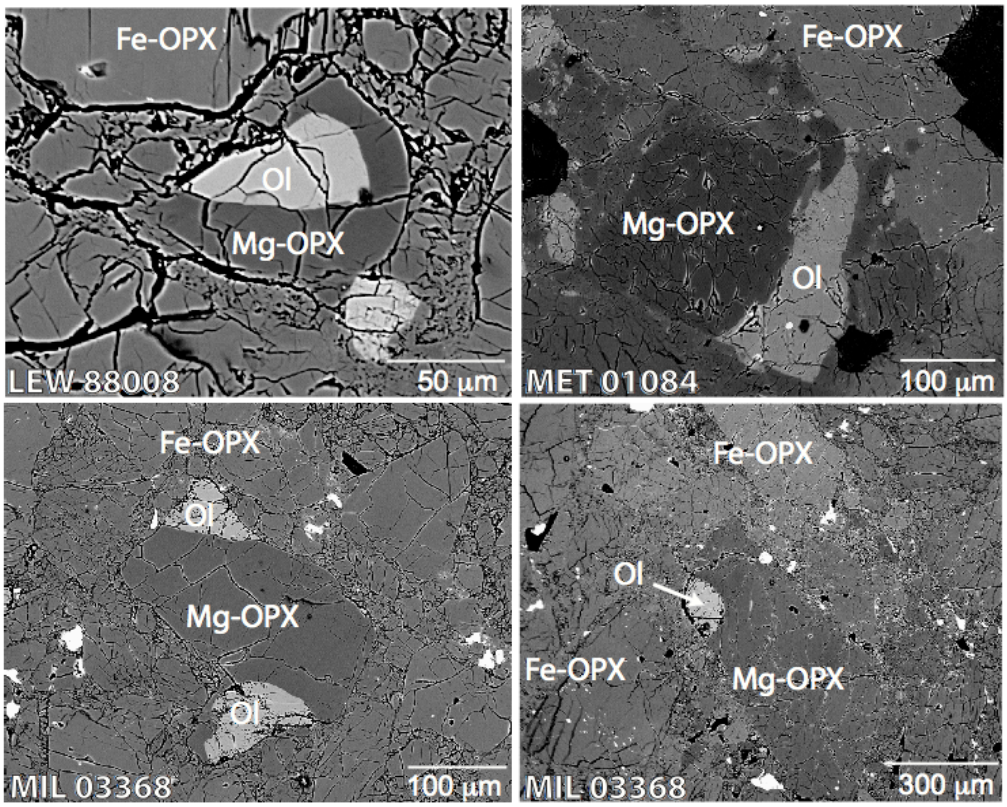


Figure A4. BSE images highlighting assemblages of olivine and magnesian pyroxene with non-brecciated (igneous) grain contacts

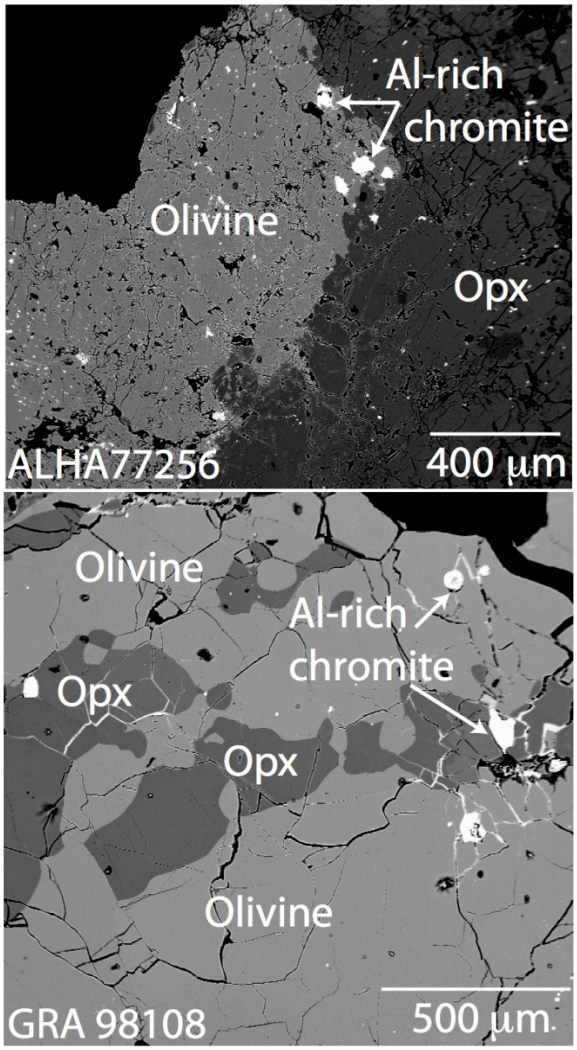


Figure A5. Representative BSE images of two olivine diogenites displaying non-brecciated grain contacts between olivine and orthopyroxene, and Al-rich chromite at those grain boundaries

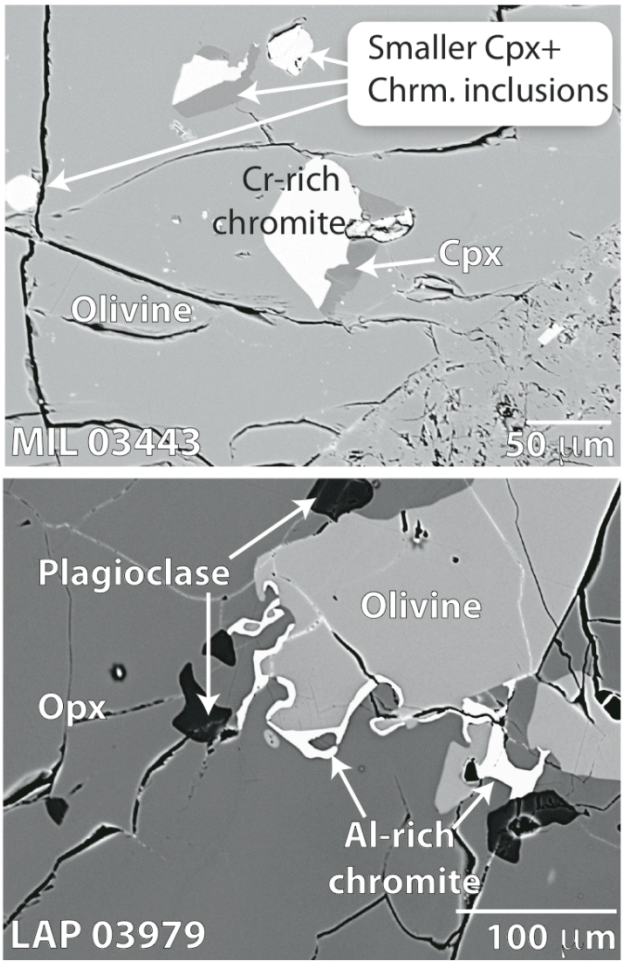


Figure A6. BSE images of chromite/clinopyroxene inclusions in the olivine (MIL 03443) and chromite at olivine/orthopyroxene grain boundaries (LAP 03979)

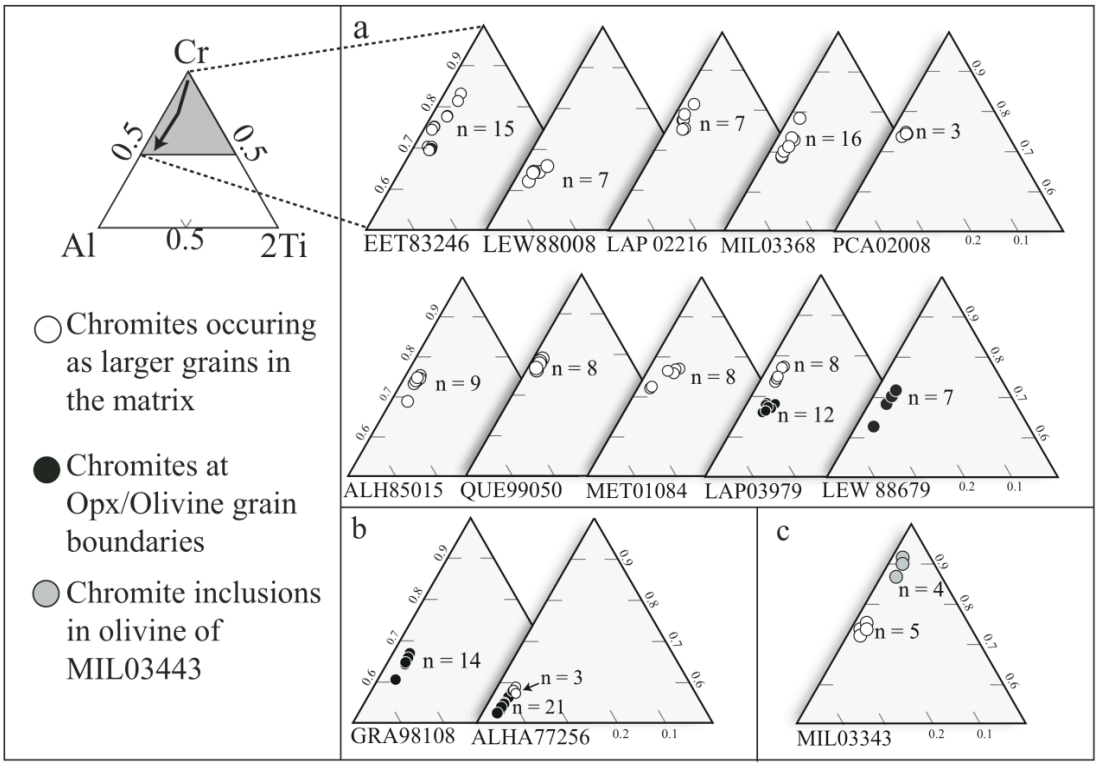


Figure A7. Ternary plots showing relative abundances of Cr, Al and Ti(X2) in chromite. All plots are of an enlarged area of the Cr, Al, Ti(X2) plot shown on the left. Samples have been grouped based on classification: (a) diogenites, (b) olivine diogenites and (c) dunite. The textural setting of chromite is distinguished by symbols with different shading. The arrows represent previously determined evolutionary paths for diogenite chromites.

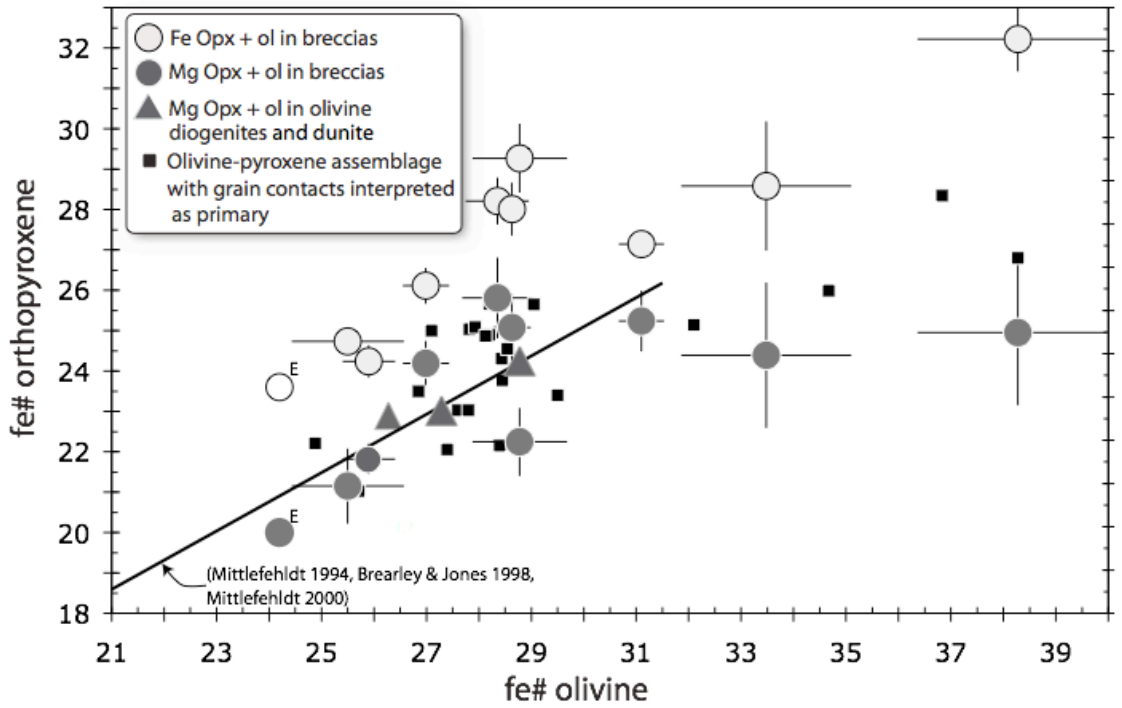


Figure A8. Average olivine Fe# versus both the average magnesian orthopyroxene and ferroan orthopyroxene for each meteorite. The open circles represent ferroan orthopyroxene vs. olivine in brecciated meteorites, and the darker circles represent magnesian orthopyroxene vs. olivine. Each open/closed circle pair at a given olivine Fe# represents a breccia. The triangles represent magnesian orthopyroxene vs. olivine in olivine diogenites and the dunite. Y-error bars represent 1s from the mean, while the x-error bars represent the range in olivine composition in that sample. Some error bars are smaller than symbol size. All data from Tables A2 and A3, except EETA 79002 (**E**) (Mittlefehldt, 2000). Small black squares represent individual clasts of magnesian orthopyroxene + olivine in non-brecciated (igneous) contact. The regression line is based on previously documented equilibrium assemblages of olivine and orthopyroxene found in other meteorites (see text). Where the equilibrium relationship has been constrained, the magnesian orthopyroxenes appear to be in equilibrium with olivines, supporting the hypothesis that they co-crystallized in the same lithology

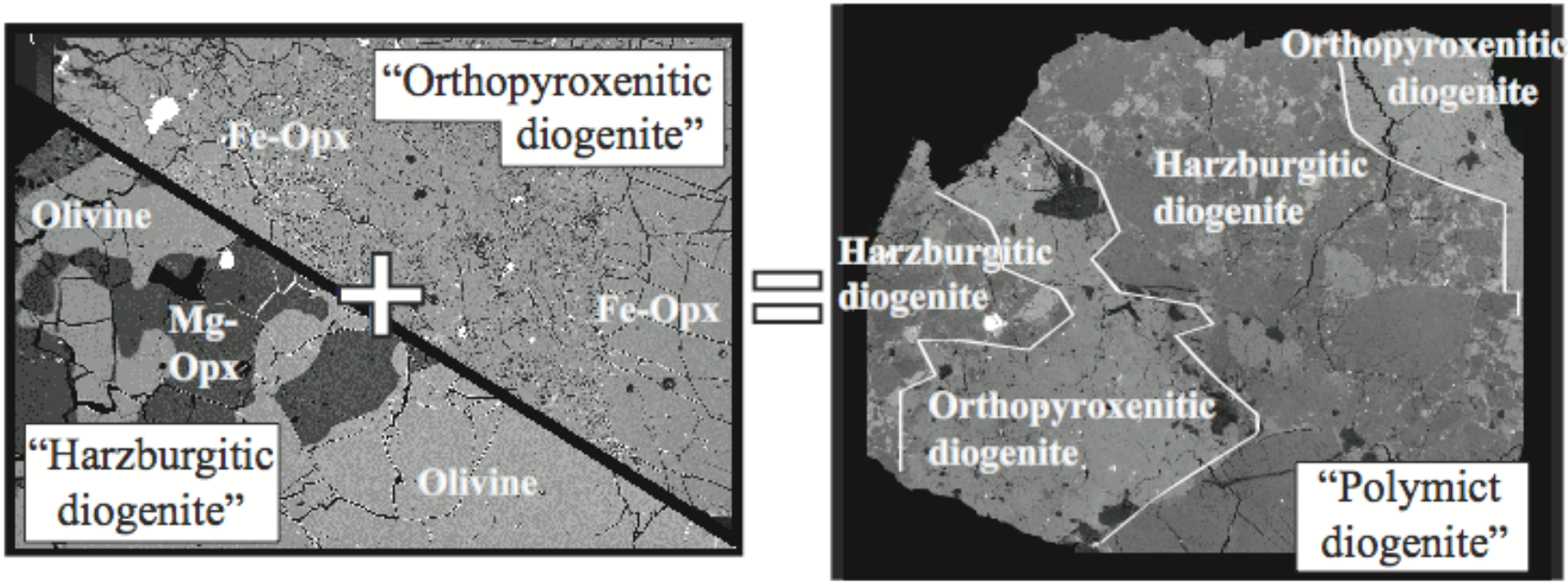


Figure A9. Illustration of a mixing model where harzburgitic and orthopyroxenitic diogenite fragments are mixed to produce polymict diogenites

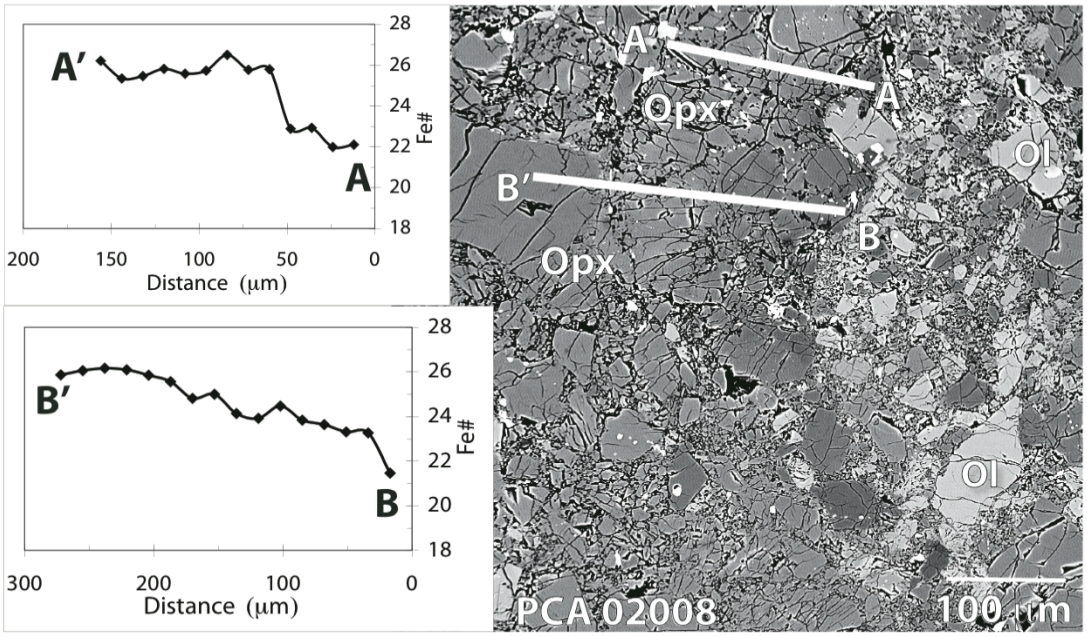


Figure A10. Two transects across a zoned orthopyroxene grain showing Mg/Fe zonation away from an adjacent olivine. Such zoning is only observed in PCA 02008.

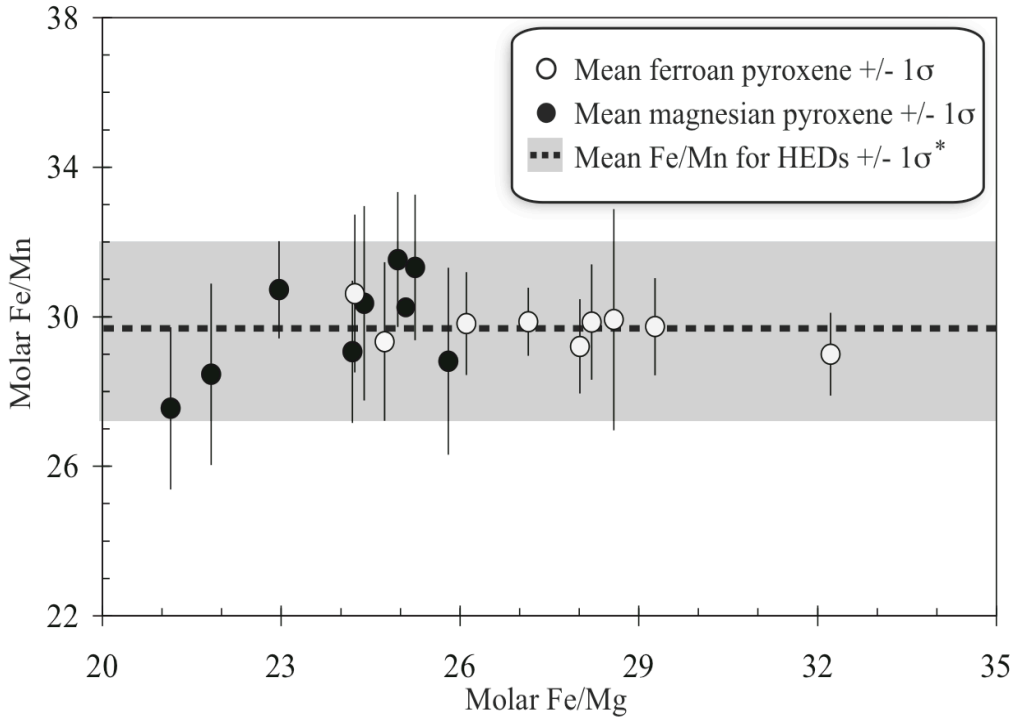


Figure A11. Average molar Fe/Mn and Fe/Mg ratios in magnesian and ferroan orthopyroxenes in diogenites. The vertical error bars reflect the ratios of relative 1s variations from the means in both Fe and Mn. *Fe/Mn ratios of pyroxenes in other HEDs are from Mayne et al. (2009) and Papike et al. (2001). The identical Fe/Mn ratios suggest that the harzburgite lithology is indigenous to Vesta

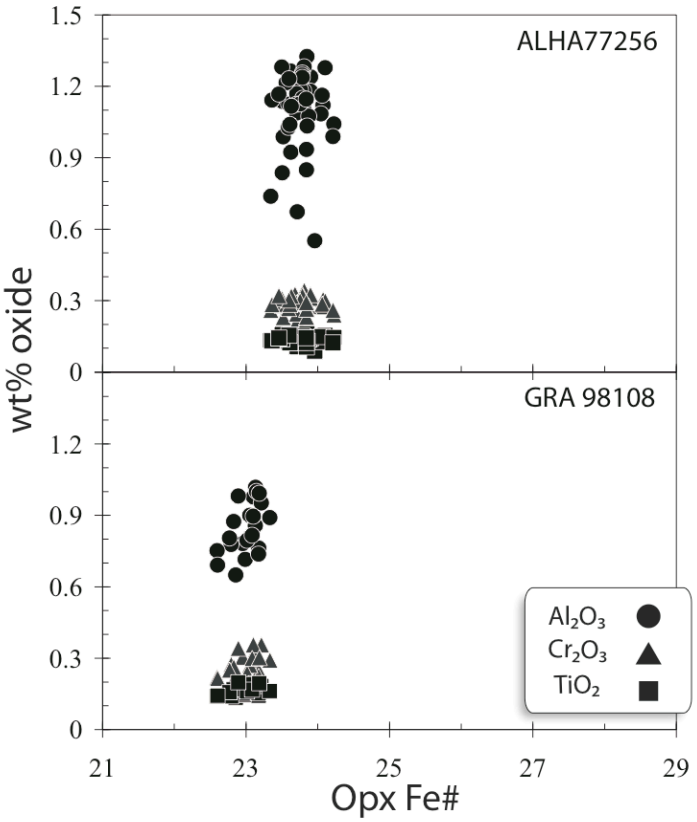


Figure A12. Minor element variation vs. Fe# diagram for orthopyroxenes in the harzburgitic diogenites. Homogenization of Fe/Mg has occurred, but variations still persist in the minor elements. This phenomenon is likely caused by secondary equilibration, and is commonly seen in other diogenites, especially those containing one lithology (Fowler et al. 1994; Mittlefehldt 1994). 3σ counting errors are Al_2O_3 = 0.03 wt.%, Cr_2O_3 = 0.02 wt.%, TiO_2 = 0.01 wt.%, which are smaller than the symbol sizes

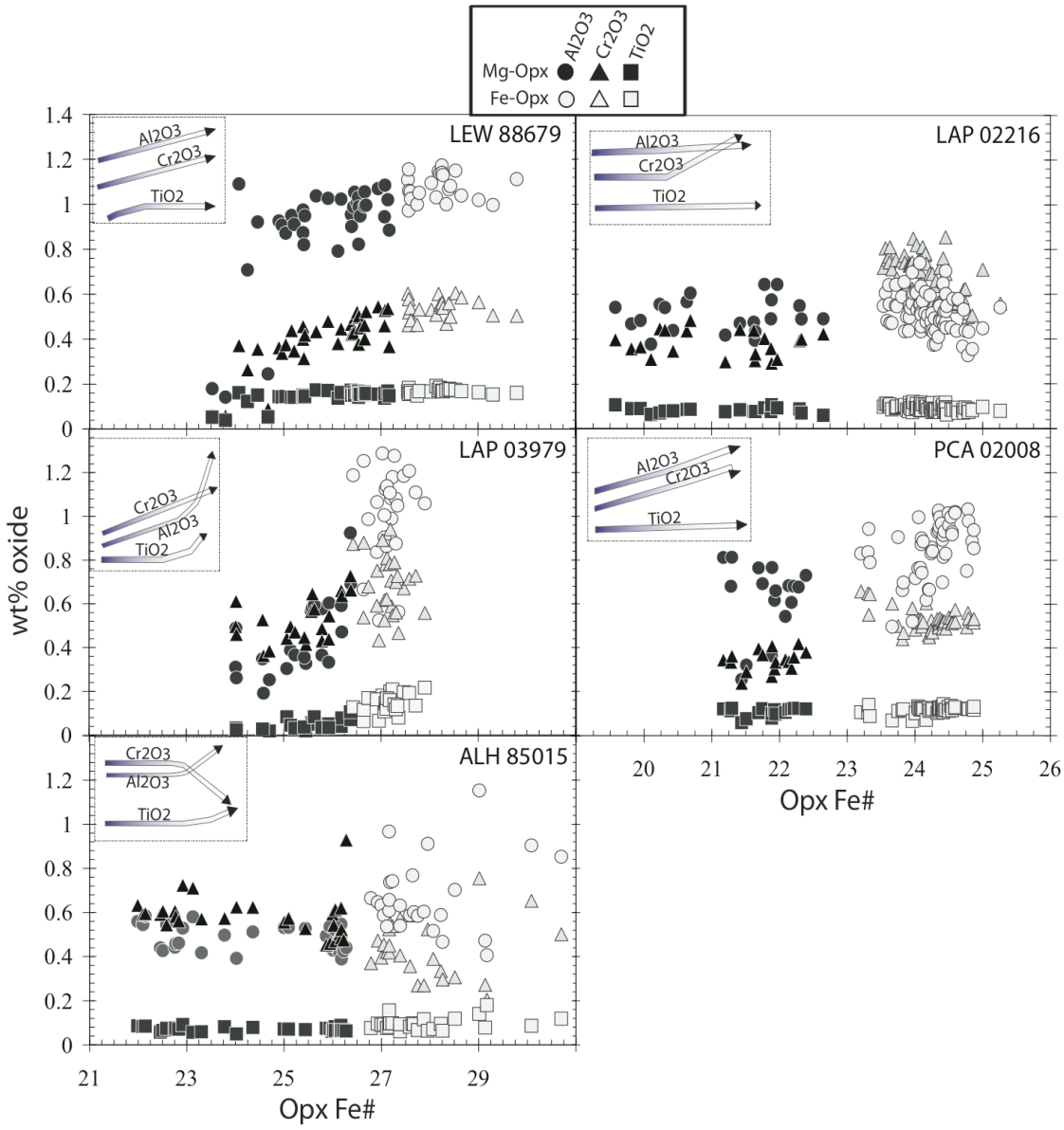


Figure A13. Trend 1 in minor element variation vs. Fe# for orthopyroxenes in polymict diogenites. Because these samples contain clasts from two lithologies, analyses have also been separated into harzburgite and orthopyroxenite (closed and open symbols respectively). Interpretive trends in minor elements appear in the upper left corner of each plot. Together these samples show overall increases in Al_2O_3 and T_iO_2 from harzburgite to orthopyroxenite, indicative of crystallization of a less primitive melt. 3σ counting errors are Al_2O_3 = 0.03 wt.%, Cr_2O_3 = 0.02 wt.%, TiO_2 = 0.01 wt.%, which are smaller than the symbol size.

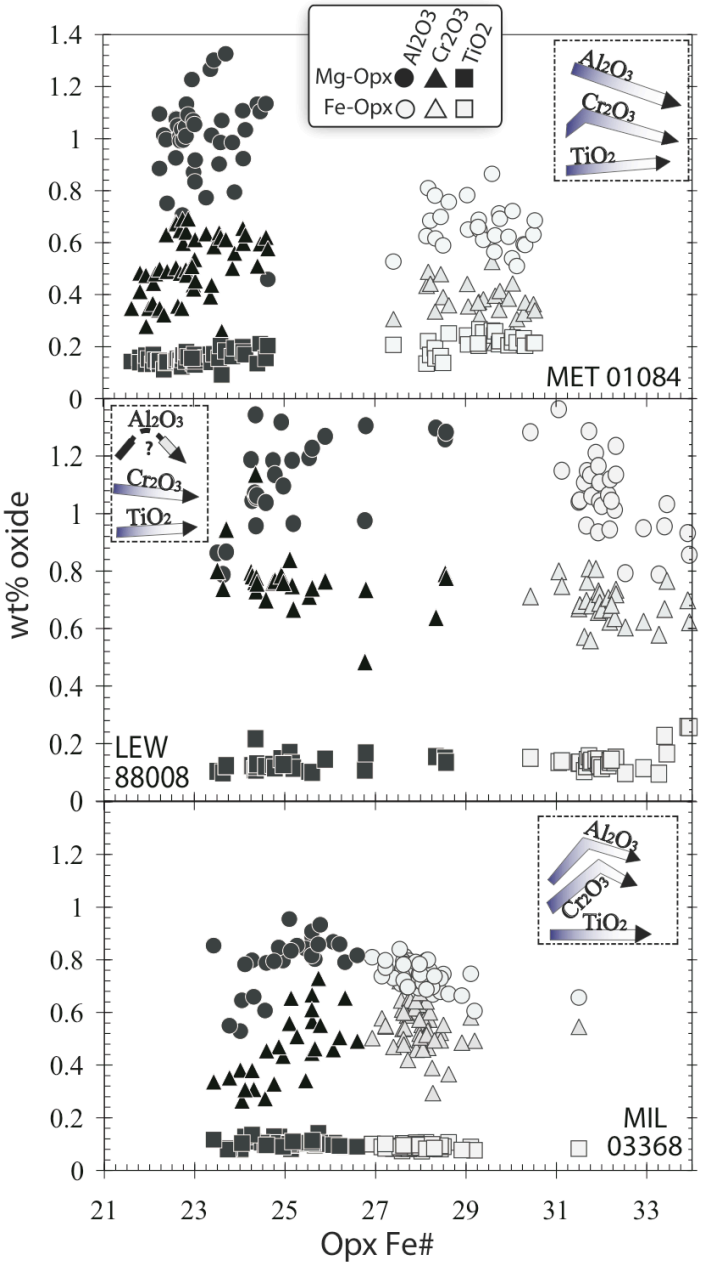


Figure A14. Trend 2 in minor element variation vs. Fe# for orthopyroxenes in polymict diogenites. Interpretive trends appear in each plot. These patterns in minor elements suggest crystallization of a more primitive melt. 3σ counting errors are Al2O3 = 0.03 wt.%, Cr2O3 = 0.02 wt.%, TiO2 = 0.01 wt.%, which are smaller than the symbol sizes.

Part 3
MIL 03443, a Dunite from Asteroid 4 Vesta: Evidence for its Classification and Cumulate Origin

This part is a reformatted version of a paper of the same name that has been accepted for publication in Meteoritics and Planetary Science. Andrew Beck, David Mittlefehldt, Hap McSween, Doug Rumble, Cin-Ty Lee and Bob Bodnar are authors of this paper. Andrew preformed all data analyses, except EMP analyses on sections 10 and 11, and oxygen isotope analysis.

A. W. Beck, D. W. Mittlefehldt, H. Y. McSween, D. Rumble, C-T A. Lee, and R. J. Bodnar. MIL 03443, a Dunite from Asteroid 4 Vesta: Evidence for its Classification and Cumulate origin. *Meteoritics and Planetary Science* (2011) in press.

ABSTRACT

The absence of dunite (>90 vol.% olivine) in the howardite, eucrite, diogenite (HED) meteorite suite, when viewed with respect to spectroscopic and petrologic evidence for olivine on Vesta, is problematic. Here we present petrologic, geochemical and isotopic evidence confirming that MIL 03443, containing 91 vol.% olivine, should be classified with the HED clan rather than with mesosiderites. Similarities in olivine and pyroxene FeO/MnO ratios, mineral compositions, and unusual mineral inclusions between MIL 03443 and the diogenites support their formation on a common parent body. This hypothesis is bolstered by oxygen isotopic and bulk geochemical data. Beyond evidence for its reclassification, we present observations and interpretations that MIL 03443 is likely a crustal cumulate rock like the diogenites, rather than a sample of the Vestan mantle.

1.0 INTRODUCTION

Differentiated bodies with chondritic starting compositions should contain olivine-rich lithologies such as peridotite (Ol+Opx+Cpx), harzburgite (Ol+Opx), and/or dunite (>90 vol.% Ol) (Herzberg and O'Hara 1985). Melting models for asteroid 4 Vesta, the largest differentiated rocky body in the asteroid belt, suggest that it should contain dunite in its mantle or in crustal cumulates (Righter and Drake 1997; Ruzicka et al. 1997; Takeda 1997). Visible/near-infrared spectra of Vesta collected by ground-based telescopes and the Hubble Space Telescope (HST), interpreted to show regions containing significant olivine in the eastern hemisphere (Binzel et al. 1997; Gaffey 1997), support this hypothesis. The discovery of a large impact basin (460 km wide) at the southern pole of Vesta, which contains either an olivine-rich or high-calcium pyroxene-rich lithology (Thomas et al. 1997), may add further support for olivine-bearing ultramafic rocks on Vesta. This deeply excavated crater (13 km depth) would provide a geologically reasonable location for a Vestan dunite (Takeda 1997). However, other ground-based and HST investigations do not support the presence of extensive regions dominated by olivine-rich lithologies in the eastern hemisphere, or in ejecta material from the southern crater (Reddy et al. 2010 and Li et al. 2010, respectively). Nevertheless, modeling of HST images taken at four different band-passes suggests that olivine is a minor component intermixed with basaltic and orthopyroxenitic material, especially in the western hemisphere (Shestopalov et al. 2010). Excavation of olivine-rich plutons smaller than the resolution of the HST imaging would be plausible sources for the olivine debris in the western hemisphere.

Given the geochemical models suggesting olivine-rich rocks on Vesta, and the possibility of olivine-rich regions exposed by impacts, it would seem likely that dunites might be present among HED (howardite, eucrite, diogenite) meteorites, commonly thought to be samples from Vesta. However, HEDs containing up to only 60 vol.% olivine have been reported (Bowman et al. 1997). These harzburgite diogenites make up a very small fraction (<1%) of the entire HED suite and show large intra-sample variation in olivine abundance (Bowman et al. 1997; Beck and McSween 2010a; Shearer et al. 2010). A few heterogeneous harzburgites such as these cannot account for the abundance of olivine predicted by differentiation models. Furthermore, identifying a dunite in the HED suite would provide support for spectroscopic interpretations of olivine-rich lithologies on the surface of Vesta.

Bunch et al. (2006) have suggested that Northwest Africa 2968 may be a dunite sample related to the HED suite because the FeO/MnO ratios of its olivine and orthopyroxene are similar to those of olivine-bearing diogenites, and because its oxygen isotopic composition is similar to HEDs. However, the mg#s (molar Mg/(Mg+Fe)*100) of olivine (92.5) and orthopyroxene (93) are slightly higher than the ranges typically observed for howardites or diogenites (see McSween et al. 2011), though some more magnesian olivines have been observed in other HED samples (Fuhrman and Papike 1981). NWA 5784 and NWA 5968 are also dunites that have been suggested to be related to the HED clan, but little information is available on them (Bunch et al. 2010).

The anomalous brecciated dunite Miller Range (MIL) 03443 (hereafter "MIL") is an olivine-rich achondrite. MIL was originally classified as a mesosiderite (McBride and McCoy 2006), based on its similarity to olivine-rich lithic clasts that have been reported

in that group (e.g. McCall and Cleverly 1965; Ntaflos et al. 1993). However, during classification it was noted that MIL displayed some characteristics that were similar to the HEDs. Preliminary reports have favored the reclassification of MIL as an HED with genetic relationships to diogenites (Krawczynski et al. 2008, Mittlefehldt 2008; Beck and McSween 2010b). Here we present a full petrographic description and detailed geochemical analysis of the meteorite using several different sections and splits from MIL 03443.

Given the high olivine abundance of MIL, it seems plausible that it would share the most commonalities with the other ultramafic member of the HEDs, the diogenites. We examine similarities between MIL and the diogenites using petrographic analyses of thin sections, bulk-rock chemistry, and oxygen isotope data. We also assess its petrogenesis in the context of magmatism on Vesta.

2.0 METHODS

Three thin sections of MIL were analyzed: 10, 11 (allocated to DWM) and 17 (allocated to HYM). Sections 10 and 11 were made from separate chips. Sections 11 and 17 were prepared from the same potted butt; three other sections were made from this same potted butt, between 11 and 17. Chemical analyses of section 17 were conducted at the University of Tennessee (UT) and sections 10 and 11 were analyzed at Johnson Space Center (JSC), both using Cameca SX-100 electron microprobes (EMP). Analytical conditions for sections 10 and 11 are as described by Mittlefehldt (1994), and those for section 17 are as described by Beck and McSween (2010a). Much of the diogenite data presented here for comparison is taken from referenced literature. However, for

FeO/MnO ratios of diogenite orthopyroxene and olivine, we combine literature data with our own mineral analyses of 12 olivine-bearing diogenites, described by Beck and McSween (2010a).

A backscatter electron (BSE) image map of section 17 was used to calculate the modal mineralogy. Each mineral on the BSE map was assigned a specific grayscale threshold, and its relative abundance was calculated using ImageJ (Abramoff et al. 2004).

Mineral trace element compositions in MIL were acquired using an Agilent 7500ce Inductively Coupled Plasma Mass Spectrometer (ICP-MS) combined with an Excimer 193-nm GeoLasPro Laser Ablation system (LA) at the Virginia Tech. The He gas flow was ~0.8 ml/min through an ablation cell with a volume of ~1.5 cm^3. Spot size ranged from 24-44 μm and dwell times ranged from ~15-30 sec. NIST 610/612 glass was used as an external standard and analyzed four times before and after analysis. Previous workers have shown that abundances of most elements in silicate phases can be determined with better than 10% accuracy using the NIST 610/612 standards combined with a 193-nm excimer laser (Sylvester 2008; Guillong et al. 2003). Summation of major elements to 100% was used as an internal standard. Data reduction was achieved using the Analysis Management System software (Mutchler et al. 2008).

For bulk-rock geochemical analysis, a ~500 mg split was ground in a corundum mortar and pestle. The powder was quartered and mixed until an ~80 mg split was achieved. Similar sized powders of the United States Geological Survey (USGS) standards BCR2, PCC-1, and DTS-1 were also prepared. The sample and standard powders were then put into Savillex® beakers, and washed with 0.25 mLs of concentrated HF and $HClO_4$ acids three times. The contents of the beakers were added to

125 mL polypropylene bottles and diluted with 2 wt.% HNO_3 solution. A precisely weighed quantity of In solution was then added to each bottle, such the concentration of In would be ~1 ppb. The solutions were then introduced into a ThermoFinnigan Element 2 magnetic sector ICP-MS using a small-volume cyclonic spray chamber with an Elemental Scientific Teflon nebulizer with a free aspiration uptake rate of ~100 μL/min. A Pt guard electrode and a high sensitivity Ni skimmer cone were used. Relevant parameters were 13.43 L/min of Ar cool gas, 0.94 L/min of Ar sample gas, and 0.97 L/min of Ar carrier ("auxiliary") gas. Forward power was 1370 W and reflected power was 2 W. Major elements were analyzed using a mass resolution (m/Dm) of ~3000 and trace elements at a resolution of ~300, which was sufficient to resolve all isobaric interferences (argides, oxides, and double-charged ions) relevant to the masses of interest in medium mass resolution (^{23}Na ^{27}Al, ^{39}K, ^{44}Ca, ^{45}Sc, ^{49}Ti, ^{51}V, ^{52}Cr, ^{53}Cr, ^{55}Mn, ^{56}Fe, ^{57}Fe, ^{59}Co, ^{60}Ni, ^{65}Cu, ^{66}Zn, ^{68}Zn). The USGS standards listed above were used for external calibration (standard values from Eggins et al. (1997) were used), and the 1 ppb In spike was used to compensate for instrumental drift. Procedural blanks were treated in the same as samples and standards, and after corrected for instrumental drift, the blank intensities were subtracted from all samples and standards prior to external calibration. Uncertainties for measurements are <5 %.

Another crushed aliquot of MIL, weighing ~300 mg, was processed for oxygen isotope analysis. The entire aliquot was ultrasonicated for 5 min in dilute HCl, washed 3 times in de-ionized distilled water, and dried. Visual inspection of the acid-washed sample revealed sub-mm grains of a blue opaque phase, with thin brown filaments attached, that was interpreted to be a contaminant. The contaminant was removed by

hand-picking under a 25X binocular microscope. Duplicate aliquots of the remaining sample weighing ~2 mg were loaded for oxygen isotope analysis. The resulting analyses, however, showed a higher dispersion in oxygen isotope ratios than is normally obtained for a homogeneous sample. Further characterization showed additional contaminant, eventually identified as scraps of plastic, scraped from a threaded cap that had been forced onto the top of an unthreaded storage vial. After removal of contaminants by additional hand-picking, the remaining sample was reanalyzed for oxygen isotopes.

The repeatedly hand-picked, duplicate aliquots of MIL weighing ~2 mg were loaded into a reaction chamber for isotopic analysis (Sharp 1990). The loaded reaction chamber was heated and evacuated for several hours, repeatedly fluorinated with 25 torr of BrF_5 and evacuated, and then fluorinated overnight. Evacuation and fluorination were repeated the next morning until measured room-temperature fluorination products non-condensable in liquid nitrogen were reduced to a negligible blank. Analyses of individual samples were made by loading 25-30 torr of BrF_5 into the reaction chamber and heating the sample with a Synrad CO_2 infrared laser (30 w, 10.6 μm wavelength). The laser beam was defocused to a spot size of 100 μm diameter to minimize scattering of sample particles. The resulting mixture of O_2, SiF_4, and residual interhalogen compounds was purified by passage through 2 liquid nitrogen traps, and pumped by a single-stage Hg diffusion pump onto molecular sieve 5A chilled by liquid nitrogen. The purified sample was transferred to the dual inlet of a Thermo-Fisher MAT 252 mass spectrometer where the ion beams of $^{16}O^{16}O$, $^{16}O^{17}O$, and $^{16}O^{18}O$ were measured (Rumble and Hoering 1994). Every sample was tested for NF_3 and CF_4 contamination by scanning the mass range from 40 to 75 Da with a Faraday cup whose pre-amplifier resistor had a value of 3×10^{11}

ohms. Two aliquots of a reference material, Gore Mountain garnet (USNM 107144), were analyzed for every 4 unknowns. The reference garnet gives a value of $d^{18}O_{VSMOW}$ of 6.0 per mil in comparison to UWG-2 (Rumble et al. 1997; Valley et al. 1995). The 2s standard deviations of Gore Mountain garnet analyses were as follows: $D^{17}O$ +/- 0.03, $d^{17}O$ +/- 0.09; and $d^{18}O$ +/- 0.17 per mil. The value used for the slope of the Terrestrial Fractionation Line (TFL) in this study is 0.526 (+/- 0.001) (Rumble et al. 2007).

3.0 RESULTS

3.1 Petrographic Description and Mineral Abundances

MIL is a brecciated dunite dominated by 200-400 μm angular olivine grains set in a fine-grained, predominantly silicate, matrix. Olivine grains of up to 2.5 mm were observed (Fig. B1a). No "zoned phase sequence" coronas around olivine grains, which are common in mesosiderites (Nehru et al. 1980), were seen in any of the thin sections of MIL. Minor amounts of orthopyroxene, troilite and chromite occur throughout the matrix. Fragmental orthopyroxene grains are subhedral and ~300 μm in size, whereas chromites are more euhedral and ~200 μm. Some grain fragments are composite grains containing olivine, orthopyroxene and chromite preserving primary (non-brecciated) contacts (Mittlefehldt 2008). The longest olivine-orthopyroxene contact is ~270 μm and the few preserved contacts do not give clear evidence whether they are igneous or metamorphic contacts. Troilite in the matrix occurs as large (~800 μm) amoeboid blobs, possibly formed through impact melting. Metal is rare and only found as small blebs associated with troilite. Olivine grains contain small (50-75 μm) agglomerate inclusions that are euhedral, and composed of clinopyroxene ± troilite ± chromite ± metal. At low

magnification these inclusions appear as bright areas scattered throughout larger olivine grains (Figs. B1a and B1b). At higher magnification their euhedral, negative-crystal shapes and individual components are revealed (Figs. B1c and B1d). Well-developed fusion crust can be seen on one side of section 17 (Fig. B1a). Oxidation due to terrestrial weathering is present along most of the fusion crust.

The modal mineralogy of section 17 is: 91 vol.% olivine, 5 vol.% orthopyroxene, 1 vol.% chromite, 0.7 vol.% clinopyroxene, 2.3 vol.% troilite, and <1 vol.% metal (Beck and McSween 2010a). Visual estimates of sections 10 and 11 give similar modes. Mineral abundances of another section of MIL (section 9) were estimated by Krawczynski et al. (2008) as >90 vol.% olivine, <2 vol.% orthopyroxene and ~5 vol.% chromite. Troilite was identified in section 9, but its abundance was not reported (Krawczynski et al. 2008). The similarity in modal abundances between these four sections suggests that mineral distributions are relatively homogeneous and that MIL can be best described as a fragmental monomict dunite breccia.

3.2 Mineral Compositions

Representative major, minor and trace element concentrations for each mineral are given in Table B1. LA ICP-MS analyses were only conducted on section 17. Mineral major and minor element concentrations were not significantly different between the three thin sections studied; therefore only one composition is listed for each mineral. Accordingly, in subsequent figures results are not separated based on section number.

3.2.1 Olivine and Pyroxene

Compositions of pyroxene and olivine in MIL fall near the magnesian end of known diogenite mineral compositions (Fig. B2). Some diogenites contain more Mg-rich

orthopyroxene and olivine than MIL. Calcium concentrations in MIL olivine are on the high end of diogenite olivine compositions, which range from <0.02 – 0.12 wt.% CaO (Beck and McSween 2010a, Shearer et al. 2010). Other olivine minor and trace element abundances are quite low. Ni is below detection limits for the EMP (<0.02 wt.%), and Cr_2O_3 is barely detectable at 0.02 wt.%. Ni was not measured in olivine with LA ICP-MS. Abundances of Y and Zr in olivine were measured with LA ICP-MS, and their concentrations are 0.04 and 0.05 ppm, respectively. No Fe/Mg zoning was observed in MIL olivine, suggesting equilibration after crystallization. A high current P x-ray map of one grain in section 17 was acquired. This high-current x-ray map revealed no P zoning in olivine (Balta and Beck 2011).

As described above, orthopyroxene (Ca-poor) occurs as larger grains in the matrix, whereas clinopyroxene (Ca-rich) forms small agglomerate inclusions within olivine. MIL orthopyroxene and clinopyroxene differ not only in textural setting, but also in their Fe#'s (molar Fe# = Fe/(Fe+Mg)*100). Clinopyroxene inclusions are much more Mg-rich (low Fe#) than orthopyroxene (Table B1). MIL orthopyroxene has TiO_2 and Al_2O_3 concentrations that are generally in the middle of the range for diogenite orthopyroxene (see Fig. B3). The concentration of Cr_2O_3 in MIL orthopyroxene tends to be on the high end of the diogenite range (MIL = 0.64 wt.% Cr_2O_3, diogenites 0.25 – 0.78 wt.%, Beck and McSween 2010a; Fowler et al. 1994; Mittlefehldt 1994). As with the minor elements which are incompatible in orthopyroxene (Al_2O_3 and TiO_2), most incompatible trace elements in MIL orthopyroxene fall near the median of diogenite ranges as well (Fig. B3). The concentrations of the incompatible elements Y and Zr in MIL orthopyroxene (Y = 1.23 mg/g, Zr = 0.93 mg/g) are also in the mid ranges

determined for diogenite orthopyroxenes (Y = 0.001 – 3.13 mg/g, Zr = 0.023 – 3.31 mg/g; Fowler et al. 1995).

Clinopyroxenes included in olivine were too small to acquire reliable LA ICP-MS data. While clinopyroxene has been reported in some diogenites, it typically occurs as either exsolution lamellae in orthopyroxene (Mittlefehldt 1994; Mittlefehldt and Lindstrom 1993) or interstitially between orthopyroxene grains (Domanik et al. 2004), and has not been previously reported as inclusions in olivine (but see below).

The FeO/MnO wt.% ratios in pyroxene and olivine can be used to identify a sample's parent body, and thus may be utilized in achondrite meteorite classification (Papike et al. 2003). Initial findings suggested that MIL olivine had ambiguous FeO/MnO values, falling between the mesosiderite and HED groups (McBride and McCoy 2006, Mittlefehldt 2008). Although compositions of some MIL olivine grains overlap both fields, the majority of the olivine FeO/MnO values clearly match the diogenites (Fig. B4a). Orthopyroxenes overlap both fields to a greater degree, but again, the majority of grains match the diogenites (Fig. B4b). MIL clinopyroxene inclusions, however, have FeO/MnO values that fall well below both the diogenite and mesosiderite pyroxene fields (Fig B4b). This is likely due to the preferential distribution of $Ca>Mn^{2+}>Fe^{2+}>Mg$ into the pyroxene M2 site, leading to lower Fe and Mn in high-Ca pyroxenes relative to low-Ca pyroxenes (Papike 1981).

Our investigation has identified mineral inclusions in diogenite olivine that are texturally and compositionally very similar to those found in MIL olivine. We found these inclusions in 3 samples: Graves Nunataks (GRA) 98108, LaPaz Icefield (LAP) 03979, and Lewis Cliff (LEW) 88679. Pyroxene compositions in these diogenite olivine

inclusions are plotted as triangles in Figure B4b, where it can be seen that they match MIL in both FeO/MnO and Fe#. The pyroxenes in the diogenite inclusions have high Ca contents, include agglomerates of chromite and/or troilite, are subhedral and commonly display negative crystal forms (Fig. B5). All of these properties are also characteristic of the inclusions in MIL olivine. These clinopyroxenes included in diogenite olivine range in minor element concentration from 0.08 wt.% TiO_2, 0.31 wt.% Al_2O_3, and 0.12 wt.% Cr_2O_3 in LEW 88679, to 0.30 wt.% TiO_2, 1.50 wt.% Al_2O_3, and 0.86 wt.% Cr_2O_3 in LAP 03979. GRA 98108 clinopyroxene inclusions have compositions between these meteorites.

3.2.2 Chromite, Troilite and FeNi-Metal

Troilite in MIL does not show any significant compositional variation. Nor does FeNi metal, ranging from 0.67-0.95 wt.% Ni and 0.94-2.15 wt.% Co. Chromites, however, show variations in chemistry that are linked to textural setting (Fig. B6). Large, euhedral chromites in the matrix tend to be Al-rich with Cr#s (Cr# = Cr/(Cr+Al)*100) ranging from 76-81. These chromites are similar in composition and texture to those found in diogenites (Bowman et al. 1999). We note that this range also overlaps chromites in mesosiderites (Powell 1971). Although indices similar to FeO/MnO in silicates have been developed to identify meteorite groupings for spinel (Papike et al. 2004), there are insufficient data at this time to chemically distinguish HED chromites from those in mesosiderites. The second chromite composition in MIL occurs as inclusions in olivine. These spinels are much more Cr-rich (Cr# 94) and fall well outside the field of known diogenite compositions (Fig. B6). Such spinels inclusions in olivine may have crystallized early from diogenite melts (Bowman et al. 1999).

3.3 Geochemistry

3.3.1 Bulk Geochemistry

The results of the ICP-MS analysis of MIL are presented in Table B2. Select elements are shown in element-element plots in Figure B6, where they are compared to diogenite data obtained by ICP-MS analysis (Barrat et al. 1999, 2008, 2010a; Mittlefehldt et al. forthcoming). MIL has a higher Cr content than typically found for diogenite whole-rock samples (Fig. B7a) although Ellemeet, Garland, MET 00436, NWA 4215 and Shalka have comparable Cr contents (Barrat et al. 2006, 2008; Fredriksson et al. 1976; McCarthy et al. 1972; Mittlefehldt 1979, 1994; Mittlefehldt et al. 2010, in preparation). The high Cr content is most plausibly a reflection of a higher modal chromite content for MIL compared to that typical of diogenites (diogenites can contain up to 5 vol.% chromite, but typically contain 0.5-1 vol.% chromite, Bowman et al. 1997). Chromite is a major host for V in MIL (Table B1) and diogenites (Bowman et al. 1999; Mittlefehldt 1994). In spite of its higher chromite content, the V content of MIL is at the lower end of the range observed for diogenites. Based on in situ measurements of diogenites (Shearer et al. 2010), we expect that orthopyroxene in MIL has a much higher V content than does the olivine. The V_{opx}/V_{ol} ratios of the seven diogenites measured by Shearer et al. (2010) vary from 6.4 to 27.1. The low V content for MIL compared to many diogenites plausibly represents a lower V content of the silicate minerals because of the much higher modal olivine content. The contents of the incompatible lithophile elements Al, Ti, Sm and Yb are lower in MIL than in diogenites, with a few exceptions (Figs. B7b and B7c). The moderately siderophile element Co is higher in MIL than found for any of the diogenites, whereas the Ni content is at the high end of the diogenite range (Fig. B7d).

3.3.2 Oxygen Isotopes

Oxygen isotopic composition is a proven method of classifying achondrite meteorites (Clayton and Mayeda 1996). Achondrite parent bodies became homogenized in oxygen isotopes (^{16}O, ^{17}O and ^{18}O) during differentiation, and subsequent mass-dependant fractionation causes all samples from a particular body to fall upon a single oxygen isotope fractionation line (Clayton and Mayeda 1996). Here we compare MIL oxygen isotopic compositions to those of other HEDs. Our data are reported in $d^{18}O$ [$d^{18}O = (^{18}O/^{16}O)_{MIL}/(^{18}O/^{16}O)_{SMOW}$; where SMOW = standard mean ocean water] and $D^{17}O$ [$D^{17}O = (d^{17}O - 0.52*d^{18}O)$; where $d^{17}O$ is calculated similar to $d^{18}O$ above]. In our two analyses, we measured MIL to contain -0.197 and -0.236 $D^{17}O$, and 3.04 and 3.14 $d^{18}O$. The oxygen isotopic composition of MIL matches that of other HEDs. MIL has the same $D^{17}O$ values as individual eucrite and diogenite analyses, and is within error of the well-defined mean $D^{17}O$ for all HEDs (Fig. B8).

4.0 DISCUSSION

4.1 Classification

While the oxygen isotopic composition of MIL matches the HEDs quite well, there is sufficient overlap between mesosiderite and HED oxygen isotope values to draw a classification solely based on this evidence into question (Fig. B8) (Greenwood et al. 2005 and 2006). We turn to a comparison of mineral chemistries, specifically silicate FeO/MnO, to better determine if MIL is an HED or a mesosiderite lithic clast.

Compositions of minerals in MIL, specifically FeO/MnO in olivine and pyroxene, may be used to determine whether MIL should be classified as an HED or

mesosiderite. Because of their similar behavior in igneous systems, the ratios of FeO to MnO can be used to argue for common parent bodies for meteorites, and thus proper classification (Papike et al. 2003). Though it appears that MIL has undergone metamorphic equilibration, which will be discussed below, the original FeO/MnO ratio should not be affected. Equilibration may alter the total concentrations of FeO + MnO, but due to their similar behaviors in geochemical systems, it would preserve the original ratio.

While there is overlap between the mesosiderite and HED FeO/MnO fields, it is not as complete as for $D^{17}O$. We attempted to minimize this overlap as much as possible by comparing FeO/MnO in MIL only to the diogenites. We did not use eucrites because they have been shown to have a modest range of FeO/MnO ratios (Mayne et al. 2009), and because diogenites have measurably different FeO/MnO ratios than the eucrites (Papike et al. 2001). Similarly, we excluded howardites because they are regolith breccias and may contain chondritic and other foreign clasts (Mittlefehldt et al. 1998), which would have non-HED FeO/MnO. As shown in Figure B4, FeO/MnO ratios in both MIL olivine and pyroxene match the diogenites much better than they match the mesosiderites. The majority of grains of both of these minerals plot with the diogenites above the mesosiderite field. This suggests that MIL belongs with the HEDs.

Petrographic evidence is more ambiguous. The lack of FeNi metal in MIL and the lack of olivine coronas, both ubiquitous in mesosiderites, would seem to suggest MIL belongs with the HEDs, where these are absent. However, if MIL were a mesosiderite lithic clast, the paucity of FeNi metal and lack of olivine coronas may be expected. Other mesosiderite ultramafic lithic clasts reported contain low amounts of metal (McCall and

Cleverly 1965; Ntaflos et al. 1993), and, due to the formation of coronas in mesosiderite olivine through a redox reaction with the metal-rich matrix (Ruzicka et al. 1994), olivine coronas would be expected to be absent in a mesosiderite lithic clast containing minerals that had no direct contact to the metal-rich matrix.

The small clinopyroxene ± troilite ± chromite ± metal inclusions in MIL olivine provide an additional link to the HEDs. Three diogenites (GRA 98108, LEW 88679, and LAP 03979) contain olivine with inclusions having very similar mineral compositions and textures to the inclusions in MIL, as discussed above. In a review of 10 mesosiderites, Powell (1971) described similar inclusions to those we have observed in MIL olivine. However, the inclusions described by Powell (1971) occur predominantly in pyroxene, not olivine, and are composed solely of opaque phases, not diopside + opaques. Olivine inclusions have been described in the Budulan mesosiderite, however these inclusions appear symplectic and are composed opaques + orthopyroxene, not opaques + diopside (Lorenz et al. 2010). Two possible explanations exist for the occurrence of identical olivine inclusions in both the diogenites and MIL: either 1) MIL and the diogenites formed by similar processes and from similar melts or 2) they have been intermixed through brecciation. Both of these explanations strongly suggest that the parent body of MIL is the same as that of the diogenites, i.e., asteroid 4 Vesta.

The lack of preserved igneous zoning in MIL olivine also supports grouping it with the diogenites. It is widely thought that the diogenites have undergone substantial post-crystallization equilibration, which has erased any variability in major element concentrations from the cores to rims of pyroxene grains (Fowler et al. 1994; Mittlefehldt 1994). This same Fe/Mg equilibration is seen in diogenite olivine (Beck and McSween

2010a, Shearer et al 2010). In MIL, the lack of preserved zoning of Fe/Mg in olivine generally supports a post-crystallization equilibration history as well. The ratio of orthopyroxene Fe# to olivine Fe# in MIL (0.86) matches that calculated for an equilibrium assemblage of low-Ca pyroxene and olivine crystallizing from eucritic melts (0.86, Stolper 1977), and matches orthopyroxene to olivine Fe# ratios in harzburgitic fragments of other diogenites (0.79-0.91), which were calculated to have equilibrated at ~1100°C (Beck and McSween 2010a). The similarity in metamorphic history between MIL and the diogenites, supports the conclusion that MIL is part of the diogenite group.

As was originally proposed in Beck and McSween (2010a), MIL should be called a "dunitic diogenite", rather than inventing a new named class of HED. The subgrouping of diogenites into dunitic, harzburgitic and orthopyroxenitic follows the previous division of basaltic and cumulate eucrites (Delaney et al. 1984) and of basaltic, olivine-phyric, and lherzolitic shergottites (Goodrich 2002), where each subgroup shares a common petrologic origin. As will be shown in the next few sections, MIL shares a common petrologic origin with the diogenites and thus should be grouped with them.

4.2 NWA 2968 and other potential HED dunites

As mentioned in the introduction, Bunch et al. (2006) have suggested that Northwest Africa 2968 may be a dunite sample related to the HED suite. This meteorite contains olivine that is substantially more magnesian than olivine in MIL (NWA mg# 92.5, MIL mg# 74) but the FeO/MnO ratios are similar (NWA 48, MIL 42.3). Olivine in NWA 2968 is slightly higher in mg# than the ranges typically observed for howardites or diogenites, which typically have olivine with mg# <92 (Beck and McSween 2010a; Delaney et al. 1980; Desnoyers 1982; Fuhrman and Papike 1981; Hewins 1981;

Mittlefehldt 1994, 2000; Sack et al. 1991; Shearer et al., 2010). However, some more magnesian olivines have been observed. Desnoyers (1982) found two grains in howardites with mg#s of 98.5 and 99. The former was in a chondritic clast in Bununu, while the latter was in the matrix of Kapoeta. Fuhrman and Papike (1981) reported one grain in Bholgati with an mg# of 95.9. With the exception of one grain from a chondritic clast (Desnoyers 1982), the textural contexts for these very magnesian olivines have not been described in sufficient detail to determine whether they are innate to the HED parent asteroid or exogenic.

NWA 2968 contains orthopyroxene that is again more magnesian than MIL (NWA mg# ~93, MIL mg# 77.5) but has similar FeO/MnO (NWA 26, MIL 27.1) (Bunch et al. 2006). The NWA 2968 orthopyroxene mg# is also higher than known for diogenites or lithic clasts in howardites (max mg# reported 86-84) (Barrat et al. 2008; Fredriksson and Keil 1963; Fuhrman and Papike 1981; Labotka and Papike 1980; Mittlefehldt 2002). Thus, orthopyroxene in NWA 2968 is substantially more magnesian than found for *bona fide* HED meteorites.

The silicate compositions in NWA 2968 are not good matches to those calculated in models for the crystallization of putative Vesta compositions. Ruzicka et al. (1997) calculate that the initial olivine to form in their fractional crystallization model for Vesta has an mg# of 93, similar to that of NWA 2968 olivine. However, the most magnesian pyroxene in this model has an mg# of only ~84, much lower than that of NWA 2968. Similarly, the Vestan magma ocean model of Righter and Drake (1997) would generate olivine with mg# like those in NWA 2968, but orthopyroxene with mg# lower than those found in that meteorite. Thus, the mineral compositions for NWA 2968 are not good

matches for models that otherwise produce moderate to good simulations of HED mineralogy and composition.

NWA 2968 contains pyrrhotite with 1.7-4.7 wt.% Ni, and troilite containing 0.36 wt.% Ni (Bunch et al. 2006). In contrast, the few troilite grains analyzed in HEDs are very low in Ni, with ~0.01 wt.% (Floran et al. 1981; Mittlefehldt, 2000). Troilite in MIL contains 0.03 wt.% Ni (Table B1). Pyrrhotite has not been reported in HEDs (Rubin 1997).

The oxygen isotopic composition of NWA 2968 (Bunch et al. 2006; Scott et al. 2009a) is within the ranges reported for HEDs and mesosiderites (Greenwood et al. 2005, 2006; Scott et al. 2009b; Wiechert et al. 2004), and thus is permissive of, but does not require, an HED origin. Bulk samples of NWA 2968 have high Ni and Co contents (Barrat et al. 2008), which are not observed in diogenites (Barrat et al. 2008, 2010b; Mittlefehldt 1994, 2000) or MIL (Table B2). Barrat et al. (2010b) also report that NWA 2968 has an unusual La/Sm ratio of 5.5 times CI. Extreme light REE enrichments are known for bulk mesosiderite samples (Mittlefehldt et al. 1979), but have not been observed in bulk samples of HEDs (e.g. Barrat et al. 2008, 2010a; Mittlefehldt and Lindstrom 2003; Warren et al. 2009) or in MIL (this work).

Although it has been suggested that NWA 2968 is a dunite related to HEDs (Bunch et al. 2006), there are substantial mineralogical and compositional reasons to doubt a relationship between them. A detailed petrologic and compositional study of NWA 2968 is needed before kinship with the HED clan can be validated. Two other dunites have recently been discussed as possible HED relatives – NWA 5784 and NWA

5968 – but only limited information is available (Bunch et al. 2010). To date, only MIL 03443 can be convincingly attributed to the HED parent asteroid.

4.3 Petrogenesis: Crustal Cumulate vs. Mantle Residuum Origin

4.3.1 Mineralogic Evidence

On Earth, dunites occur in a variety of geologic settings and can be formed by different processes. They may represent solid residues from a high degree of partial melting, or cumulates formed by fractional crystallization of olivine. Both processes can produce, from bottom up, a dunite-harzburgite-orthopyroxenite stratigraphic sequence. An example of partial melting residuum is the basal dunite in an ophiolite sequence. These dunites contain olivine with higher Mg#s than any of the overlying units, which were either derived from the extruded basaltic magma or lesser degrees of partial melting (e.g. Pallister and Hopson 1981). By the same measure, residual dunites contain the most Cr-rich spinel, Mg-rich pyroxene, Cr-rich olivine, and are lacking in Ca- and Al-rich phases, relative to overlying lithologies (e.g. Pallister and Hopson 1981; Tamura and Arai 2006). In contrast, fractional crystallization may produce cumulate dunites which contain olivine and pyroxene with lower Mg#s, along with lower Cr# spinel, relative to the overlying harzburgites and orthopyroxenites (e.g. the cryptic layering of the Bushveld Complex (Eales and Cawthorn 1996) and the Stillwater Complex (Jackson 1961)). Here we consider the composition of MIL with respect to the two scenarios described above, and with respect to the diogenites, which are harzburgites and orthopyroxenites from Vesta. In a partial melting scenario, MIL would represent the residual mantle from which diogenitic melts were extracted. In the fractionation scenario, both MIL and the two types of diogenites would have formed as cumulates from fractionating magmas.

The silicates in MIL, while very Mg-rich, are not the most magnesian in the HED suite. Some diogenites contain orthopyroxene and olivine that are more Mg-rich than those found in MIL (white circles with low Fe# in Figs. B4a and B4b). Bilanga, EETA79002, LAP 02216, Mangaon, MET 00425, PCA 02008 and QUE 99050 all contain orthopyroxene with Mg#s higher than those in MIL (Mg# 77.6 to 85 vs. 77.5 in MIL; Barrat et al. 2008; Beck and McSween 2010a; Domanik et al. 2004; Mittlefehldt 1994; 2000; Table B1). Similarly, diogenites EETA79002, LAP 02016 and PCA 02008 contain olivine with Mg#s higher than those in MIL (ol Mg# 74.1 to 85.5 vs. 74 in MIL; Beck and McSween 2010a; Mittlefehldt 2000; Table B1). MIL olivine also contains Cr concentrations similar to those in other diogenites (Beck and McSween 2010a; Shearer et al. 2010). Cr#s of larger spinels in MIL are well within the range of other diogenites (Bowman et al. 1999), as seen by the overlap between the MIL data and published diogenite compositions in Figure B5. Finally, MIL orthopyroxene has incompatible minor and trace elements concentrations that fall in the middle of the diogenite orthopyroxene range (Fig. B3). All of the above lines of evidence suggest that MIL is not a mantle restite (a residuum after partial melting), but rather is a cumulate, and is likely part of a fractionation sequence that includes the diogenites. This relationship is bolstered by the presence of clinopyroxene ± troilite ± chromite ± metal inclusions in olivine from both MIL and the diogenites. These inclusions suggest that both MIL and the diogenites were formed from similar processes and from similar melts. Similarly, identical olivine to orthopyroxene Fe# ratios (0.86) of MIL and the diogenites suggests a common metamorphic history, and thus supports a common petrologic origin. We

propose that MIL represents a cumulate dunite from a fractionating magma, which, as it evolved, then produced harzburgitic and orthopyroxenitic diogenites.

4.3.2 Bulk Chemistry Evidence

The lithophile trace element contents of MIL generally support the conclusion that this dunite is a cumulate, not a mantle restite. The Yb and Sm contents of MIL are similar to those of diogenite MET 00422 (Barrat et al. 2008, 2010a), among the lowest determined for diogenites (Fig. B7c). MET 00436 has a lower Yb content, and Tatahouine a lower Sm content, while MET 00422 is lower in both elements. Most diogenites lie between fictive melts with CI Yb/Sm ratios and orthopyroxene adcumulates derived from such melts (calculated via mass balance; $D^{opx/L}_{Sm} = 0.0135$, $D^{opx/L}_{Yb} = 0.0872$, derived from Bédard 2007, using the 1310 ºC melt compositions from Righter and Drake 1997). Thus, all diogenites but MET 00424 and Tatahouine can be explained as mixtures of cumulate orthopyroxene and trapped melt. MIL plots near the cumulate orthopyroxene line, but away from the MIL cumulate line (calculated assuming 95% olivine, 5% orthopyroxene; orthopyroxene/melt partition coefficients as above; $D^{oliv/L}_{Sm} = 0.0006$, $D^{oliv/L}_{Yb} = 0.0469$ from Beattie 1994) (Fig. B7c), implying that it must contain a trapped melt component. Less than 1% trapped melt mixed with the cumulus phases can explain the Sm and Yb budget of MIL.

The parent melt used in the example model for MIL has 5x CI Sm and Yb, and plots well within the field of possible diogenite parent melts in Fig. B7c (~3-9x CI Sm and Yb). This field is calculated from mass balance by applying the orthopyroxene/melt partition coefficients given above to the Sm and Yb contents of those diogenites that plot on the "opx cumulate" line in Fig. B7c. Modeling cumulate chemistry has a high degree

of uncertainty because small errors in partition coefficients translate into large effects in the calculated cumulate composition. Nevertheless, the trace element model is in concert with the argument made above that MIL represents a cumulate from the same or similar magma sequences that produced diogenites, and not a mantle restite.

The minor incompatible lithophile elements Al and Ti are in general agreement with the modeling of Sm and Yb. The concentration of these elements in MIL is low, and as was the case for Sm and Yb, the Al and Ti contents of MIL are close to diogenite MET 00422 (Fig. B7b). We have not attempted to model the Al and Ti contents partly because their olivine/melt partition coefficients are not well known. Another complicating factor is that chromite is a major host for Al and Ti in MIL (Table B1). MIL has a higher modal chromite content than is typical of diogenites as evidenced by its high bulk Cr content (Fig. B7a), and modeling an olivine-orthopyroxene-chromite cumulate is not possible for Al and Ti because their partitioning behavior in Cr-rich spinels is poorly known.

Mineral/melt partition coefficients for Co and Ni are higher for olivine than for orthopyroxene (e.g. Adam and Green 2006); consequently, the high Co content for MIL compared to diogenites is expected (Fig. B7d). We would expect that MIL would have a higher Ni content as well, but this is not the case. MIL has a Ni content within the upper end of the range for diogenites. The moderately siderophile element contents of brecciated HEDs can be significantly affected by even small amounts of chondritic contamination (e.g. see Chou et al. 1976).

Figure B7d shows an example mixing line between an arbitrarily chosen low-Ni diogenite and a chondritic clast from the Ellemeet diogenite (Mittlefehldt 1994). The

four-pointed star on the mixing line represents a 1% admixture of chondritic material to the low-Ni diogenite. As can be seen, the range in diogenite Ni contents could be entirely due to very small amounts of chondritic material. Small amounts of chondritic contamination do not affect the Co content as much as it affects the Ni content, and the range in Co contents observed for diogenites and MIL is innate to cumulate dunites, harzburgites and orthopyroxenites on Vesta.

The case for Ni is more difficult to evaluate. Orthopyroxene separates show a range in Ni contents from <20 to 100 μg/g (Mittlefehldt 1994). The high Ni diogenite, LAP 03979, was described as an unbrecciated olivine diogenite (McBride et al. 2004). However, Beck and McSween (2010a) recognized that it contains two distinct lithologies; a more magnesian harzburgitic diogenite and a more ferroan diogenite. The high Ni content of LAP 03979 is not likely to be innate to the olivine-rich cumulate material, however. Olivine in this rock contains only 29 μg/g Ni (Shearer et al. 2010), which is lower than the whole rock datum shown in Fig. B7d. We can only surmise that the analyzed sample may have contained more than the typical amount of metal, but we cannot establish this as fact. Two labeled diogenites, ALH 85015 and PCA 02008, are polymict, or possibly so. ALH 85015 has been considered a howardite (Berkley and Boynton 1992), although it was originally classified as a diogenite. The Antarctic Meteorite curator has recently reevaluated its classification and has concluded that its correct classification is as a diogenite because "…only one [thin section] shows eucritic material" (*Antarctic Meteorite Newsletter* vol. 33, number 1). This would indicate that ALH 85015 is a polymict diogenite, containing eucritic material formed by mixing on the surface of Vesta, increasing the probability that it may contain chondritic contamination.

PCA 02008 is also a polymict diogenite and may be paired with three howardites based on their cosmogenic nuclide contents (Welten et al. 2009). Again, this increases the likelihood that the high Ni content of this stone reflects chondritic contamination. The ranges shown for all but the labeled diogenites plausibly represent true cumulate compositions.

Excluding the two polymict diogenites, MIL is within the high Ni end of the diogenite range. We have not observed chondritic clasts or eucritic material in the three thin sections we have examined, nor have Krawczynski et al. (2008), though small amounts of fine grained chondritic or eucritic material in the matrix would be difficult to identify. There is no evidence that MIL is polymict, and we thus discount the possibility that its high Ni content is the result of chondritic contamination. Because the Ni content of MIL is within the diogenite range, the parent melt for this olivine-rich cumulate must have had a lower Ni content than those for diogenites with the highest Ni. This is consistent with the inference from lithophile elements that the MIL parent magma was not more primitive than those of diogenites. The very high olivine content of MIL may simply represent a localized accumulation of olivine in an otherwise typical diogenitic intrusive body.

4.4 Melt Inclusions

The inclusions in MIL and diogenite olivine were likely melts that were trapped, and later crystallized into separate daughter phases, as is common for melt inclusions that cool relatively slowly in intrusive rocks (Roedder 1979; Bodnar and Student 2006). Multiple lines of evidence support this model.

Diffusive FeO-loss has been observed between melt inclusions and host olivines in many terrestrial rocks (e.g. Gurenko et al. 1992; Sobolev and Danyushevsky 1994). This FeO-loss leads to the crystallization of Mg-rich diopside from the trapped melt (Danyushevsky et al. 2000), and can lead to sulfide crystallization from parts of the melt incompatible with olivine (Danyushevsky et al. 2002). Also, inclusions that are trapped as melt may recrystallize to form very sharply faceted, negative crystal forms (Roedder 1979; Roedder 1984). We observe Mg-rich diopside and abundant sulfide, indicative of FeO-loss, along with negative-crystal forms in the MIL olivine inclusions (Fig. B1), supporting the hypothesis that these inclusions were trapped as melts.

"Uniform phase ratio" is another criterion for distinguishing inclusions that were once melt from inclusions that were crystalline when incorporated into mineral hosts (Roedder 1984). Modal abundances of phases in MIL inclusions are relatively uniform, with the majority of inclusions containing approximately 40 vol.% troilite, 30 vol.% clinopyroxene and 30 vol.% chromite or metal. This uniform phase ratio was observed in ten inclusions across the three sections, nine of which were in section 17, and one in section 11. Deviations from this average are likely due to different slices through the inclusions, or are a result of different degrees of metastability (Roedder 1984).

The identification of similar melt inclusions in the olivine-rich achondrite QUE 93148 also supports our interpretation. Goodrich and Righter (2000) identified several types of inclusions in QUE 93148 olivine. Their "type 4" inclusions, which they concluded were trapped melt, have the same relative size, shape, and proportion of opaques to silicate as the inclusions in MIL. This supports the interpretation that the inclusions in MIL olivine were trapped as melt. It is important to note that Goodrich and

Righter (2000) also identify olivine inclusions (types 1-3) that they hypothesize formed from exsolution of olivine. This hypothesis is primarily based on the symplectic and lamellar morphologies of the inclusions. We do not see any of these textures in MIL inclusions. If the inclusions in MIL did form through exsolution, symplectic and lamellar textures were likely erased during metamorphism, when the phases redistributed into a more equilibrated distribution (triple junctions).

Several processes can be invoked to explain the incorporation of melt inclusions in MIL olivine. First, melt may have been included during primary olivine growth. Second, melt may have infiltrated through cracks in the olivine and became trapped as melt inclusions as the cracks healed. This is supported by the linear distribution of inclusions in some grains (Fig. B9a), and similar occurrences in diogenite orthopyroxene (Gooley and Moore 1976). Also, some of the inclusions may be have been formed when selvages of melt adhered to crystalline phases, which were both then included in olivine. A few of the MIL inclusions contain chromite with very high Cr#s (94), indicative of early crystallization from a melt (Bowman et al. 1999). It is possible that small, high Cr# chromite crystallized very early from the melt, adhered to small bits of melt, which were both then included in olivine. Finally, these inclusions may have been incorporated during "pseudo-secondary processes" (Roedder 1984), such as adcumulus growth. In such a scenario, olivine grains would have settled at the base or walls of the magma chamber and continued to grow outward at the expense of trapped intercumulus melt. As olivine expands, it incorporates portions of that trapped melt. The included melt would be trapped as inclusions near the edges of grains, where adcumulus growth occurred

(Hunter 1996). The general distribution of inclusions away from the core of one of the larger grains may support this scenario (Fig. B9b).

We have presented sufficient evidence to conclude that these inclusions were trapped melts. Though it is possible that they exsolved from olivine, we think this is less likely.

5.0 CONCLUSIONS

- Meteorite MIL 03443, a dunite breccia originally classified as a mesosiderite, is more likely a member of the HED group. Similarities in oxygen isotopes, silicate FeO/MnO ratios, and mineral compositions between MIL and the diogenites strongly support this grouping.
- The observation of similar, unusual olivine inclusions in both MIL and the diogenites provides further evidence for their grouping. The uniform phase distribution, phases present, and generally morphologies of these inclusions suggest they were trapped as melt.
- We present findings that suggest a cumulate origin for this meteorite. MIL contains more ferroan olivine and orthopyroxene relative to some diogenites. This, coupled with the presence of similar olivine inclusions in both groups, leads us to propose that MIL represents a cumulate akin to the diogenites, not a mantle restite.
- Bulk compositional evidence supports a close link between MIL and diogenites as well. The trace element contents suggest a parent melt similar to those that produced diogenites. The olivine-rich nature of MIL plausibly reflects a localized accumulation of olivine in an otherwise typical diogenitic pluton.

- As a cumulate that likely formed in one of the same plutons and by similar processes as diogenites, MIL should be classified as a *dunitic diogenite*.
- HST and ground-based spectra were initially interpreted to show olivine-rich lithologies in the eastern hemisphere of Vesta (Binzel et al. 1997; Gaffey 1997). However, this conclusion has been challenged by subsequent studies (Li et al. 2010; Reddy et al. 2010). Similarly, ambiguity exists in the interpretation of HST spectra of the South Polar basin, which may show abundant olivine (Thomas et al. 1997). Our study provides evidence of an olivine-rich lithology in the HED suite and thus supports the presence of such a lithology on Vesta.

ACKNOWLEDGEMENTS

The authors thank L. Fedele (Virginia Tech) and P. Luffi (Rice) for their assistance in this project, and A. Yamaguchi, K. Righter and an anonymous reviewer for thoughtful reviews that significantly improved this manuscript. We also acknowledge C. Satterwhite for providing curation information, the MWG for allocating meteorite samples, and J. A. Barrat for his comments. This work was partially supported by NASA Cosmochemistry Grant NNG06GG36G to HYM. Work done at JSC was funded by the NASA Cosmochemistry Program to DWM.

REFERENCES

Abramoff M. D., Magelhaes P. J., and Ram S. J. (2004) Image processing with ImageJ. *Biophotonics International* **11**:36-42.

Adam J., and Green T. (2006). Trace element partitioning between mica- and amphibole-bearing garnet lherzolite and hydrous basanitic melt: 1. Experimental results and the investigation of controls on partitioning behavior. *Contributions to Mineralogy and Petrology* **152**:1-17.

Balta J. B. and Beck A. W. (2011) Magmatic cumulate textures preserved by trace elements in diogenite meteorites (abstract). Lunar and Planetary Science Conference **41**:CD #1107.

Barrat J. A., Gillet Ph., Lesourd M., Blichert-Toft J., and Poupeau G. R. (1999) The Tatahouine diogenite: Mineralogical and chemical effects of sixty-three years of terrestrial residence. *Meteoritics and Planetary Science* **34**:91-97.

Barrat J. A., Beck P., Bohn M., Cotten J., Gillet Ph., Greenwood R. C. and Franchi I. A. (2006) Petrology and geochemistry of the fine-grained unbrecciated diogenite Northwest Africa 4215. *Meteoritics and Planetary Science* **41**:1045-1057.

Barrat J. A., Yamaguchi A., Greenwood R. C., Benoit M., Cotton J., Bohn M., and Franchi I. (2008) Geochemistry of diogenites: Still more diversity in their parent melts. *Meteoritics and Planetary Science* **43**:1759-1775.

Barrat J. A., Yamaguchi A., Zanda B., Bollinger C., and Bohn M. (2010a) Relative chronology of crust formation on asteroid Vesta: Insights from the geochemistry of diogenites. *Geochimica et Cosmochimica Acta* **74**:6218-6231.

Barrat J. A., Greenwood R. C., Yamaguchi A., Bohn M., Bollinger C., and Franchi I. A. (2010b) Northwest Africa 2968/3329: Dunitic and diogenitic pebbles from the same mesosiderite fall? (abstract). *Meteoritics and Planetary Science* **45**:A11.

Beattie P. (1994) Systematics and energetics of trace-element partitioning between olivine and silicate melts: Implications for the nature of mineral/melt partitioning. *Chemical Geology* **117**:57-71.

Beck A. W. and McSween H. Y. (2010a) Diogenites as polymict breccias composed of orthopyroxenite and harzburgite. *Meteoritics and Planetary Science* **45**:850-872.

Beck A. W. and McSween H. Y. (2010b) Connections between dunite MIL 03443 and the diogenite meteorites (abstract). *Lunar and Planetary Science Conference* **40**: CD#1533.

Bédard J. H. (2007) Trace element partitioning coefficients between silicate melts and orthopyroxene: Parameterizations of D variations. *Chemical Geology* **244**:263-303.

Berkley J. L. and Boynton N. J. (1992) Minor/major element variation within and among diogenite and howardite orthopyroxenite groups. *Meteoritics* **27**:387-394.

Binzel R. P., Gaffey M. J., Thomas P. C., Zellner B. H., Storrs A. D., and Wells E. N. (1997) Geologic mapping of Vesta from 1994 Hubble Space Telescope images. *Icarus* **128**:95-103.

Bodnar R. J. and Student J. J. (2006) Melt inclusions in plutonic rocks: Petrography and microthermometry. In *Melt Inclusions in Plutonic Rocks* (J. D. Webster, *ed.*) Mineral. Assoc. Canada, Short Course **36**:1-26.

Bowman L. E., Papike J. J., and Spilde M. N. (1999) Diogenites as asteroidal cumulates: Insights from spinel chemistry. *American Mineralogist* **84**:1020-1026.

Bowman L. E., Spilde M. N., and Papike J. J. (1997) Automated energy dispersive spectrometer modal analysis applied to the diogenites. *Meteoritics and Planetary Science* **32**:869-875.

Bunch T. E., Wittke J. H., Rumble D. III Irving A. J., and Reed B. (2006) Northwest Africa 2968: A dunite from 4 Vesta (abstract). *Meteoritics and Planetary Science* **41**:A31.

Bunch T. E., Irving A. J., Wittke J. H., Kuehner S. M., Rumble D. III and Sipiera P. P. (2010) Northwest Africa 5784, Northwest Africa 5968 and Northwest Africa 6157: More Vestan dunites and olivine diogenites (abstract). *Meteoritics and Planetary Science*, **45**:A27.

Chou C.-L., Boynton W. V., Bild R. W., Kimberlin J., and Wasson J. T. (1976) Trace element evidence regarding a chondritic component in howardite meteorites. *Procedings of the 7th Lunar and Planetary Science Conference*, 3501-3518.

Clayton R. N. and Mayeda T. K. (1996) Oxygen isotope studies of achondrites. *Geochimica et Cosmochimica Acta* **60**:1999-2017.

Danyushevsky L. V., Della-Pasqua F. N., and Sokolov S. (2000) Re-equilibration of melt inclusions trapped by magnesian olivine phenocrysts from subduction-related magmas: petrological implications. *Contributions to Mineralogy and Petrology* **138**:68-83.

Danyushevsky L. V., McNeill A. W., and Sobolev A. V. (2002) Experimental and petrological studies of melt inclusions in phenocrysts from mantle-derived magmas: an overview of techniques, advantages and complications. *Chemical Geology* **183**:5-24.

Delaney J. S., Prinz M., and Nehru C. E. (1980) Olivine clasts from mesosiderites and howardites - Clues to the nature of achondritic parent bodies. In *Lunar and Planetary Science Conference Proceedings*, 1073-1087.

Delaney J. S., Prinz M., and Takeda H. (1984) The polymict eucrites. In *Lunar and Planetary Science Conference Proceedings* Part I, *Jorunal of Geophysical Research* **89**:C251-C288.

Desnoyers C. (1982) L'Olivine dans les howardites: origine, et implications pour le corps parent de ces météorites achondritiques. *Geochimica et Cosmochimica Acta* **46**:667-680.

Domanik K., Kolar S., Musselwhite D. and Drake M. J. (2004) Accessory silicate mineral assemblages in the Bilanga diogenite: A petrographic study. *Meteoritics and Planetary Science* 3**9**:567-579.

Eales H. V. and Cawthorn R. G. (1996) The Bushveld Complex. In *Layered Intrusions*, eddited by Cawthorn R. G., Amsterdam: Elsevier Science, pp. **181**-229.

Eggins S. M., Woodhead J. D., Kinsley L. P. J., Mortimer G. E., Sylvester P., McCulloch M. T., Hergt J. M., and Handler R. (1997) A simple method for precise determination of ≥40 trace elements in geological samples by ICPMS using enriched isotope internal standardisation. *Chemical Geology* **134**:311-326.

Floran R. J., Prinz M., Hlava P. F., Keil K., Spettel B., and Wänke H. (1981) Mileralogy, petrology, and trace element geochemistry of the Johnstown meteorite: a brecciated orthopyroxenite with siderophile and REE-rich components. *Geochimica et Cosmochimica Acta* **45**:2385-2391.

Fowler G. W., Papike J. J., Spilde M. N., and Shearer C. K. (1994) Diogenites as asteroidal cumulates: Insights from orthopyroxene major and minor element chemistry. *Geochimica et Cosmochimica Acta* **58**:3921-3929.

Fowler G. W., Shearer C. K., Papike J. J., and Layne G. D. (1995) Diogenites as asteroidal cumulates: Insights from orthopyroxene trace element chemistry. *Geochimica et Cosmochimica Acta* **59**:3071-3084.

Fredriksson K., and Keil K. (1963) The light-dark structure in the Pantar and Kapoeta stone meteorites. *Geochimica et Cosmochimica Acta* **27**:717-739.

Fredriksson K., Noonan A., Brenner P., and Sudre C. (1976) Bulk and major phase composition of eight hypersthene achondrites (abstract). *Meteoritics* **11**:278-280.

Fuhrman M., and Papike J. J. (1981) Howardites and ploymict eucrites: Regolith samples from the eucrite parent body. Petrology of Bholgati, Bununu, Kapoeta, and ALHA76005. *Proceedings of Lunar and Planetary Science* **12B**:1257-1279.

Gaffey M. J. (1997) Surface lithologic heterogeneity of asteroid 4 Vesta. *Icarus* **127**:130-157.

Greenwood R. C., Franchi I. A., Jambon A. and Buchanan P. C. (2005) Widespread magma oceans on asteroidal bodies in the early Solar System. *Nature* **435**:916-918.

Greenwood R. C., Franchi I. A., Jambon A., Barrat J. A. and Burbine T. H. (2006) Oxygen isotope variation in stony-iron meteorites. *Science* **313**:1763-1765.

Goodrich C. A. and Righter K. (2000) Petrology of unique achondrite Queen Alexandra Range 93148: A piece of the pallasite (howardite-eucrite-diogenite?) parent body? *Meteoritics and Planetary Science*, **35**:521-535.

Goodrich C. A. (2002) Olivine-phyric martian basalts: A new type of shergottite. *Meteoritics and Planetary Science,* **37**:31-34.

Gooley R. and Moore C. B. (1976) Native metal in diogenite meteorites. *American Mineralogist* **61**:373-378.

Govindaraju, K. (1994) 1994 compilation of working values and sample descriptions for 383 geostandards. *Geostandards Newsletter,* **18**:1-158.

Guillong M., Horn I., Gunther D. (2003) A comparison of 266 nm, 213 nm and 193 nm produced from a single solid state Nd:YAG laser for laser ablation. Journal of Analytical Atomic Spectroscopy, **18**:1224-1230.

Gurenko A. A., Sobolev A. V., and Kononkova N. N. (1992) New petrological data on Icelandic rift alkali basalts. *Geochemistry International* **29**:41-53.

Herzberg C. T. and O'Hara M. J. (1985) Origin of mantle peridotite and komatiite by partial melting. *Geophysical Research Letters* **12**:541-544.

Hewins R. H. (1981) Orthopyroxene-olivine assemblages in diogenites and mesosiderites. *Geochimica et Cosmochimica Acta* **45**:123-126.

Hunter R. H. (1996) Texture development in cumulate rocks. In *Layered Intrusions*, eddited by Cawthorn R. G., Amsterdam: Elsevier Science, pp. 77-101.

Jackson E. D. (1961) Primary Textures and Mineral Associations in the Ultramafic Zone of the Stillwater Complex. *U. S. Geological Survey Professional Paper #358*.

Kong P., Su W., Li X., Spettel B., Palme H., and Tao K. (2008) Geochemistry and origin of metal, olivine clasts, and matrix in the Dong Ujimqin Qi mesosiderite. *Meteoritics and Planetary Science* **43**:451-460.

Krawczynski M. J., Elkins-Tanton L. T., and Grove T. L. (2008) Petrology of mesosiderite(?) MIL 03443,9; constraints on eucrite parent body bulk composition and magmatic processes (abstract). *Lunar and Planetary Science Conference* 39: CD #1229.

Labotka T. C., and Papike J. J. (1980) Howardites: Samples of the regolith of the eucrite parent-body. Petrology of Frankfort, Pavlovka, Yurtuk, Malvern, and ALHA 77302. *Proceedings of the Eleventh Lunar and Planetary Science Conference*, 1103-1130.

Li J. –Y., McFadden L. A., Thomas P. C., Mutchler M. J., Parker J. W., Young E. F., Russell C. T., Sykes M. V. and Schmidt B. E. (2010) Photometric mapping of asteroid (4) Vesta's southern hemisphere with Hubble Space Telescop. *Icarus* **208**:238-251.

Lorenz C. A., Nazarov M. A., Branstaetter F. and Ntaflos Th. (2010) Metasomatic alteration of olivine inclusions in the Budulan mesosiderite. *Petrology* **18**:461-470.

Mayne R. G., McSween H. Y., McCoy T. J. and Gale A. (2009) Petrology of the unbrecciated eucrites. *Geochimica et Cosmochimica Acta* **73**:794-819.

McBride K. and McCoy T. J. (2006) *Antarctic Meteorite Newsletter* **29**(2): p. 32.

McBride K., McCoy T. J., and Welzenbach L. (2004) *Antarctic Meteorite Newsletter* **27**(3): p. 19.

McCall G. J. and Cleverly W. H. (1965) Newly discovered mesosiderite containing achondrite fragments; the Mount Padbury mesosiderite. *Nature* **207**:851.

McCarthy T. S., Ahrens L. H., and Erlank A. J. (1972) Further evidence in support of the mixing model for howardite origin. *Earth Planetary Science Letters* **15**:86-93.

McSween H. Y, Mittlefehldt D. W., Beck A. W, Mayne R. G., and McCoy T. J. (2011) HED meteorites and their relationship to the geology of Vesta and the Dawn mission. *Space Science Reviews*, doi: 10.1007/s11214-010-9637-z.

Mittlefehldt D. W. (1979) Petrographic and chemical characterization of igneous lithic clasts from mesosiderites and howardites and comparison with eucrites and diogenites. *Geochimica et Cosmochimica Acta* **43**: 1917-1935.

Mittlefehldt D. W. (1980) The composition of mesosiderite olivine clasts and implications for the origin of pallasites. *Earth and Planetary Science Letters* **51:**29-40.

Mittlefehldt D. W. (1994) The genesis of diogenites and HED parent body petrogenesis. *Geochimica et Cosmochimica Acta* **58**: 1537-1552.

Mittlefehldt D. W. (2000) Petrology and geochemistry of the Elephant Moraine A79002 diogenite. *Meteoritics and Planetary Science* **35**:901-912.

Mittlefehldt D. W. (2002) Geochemistry of new, unusual diogenites and constraints on diogenite genesis (abstract). *Meteoritics and Planetary Science* **37**:A100.

Mittlefehldt D. W. (2008) Meteorite dunite breccia MIL 03443: A probable crustal cumulate closely related to diogenites from the HED parent asteroid (abstract). *Lunar and Planetary Science Conference* 39:CD.#1919.

Mittlefehldt D. W. and Lindstrom M. M. (1993) Geochemistry and petrology of a suite of ten Yamato HED meteorites. *Antarctic Meteorite Research* **6**:268.

Mittlefehldt D. W. and Lindstrom M. M. (2003) Geochemistry of eucrites: Genesis of basaltic eucrites, and Hf and Ta as petrogenetic indicators for altered antarctic eucrites. *Geochimica et Cosmochimica Acta* **67**:1911-1935.

Mittlefehldt D. W., Chou C.-L. and Wasson J. T. (1979) Mesosiderites and howardites; igneous formation and possible genetic relationships. *Geochimica et Cosmochimica Acta* **43**:673-688.

Mittlefehldt D. W., McCoy T. J., Goodrich C. A., and Kracher A. (1998) Non-chondritic meteorites from asteroidal bodies. In *Planetary materials*, edited by Papike J. J. Reviews in Mineralogy and Geochemistry, vol. 36. Washington, D.C.: Mineralogical Society of America. pp. 4.1–4.195.

Mittlefehldt D. W., Beck A. W., Lee C-T. A., McSween H. Y., Buchanan P. C., and Burbine T. Forthcoming. Compositional constraints on the genesis of diogenites. *Meteoritics and Planetary Science.*

Mutchler, S. T., Fedele, L. and Bodnar, R. J. (2008) Analysis Management System (AMS) for reduction of laser ablation ICP-MS data In *Laser Ablation ICP-MS in the Earth Sciences: Current Practices and Outstanding Issues*, edited by Sylvester P. Mineralogical Association of Canada, Short Course **40**:503-353.

Ntaflos T., Kurat G., Koeberl C., and Brandstatter F. (1993) Mincy dunite F6241B: The missing ultramafic component from mesosiderites (abstract). *Meteoritics* **28**:414.

Nehru C. E., Zucker S. M., Harlow G. E., and Prinz M. (1980) Olivines and olivine coronas in mesosiderites. *Geochimica et Cosmochimica Acta* **44**:1103-1118.

Pallister J. S. and Hopson C. A. (1981) Samail ophiolite plutonic suite: Field relations, phase variation, cryptic variation and layering, and a model of a spreading ridge magma chamber. *Journal of Geophysical Research* **86**:2593-2644.

Papike J. J. (1981) Silicate mineralogy of planetary basalts. In *Basaltic Volcanism on the Terrestrial Planets*, edited by Merrill R. B. and Ridings R. New York: Pergamon, pp. 340-363.

Papike J. J., Karner J. M., and Shearer C. K. (2001) Mn-Fe systematics in pyroxene from planetary basalts: An indicator of planetary parentage (abstract) *32rd Lunar and Planetary Science Conference,* p. 1009.

Papike J. J., Karner J. M., and Shearer C. K. (2003) Determination of planetary basalt parentage: A simple technique using the electron microprobe. *American Mineralogist* **88**:469-472.

Papike J. J., Karner J. M., and Shearer C. K. (2004) Comparative planetary mineralogy: V/(Cr + Al) systematics in chromite as an indicator of relative oxygen fugacity. *American Mineralogist* **89**:1557-1560.

Powell B. N. (1971) Petrology and chemistry of mesosiderites--II. Silicate textures and compositions and metal-silicate relationships. *Geochimica et Cosmochimica Acta* **35**:11-34.

Prinz M., Delaney J. S., Harlow G. E., Bedell R. L., and Nehru C. E. (1980) Modal studies of mesosiderites and related achondrites, including the new mesosiderite ALHA 77219. In *Lunar and Planetary Science Conference Proceedings*, 1055-1071.

Reddy V., Gaffey M. J., Kelley M. S., Nathues A., Li J.-Y. and Yarbrough R. (2010) Compositional heterogeneity of Asteroid 4 Vesta's southern hemisphere: Implications for the Dawn mission. *Icarus*, doi:10.1016/j.icarus.2010.07.015.

Righter K. and Drake M. J. (1997) A magma ocean on Vesta: Core formation and petrogenesis of eucrites and diogenites. *Meteoritics and Planetary Science* **32**:929-944.

Roedder E. (1984) Fluid Inclusions. *Reviews in Mineralogy and Geochemistry* vol. 12.

Roedder, E. (1979): Origin and significance of magmatic inclusions: *Bull. de Miner*. **102**:487–510.

Rubin A. E. (1997) Mineralogy of meteorite groups. *Meteoritics and Planetary Science* **32**:231-247.

Rumble D. III and Hoering T. C. (1994) Analysis of oxygen and sulfur isotopes ratios in oxide and sulfide minerals by spot heating with a carbon dioxide laser in a fluorine atmosphere. *Accounts of Chemical Research* **27**:237-241.

Rumble D. III, Farquhar J., Young E. D. and Christensen C. P. (1997) In situ oxygen isotope analysis with an excimer laser using F_2 and BrF_5 reagents and O_2 gas as analyte. *Geochimica et Cosmochimica Acta* **61**:4229-4234.

Rumble D. III, Miller M. F., Franchi I. A. and Greenwood R. C. (2007) Oxygen three-isotope fractionation lines in terrestrial silicate minerals: an inter-laboratory comparison

of hydrothermal quartz and eclogitic garnet. *Geochimica et Cosmochimica Acta* **71**:3592-3600.

Ruzicka A., Boynton W. V., and Ganguly J. (1994) Olivine coronas, metamorphism, and the thermal history of the Morristown and Emery mesosiderites. *Geochimica et Cosmochimica Acta* **58**:2725-2741.

Ruzicka A., Snyder G. A., and Taylor L. A. (1997) Vesta as the howardite, eucrite and diogenite parent body: Implications for the size of a core and for large-scale differentiation. *Meteoritics and Planetary Science* **32**:825-840.

Sack R. O., Azeredo W. J. and Lipschutz M. E. (1991) Olivine diogenites: The mantle of the eucrite parent body. *Geochimica et Cosmochimica Acta* **55**:1111-1120.

Scott E. R. D., Greenwood R. C., Franchi I. A., and Sanders I. S. (2009a) Oxygen isotopic constraints on the origin and parent bodies of eucrites, diogenites, and howardites (abstract). *Lunar and Planetary Science Conference* 40: CD #2263.

Scott E. R. D., Greenwood R. C., Franchi I. A., and Sanders I. S. (2009b) Oxygen isotopic constraints on the origin and parent bodies of eucrites, diogenites, and howardites. *Geochimica et Cosmochimica Acta* **73**:5835-5853.

Sharp Z. D. (1990) A laser-based microanalytical method for the in-situ determination of oxygen isotope ratios of silicates and oxides. *Geochimica et Cosmochimica Acta* **54**:1353-1357.

Shearer C. K., Burger P., and Papike J. J. (2010) Petrogenetic relationships between diogenites and olivine diogenites: Implications for magmatism on the HED parent body. *Geochimica et Cosmochimica Acta* **74**:4865-4880.

Shestopalov D. I., McFadden L. A., Golubeva L. F., and Orujova L. O. (2010) About mineral composition of geologic units in the northern hemisphere of Vesta. *Icarus* **209**:575-585.

Sobolev A. V. and Danyushevsky L. V. (1994) Petrology and geochemistry of boninites from the north termination of the Tonga Trench - Constraints on the generation conditions of primary high-Ca boninite magmas. *Journal of Petrology* **35**:1183-1211.

Stolper E. (1977) Experimental petrology of eucritic meteorites. *Geochim. Cosmochim. Acta* **41**:587-611.

Sylvester P. (2008) Chapter 5. Matrix effects in laser ablation ICPMS. In *Laser Ablation ICP-MS in the Earth Sciences: Current Practices and Outstanding Issues*, edited by Sylvester P. Mineralogical Association of Canada, Short Course **40**:67-78.

Takeda H. (1997) Mineralogical records of early planetary processes on the howardite, eucrite, diogenite parent body with reference to Vesta. *Meteoritics and Planetary Science* **32**:841-853.

Thomas P. C., Binzel R. P., Gaffey M. J., Storrs A. D., Wells E. N. and Zellner B. H. (1997) Impact excavation asteroid 4 Vesta: Hubble Space Telescope results. *Science* **227**:1492-1495.

Tamura A. and Arai S. (2006) Harzburgite-dunite-orthopyroxenite suite as a record of supra-subduction zone setting for the Oman ophiolite mantle. *Lithos* **90**:43-56.

Valley J. W., Kitchen N. E., Kohn M. J., Niendorf C. R. and Spicuzza M. J. (1995) UWG-2, a garnet standard for oxygen isotope ratios: Strategies for high precision and accuracy with laser heating. *Geochimica et Cosmochimica Acta* **59**:5223-5231.

Wadhwa M., Shukolyukov A., Davis A. M., Lugmair G. W., and Mittlefehldt D. W. (2003) Differentiation history of the mesosiderite parent body: Constraints from trace elements and manganese-chromium isotope systematics in Vaca Muerta silicate clasts. *Geochimica et Cosmochimica Acta* **67**:5047-5069.

Warren P. H., Kallemeyn G. W., Huber H., Ulff-Møller F., and Choe W. (2009) Siderophile and other geochemical constraints on mixing relationships among HED-meteoritic breccias. *Geochimica et Cosmochimica Acta* **73**:5918-5943.

Welten K. C., Caffee M. W., and Beck A. W. (2009) Cosmogenic radionuclides in three paired howardites and a polymict diogenite from Pecora Escarpment icefield, Antarctica (abstract). *Meteoritics and Planetary Science* **44:**A216.

Wiechert U. H., Halliday A. N., Palme H. and Rumble D. (2004) Oxygen isotope evidence for rapid mixing of the HED meteorite parent body. *Earth and Planetary Science Letters* **221**:373-382.

Appendix B

Table B1. Representative Mineral Compositions Grouped by Textural Setting

Textural Setting	Large grains in the matrix					Small inclusions in olivine		
Mineral	Olivine	Opx.	Chromite	FeNi Metal	Troilite	Cpx.	Chromite	Troilite
Microprobe analyses (wt. %)								
SiO_2	38.2	55.0	0.09	b.d.	b.d.	54.2	0.08	b.d.
TiO_2	b.d.[1]	0.09	0.93			0.02	0.27	
Al_2O_3	b.d.	0.65	11.1			0.15	2.98	
Cr_2O_3	0.02	0.64	53.7			0.40	62.0	
V_2O_3	b.d.	b.d.	0.49			b.d.	0.90	
FeO_T	23.5	14.1	29.2			6.09	29.7	
MnO	0.55	0.51	0.64			0.29	0.70	
MgO	37.5	27.3	3.04			17.4	1.79	
CaO	0.12	1.40	b.d.			21.9	b.d.	
S				0.02	36.3			36.2
Fe				97.1	63.1			62.8
Ni	b.d.			0.95	0.03			b.d.
Co				0.94	b.d.			b.d.
P				b.d.	b.d.			b.d.
Total	99.9	99.7	99.2	99.0	99.4	100.5	98.5	99.0
Atomic formula								
Si	1.00	1.98	-			1.98	0.00	
Ti	-	0.00	0.02			0.00	0.01	
Al	-	0.03	0.46			0.01	0.13	
Cr	-	0.02	1.48			0.01	1.81	
V	-	-	0.01			-	0.03	
Fe	0.52	0.42	0.85			0.19	0.91	
Mn	0.01	0.02	0.02			0.01	0.02	
Mg	1.46	1.46	0.16			0.95	0.10	
Ca	0.00	0.05	-			0.86	-	
Total	3.00	3.99	3.00			4.01	3.01	
Wo	-	2.8	-			43.0	-	
En	-	75.4	-			47.6	-	
Fs	-	21.9	-			9.3	-	
Fe/Mn	42.3	27.1	-			20.6	-	
Fe#	26.0	22.5	-			16.4	-	
Laser ablation analyses (ppm)								
Sr	b.d.	0.36	b.d.					
Y	0.04	1.23	b.d.					
Zr	0.05	0.93	2.45					
Nb	b.d.	b.d.	0.23					
La	b.d.	0.03	b.d.					
Ce	b.d.	0.13	b.d.					
Nd	b.d.	0.18	b.d.					
Sm	b.d.	b.d.	b.d.					
Eu	b.d.	b.d.	b.d.					
Dy	b.d.	0.16	b.d.					
Er	b.d.	0.17	b.d.					
Yb	0.06	0.17	b.d.					

[1] Indicates analysis falls below detection limit

Table B2. Bulk composition of MIL 03443,14 and control samples determined by ICP-MS.

		MIL 03443,14	DTS-1		PCC-1		BCR-2		
			this work	G-94	this work	G-94	this work	USGS	GeoReM
Li	µg/g	0.48	1.91	**2.1**	1.18	1.6	8.95	*9*	*9*
Mg	mg/g	218	298	**299**	284	**261.9**	20.3	**21.6**	**21.6**
Al	mg/g	2.5	1.12	1	3.94	**3.57**	69.9	**71.4**	**71.4**
P	µg/g	13.4	7.8	9	11.8	9	1570	**1500**	**1530**
Ca	mg/g	1.87	0.922	**1.2**	4.07	**3.7**	47.5	**50.9**	**50.9**
Sc	µg/g	5.2	3.80	3.5	8.75	**8.4**	31.4	**33**	**33**
Ti	µg/g	171	25.0	30	33.4	60	13500	**13500**	**13500**
V	µg/g	104	12.5	11	34.8	**31**	404	**416**	**416**
Cr	mg/g	10.1	3.52	**3.99**	2.63	**2.73**	0.0272	**0.018**	**0.018**
Mn	mg/g	4.07	0.987	**0.93**	0.998	**0.93**	1.47	**1.52**	**1.52**
Fe	mg/g	197	61.5	**60.7**	60.8	**57.7**	87.3	-	**96.5**
Co	µg/g	49	140	**137**	118	**112**	36.4	**37**	**37**
Ni	µg/g	61	2400	**2360**	2450	**2380**	14.4	-	*18*
Cu	µg/g	10.1	8.00	7.1	7.85	10	24.4	*19*	*21*
Zn	µg/g	6.3	49.1	46	45.2	42	128	**127**	**127**
Ga	µg/g	0.99	0.552	*0.5*	0.813	*0.7*	22.3	**23**	**23**
Rb	ng/g	50	72	58	73.6	**66**	46100	**48000**	46900
Sr	µg/g	0.108	0.3	0.32	0.578	**0.4**	332	**346**	340
Y	µg/g	0.208	0.0399	0.04	0.0949	*0.1*	37.7	**37**	**37**
Zr	µg/g	0.46	0.209	*4*	0.216	10	192	**188**	184
Nb	ng/g	58	37.3	*2200*	19.8	*1000*	12400	-	12600
La	ng/g	6	25.7	29	36.9	52	25100	**25000**	24900
Ce	ng/g	13.9	48.2	72	64.6	100	53400	**53000**	52900
Pr	ng/g	1.7	5.9	**6.3**	7.9	13	6660	*6800*	6700
Nd	ng/g	9.2	22.7	29	29.4	42	28400	**28000**	28700
Sm	ng/g	5.2	5.3	4.6	5.2	6.6	6440	*6700*	6580
Eu	ng/g	1.1	1.4	1.2	2.4	1.8	2200	**2000**	1960
Gd	ng/g	10.4	4.3	*3.8*	7.2	*14*	6780	**6800**	6750
Tb	ng/g	2.3	0.7	0.8	1.3	1.5	1070	*1070*	1070
Dy	ng/g	20.3	5.0	*3*	9.7	10	6300	-	6410
Ho	ng/g	6.7	1.3	*1.3*	3	2.5	1270	*1330*	1280
Er	ng/g	29.1	4.9	*4*	12.4	*12*	3630	-	3660
Tm	ng/g	5.5	1.1	1.4	2.5	2.7	524	*540*	540
Yb	ng/g	45	9.4	10	23.6	24	3300	**3500**	3380
Lu	ng/g	9.3	2.0	2.4	4.8	5.7	486	*510*	503
Hf	ng/g	9.8	4.3	15	4.6	*40*	4590	*4800*	4900
Ta	ng/g	1.9	1.6	39	2.9	*20*	736	-	740
Th	ng/g	2.4	10	10	10.9	13	6010	**6200**	5700

For control samples, recommended or certified values in bold font, proposed values in regular font and information only values in italic font. References for literature values: G-94 – Govindaraju (1994); USGS - Certificate of Analysis (available on the USGS website: http://minerals.cr.usgs.gov/geo_chem_stand/basaltbcr2.html); GeoReM – preferred values from the Geological and Environmental Reference Materials website (http://georem.mpch-mainz.gwdg.de/).

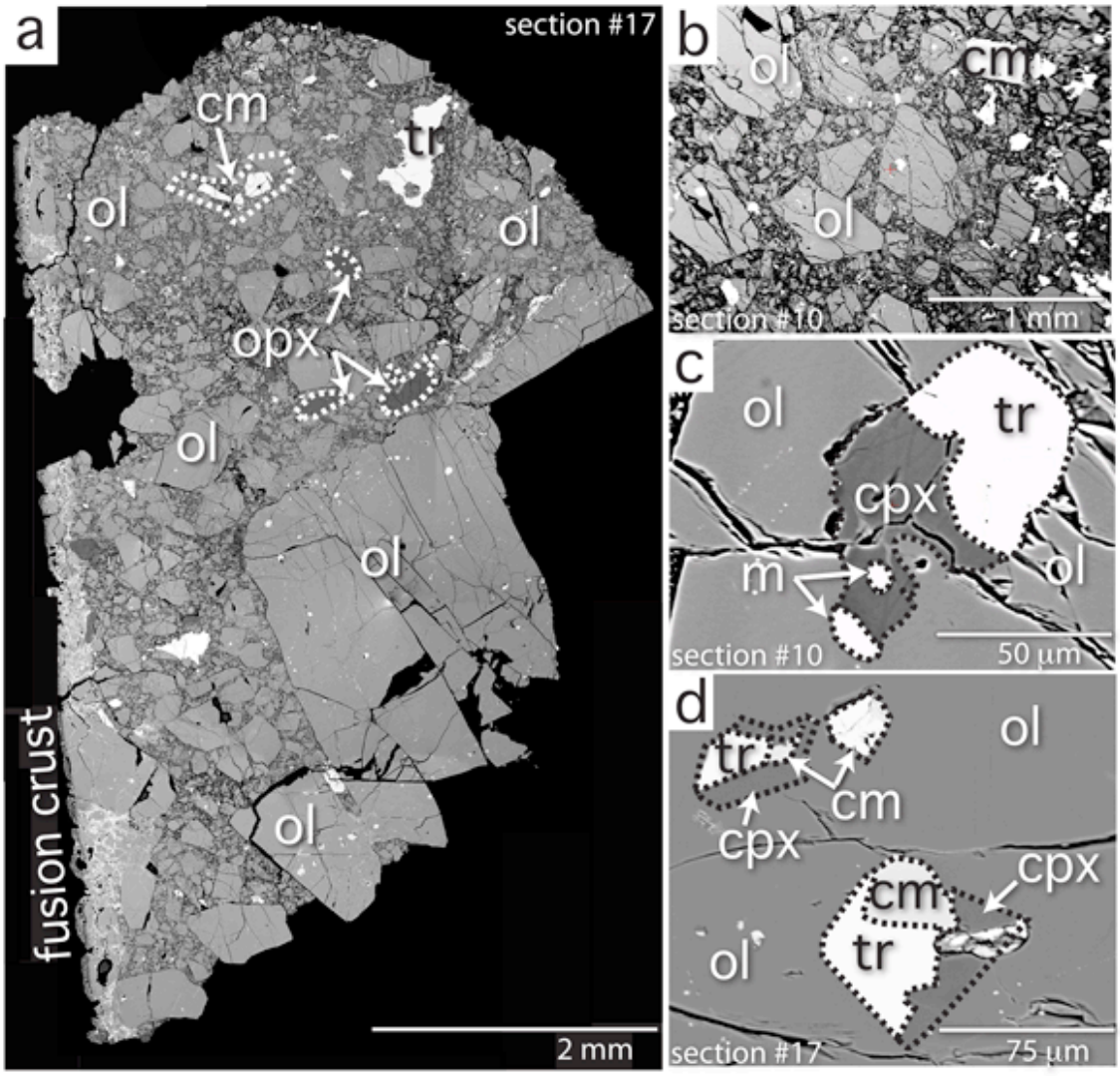


Figure B1. (a) BSE map of MIL 03443,17 showing its fragmental texture comprised mainly of olivine (ol) with smaller amounts of orthopyroxene (opx), chromite (cm) and troilite (tr). This composite image is 3340 x 2258 pixels. (a, b) Larger olivine grains contain bright inclusions in backscatter that are composed of diopside (cpx), tr, ±cm, ± metal (m). (c, d) Higher magnification images of these inclusions reveals relatively constant mineral proportions and negative-crystal shape

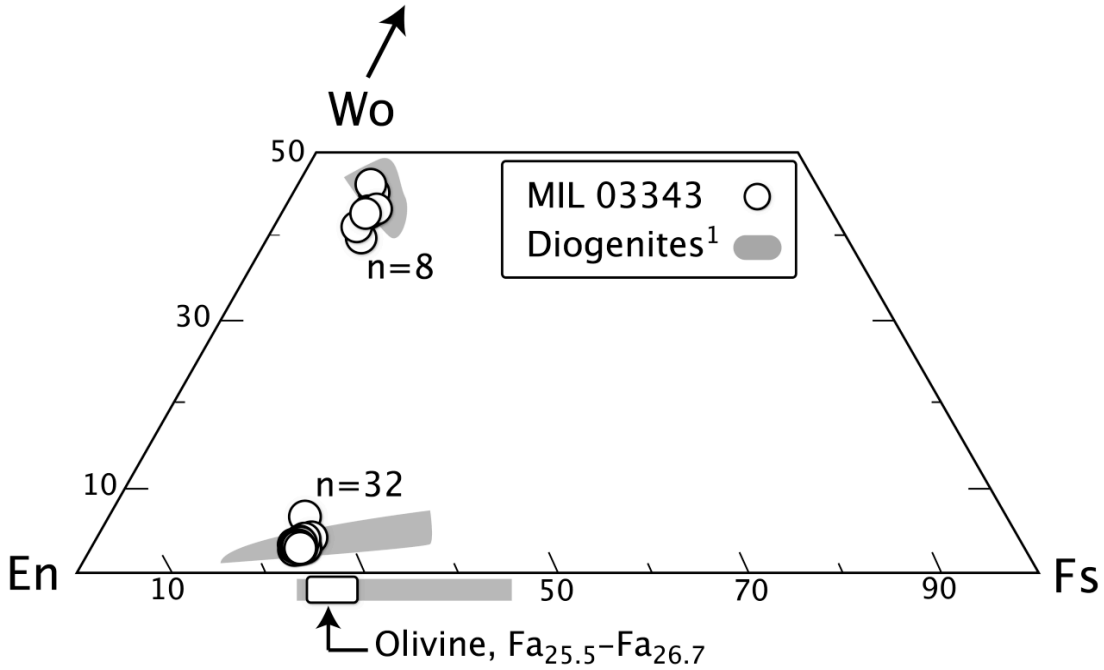


Figure B2. Comparison of pyroxene and olivine compositions in MIL 03443 with those in diogenites. Olivine compositions are shown along the base. [1]Beck and McSween (2010a), Domanik et al. (2004), Fowler et al. (1994), Mittlefehldt (1994, 2000), Mittlefehldt and Lindstrom (1993), Shearer et al. (2010)

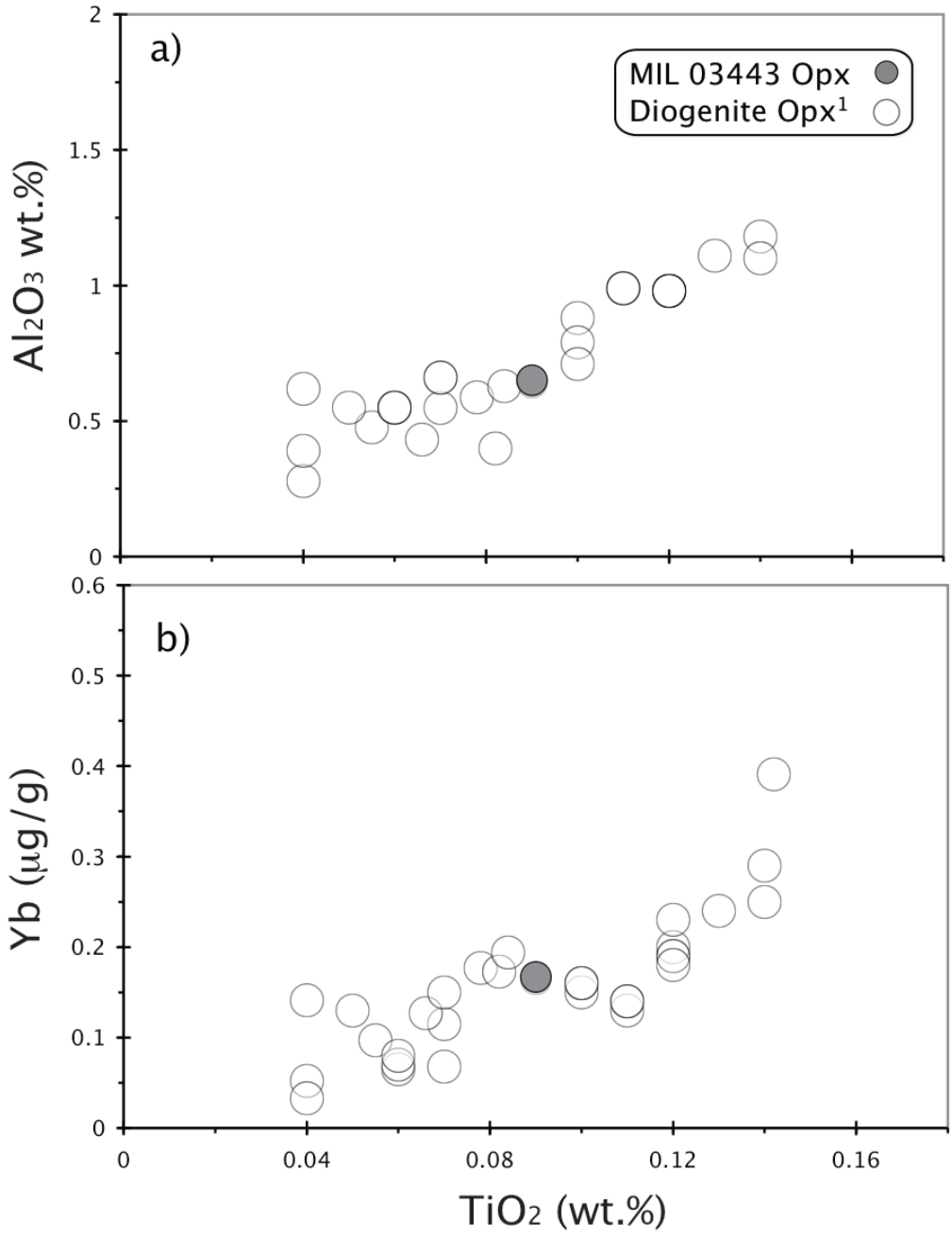


Figure B3. MIL 03443 orthopyroxene (a) Al_2O_3 vs. TiO_2 and (b) Yb vs. TiO_2 concentrations compared to diogenite orthopyroxene. Similarities between orthopyroxene trace element concentrations between MIL 03443 suggest that they likely belong to the same meteorite group (HEDs), and that they had a similar origin (crustal cumulates). [1]Fowler et al. (1995), Mittlefehldt (1994)

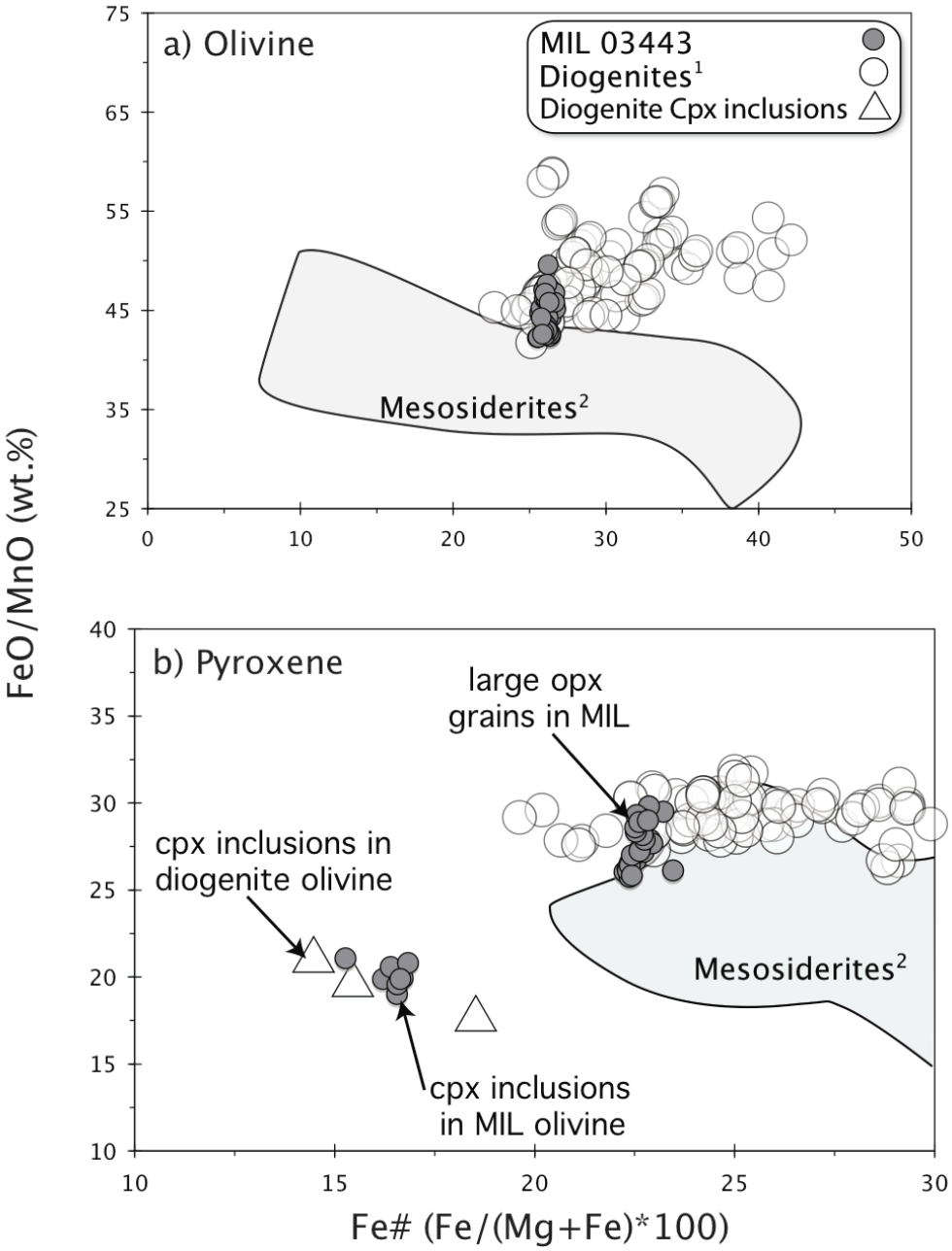


Figure B4. FeO/MnO wt. ratios in MIL 03443 (a) olivine and (b) pyroxene compared to diogenites. Mesosiderite compositional ranges for these two minerals are enclosed by shaded area. Similarity in FeO/MnO ratios between MIL 03443 and diogenites suggests a common origin. [1]New data and McSween et al. 2011, including references therein; [2]Delaney et al. 1980, Kong et al. 2008, Mittlefehldt 1979, 1980, Mittlefehldt et al. 1998, Nehru et al. 1980, Prinz et al. 1980, Ruzicka et al. 1994 and Wadhwa et al. 2003

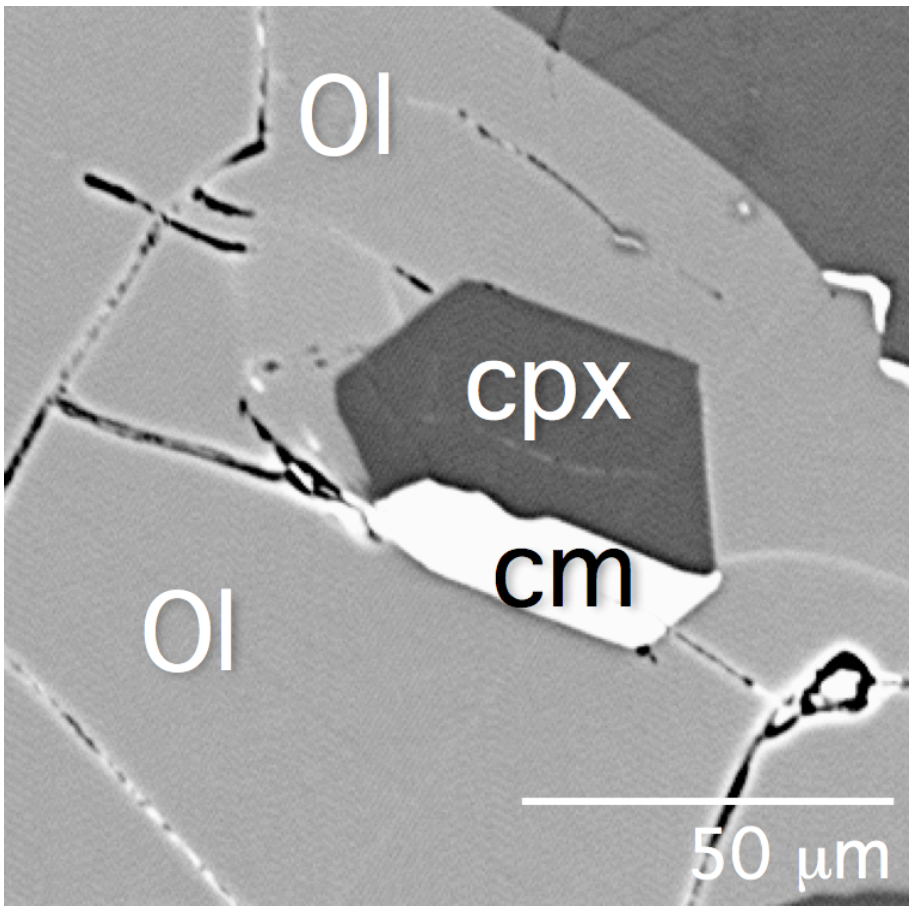


Figure B5. A diopside (cpx)+chromite (cm) inclusion in olivine observed in diogenite LAP 03979. This inclusion is very similar in composition and texture to those in MIL 03443

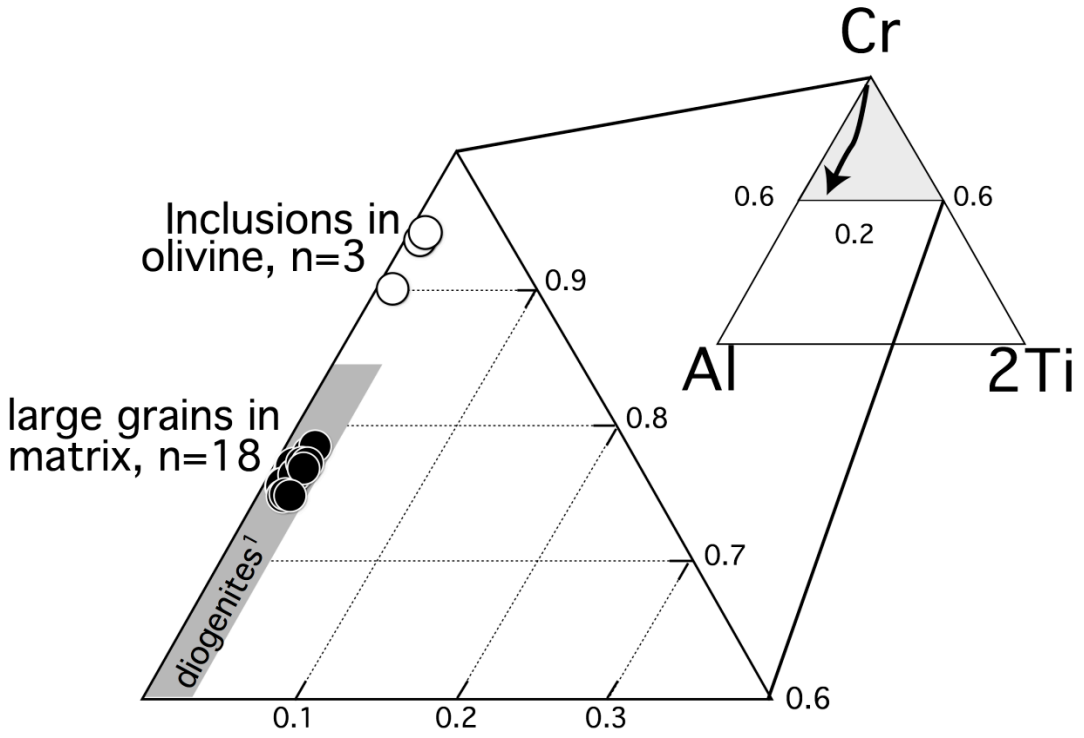


Figure B6. Comparison of chromite compositions in MIL 03443 and diogenites. Black and white circles correspond to different textural settings. Gray area of plot at right indicates area of enlargement and also displays typical path of chromite chemical evolution. [1]Bowman et al. 1999

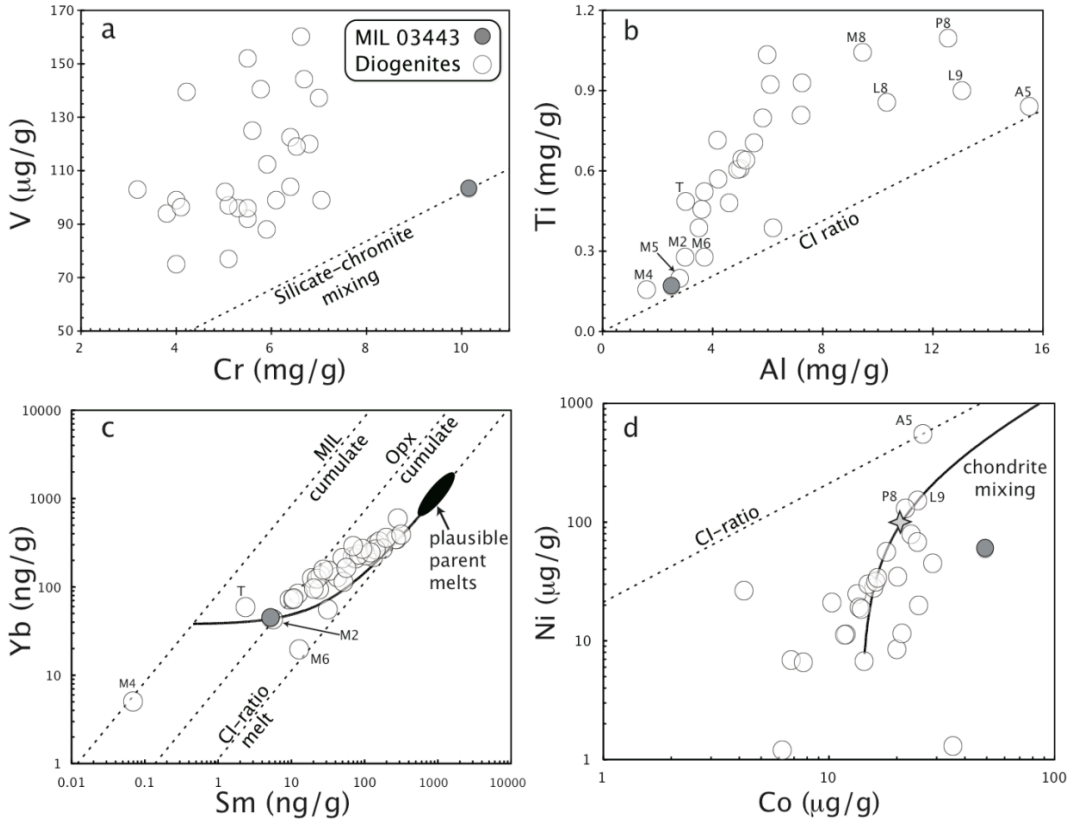


Figure B7. Comparison of element-element diagrams for MIL 03443 and diogenites. In (a), the silicate-chromite mixing line is a tie-line between average chromite (Table 1) and an olivine-orthopyroxene mixture as given by the modal mineralogy of MIL 03443, ~95:5. The Cr contents for olivine, orthopyroxene and chromite, and the V content of chromite, were taken from Table B1. Vanadium in the olivine-orthopyroxene mixture was assumed to be 15 μg/g. This is a plausible estimate based on the V contents of olivine and orthopyroxene in diogenites for the mixing ratios we have used (Shearer et al. 2010). In (b), labeled diogenites with >8 mg/g Al are all plagioclase-bearing. In (c), the CI-ratio melt line is a locus of fictive melts with CI Yb/Sm ratios. The cumulate opx line is the locus of orthopyroxenes that would be in equilibrium with such melts. The MIL cumulate line is the locus of cumulates with the olivine/orthopyroxene ratio of MIL 03443 that would be in equilibrium with such melts. The field labeled "plausible parent melts" is the area where melts parental to those diogenites that plot on the cumulate orthopyroxene line would lie. The curved line is a mixing line between a MIL cumulate and its equilibrium melt, constrained to pass through the MIL 03443 datum. The partition coefficients used to calculate these lines and field are given in the text. In (d), the curve is a mixing line between a low-Ni diogenite and a chondritic clast from the diogenite Ellemeet (Mittlefehldt 1994). The four-pointed star indicates a 1% contamination level. Labeled diogenites are polymict mixtures of diogenitic and eucritic material. The labeled diogenites are: A5 – ALH 85015, L8 – LEW 88008, L9 – LAP 03979, M2 – MET 00422, M4 – MET 00424, M5 – MET 00425, M6 – MET 00436, M8 – MET 01084, P8 – PCA 02008, T – Tatahouine. Sources of diogenite data are given in the text.

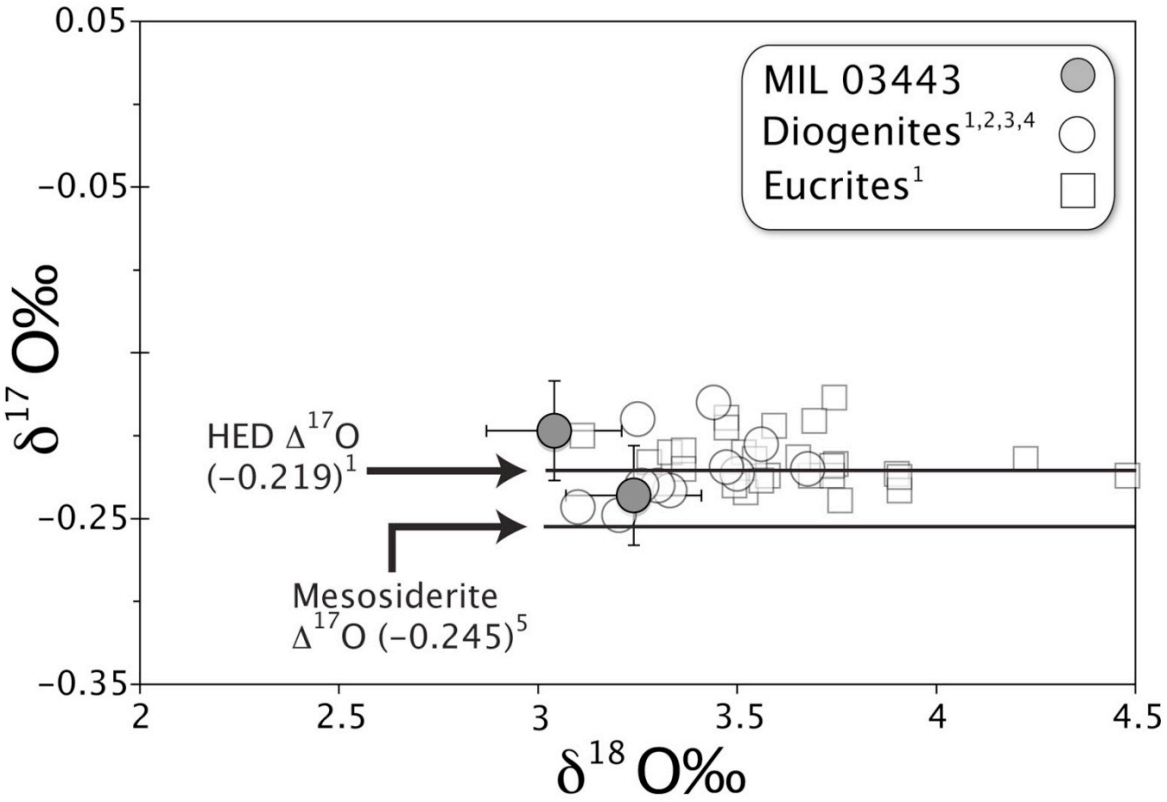


Figure B8. Comparison of oxygen isotope compositions of MIL 03443 to the HED $D^{17}O$ average and individual eucrite and diogenite analyses. [1]Wiechert et al. (2004), [2]Clayton and Mayeda (1996), [3]Barrat et al. (2006), [4]Bunch et al. (2010), [5]Greenwood et al. (2006)

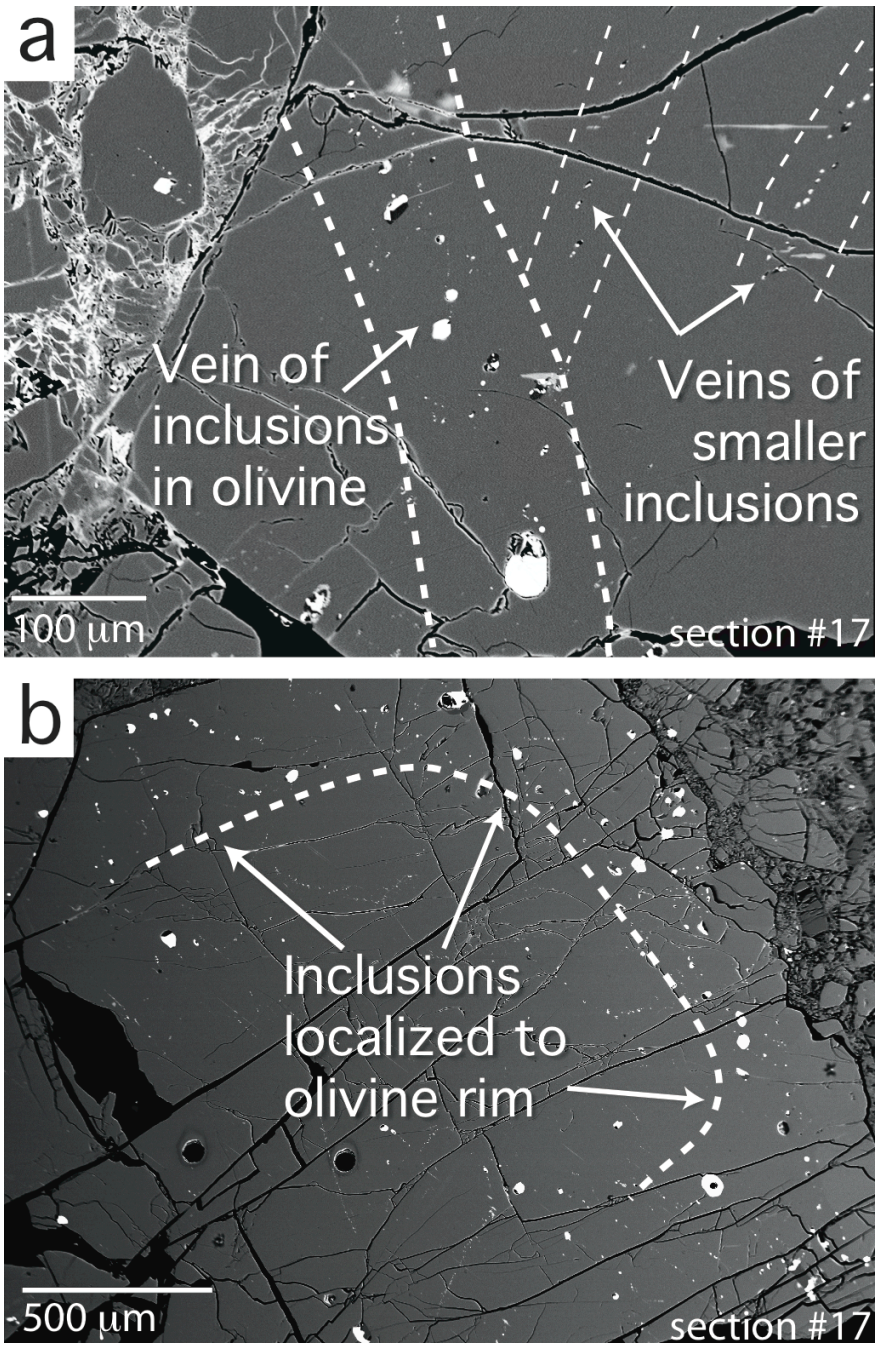


Figure B9. BSE images showing the systematic distributions of melt inclusions in MIL 03443 olivine. (a) Some inclusions display a linear distribution suggesting melt entry along fractures. (b) Larger grains have inclusions concentrated near the rim, suggesting melt was included during adcumulus growth

Part 4
In situ trace element concentrations in dimict diogenites: Further evidence for harzburgitic and orthopyroxenitic lithologies

This part is a reformatted version of a paper of the same name that is being submitted to Meteoritics and Planetary Science. Andrew Beck, Hap McSween and Bob Bodnar are the authors of this paper. Andrew preformed all data analyses.

ABSTRACT

Measured in situ trace element concentrations in orthopyroxenes of five diogenite breccias, previously identified as containing distinct harzburgitic and orthopyroxenitic lithologies, test their classification as dimict. Three of the samples show increases in Y, Yb and HREE concentrations from harzburgitic to orthopyroxenitic pyroxenes, confirming their classification as dimict and suggesting that the lithologies are related through fractional crystallization in which harzburgite crystallized before orthopyroxenite. In two of these three samples, Eu concentrations range from ~0.011 ppm in harzburgitic pyroxene to below detection in orthopyroxenitic pyroxene. It is plausible that this decrease in Eu concentration is attributable to plagioclase crystallization in the orthopyroxenitic lithology. These three samples also show a decrease in LREE abundance from harzburgitic to orthopyroxenitic pyroxenes. This decrease is inconsistent with a model where harzburgite is the initial fractionating lithology. Elevated harzburgite orthopyroxene LREE concentrations may best be explained through equilibration with LREE-enriched trapped melt or intercumulus phases.

One sample examined in this study shows pyroxene trace element variations suggesting it is composed of multiple lithologies, which are likely unrelated. Another samples examined here has no pyroxene trace element variation, suggesting it may be actually be monomict.

1.0 INTRODUCTION

Diogenite meteorites are part of the HED (howardite, eucrite and diogenite) meteorite group, and are thought to be lower crustal cumulates from the asteroid 4 Vesta (McSween et al. 2011). Traditionally, diogenites were interpreted as orthopyroxenites with small amounts of primary olivine. However, the observation of large amounts of olivine in a few samples, suggests that there may be more diversity in the group (Sack et al. 1991). In previous work investigating the relationship between these olivine-rich samples and the rest of the group, and where the occurrence of smaller amounts of olivine in diogenite breccias was explored, Beck and McSween (2010) identified nine brecciated diogenites as dimict, being comprised of two distinct diogenitic lithologies. One lithology is harzburgitic (Hzbg), containing relatively high concentrations of olivine (~10-20 vol.%) and Mg-rich orthopyroxene, akin to the olivine-rich lithology first described by Sack et al. (2011). The other lithology is orthopyroxenitic (Opxn), containing relatively Fe-rich orthopyroxene and also small amounts of plagioclase ($\leq$ 3.6 vol.%) in some samples. Note that Beck and McSween (2010) originally referred to these nine samples as "polymict breccias". However, given evidence for only two lithologies in these samples, "dimict breccia" is a more accurate term (Bischoff et al. 2006), and will be used for the remainder of this work.

Orthopyroxene is the common phase of both diogenite lithologies, and the most dominant phase modally. Beck and McSween (2010) investigated trends in pyroxene major and minor element compositions from Hzbg to Opxn in each sample to constrain the petrogenetic processes separating the lithologies on Vesta. Based on trends in major element concentrations, we concluded that the Hzbg/Opxn lithology pair in each sample

was separated via fractional crystallization. Furthermore, similar orthopyroxene Mg# (molar 100*Mg/(Mg+Fe)) between Hzbg and Opxn in different samples indicate that these samples represent fractionation sequences from multiple plutons (Beck and McSween 2010). Minor element compositional trends suggest that the majority of the samples came from plutons that had a relatively depleted source, where plagioclase never became a major crystallizing phase. However, a few samples displayed a decrease in Al_2O_3 from Hzbg to Opxn orthopyroxenes, suggesting that plagioclase began crystallizing in the Opxn lithology. This is supported by the occurrence of plagioclase grains localized to the Opxn lithology (Beck and McSween 2010).

Diogenites have undergone significant post-crystallization equilibration, which likely erased original igneous trends in major element concentrations (McSween et al. 2011). However, the slower-to-equilibrate minor elements still, to some extent, preserve original igneous signatures (Fowler et al. 1994), as with Al_2O_3 described above. Therefore, trace incompatible elements, those elements that have the slowest diffusion rates in orthopyroxene, may be the best indicators of original igneous signatures (Fowler et al. 1995; Mittlefehldt 1994). Here we measure in situ orthopyroxene trace concentrations in the dimict diogenites to test two hypotheses. We first test whether five of the samples presented in Beck and McSween (2010) are in fact composed to two distinct lithologies. If the orthopyroxene trace element concentrations fall into two distinct groups, this will support the hypothesis that the breccias are dimict. Second, provided the first hypothesis is true, we wish to test whether pyroxene compositional groups in each sample may have been separated via fractional crystallization on Vesta, as proposed by Beck and McSween (2010). This will be accomplished by examining trends

in orthopyroxene trace elements between lithologic units in a given sample, and also examining trace elements in olivine and plagioclase, which exclusively occur in the Hzbg and Opxn lithologies respectively (Beck and McSween 2010).

2.0 METHODS

Due to the dimict brecciated nature of these diogenites, it would be difficult to constrain the mineral trace element variations between the lithologies in a given sample using bulk analysis techniques. Instead, we chose in situ trace element analysis of clasts of the two lithologies previously mapped in thin sections from our previous work. A subsample of five dimict diogenites from the nine reported by Beck and McSween (2010) includes: Lewis Cliff (LEW) 88008 section#1, LEW 88679 #8, Pecora Escarpment (PCA) 02008 #8, Meteorite Hills (MET) 01084 #5, and Miller Range (MIL) 03368 #7. Of these five, three were reported to show trends in orthopyroxene minor elements that was suggestive of plagioclase crystallization in the Opxn lithology (LEW 88008, MET 01084, MIL 03368), while the other two (PCA 02008 and LEW 88679) have trends in minor elements that do not suggest plagioclase fractionation in the Opxn lithology (Beck and McSween 2010).

An Agilent 7500ce Inductively Coupled Plasma Mass Spectrometer (ICP-MS) combined with an Excimer 193-nm GeoLasPro Laser Ablation system (LA) was used to measure mineral trace element concentrations. Because incompatible trace element depletion at orthopyroxene rims have been noted in terrestrial cumulates (Papike et al. 1995), we only measured cores for this study. Spot sizes ranged from 24-44 μm, and dwell times were typically 30-40 seconds. The LEW 88679 section is exceptionally thin,

and therefore, dwell times were < 20 seconds in most cases. These lower count times lead to higher limits of detection (LOD) for this sample. Approximately 10 orthopyroxene grains per lithology were measured in each sample. Approximately 5 olivine and plagioclase grains were measured in each sample, where present.

During analysis the He gas flow was ~0.8 ml/min through an ablation cell with a volume of ~1.5 cm^3. NIST 610 glass was used as an external standard and analyzed four times before and after analysis. Previous workers have shown that abundances of most elements in silicate phases can be determined with better than 10% accuracy using the NIST 610 and 612 standards combined with a 193-nm excimer laser (Sylvester 2008; Guillong et al. 2003). Summation of major elements to 100% was used as an internal standard. For comparison, data were also reduced using known EMP concentrations and the values did not vary significantly from those reduced using summation to 100%. Data reduction was achieved with the Analysis Management System (AMS) software using a 3s LOD (Mutchler et al. 2008). Due to the evidence in minor element trends suggesting that plagioclase crystallization may have been an important process in the petrogenetic history of these lithologies, variations in orthopyroxene Eu concentrations between Hzbg and Opxn were of particular interest. However, all of the analysis of orthopyroxene Eu concentrations fell below the 3σ LOD. Therefore, we reduced the Eu data for orthopyroxene in each lithology using a relaxed 2σ LOD with the SILLS program (Guillong et al. 2008). We measured 25 isotopes in total, most of which are displayed in subsequent tables. ^{85}Rb and ^{133}Cs were in our analytical package, but they fell below detection limits in all phases and so are not reported.

We report representative compositions for all phases except orthopyroxene, where we report a single mean composition. Before averaging orthopyroxene data, however, we examined the distribution of the data being averaged. All orthopyroxene data appeared to have normal distributions, except for one sample (PCA 02008) that will be discussed later. Because the data are normally distributed, the averages and deviations we report hold statistical significance.

3.0 RESULTS

3.1 Orthopyroxene

Average orthopyroxene compositions and 1s deviations from the mean are listed in Table C1. Analyzed major element concentrations in orthopyroxenes from the two lithologies in each sample closely match those reported earlier by Beck and McSween (2010). Hzbg pyroxenes are more Mg-rich and, in most cases, have lower concentrations of the incompatible minor elements TiO_2, Al_2O_3, and Cr_2O_3 than Opxn pyroxenes. MET 01084, however, shows an increase in TiO_2 but decreases in Al_2O_3 and Cr_2O_3 from Hzbg to Opxn, as recognized by Beck and McSween (2010) and attributed to plagioclase crystallization. In the majority of the samples, the concentration of Na_2O appears to increase from Hzbg to Opxn; however, Na_2O concentrations show considerable intra-lithology variation in most samples, making interpretation of compositional trends difficult. Similarly, orthopyroxene Sr appears to decrease from Hzbg to Opxn in most of the samples, but varies in concentration sufficiently to draw interpretations of compositional trends into question. MET 01084 is the one exception, where an increase can be seen in Sr from Hzbg to Opxn orthopyroxene. Similar intra-lithology pyroxene

variability rule out discerning consistent V and Zr compositional trends between the lithologies in most samples as well.

Yb, an incompatible trace element in orthopyroxene, does not suffer from the same variability. A clear increase in Yb concentration can be seen from Hzbg to Opxn pyroxene in LEW 88679, LEW 88008 and MET 01084 (Fig. C1a, left). Yb shows no change in concentration from Hzbg to Opxn in MIL 03368, and generally decreases from Hzbg to Opxn in PCA 02008, though it varies considerably in the Hzbg pyroxenes of this sample (Fig. C1a, right). Orthopyroxenes from the Ultramafic Series of the Stillwater Complex, a suite of analogous terrestrial ultramafic rocks, show similar patterns to the majority of the diogenite samples studied here. The Ultramafic Series can be broadly separated into two lithologies based on dominant cumulus phase(s): the Peridotite or Hzbg Zone (cumulate Ol + Opx + Cm) and the Bronzitite or Opxn Zone (cumulate Opx) (Jackson 1961). Between these two Stillwater lithologies an increasing trend in orthopyroxene Yb concentration occurs from Hzbg to Opxn (Lambert and Simmons 1987; Papike et al. 1995) (Fig. C1b). Note, however, that this is a general trend and does not hold true for every sample in these two Stillwater lithologies.

Another incompatible trace element in orthopyroxene, Y, displays a similar trend between Hzbg and Opxn lithologies. As with Yb, LEW 88679, LEW 88008 and MET 01084 all show an increase in Y concentration from Hzbg to Opxn orthopyroxene (Fig, C2a, left). MIL 03368 shows no change in orthopyroxene Y concentration between the lithologies, and the orthopyroxenes in the Hzbg portion of PCA 02008 vary significantly in Y concentration (Fig. C2a, right). The non-normal distribution of the PCA 02008 data is especially apparent here.

As in Y and Yb, the diogenites LEW 88679, LEW 88008, and MET 01084 also show corresponding variations in orthopyroxene REE patterns from Hzbg to Opxn (Fig. C3a). The variation in orthopyroxene REE pattern between the two lithologies in each of these three samples is manifested in three distinct ways. First, Hzbg orthopyroxenes have higher concentrations of La-Nd, (LREE) relative to the Opxn orthopyroxene in each of the three samples. Second, Hzbg orthopyroxenes have detectable amounts of Eu, whereas Opxn orthopyroxenes in each of the three samples have lower Eu concentrations, all falling below the 2σ LOD. LEW 88679, which is exceptionally thin, had very low count times and as such has a very high LOD. Because of this, Eu was not detectable in either Hzbg or Opxn orthopyroxene in LEW 88679. The third way in which orthopyroxene REEs vary in these three samples is that Hzbg orthopyroxenes consistently have lower concentrations of Gd-Yb (HREE) relative to the Opxn orthopyroxenes in each sample. Orthopyroxenes from the Hzbg and Opxn lithologies of the Stillwater Complex broadly display these three REE relationships as well (Fig. C3b) (Lambert and Simmons 1987; Papike et al. 1995). The exception to this is that no depletion of Eu is observed from Hzbg to Opxn in the Stillwater samples. This is most likely due to higher oxygen fugacity (fO_2) at Stillwater relative to Vesta, which would severely reduce the effect plagioclase crystallization would have on the development of a negative Eu anomaly (Weill and Drake 1973).

Variations between orthopyroxene REE concentrations from Hzbg to Opxn in MIL 03368 and PCA 02008 correspond to the variations observed between Y an Yb in those two samples. Hzbg and Opxn orthopyroxene REE patterns in MIL 03368 are essentially identical, whereas in PCA 02008 REE concentrations in Hzbg orthopyroxene

are highly variable and not normally distributed (Fig. C4). Some Hzbg orthopyroxenes in PCA 02008 also have higher REE concentrations than Opxn orthopyroxenes in that sample (Fig. C4).

3.2. Olivine and plagioclase

Olivine, found exclusively in the Hzbg portion of each sample, was measured for trace elements and representative analyses from each sample can be found on the left side of Table C2. Er and Yb are the only REE in olivine we measured that were above the LOD, and were only detectable in LEW 88008 and MIL 03368. Other olivine trace elements, in all samples except MET 01084, fall within the range known for diogenites (Shearer et al. 2010). MET 01084, which was measured by Shearer et al. (2010) to have 3.1 ppm V, was measured here to contain 0.942 ppm V. Shearer et al. (2010) examined a different section of MET 01084 (,6), which may explain this discrepancy. We have found MET 01084 olivine to also have significantly lower concentrations of Cr relative to the reset of the samples (MET = 6.64 ppm Cr vs. group = 42.2-179 ppm Cr), and $\geq$2 times the concentrations of Zr and Sr (MET Zr = 0.140 ppm vs. group = 0.051-0.064 ppm Zr, MET Sr = 0.234 vs. group = <0.023-0.057 Sr).

Representative analyses of plagioclase are shown on the three right columns of Table C2. This phase is found primarily, but not exclusively, in the Opxn lithology, and is only large enough to be analyzed in LEW 88008, LEW 88679 and MET 01084. Plagioclase in these samples has a wide range of K concentrations (27.4 - 288 ppm K) and is enriched in Sr relative to orthopyroxene and olivine (plag = ~135 ppm Sr, opx = ~0.200 ppm Sr, ol = ~0.100 ppm Sr). In MET 01084 plagioclase, LREE (La, Ce, Nd, Sm) and Eu were detectable and display a typical plagioclase REE pattern, including a

sizeable positive Eu anomaly (Fig. C5). Plagioclase in LEW 88008 and LEW 88679 only contained detectable amounts of La, Ce and Eu, where a large positive Eu anomaly was also observed (Fig. C5). There are few plagioclase trace element data in the diogenite literature with which to compare these results, save an analysis of plagioclase in Dhofar 700 reported by Barrat et al. (2010). The Eu concentration of LEW 88679 (1.37 ppm Eu) and MET 01084 (0.949 ppm Eu) are much higher than those reported in Dhofar 700 (0.418 ppm Eu, Barrat et al. 2010), and than those we measured in LEW (0.394 ppm Eu). Likewise, the Sr concentrations of plagioclase in LEW 88679 (179 ppm Sr) and MET 01084 (127 ppm Sr) are higher than Dhofar 700 (101 ppm Sr, Barrat et al. 2010) and LEW 88008 (96.9 ppm Sr).

4.0 DISCUSSION

The purposes of this work are to 1) test the hypothesis that these diogenite breccias are composed of two lithologies by examining trace element variations in orthopyroxene, and 2) use these data to constrain the processes that formed them. In the following sections we will address the trends in orthopyroxene Y and Yb, along with orthopyroxene and plagioclase REE patterns with regards to these two points. The diogenite samples will be discussed in two different groups, based on similarities in trace element concentrations that have been outlined above.

4.1 Group 1: LEW 88008, LEW 88679 and MET 01084

Y and Yb are incompatible in orthopyroxene, and therefore should increase in concentration with increased fractionation. This occurs at the Stillwater Complex, where fractional crystallization has caused an increase in Y and Yb concentration in

orthopyroxene from the Hzbg to Opxn lithologies (Figs. C1b and C2b). In the dimict diogenites LEW 88008, LEW 88679 and MET 01084, increases in these incompatible trace elements from Hzbg to Opxn orthopyroxenes also occur (Figs. C1a and C2a, left). This suggests that Hzbg orthopyroxene fractionated prior to the fractionation of orthopyroxene in the Opxn lithology. This supports the hypothesis that these samples are composed of two distinct diogenitic lithologies. An increasing trend in Y and Yb abundance in orthopyroxene from Hzbg to Opxn suggests that increasing orthopyroxene fractionation could explain the two lithologies. Because these trace elements are so low in the olivine and plagioclase (Table C2), they cannot be used to constrain the their relative timing of crystallization.

LEW 88008, LEW 88679 and MET 01084 all have similar variations in orthopyroxene REE from Hzbg to Opxn in their respective samples, as seen in Figure C3a. First, in each sample Opxn orthopyroxenes have higher concentrations of HREE, relative to Hzbg. Second, Hzbg orthopyroxenes contain measurable amounts of Eu, while Opxn orthopyroxenes do not (except for LEW 88679, where the LOD is too high to measure Eu in either lithology). Finally, Hzbg orthopyroxenes are consistently enriched in LREE relative to Opxn in each sample. These three variations support our first hypothesis, that these samples are in fact dimict. If all the pyroxene originated from a single lithology, they should contain near identical REE patterns.

Enrichment of HREE in Opxn fragments relative to Hzbg fragments is likely the result of increased orthopyroxene fractional crystallization. Distribution coefficients of HREE in orthopyroxene (Jones 1995) suggest that fractional crystallization of orthopyroxene should produce a melt relatively enriched in HREE as fractionation

continues, causing subsequent fractionating orthopyroxene to be enriched in these elements as well. This supports our hypothesis that the Hzbg and Opxn lithologies were separated via fractional crystallization of orthopyroxene in which the Hzbg lithology was removed first, followed by the Opxn lithology. The HREE concentrations are sufficiently low in the other two phases we measured, olivine and plagioclase, that their crystallization is not likely to affect the overall abundance of the HREE in the melt.

4.1.2 Effect of plagioclase crystallization Eu concentrations

Plagioclase preferentially incorporates Eu^{2+} and depletes a melt in Eu when it becomes a fractionating phase (Drake and Weill 1975); this effect is magnified in low fO_2 environments like the Moon and Vesta (Karner et al. 2004). Therefore, it is possible that plagioclase crystallization in the Opxn lithology depleted the melt in Eu, leading to co-crystallization of orthopyroxenes with very low Eu concentrations in the Opxn lithology relative to Hzbg. This idea is supported by the findings in Beck and McSween (2010), where trends in Al_2O_3 concentrations in MET 01084 and LEW 88008 were explained by plagioclase crystallization in the Opxn lithology, and where plagioclase was found almost exclusively in the Opxn lithologies of those samples. To further test this idea, we made a simple mass-balance calculation to quantify the amount of plagioclase co-crystallization in the Opxn lithology needed to deplete Eu in the melt to sufficiently achieve the measured depletion in Eu between Hzbg and Opxn orthopyroxenes. We used the Hzbg Eu concentrations for MET 01084 and LEW 88008 listed in Table 1 as a starting point. Because the Opxn orthopyroxene Eu concentrations are below the LOD in MET 01084 and LEW 88008, we used the lowest Eu concentration reported for diogenite orthopyroxene as our Opxn value (Bilanga = 0.002 ppm Eu, Barrat et al. 2010). We then

used the plagioclase Eu concentrations for both of these samples to calculate the amount of crystallization required to go from Hzbg to Opxn orthopyroxenes. The resulting mass balance calculation yielded 1.0% and 2.0% plagioclase crystallization required in MET 01084 and LEW 88008, respectively. Note that this calculation yields a minimum amount of plagioclase crystallization required to produce these effects, and it may have been much more. The values calculated here compare quite well to the amount of plagioclase that is observed in these thin sections, 3.6 and 2.2 vol.%, respectively (Beck and McSween 2010). Because Eu was below the LOD in LEW 88679 Hzbg orthopyroxene, we could not make the analogous calculation.

It should be noted that using plagioclase Eu K_D's instead of actual concentrations in these calculations might yield different results. It should also be noted that the rock mode that is implied here for the Opxn (~3 vol.% plagioclase, 97 vol.% pyroxene) is not supported by phase diagram compositions. Also, the above paragraph suggests 3% plagioclase crystallization, reducing the melt in Eu concentration, followed by the crystallization of pyroxene containing depleted Eu concentrations. This sequence of plagioclase crystallization prior to pyroxene crystallization is also problematic when considering typical phase diagrams and sequences of crystallization. However, even with these caveats, there is still a measureable decrease in abundance of Eu in Hzbg to Opxn orthopyorxene, and given the unique partitioning of this element in plagioclase, would seem to have to be linked to this phases crystallization in some form.

4.1.3 Possible causes for lower LREE in Opxn orthopyroxene

The LREE difference between Hzbg and Opxn orthopyroxenes in these samples is difficult to justify using simple fractional crystallization. Given the REE partitioning

coefficients for pyroxene (Jones 1995), fractionating systems should produce orthopyroxenes that have an increased concentration of both LREE and HREE as fractionation continues. In other words, the vertical offset of the CI normalized orthopyroxene REE pattern should increase, but the overall slope of the line should not change significantly. As previously mentioned, there is an increase in HREE in the Opxn lithology, which is consistent with the fractionation model. However, the Opxn orthopyroxenes are more depleted in LREE than the Hzbg (Fig. C3a), which is inconsistent with a fractionation model where orthopyroxene is the dominant crystallizing phase. If the Opxn orthopyroxenes fractionated from the melt following the Hzbg orthopyroxene, they should have higher LREE. While plagioclase is relatively enriched in LREE elements (Fig. C5), LREE K_D's in plagioclase are <1, and thus plagioclase crystallization in the Opxn lithology cannot be used as an explanation for the decrease in LREE observed.

For other possible causes of this LREE depletion in Opxn pyroxene, we turn back to REE patterns of orthopyroxenes from the Hzbg and Opxn lithologies at the Stillwater Complex (Fig. C3b). Here, a similar phenomenon has been documented. Lambert and Simmons (1987) noted a decrease in orthopyroxene LREE abundance with stratigraphic height (increased fractionation) within the Harzburgite Zone. They proposed that this might have been caused by equilibration with trapped, LREE-enriched liquids or phases at the base of the Harzburgite Zone, leading to LREE-enrichment of orthopyroxenes from that zone, relative to LREE concentrations of orthopyroxene that fractionated later. It is possible that similar processes might have affected the Hzbg orthopyroxene in the diogenites examined here, and have cause the LREE enrichment in Hzbg relative to

Opxn. To test this, we compare the orthopyroxene REE patterns in both the Hzbg and Opxn portions of one sample, LEW 88008, to "expected" orthopyroxene REE patterns calculated from orthopyroxene/melt distribution coefficients for that sample. We scale orthopyroxene/melt K_D's (Jones 1995) to match the Yb concentrations in both the Hzbg and Opxn orthopyroxenes from LEW 88008 (Fig. C6a). We then compare these expected orthopyroxene REE patterns to those that were actually measured in both lithologies of that sample, which are labeled "actual" (Fig. C6b). The expected orthopyroxene REE pattern for the Opxn lithology matches the actual values well, while the expected Hzbg orthopyroxene have much lower concentrations of LREE compared to the actual measured values. This supports the hypothesis that the Hzbg orthopyroxene have been enriched in LREE after crystallization, and likely were enriched through equilibration with LREE-enriched intercumulus liquid or phases. Similar processes have been proposed for the Roda diogenite, where equilibration between LREE enriched whitlockite and adjacent orthopyroxene may have caused increased concentrations of LREE in orthopyroxene (Treiman 1996)

4.2 Group 2: MIL 03368 and PCA 02008

MIL 03368 displays no measurable change in orthopyroxene Y or Yb concentration from Hzbg to Opxn (Fig. C1a, right). Similarly, REE patterns in Hzbg and Opxn orthopyroxenes in this sample are near identical (Fig. C4). This suggests that the orthopyroxenes in this sample all come from the same lithology, and that it is not dimict. This interpretation is complicated by the measurable distinction in Mg# between these pyroxenes (Table C1), and the documentation that the more Mg-rich orthopyroxene is almost always in close proximity to olivine (Beck and McSween 2010). We propose that

all of the orthopyroxenes in MIL 03368 come from the same lithology, and that adjacent olivine-orthopyroxene pairs have equilibrated, leaving some pyroxenes in this sample relatively more Mg-rich.

This scenario has implications for the proposed classification scheme of Beck and McSween (2010), where two orthopyroxene Mg#s in a diogenite with olivine was proposed as an indication of a dimict sample. There is not enough information here to distinguish a way to circumvent this problem. Perhaps with more orthopyroxene trace element work in the dimict samples coupled with detailed petrography, a possible petrographic indicator can be found to distinguish those Mg-rich orthopyroxenes which are from Hzbg lithologies and those which form simply by equilibrating with adjacent olivine. This would be preferable to analyzing the in situ trace element chemistries of each sample that appears dimict.

Hzbg orthopyroxene in PCA 02008 is highly variable, and some grains are more enriched in Y and Yb than Opxn orthopyroxene in that sample (Fig. C1a, right). Similar variability and relative concentrations can be seen in the orthopyroxene REE in this sample (Fig. C4). The high variability in the Hzbg orthopyroxenes suggests that they come from multiple lithologies. The high concentration of incompatible trace elements in the Hzbg relative to the Opxn orthopyroxenes suggests that they are not petrogenetically related. This is supported with this sample's pairing with a group of howardites (Welten et al. 2009), indicating it is likely composed of minerals from a wide variety of unrelated lithologies.

5.0 CONCLUSIONS

1. In situ trace element concentrations of orthopyroxene, plagioclase and olivine in three dimict diogenites confirm that they are composed of two distinct lithologies: harzburgite and orthopyroxenite.

2. Increases in incompatible trace elements and HREEs from harzburgite to orthopyroxenite support the hypothesis that these two lithologies were separated through fractional crystallization.

3. Decreases in Eu abundance from harzburgite to orthopyroxenite orthopyroxenes might be attributable to small amounts of plagioclase crystallization in the orthopyroxenite lithology.

4. Lower LREE concentrations were observed in the orthopyroxenite lithology relative to the harzburgite lithology. This was likely caused by equilibration with LREE-rich trapped intercumulus liquid or phases in the harzburgite lithology.

5. One sample, MIL 03368, does not show trace element variation between pyroxenes from what we interpreted as originating from different lithologies. Because these pyroxenes do not show trace element variation, this sample is likely not dimict.

ACKNOWLEDGEMENTS

We wish to thank L. Fedele (VT) for his assistance both in data acquisition and data reduction. The authors also thank the MWG for allocating meteorite samples. This work was partially supported by NASA Cosmochemistry Grant NNG06GG36G to HYM.

REFERENCES

Anders E. and Grevesse N. (1989) Abundances of the elements: Meteoritic and solar. *Geochimica et Cosmochimica Acta* **53**:197-214.

Barrat J.-A., Yamaguchi A., Zanda B., Bollinger C. and Bohn M. (2010) Relative chronology of crust formation on asteroid Vesta: Insights from the geochemistry of diogenites. *Geochimica et Cosmochimica Acta* **74**:6218–6231.

Beck A. W. and McSween H. Y. (2010) Diogenites as polymict breccias composed of orthopyroxenite and harzburgite. *Meteoritics and Planetary Science* **45**:850-872.

Bischoff A., Scott E., Metzler K., and Goodrich C. (2006) Nature and origin of meteorite breccias. In *Meteorites and the Early Solar System II*. Lauretta D. and McSween H. eds. The University of Arizona Press, Tucson AZ.

Drake M. J. and Weill D. F. (1975) Partition of Sr, Bs, Ca, Y, Eu^{2+}, Eu^{3+} and other REE between plagioclase feldspare and magmatic liquid: An experimental study. *Geochimica et Cosmochimica Acta* **39**:689-712.

Fowler G. W., Papike J. J., Spilde M. N., and Shearer C. K. (1994) Diogenites as asteroidal cumulates: Insights from orthopyroxene major and minor element chemistry. *Geochimica et Cosmochimica Acta* **58**:3921-3929.

Fowler G. W., Shearer C. K., Papike J. J., and Layne G. D. (1995) Diogenites as asteroidal cumulates: Insights from orthopyroxene trace element chemistry. *Geochimica et Cosmochimica Acta* **59**:3071-3084.

Guillong M., Horn I., Gunther D. (2003) A comparison of 266 nm, 213 nm and 193 nm produced from a single solid state Nd:YAG laser for laser ablation. *Journal of Analytical Atomic Spectroscopy,* **18**:1224-1230.

Guillong M., Meier D. L., Allan M. M., Heinrich C. A., and Yardley B. W. D. (2008) SILLS: A MATLAB-based program for the reduction of laser ablation ICP-MS data of homogeneous materials and inclusions. In *Laser ablation ICP-MS in the earth sciences: current practices and outstanding issues*, edited by Sylvester P., Mineralogical Association of Canada, Short Course **40**:328–333.

Jackson E. D. (1961) Primary Textures and Mineral Associations in the Ultramafic Zone of the Stillwater Complex. *U. S. Geological Survey Professional Paper* **#358**, p.358

Karner J., Papike J. J., and Shearer C. K. (2004) Plagioclase from planetary basalts: Chemical signatures that reflect planetary volatile budgets, oxygen fugacity, and styles of igneous differentiation. *American Mineralogist* **89**:1101-1109.

Jones J.H. 1995. Experimental trace element partitioning. In *Rock Physics and Phase Relations. A Handbook of Physical Constants, AGU Reference Shelf 3*, edited by Ahrens T.J. Washington: The American Geophysical Union. pp. 73-104.

Lambert D. D. and Simmons E. C. (1987) Magma evolution in the Stillwater Complex Montana: I. Rare-earth element evidence for the formation of the Ultramafic Series. *American Journal of Science* **287**:1-32.

McSween H. Y., Mittlefehldt D. W., Beck A. W., Mayne R. G., and McCoy T. J. (2011) HED meteorites and their relationship to the geology of Vesta and the Dawn mission. *Space Science Reviews*, doi: 10.1007/s11214-010-9637-z.

Mittlefehldt D. W. (1994) The genesis of diogenites and HED parent body petrogenesis. *Geochimica et Cosmochimica Acta* **58**:1537-1552.

Mutchler, S. T., Fedele, L. and Bodnar, R. J. (2008) Analysis Management System (AMS) for reduction of laser ablation ICP-MS data In *Laser Ablation ICP-MS in the Earth Sciences: Current Practices and Outstanding Issues*, edited by Sylvester P. Mineralogical Association of Canada, Short Course **40**:503-353.

Papike J. J., Spilde M. N., Fowler G. W., and McCallum I. S. (1995) SIMS studies of planetary cumulates; Orthopyroxene from the Stillwater Complex, Montana. *American Mineralogist* **80**:1208-1221.

Shearer C. K., Burger P., and Papike J. J. (2010) Petrogenetic relationships between diogenites and olivine diogenites: Implications for magmatism on the HED parent body. *Geochimica et Cosmochica Acta* **74**:4865-4880.

Sylvester P. (2008) Matrix effects in laser ablation ICPMS. In *Laser Ablation ICP-MS in the Earth Sciences: Current Practices and Outstanding Issues*, edited by Sylvester P., Mineralogical Association of Canada, Short Course **40**:67-78.

Treiman A. (1996) The perils of partition: Difficulties in retrieving magma compositions from chemically equilibrated basaltic meteorites. *Geochimica et Cosmochica Acta* **60**:147-155.

Weill D. F. and Drake M. J. (1973) Europium anomaly in plagioclase feldspar: Experimental results and semiquantitative model. *Science* **180**:1059-1060.

Welten K. C., Caffee M. W. and Beck A. W. (2009) Cosmogenic radionuclides in three paired howardites and a polymict diogenite from Pecora Escarpment icefield, Antarctica (abstract). *Meteoritics & Planetary Science* **44**:A216.

Appendix C

Table C1. Average Orthopyroxene Compositions

Sample, section#	LEW 88008,1				LEW 88679,8				MET 01084,5				MIL 03368,7				PCA 02008,8			
Lithology	Hzbg.		Opxn.		Hzbg.		Opxn		Hzbg.		Opxn.		Hzbg.		Opxn.		Hzbg.[f]		Opxn.	
Time (s)[a]	35		36		13		16		30		28		40		36		30		30	
N	**15**	(1σ)[d]	**14**	(1σ)	**8**	(1σ)	**10**	(1σ)	**9**	(1σ)	**8**	(1σ)	**5**	(1σ)	**6**	(1σ)	**5**	(1σ)	**6**	(1σ)
Concentrations in wt.% oxide																				
SiO_2	54.8	(3)	53.7	(4)	55.3	(3)	54.6	(2)	55.6	(4)	54.9	(3)	56.4	(4)	55.4	(3)	56.5	(4)	55.4	(3)
TiO_2	0.108	(11)	0.126	(12)	0.137	(5)	0.157	(10)	0.128	(7)	0.214	(16)	0.080	(1)	0.080	(0)	0.108	(37)	0.100	(20)
Al_2O_3	1.10	(14)	1.22	(10)	0.983	(40)	1.38	(4)	1.01	(9)	0.795	(94)	0.726	(179)	0.740	(20)	0.610	(244)	0.928	(183)
Cr_2O_3	0.708	(21)	0.717	(12)	0.470	(74)	0.530	(45)	0.496	(94)	0.365	(62)	0.430	(93)	0.532	(67)	0.344	(100)	0.485	(33)
FeO_T	15.0	(3)	18.8	(3)	15.9	(6)	16.4	(3)	13.8	(2)	17.9	(5)	14.8	(4)	16.6	(1)	13.6	(7)	14.9	(5)
MnO	0.475	(5)	0.640	(9)	0.537	(6)	0.551	(9)	0.454	(7)	0.601	(16)	0.516	(9)	0.576	(15)	0.462	(23)	0.485	(10
CaO	1.23	(12)	2.30	(16)	1.59	(12)	1.89	(6)	1.23	(11)	1.39	(8)	1.48	(2)	1.60	(17)	1.04	(10)	1.17	(9)
MgO	26.4	(3)	22.5	(3)	24.9	(6)	24.3	(3)	27.2	(2)	23.9	(5)	25.4	(3)	24.2	(4)	27.1	(8)	26.4	(2)
Total[b]	99.8		100		99.8		99.9		99.9		100		99.8		99.8		99.8		99.9	
Concentrations in ppm																				
Na	87.3	(154)	106	(13)	60.1	(200)	80.6	(190)	75.6	(210)	41.9	(140)	53.5	(195)	97.2	(191)	43.6	(75)	54.0	(114)
V	99.3	(5)	144	(10)	112	(6)	112	(8)	83.8	(60)	129	(15)	124	(14)	110	(7)	75.1	(120)	87.5	(42)
Sr	0.420	(310)	0.318	(224)	0.136	(66)	0.080	(22)	0.356	(30)	0.114	(99)	0.132	(15)	0.148	(36)	0.106	(62)	0.163	(92)
Y	1.14	(29)	2.13	(64)	2.12	(10)	2.60	(13)	1.68	(23)	3.75	(26)	0.773	(68)	0.632	(84)	1.67	(113)	0.913	(201)
Zr	1.67	(82)	1.16	(37)	1.50	(25)	2.22	(40)	2.26	(97)	4.21	(94)	0.235	(41)	0.187	(59)	3.81	(378)	0.706	(207)
Nb	0.035	(17)	<0.030[e]		<0.108		<0.034		0.088	(50)	0.182	(143)	<0.059		<0.050		<0.033		<0.033	
La	0.037	(22)	0.017	(10)	<0.040		<0.011		0.024	(10)	<0.011		<0.018		<0.012		<0.020		<0.012	
Ce	0.119	(80)	0.066	(30)	0.038	(14)	<0.012		0.114	(86)	0.046	(21)	0.021	(6)	0.012	(2)	0.030	(25)	0.036	(9)
Nd	0.162	(74)	0.109	(50)	<0.294		<0.100		0.161	(39)	0.120	(52)	<0.171		<0.092		<0.110		<0.110	
Sm	0.097	(53)	0.071	(43)	0.069	(50)	0.093	(47)	0.081	(26)	0.130	(90)	<0.074		<0.050		<0.073		<0.062	
Eu[c]	0.010	(5)	<0.008		<0.015		<0.015		0.012	(4)	<0.008		<0.009		<0.009		<0.010		<0.010	
Dy	0.226	(66)	0.308	(42)	0.253	(33)	0.417	(64)	0.288	(63)	0.609	(49)	0.109	(20)	0.090	(16)	0.292	(196)	0.131	(41)
Er	0.172	(31)	0.256	(39)	0.275	(17)	0.360	(34)	0.200	(19)	0.481	(63)	0.100	(32)	0.084	(17)	0.196	(114)	0.125	(32)
Yb	0.219	(49)	0.334	(61)	0.264	(77)	0.419	(67)	0.266	(56)	0.534	(71)	0.123	(34)	0.120	(31)	0.241	(112)	0.188	(41)

[a] Average duration of ablation, in seconds. Variations due to section thicknesses.

[b] Though summation to 100% was used in data reduction, totals <100% are due to ommison of NiO, which was measured incorrectly.

[c] Eu values were reduced using a 2σ detection limit.

[d] 1σ deviation from the mean is given in terms of the last decimal place.

[e] Indicates analysis falls below a 3σ detection limit. Differences in elemental detection limits between samples is due to varied count times.

[f] The majority of the trace element data for the Hzbg pyroxene in PCA 02008 is not normally distributed

Table C2. Representative olivine and plagioclase trace element compositions

Sample	LEW 88008	LEW 88679	MET 01084	MIL 03368	PCA 02008	LEW 88008	LEW 88679	MET 01084
Mineral	Olivine	Olivine	Olivine	Olivine	Olivine	Plag	Plag	Plag
Lithology	Hzbg.	Hzbg.	Hzbg.	Hzbg.	Hzbg.	Opxn.	Opxn.	Opxn.
Time (s)[a]	34	9	13	43	24	44	25	25
Concentrations in ppm								
K	<3.20	14.6	<5.93	<3.12	<5.24	27.4	89.6	288
Ca[b]	485	140	52.6	117	387	-	-	-
Ti	56.1	38.8	29.8	92.9	19.8	2.58	39.9	41.3
V	12.2	3.48	0.942	5.20	9.36	4.24	<0.816	1.00
Cr	179	42.2	6.64	46.3	61.8	4.03	<0.751	1.07
Sr	0.057	0.053	0.234	<0.023	<0.030	96.9	179	127
Y	0.067	<0.076	<0.071	<0.036	<0.040	0.043	<0.122	<0.100
Zr	0.051	0.064	0.140	0.052	0.051	<0.031	<0.197	<0.075
La	<0.013	<0.037	<0.035	<0.024	<0.039	0.040	0.199	1.17
Ce	0.010	<0.014	<0.021	<0.016	<0.017	0.073	0.308	2.58
Nd	<0.121	<0.353	<0.364	<0.172	<0.296	<0.195	<0.195	0.943
Sm	<0.078	<0.183	<0.183	<0.093	<0.166	<0.120	<0.356	0.241
Eu	<0.021	<0.053	<0.046	<0.021	<0.037	0.394	1.37	0.949
Dy	<0.086[c]	<0.104	<0.159	<0.086	<0.089	<0.099	<0.434	<0.225
Er	0.055	<0.030	<0.066	0.030	<0.032	<0.037	<0.183	<0.066
Yb	0.045	<0.073	<0.060	0.044	<0.054	<0.040	<0.234	<0.080

[a] Ablation duration, in seconds, for the analysis listed. Intersample elemental detection limit variation attributable to range in count times.

[b] Major element concentrations, including Ca in plag, were similar to those reported in Beck and McSween (2010) and are not reported here.

[c] Indicates analysis fall below the 3σ detection limit, listed here

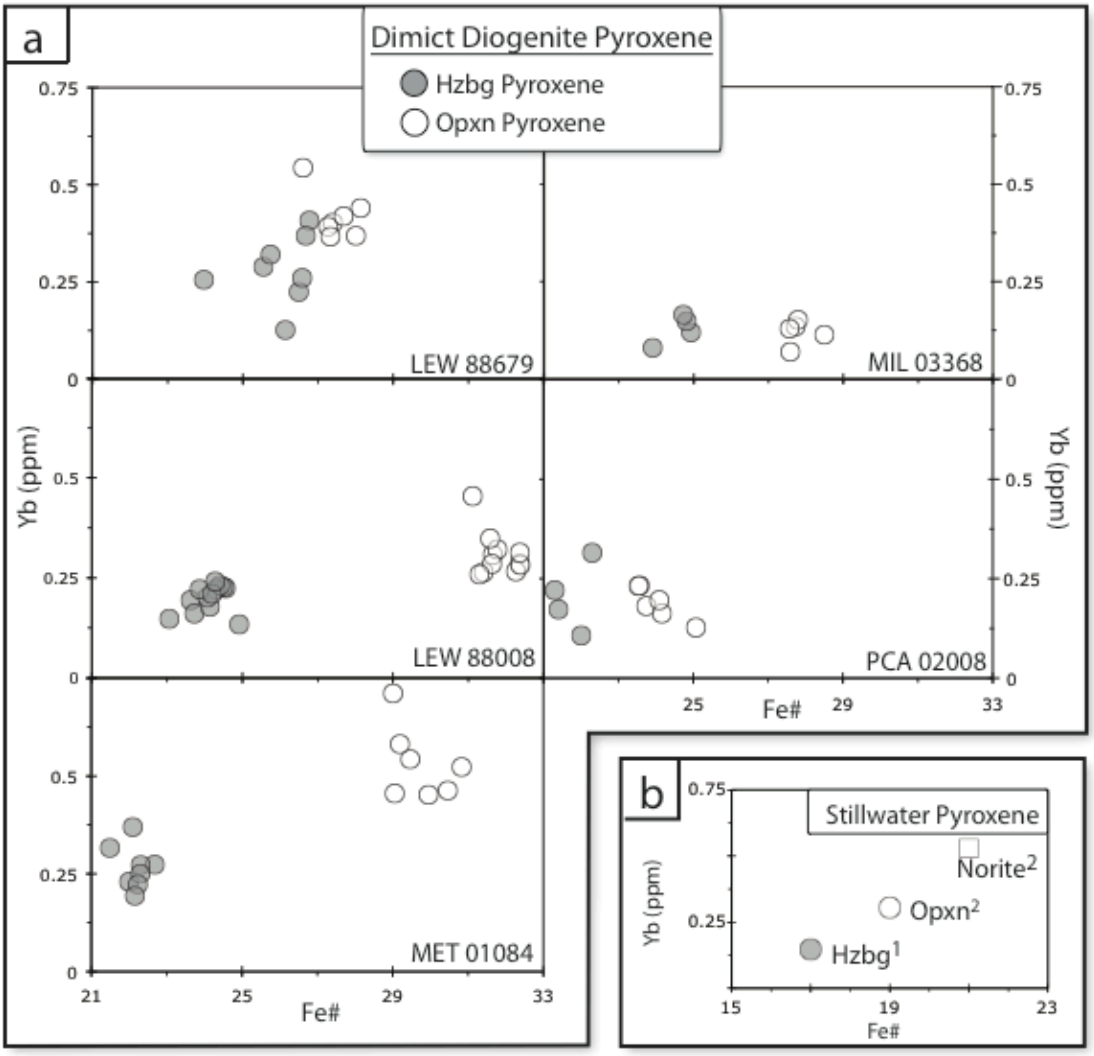


Figure C1. Orthopyroxene Yb vs. Fe# (molar Fe/(Fe+Mg)*100) in (a) five dimict diogenites and (b) samples from the Ultramafic Zone of the Stillwater Complex. Stillwater analyses from [1]Lambert and Simmons (1987), [2]Papike et al. (1995).

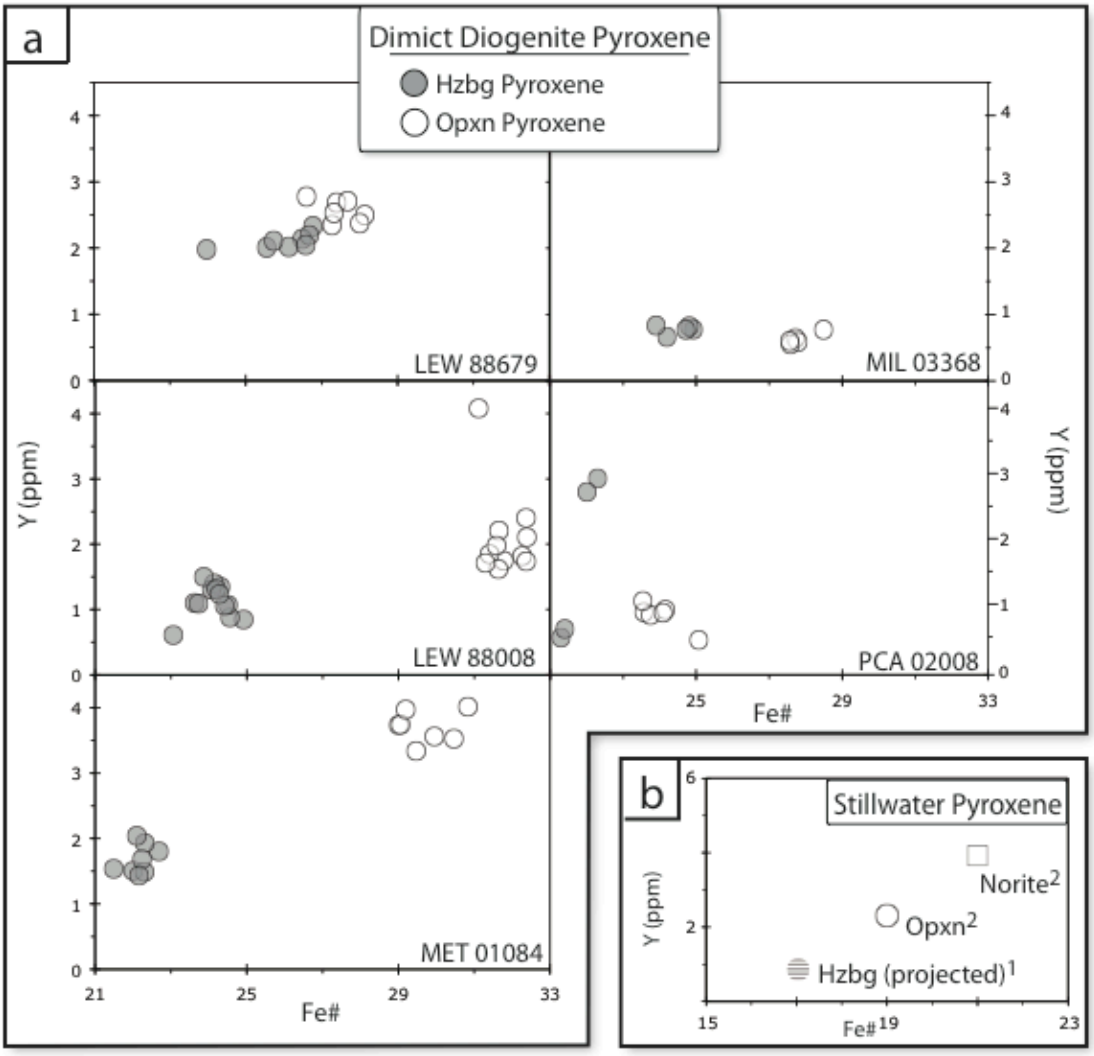


Figure C2. Orthopyroxene Y vs. Fe# in (a) five dimict diogenites and (b) samples from the Ultramafic Zone of the Stillwater Complex. Stillwater analyses from [1]Lambert and Simmons (1987), [2]Papike et al. (1995).

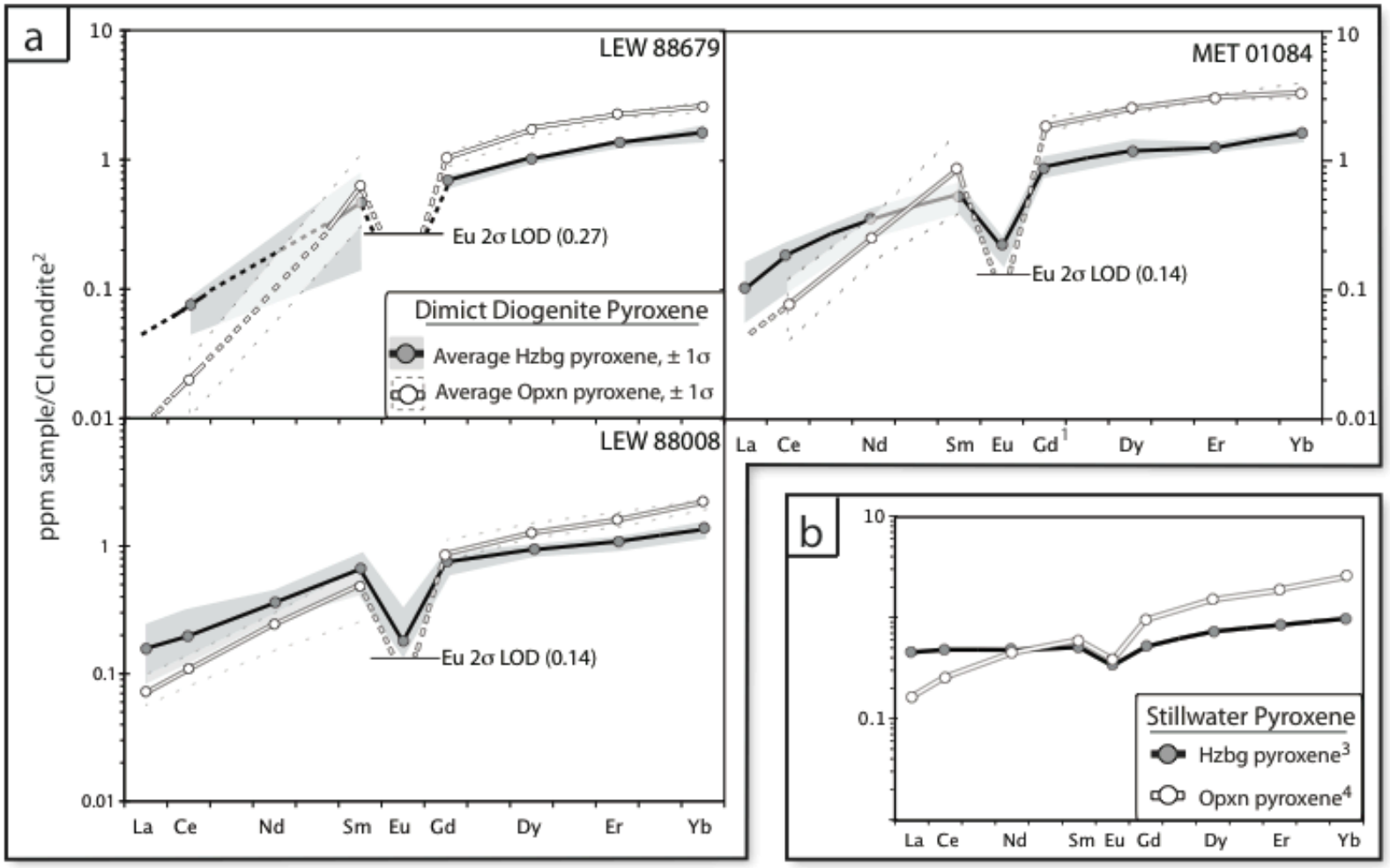


Figure C3. Orthopyroxene REE/CI for (a) three dimict diogenites and (b) samples from the Ultramafic Zone of the Stillwater Complex. [1]Gd concentrations were inferred from REE trends. CI chondrite from [2]Anders and Grevesse (1989), Stillwater analyses from [3]Lambert and Simmons (1987), [4]Papike et al. (1995).

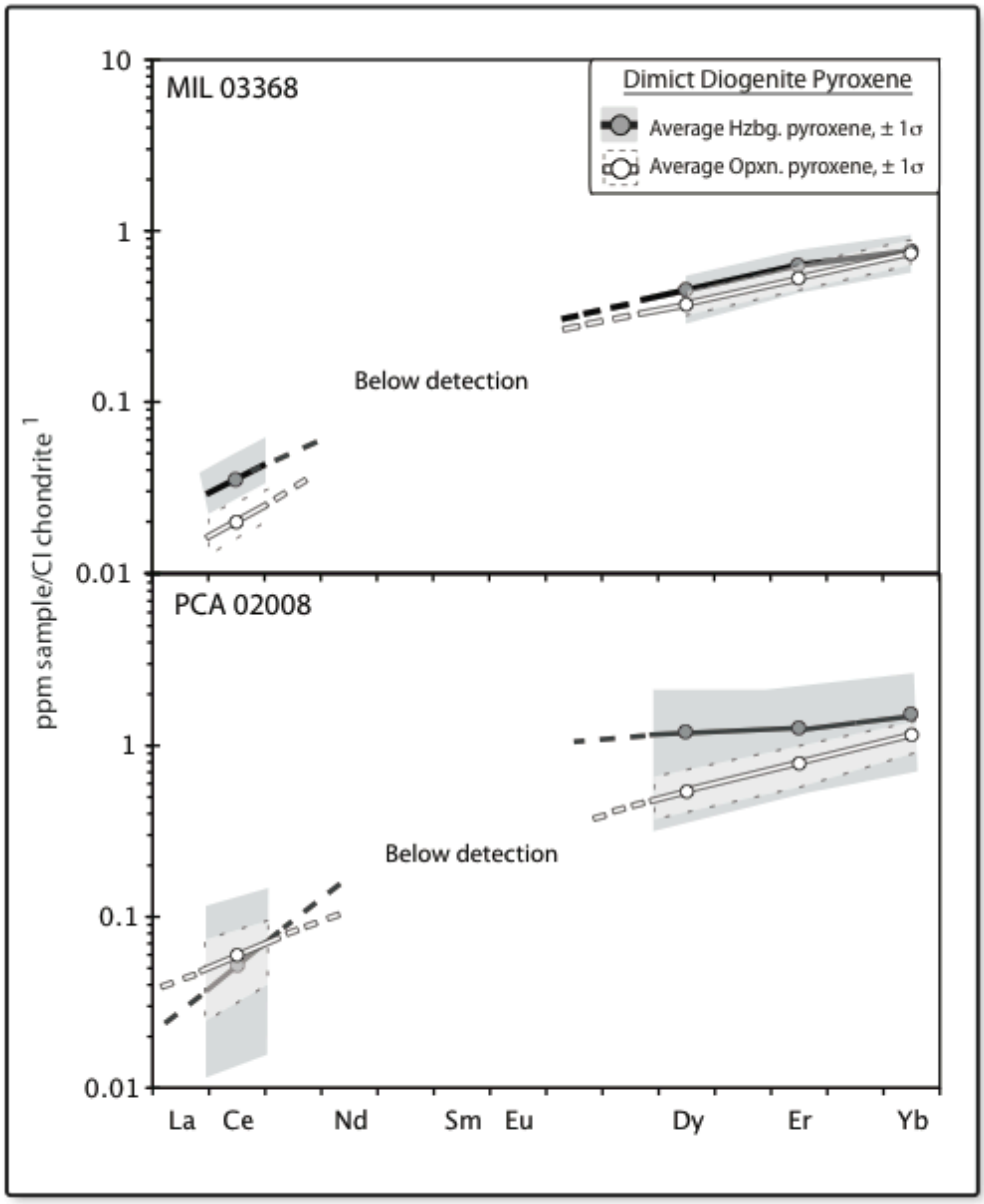


Figure C4. Orthopyroxene REE/CI for two dimict diogenites. CI chondrite from [1]Anders and Grevesse (1989).

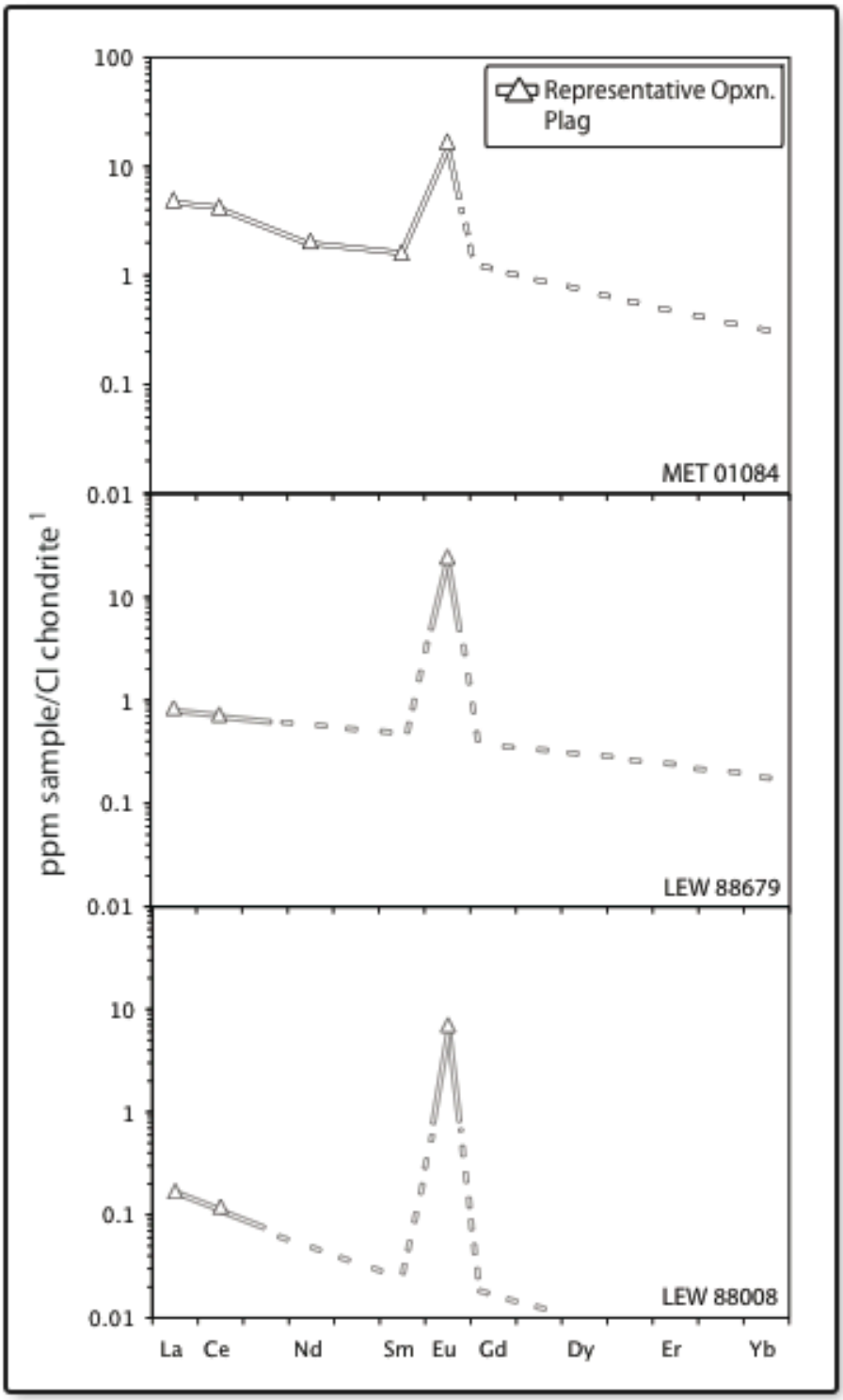


Figure C5. Plagioclase REE/CI in the orthopyroxenite fraction of three dimict diogenites. CI chondrite from [1]Anders and Grevesse (1989).

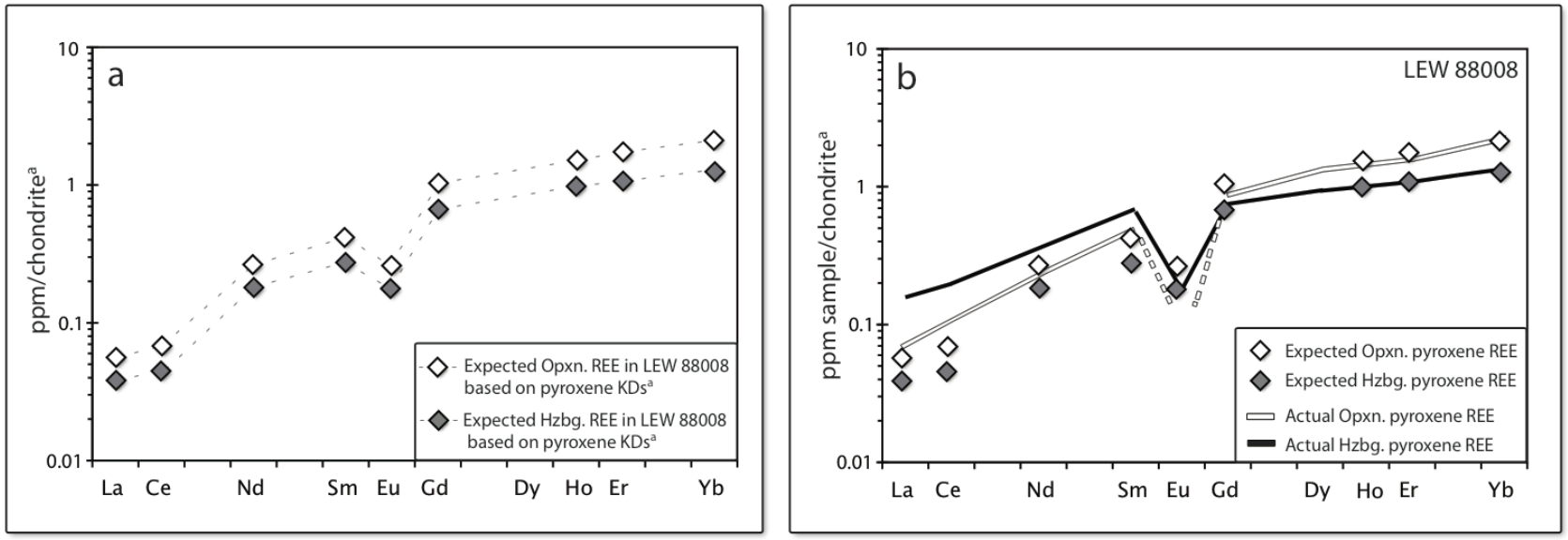


Figure C6. (a) Expected orthopyroxene REE/CI for the two lithologies in LEW 88008, calculated after [a]Jones (1995), and (b) expected orthopyroxene REE/CI vs. actual (measured) REE/CI for LEW 88008.

Part 5
Compositional constraints on the genesis of diogenites

This part is a reformatted version of a paper of the same name that has been submitted for publication in Meteoritics and Planetary Science. David Mittlefehldt, Andrew Beck, Cin-Ty Lee, Hap McSween, Paul Buchanan, and Thomas Burbine are authors of this paper. Andrew preformed all solution ICP-MS and LA ICP-MS analyses. Because David Mittlefehldt is the primary author of this work, please cite the submitted manuscript when referring to this part of the dissertation.

D. W. Mittlefehldt, A. W. Beck, C-T A. Lee, H. Y. McSween, P. Buchanan, and T. Burbine. Compositional Constraints of the Genesis of Diogenites. *Meteoritics and Planetary Science*, submitted.

ABSTRACT

We have done bulk rock compositional analyses (INAA, ICP-MS) and petrologic study of a suite of diogenite meteorites. Most contain orthopyroxenes with mg#s of 70.6 to 79.0. MET 00425 is magnesian (mg# of 83.9). LEW 88011 contains orthopyroxene grains of varying mg# (76.3 to 68.6). QUE 93009 (orthopyroxene mg# 70.6) contains coarse-grained noritic clasts (plagioclase $An_{84.7-88.3}$). It is enriched in incompatible trace elements, but does not contain eucritic debris. It has Eu/Eu* <1, indicating that cumulate norites do not dominate its trace element inventory. QUE 93009 may be transitional between diogenites and magnesian cumulate eucrites. LEW 88679 has anomalous depletions in the most highly incompatible elements (e.g. Nb, La, Ta, U) compared to other diogenites, but is similar to them in less highly incompatible elements (e.g. Y, Zr, Yb, Hf). LEW 88679 is a dimict breccia. It is unlikely that its unusual composition reflects a low trapped melt component. The highly incompatible elements were likely mobilized after impact mixing of the parent lithologies. Graves Nunataks (GRA) 98108 shows an extreme range in Eu/Eu* attributable to the heterogeneous distribution of plagioclase. One sample has a lower Eu/Eu* than does any other diogenite.

We find no compelling evidence to support the hypothesis that diogenite parent magmas were contaminated by small-degree partial melts of the eucritic crust. We posit that subsolidus equilibration between orthopyroxene, phosphates and/or plagioclase resulted in preferential redistribution of Eu^{2+} relative to Eu^{3+} and other REE, and causes anomalously low Eu/Eu* in samples leached in acids that dissolve phosphates.

1.0 INTRODUCTION

Asteroid 4 Vesta has been called "the smallest terrestrial planet" because it is the only large asteroid with a basaltic surface (Keil 2002). Identification of the basaltic nature of Vesta's surface was accomplished through reflectance spectroscopy in the visible and near infrared wavelength region utilizing ground-based telescopes, with comparison to laboratory spectra of basaltic achondrites (McCord et al. 1970). McCord et al. (1970) found that the reflectance spectrum of Vesta is a very close match to that of the basaltic eucrite Nuevo Laredo; this led to the hypothesis that Vesta was the parent asteroid of the howardite, eucrite and diogenite (HED) clan of meteorites (Consolmagno 1979; Consolmagno and Drake 1977; Drake 1979). This hypothesis garnered widespread support when it was shown that there were numerous, <10 km-sized basaltic asteroids distributed in space from near Vesta out to the 3:1 Kirkwood Gap and the ν6 resonance from which gravitational perturbations can send meteoroids into Earth-intersecting orbits (Binzel and Xu 1993).

The study of basaltic eucrites has yielded a consensus view that the eucrite parent asteroid was substantially molten early in its history, and subsequently crystallized. Basaltic eucrites are thought to be quenched residual melts formed during the waning stages of igneous differentiation (see for example Greenwood et al. 2005; Righter and Drake 1997; Ruzicka et al. 1997; Warren 1997). Modeling of the differentiation process to try to match basaltic eucrite major and trace lithophile element and siderophile element contents has resulted in conflicting claims of success (e.g. Righter and Drake 1997; Ruzicka et al. 1997). Nevertheless, it is clear that within the uncertainties of the

modeling process, basaltic eucrite compositions can be successfully described as being those of residual melts.

The competing high-order hypothesis for differentiation of the eucrite parent asteroid is that partial melting produced a series of primary melts from primitive, chondritic source regions of the proto-Vestan interior (Stolper 1977). This hypothesis has lost favor for a variety of reasons, including arguments based on major-element mass balance (Warren 1985, 1997), the difficulty of explaining the very low siderophile element contents of eucrites (see McSween et al. 2011), and the homogeneity in oxygen isotopic compositions (Greenwood et al. 2005).

Although a eucrite-centric view of the differentiation of Vesta permits fairly simple models, diogenites are difficult to fit into such models. Diogenites are a suit of cumulate orthopyroxenites, harzburgites and a dunite (e.g. Barrat et al. 2008, 2010; Beck and McSween 2010 2011; Fowler et al. 1994, 1995; Fukuoka et al. 1977; Mittlefehldt 1994, 2000; Shearer et al. 1997, 2010). Mittlefehldt (1994) first noted that diogenite minor and trace element compositions suggested that the suite would represent cumulates from a fairly extensive range in crystallization, and that this was difficult to understand for rocks that are virtually monomineralic. One would expect that plagioclase crystallization would have occurred if the parent was a magnesian mafic magma (Mittlefehldt 1994). This view was echoed by Fowler et al. (1995) and Shearer et al. (1997, 2010) who suggested that the diogenite suite can most simply be understood as representing a set of cumulates derived from a series of parent magmas with differing initial trace element contents.

Recent compositional study of diogenites has led to the hypothesis that many diogenites were formed by remelting of magma ocean cumulates (Barrat et al. 2008). Further, extremely low Eu contents relative to Sm and Gd for many diogenites that had been leached in acid to remove phosphates led to the hypothesis that many diogenite parent melts were contaminated by melts derived by anatexis of the basaltic (eucritic) crust, and thus must be younger than much of the crust of Vesta (Barrat et al. 2010).

We have undertaken petrologic and bulk compositional studies of a large suite of US Antarctic diogenites and the fall Bilanga to test hypotheses for diogenite petrogenesis and to further understand the constraints diogenites impose on the differentiation of 4 Vesta. One set of bulk samples has been analyzed by instrumental neutron activation analysis at NASA/Johnson Space Center, and a second set by inductively coupled plasma mass spectrometry at Rice University. Petrologic study of thin sections and/or grain mounts has been done at NASA/JSC and the University of Tennessee. Preliminary results focusing on the bulk rock compositional studies have been presented (Mittlefehldt 2002; Mittlefehldt et al. 2009). Beck and McSween (2010) presented the petrologic study of several of the diogenites including those analyzed by ICP-MS, and Beck et al. (2011) presented and the petrologic and bulk compositional study of the dunitic diogenite Miller Range (MIL) 03443. Here we finalize our compositional studies of diogenites.

2.0 METHODS

We obtained 27 samples of 20 Antarctic diogenites from the NASA/JSC Astromaterials Curation Office through the Meteorite Working Group, and one sample of

the fall Bilanga from the University of Arizona. Table 1 gives details of the samples studied.

2.1 Sample preparation

The samples were of various masses (Table D1). For the samples requested for instrumental neutron activation analysis, when the sample mass and character allowed, individual coarse-grained clasts or collections of mm-sized pyroxene grain separates were prepared for analysis. For other diogenites, whole rock samples were prepared. These were coarsely crushed, homogenized, coned-and-quartered, and representative splits taken for analysis. For some of these samples, small chips were taken to prepare grain mounts for electron microprobe analysis. The samples requested for inductively coupled plasma mass spectrometry were ground to a fine powder, homogenized, and coned-and-quartered to obtain representative splits for analysis. In all cases, fresh interior samples were requested, but the vagaries of breaking irregular rocks do not always permit 100% exclusion of exterior material. Prior to crushing, any exterior material was removed.

2.2 Electron microprobe analysis (EMPA).

Grain mounts and/or thin sections were studied for all meteorites. Beck and McSween (2010) presented their EMPA work on thin sections for some of the samples analyzed here. Mineral analyses reported here were done at JSC using a Cameca SX100 electron microprobe. Pyroxene, olivine and chromite were analyzed using 20 KV, 40 nA focused electron beam to enhance excitation of the minor transition elements. Plagioclase analyses were performed using a 15 KV, 20 nA focused electron beam, conditions which do not result in measurable mobilization of Na_2O or K_2O from the calcic plagioclases typical of HEDs. However, for Lewis Cliff (LEW) 88011, plagioclase

analyses for the more sodic grains showed departures from stoichiometry consistent with loss of Na_2O and K_2O. These analyses were repeated using a 15 KV, 20 nA electron beam rastered over a 10 × 10 μm area. These conditions allow analysis of the albitic plagioclases of chondrites without loss of Na_2O or K_2O (see Mittlefehldt and Lindstrom 2001). The JSC EMPA standard minerals collection provided the standardization base for the analyses. The Cameca PAP data reduction software was used to calculate mineral compositions.

2.3 Instrumental neutron activation analysis (INAA)

Samples massing between 15 and 180 mg were encapsulated in ultrapure T21 silica glass tubes for neutron irradiation. Six separate INAA irradiations were performed at the University of Missouri Research Reactor Facility. The irradiation conditions differed slightly from experiment to experiment, with total neutron fluence varying between 2.8×10^{18} and 4.0×10^{18} n cm^{-2}. For each irradiation, four count sets were performed over a period of about 3 months from the time of irradiation in order to obtain data from nuclides of differing half-lives. Standards used were NIST NBS 1633a (coal flyash) for K, Sc, Se, Br, Sr, Zr, La, Ce, Sm, Eu, Tb, Yb, Lu, Hf, Ta and Th; GIT-IWG AN-G (Fiskenaesset anorthosite) for Na and Ca; SABS-MINTEK SARM-7 (Merensky Reef precious-metal ore) for Cr, Fe, Co, Ni and Ir. Raw spectral data were reduced using a modified version of the TEABAGS program of Lindstrom and Korotev (1982). Interference corrections, element concentrations and final data evaluation were carried out using additional in-house programs. All data were rigorously scrutinized for unanticipated interferences, improperly chosen backgrounds or other problems, and

corrections were made as necessary. USGS standard BHVO-1 (Hawaiian basalt) was analyzed in each experiment as a control sample.

Some Na is produced via the ^{24}Mg (n,p) ^{24}Na reaction. This was corrected using the procedure described in Mittlefehldt (1994). The pure silica tubes used to encapsulate samples contain tiny amounts of La. A blank correction was made for La based on several analyses of empty silica tubes as described in Mittlefehldt (1994). For some samples the irradiated rock was transferred to an unirradiated vial prior to counting and blank corrections were unnecessary.

2.4 Inductively coupled plasma mass spectrometry (ICP-MS) analysis

Two separate ICP-MS analysis sequences were done, one each in 2008 and 2009. Sample powders used for solution ICP-MS analysis ranged from 49-69 mg in mass. Similar sized powders of the standards USGS AGV-1 (Guano Valley andesite), BCR-2 (Columbia River basalt), BIR-1 (Iceland basalt), BHVO-1, DTS-1 (Twin Sisters dunite), PCC-1 (California peridotite), GIT-IWG AN-G and GSJ JP-1 (Horoman peridotite [dunite]) were also prepared. Sample and standard powders were put into Savillex®[1] beakers, 0.25 mL of concentrated HF and $HClO_4$ acids were added, and placed in a gravity oven set to 135°C for ~12 hours. A procedural blank was run in parallel. After removing the beakers from the oven and allowing them to cool, they were placed on a ~170°C hotplate until complete dryness was attained. This entire process (acid digestion, dry-down) was repeated twice more. After the third repetition, ~2 mL of 2% HNO_3 was

added to each beaker. New 125 mL polypropylene bottles were weighed and 10-15 mL of 2% HNO_3 followed by ~0.28 mL of concentrated In solution (~446 μg g^{-1}) were added. The contents of the Savillex® beakers were transferred to the polypropylene bottles, which were filled to capacity with 2% HNO_3, and 0.025 mL of concentrated HCl was added to keep Fe in solution. The In concentration of the final solution was ~1 ng g^{-1}. The following day the sample solutions were transferred to vials and analyzed using a ThermoFinnigan Element2 Magnetic Sector ICP-MS at Rice University. Analysis parameters were 13.43 L min^{-1} of Ar cool gas, 0.94 L min^{-1} of Ar sample gas, and 0.97 L min^{-1} of Ar carrier ("auxiliary") gas. Forward power was 1370 W and reflected power was 2 W. Elements Li, Be, Sc, Ti, V, Cr, Co, Ni, Cu, Zn, Ga, Rb, Sr, Y, Zr, Nb, Cs, Ba, La, Ce, Pr, Nd, Sm, Eu, Gd, Tb, Dy, Ho, Er, Tm, Yb, Lu, Hf, Ta, Tl, Pb, Th and U were measured in low mass resolution mode (m/Dm of 300), and Na, Al, P, Ca, Sc, Ti, V, Cr, Mn, Fe, Co, Ni, Cu, Zn, Ge, Zr and Nb were measured in medium mass resolution mode (m/Dm of 4000). BHVO-1 and BIR-1 were used for quantification. Standard JP-1 was also used for quantification of Al, Ca, Sc, V, Cr, Mn, Fe, Co, Ni and Cu in the 2009 analysis set. Standard values reported by Eggins et al. (1997) were used for quantification. The count rate on ^{115}In was used to compensate for instrumental drift. Procedural blanks were treated in the same manner as samples and standards, and drift-corrected blank intensities were subtracted from all samples and standards prior to external calibration. Uncertainties for measurements are <5 %.

Splits of the powders prepared for solution ICP-MS were fused into glass beads for major element analysis using a fused-bead furnace at the University of Tennessee, similar to the method described in Brown (1977). Too little powder of Meteorite Hills

(MET) 01084 was left to make a fused bead of this sample. We initially planned to measure major element compositions of the glass beads by electron microprobe. However, it was discovered that Fe and Mg distributions in the beads were heterogeneous with depth as exposed by sample preparation (Beck et al. 2008). Because of this, we opted to use a laser ablation inductively coupled mass spectrometry (LA ICP-MS) technique to analyze the beads. The laser ablation method "drills down" into the bead and mitigates problems associated with surface analyses by EMPA when depth-related heterogeneities are present. The LA ICP-MS analysis was done at Rice University on the same ICP-MS as used for solution analyses, but coupled to a 213 nm laser (New Wave UP-213SS). The Rice University LA ICP-MS procedures are documented in Lee et al. (2008). Five spots with a size of 44 μm were analyzed on each bead. The beads were ablated with an energy flux of 16–18 J cm^{-2} at a 10 Hz repetition rate. Ablation duration ranged from 30-40 seconds. The ablated material was transported with He carrier gas and mixed with Ar gas before entering the ICP torch. The concentration of Ca was measured in each bead by EMPA prior to laser ablation and was used as an internal standard. The Ca concentration is homogeneous throughout the bead (Beck and McSween 2008). Count rates of ^{23}Na, ^{25}Mg, ^{27}Al, ^{30}Si, ^{49}Ti, ^{52}Cr, ^{55}Mn and ^{57}Fe were determined in medium mass resolution mode ($m/\Delta m$ of 4000), which was sufficient to resolve all isobaric interferences. USGS basaltic glasses BHVO1, BIR1 and BCR2 were used as external standards for quantification. Three sigma standard deviations (internal precision) were less than 1%, except for ^{23}Na where it was 2%.

3.0 RESULTS

3.1 Mineral compositions

Beck and McSween (2010) presented their mineral compositional data which covers all the samples analyzed here by ICP-MS. The EMPA work done at JSC includes some of these meteorites plus those we have analyzed by INAA. Tables D2-D5 present representative mineral compositions for the samples studied at JSC.

Low-Ca pyroxene compositions (Table D2) are for the most part within the range typical of diogenites, with mg# (molar 100*(MgO/(MgO+FeO)) in the range 70-77. One exception is MET 00425 with an mg# of 83.8. This is the most magnesian diogenite (Barrat et al. 2008; Mittlefehldt 2002) with an average orthopyroxene mg# greater than those of Bilanga (79.8, Domanik et al. 2004), the magnesian fraction of Elephant Moraine (EETA or EET) 79002 (80.4, Mittlefehldt 2000), or the magnesian fraction of LaPaz Icefield (LAP) 02216 (78.9, Beck and McSween 2010). LEW 88011 contains the most ferroan of the orthopyroxenes we analyzed, with mg#s as low as 68.6. However, this diogenite contains pyroxenes with a range of compositions, the most magnesian of which has an mg# 76.3, within the range typical of diogenites (e.g. Mittlefehldt 1994). Queen Alexandra Range (QUE) 93009 is also ferroan; most pyroxene grains in it have mg#s of 70.1 to 70.7, but a few are as magnesian as mg# 71.4. Figure D1 is an mg# histogram for average low-Ca pyroxene grains in diogenites from this work and the literature. Some diogenites have two or more distinct populations of pyroxenes (Beck and McSween 2010; Mittlefehldt 2000) and for these, population averages are shown. For LEW 88011, which shows an unusually wide range in pyroxene mg#, grain averages shown.

Oxide compositions are given in Table D3. Chromite is found in all diogenites. Among the diogenites we have analyzed, ilmenite is present in only QUE 93009. As noted by Bowman et al. (1999) and Mittlefehldt (1994), Allan Hills (ALHA or ALH) 77256 contains the most aluminous chromites. The most Al-poor grain in this meteorite has a higher Al content than all but one grain from all other diogenites studied here (Fig. D2). However, some chromite grains in Ellemeet, EET 83246 and LEW 88008 are as aluminous as or more so than those in ALHA77256 (Bowman et al. 1999). ALHA77256 chromites are also the most magnesian; the least magnesian grain has the lowest Al content. Chromite grains in magnesian diogenite MET 00425 have mg#s within the range of other diogenites, and have an Al contents at the low end of the range (Fig. D2). Chromite grains in ferroan diogenite QUE 93009 are the most ferroan studied here. They are comparable to chromite grains in Yamato Type B (Y-75032-type) diogenites in mg# and Al content (Mittlefehldt and Lindstrom 1993). Ilmenite is rarely reported as a discrete phase from diogenites but is present in Yamato Type B diogenites (Mittlefehldt and Lindstrom 1993). Ilmenite exsolution lamellae are present in the chromite grains in QUE 93009.

Only a few of the diogenites investigated here contain olivine; representative data are presented in Table D4. Our analyses agree with those of Beck and McSween (2010). We analyzed four olivine grains in Pecora Escarpment (PCA) 02017. This diogenite is paired with PCA 02008, which was studied by Beck and McSween (2010). Olivines in PCA 02017 are similar in composition to those in PCA 02008 except that they have higher CaO contents, 0.13-0.17 wt% vs. 0.07±0.03.

Several of the diogenites we have studied contain plagioclase; representative analyses are given in Table D5. For those diogenites investigated by Beck and McSween (2010) and us, plagioclase compositions agree well for LEW 88679 and MET 01084. For GRA 98108, our plagioclase grains are more sodic ($Ab_{10.5-13.0}$) compared to the representative analysis presented by Beck and McSween (2010), $Ab_{8.6}$. Plagioclase grains in PCA 02017 and QUE 93009 have compositions ($Ab_{6.7-10.0}$ and $Ab_{9.9-16.0}$) that are within the range found for diogenites ($Ab_{4.3-16.1}$, Beck and McSween 2010). The representative plagioclase analysis for PCA 02008 presented by Back and McSween (2010) is more sodic that those we have measured in paired meteorite PCA 02017. LEW 88011 is unique. Plagioclase in this diogenite is quite variable in composition from $Ab_{10.0-21.4}$, and individual grains can be heterogeneous ($Ab_{17.1-24.6}$ in an extreme case; Table D5). Because of the difficulty in analyzing these plagioclase grains (see above), we did not attempt to determine whether systematic zoning is present. In the grain showing extreme heterogeneity, the randomly selected analysis regions do not show obvious zoning. Plagioclase grains in LEW 88011 show departures from stoichiometry that are correlated with Na content. This is not an artifact of the analyses as our most recent analyses were done using conditions that produce stoichiometric analyses of chondritic plagioclase grains that are as sodic as Ab_{83} (Mittlefehldt and Lindstrom 2001).

3.2 Bulk Compositions

Concentrations of major and minor elements determined by LA-ICP-MS on fused beads are given in Table D6. The concentrations of MgO, CaO and FeO fall within ranges found for diogenites (e.g., Fukuoka et al. 1977; Mittlefehldt 1994, Barrat et al. 2008). The two harzburgite samples, ALHA77256 and GRA 98108, are the most

magnesian of the group. GRA 98108 is very close in MgO concentration to the most magnesian diogenites, MET 00425 and NWA 1461 (Figs. D3a and D3b) (Barrat et al. 2008; Warren et al. 2009). The magnesian nature of the harzburgitic samples is attributed to their high content of olivine (Beck and McSween 2010), which has a higher cation/SiO_2 than does orthopyroxene. LEW 88008 contains a high FeO concentration, which is consistent with the relatively Fe-rich orthopyroxene it contains (Beck and McSween 2010; Mittlefehldt 1994). The CaO contents of samples from this study are also within the range found for diogenites (Fig. D3a), but four stand out as being enriched in CaO compared to most diogenites. These are ALH 85015, LAP 03979, LEW 88008 and PCA 02008. These meteorites contain higher modal plagioclase than other diogenites, 1.3-5.0 vol.% vs. <0.4 vol.% (Beck and McSween 2010). The four diogenites with high bulk CaO contents also are enriched in Al_2O_3 compared to most diogenites, consistent with their higher modal plagioclase content (Fig. D3b). Excluding the four with high modal plagioclase, the diogenites we analyzed via LA-ICP-MS show increasing Al_2O_3 with TiO_2, within the ranges determined for diogenites generally (Fig. D3c).

The results of our INAA on 21 samples of 13 diogenites are presented in Table D7. Our INAA results on standard reference materials run as control samples are compared to recommended values in the electronic annex. For most diogenites, only whole rock samples were analyzed. However, for LAP 91900 and QUE 93009 we analyzed both whole rock and separated clast samples. For LAP 91900, two orthopyroxene separates are essentially the same in composition as two whole rock samples. In contrast, the whole rock sample of QUE 93009 shows substantial enrichment

in incompatible elements compared to the separated orthopyroxene, with the more highly incompatible elements (e.g. Na, K, La) showing greater enrichments than the less highly incompatible elements (e.g. Sc, Yb, Lu) (Table D7). We analyzed two orthopyroxene separates for EET 83247. A whole rock sample was previously analyzed at JSC (Mittlefehldt 1994); those data are repeated in Table D7. The whole rock sample of EET 83247 is enriched in Ca, La, Yb and Lu ~2.3-2.5 times the orthopyroxene separates, while Sc and Na are roughly the same (0.9-1.2 times). Several diogenites are unusually Na-rich. The separated clast from QUE 93009 contains 365 μg g^{-1} Na, compared to a range of 20-120 μg g^{-1} for most orthopyroxene separates (Mittlefehldt 1994, 2000). High Na content in some diogenite samples, including in some orthopyroxene separates, was ascribed to inclusion of plagioclase (Mittlefehldt 1994). This is plausible for QUE 93009 as it contains abundant plagioclase, and some coarse igneous clasts are noritic. One of the two orthopyroxene separates of EET 83247 is also enriched in Na (669 μg g^{-1}) and K (360 μg g^{-1}). Plagioclase has not been reported in this diogenite, and we have not studied it in thin section.

Table D8 presents our solution ICP-MS analyses on duplicate whole rock samples of ten diogenites. Our ICP-MS results on standard reference materials run as control samples are compared to recommended values in the electronic annex. For the most part, the data fall within the ranges previously established for diogenites. Split (c) of ALH 85015 has a Ni content of 979 μg g^{-1}, higher than found for any other diogenite sample, excluding sample E-4 of Ellemeet which was a chondritic clast (Mittlefehldt 1994). Split (a) of ALH 85015 has a much lower Ni content, 130 μg g^{-1}. For all other samples, our analyses replicate the Ni content to within 30% or less. ALH 85015 and PCA 02008 are

enriched in the most highly incompatible lithophile elements. The *minimum* analysis for these two meteorites is greater than the *maximum* analysis for the other eight diogenites for P, Sr, Nb, Ba, La, Ce, Pr, Nd, Eu, Ta and Th.

4.0 DISCUSSION

We will use our data to evaluate hypotheses for the formation of diogenites. In discussing our data, we will include recent, comparable literature data to widen the range of diogenites under consideration. Before delving into the petrogenesis of diogenites, we will discuss several unusual samples and anomalous data to eliminate non-comparable rocks or non-representative samples from consideration.

4.1 EET 83246 and LEW 88008 – altered diogenites

At the start of meteorite collecting from the stranding surfaces in Antarctica, received wisdom was that terrestrial alteration would be insignificant. Nevertheless, analyses of eucrites revealed anomalous REE patterns that were attributed to the effects of low-temperature alteration suffered while in Antarctica (Mittlefehldt and Lindstrom 1991). One key characteristic of altered eucrites is anomalous Ce contents; anomalously high Ce is often associated with low LREE samples and anomalously low Ce is associated with samples with high LREE contents (Mittlefehldt and Lindstrom 1991, 2003). The hypothesis proposed to explain these anomalies is that melt-water solutions in the Antarctic environment dissolve REE-rich phosphates and locally redistribute the REE within the rock. Because Ce can be oxidized to Ce^{4+}, this REE becomes partially

decoupled from the REE^{3+}, resulting in the observed Ce anomalies (Mittlefehldt and Lindstrom 1991).

Previous compositional studies of diogenites at JSC were done by INAA (Mittlefehldt 1994, 2000), which is not sensitive to Ce at the low concentrations typical of these meteorites. Thus, Ce anomalies caused by Antarctic alteration could not be identified. Solution ICP-MS is more sensitive for Ce and yields precise and accurate analyses of the LREE for most diogenites.

We have computed the Ce/Ce* ratios for the diogenites studied here, and find two that have anomalous ratios. (The calculated Ce* is the Ce content expected from interpolation of the LREE pattern.) The samples of EET 83246 have an average Ce/Ce* of 1.22, while the samples of LEW 88008 have an average Ce/Ce* of 2.06 (Table D8). These diogenites have likely had their Ce contents enhanced by precipitation from alteration solutions, but we cannot determine whether their REE^{3+} contents have been affected. Both of these diogenites have REE patterns (excluding Ce) that are within the ranges of those samples that have normal Ce/Ce*, and their La/Yb and Hf/Yb ratios fall within the diogenite trends (Fig. D4). The Hf contents of HEDs are unaffected by Antarctic alteration (Mittlefehldt and Lindstrom 2003). It is possible that, excluding Ce, the REE data for these two diogenites are unaffected. Nevertheless, we will not use the REE data for these samples for interpretation of diogenite petrogenesis.

4.2 ALH 85015, PCA 02008 and PCA 02017

As noted above, ALH 85015 and PCA 02008 have higher contents of the most highly incompatible elements than other diogenites we have studied. They have high Al_2O_3 and CaO contents (Fig. D3) that reflect their high modal plagioclase contents

(Beck and McSween 2010). They also have the highest TiO_2 contents of the diogenites we analyzed by LA-ICP-MS (Fig. D3c).

ALH 85015 is a very small sample; 3.2 grams recovered mass (see *Antarctic Meteorite Newsletter*, 9(3), 1986). Although originally classified as a diogenite, it was considered a howardite by Berkley and Boynton (1992). The classification of ALH 85015 was reevaluated and was confirmed as a diogenite, but the justification for this included the statement "… this is a small sample so limited sections are available. Only one shows eucritic material, so it's classification as a diogenite stands" (*Antarctic Meteorite Newsletter*, 33(1), 2010). Based on this statement, ALH 85015 fits the definition of a polymict diogenite (Delaney et al. 1983). Beck and McSween (2010) confirm the presence of small basaltic clasts in this meteorite.

PCA 02008 is one of the diogenites identified as containing two distinct populations of pyroxene, with mg#s of 78.2 and 75.8 (Beck and McSween 2010). Although it and paired meteorite PCA 02017 are classified as diogenites, cosmogenic nuclide abundances indicate that PCA 02008 is paired with the PCA 02009 howardite pairing group (Welten et al. 2009). Beck and McSween (2010) note the presence of small basaltic clasts in PCA 02008, and we find a small amount of mafic material from several distinct lithologies in PCA 02017 (see Table D2). Thus, these meteorites are polymict diogenites as defined following Delaney et al. (1983). If these two meteorites are indeed paired with the PCA 02009 howardite, then possibly they should also be classified as howardites.

The enhanced incompatible lithophile element contents of ALH 85015 and PCA 02008 are plausibly the result of small amounts of eucritic material admixed into the

diogenitic breccias. The presence of eucritic material would explain the high modal plagioclase contents (Beck and McSween 2010) and consequent high Al_2O_3 and CaO concentrations, and eucritic debris would enhance the TiO_2 contents (Fig. D3). Figure D4 shows La vs. Yb and Hf vs. Yb for our analyses (ICP-MS and INAA), the ICP-MS data of Barrat et al. (1999, 2008, 2010) and Beck et al. (2011), and INAA data for Yamato Type B diogenites from Mittlefehldt and Lindstrom (1993). ALH 85015 and PCA 02008 are among the most trace-element-rich, with only five diogenites having comparable or higher La contents. Two of these are A-881838 and A-881839 (Barrat et al. 2008, 2010). These meteorites have similar mineralogy including pyroxene and plagioclase compositions, and bulk rock trace element compositions (Barrat et al. 2008, 2010), and are likely paired. They lose 75-85% of their La upon mild leaching with mineral acids, indicating that phosphate is a major carrier of the light rare earth elements (LREE) in them (Barrat et al. 2010). However, both are rich in Hf (Fig. D4b), which is not appreciably removed by the acid leaching procedure (Barrat et al. 2010). Thus, these diogenites either contain a significant trapped melt component that carries the incompatible lithophile elements, or they are polymict diogenites with a small eucritic component. In either case, the LREE are mostly contained in phosphate.

MIL 07003 (Barrat et al. 2010) has higher Yb and similar La and Hf as ALH 85015 and PCA 02008. MIL 07003 is a ferroan diogenite that appears to be intermediate between classic diogenites and cumulate eucrites (*Antarctic Meteorite Newsletter*, 31(2), 2008). It may thus be similar in petrogenesis to the Yamato Type B diogenites that are thought to be mesocumulates from melts that were more evolved than typical diogenite

parent melts (Mittlefehldt and Lindstrom 1993). MIL 07003 is therefore not directly comparable to typical, magnesian diogenites.

4.3 QUE 93009

QUE 93009 is the most incompatible-element-rich diogenite shown in Figure D4. We analyzed both a bulk rock sample and a clast separate (Table D7). The high trace element content of the clast sample (lower of the two on Fig. D4) cannot be due to eucritic contamination. As noted above, the clast separate is rich in Na, and noritic clasts composed of intergrown, coarse (mm-sized) plagioclase and orthopyroxene are present in this meteorite. Pyroxenes in QUE 93009 are on the ferroan side of the range of typical diogenite orthopyroxene compositions (Fig. D1). Although there is a small range in pyroxene mg#s in this meteorite, we found no eucritic pyroxenes. Plagioclase occurs as mineral fragments in the matrix and in noritic clasts. There is no petrologic evidence for a eucritic component in this breccia; it is not a polymict diogenite in the sense of Delaney et al. (1983). Pyroxenes in QUE 93009 are less ferroan than those of Yamato Type B diogenites (Fig. D1). QUE 93009 contains ilmenite, which has been previously reported only in Yamato Type B diogenites (Mittlefehldt and Lindstrom 1993). Ilmenite occurs as exsolutions in chromite grains in QUE 93009, whereas in Y-75032 and Y-791199 ilmenite occurs as a discrete phase. Thus, QUE 93009 shows some petrologic similarities to the Yamato Type B diogenites, but is richer in incompatible trace elements than the latter diogenites (Fig. D4). We do not have petrologic evidence that QUE 93009 contains a significant trapped melt component. The clast and bulk samples have Eu/Eu* of 0.34 and 0.60, and for this reason, if the norite clasts are cumulates, they cannot dominate the incompatible trace element budget of the rocks; norite cumulates would have Eu/Eu* > 1.

(The calculated Eu* is the Eu content expected from interpolation of a REE pattern.) QUE 93009 plausibly represents a transitional rock type between typical diogenites and magnesian cumulate eucrites such as Binda. Binda is a polymict cumulate eucrite (Delaney et al. 1983) with the cumulate component containing 70-75 vol% pyroxene (Delaney et al. 1984; Duke and Silver 1967) with a primary (pre-exsolution) composition of mg# ~67 (Takeda et al. 1978). Yamato Type B diogenites are also considered to be intermediate between diogenites and cumulate eucrites (Mittlefehldt and Lindstrom 1993; Takeda and Mori 1985).

4.4 LEW 88679

LEW 88679 is one of several diogenites identified by Beck and McSween (2010) as containing two distinct lithologies, a more magnesian harzburgite and a more ferroan orthopyroxenite. Plagioclase occurs in both lithologies. This diogenite stands out on Figure D4a as having a lower La/Yb ratio than any other diogenite. The REE data for LEW 88679 are shown in Figure D5 and compared to orthopyroxene/melt K_Ds from Schwandt and McKay (1998). For this partition coefficient set, D_{Gd} is interpolated and the Eu partition coefficient is scaled for an assumed fO_2 of one log unit below the iron-wüstite buffer using the D_{Eu}/D_{Gd} relationship of McKay et al. (1990). The orthopyroxene/melt partition coefficients were adjusted to match the Yb abundance of the average of our ICP-MS analyses, with all other REE being scaled accordingly.

Although LEW 88679 has a lower La/Yb ratio than any other diogenite, it nevertheless could potentially contain a small amount of a trapped melt component. The LREE contents of LEW 88679 are higher than expected for a pure orthopyroxene cumulate assuming the partition coefficients of Schwandt and McKay (1998) are

appropriate and that the parent melt had chondritic relative REE ratios. Based on these partition coefficients, only ~0.1% of a trapped melt component could explain the difference. Also shown is a partition coefficient set calculated after Jones (1995) and also adjusted to match the Yb abundance of our ICP-MS analysis. The Jones D set has a higher LREE/HREE ratio, and if these are more applicable then no trapped melt component is indicated for LEW 88679.

The prior discussion was based only on orthopyroxene/melt partitioning, while LEW 88679 contains ~15 vol% olivine (Beck and McSween 2010). Olivine/melt partition coefficients also show extreme LREE/HREE fractionation, and have lower absolute values than orthopyroxene/melt partition coefficients (c.f. McKay 1986; Schwandt and McKay 1998). Using a bulk distribution coefficient by including olivine in the calculated cumulate does not alter the conclusion just arrived at regarding the REE pattern of LEW 88679, viz. the LREE-HREE fractionation observed for LEW 88679 could be consistent with its being an orthopyroxene-olivine cumulate sans trapped melt.

LEW 88679 is also anomalously low in Nb/Yb, Ta/Yb, Th/Yb and U/Yb among the diogenites we have studied, but is normal in Hf/Yb (Fig. 4b). Orthopyroxene/melt partition coefficients for La, Ta and Th are much lower than for Yb or Hf (Barrat et al. 2007), and we would expect the same to be true for Nb and U. Thus, elements that are most susceptible to enhancement by inclusion of a trapped melt component are low, again suggesting that LEW 88679 may be a nearly pure cumulate harzburgite.

However, in order to match the partition coefficients with the diogenite data, a parent melt with ~24 times CI abundances of REE was assumed. This is implausibly high for diogenite parent magmas given that primitive eucrites such as Sioux County only

have ~8 times CI REE (e.g. Fukuoka et al. 1977; Mittlefehldt 1979). The situation becomes even worse using partition coefficients calculated after Jones (1995) using the D_{Ca} recovered from the Schwandt and McKay (1998) experiments, and/or by including olivine as a cumulus phase. Thus, although we can match the REE *pattern* of LEW 88679 quite successfully with existing partition coefficient *ratios*, the absolute concentrations are difficult to explain by this simple model. Evaluation of experimentally determined low-Ca pyroxene/melt partition coefficients shows that as the absolute values of the Ds increase, the La/Yb ratios decrease (e.g. Bédard 2007; Jones 1995) and we cannot get relief from our quandary by appealing to vague uncertainties in partitioning.

LEW 88679 is a dimict breccia of more magnesian harzburgite and more ferroan orthopyroxenite (Beck and McSween 2010). These authors noted that orthopyroxene minor element (Al, Ti, Cr) trends between the harzburgite and orthopyroxenite components in LEW 88679 were difficult to explain as resulting from igneous fractionation within a single pluton, and that if the pyroxene minor element contents represent the original igneous compositions, then the two components were derived from unrelated source plutons. If true, it is unlikely that two cumulate lithologies randomly mixed would each be free of a trapped melt component, even if they represented different parts of the same intrusion. The anomalously low highly incompatible trace element contents of LEW 88679 would thus remain unexplained. Because LEW 88679 is dimict, it seems likely that the anomalously low trace element contents were rather developed after impact mixing of the two lithologies by some process acting on the breccia. As an alternate interpretation, Beck and McSween (2010) suggested that post-crystallization

metamorphic equilibration acting on distinct lithologies of a single pluton could explain the pyroxene minor element contents of LEW 88679. This scenario might be compatible with the anomalous depletion of highly incompatible elements in this diogenite, and could be explored through in situ trace element analyses.

4.5 Petrogenesis

Although broad-scale differentiation models for Vesta can explain the first-order mineralogy, mineral compositions and bulk major element compositions of diogenites (e.g. Righter and Drake 1997; Ruzicka et al. 1997; Warren 1997), they do not explain the details of minor and trace element distributions (Mittlefehldt 1994). As a result, models for the petrogenesis of diogenites have been at odds with the broad-scale models for eucrite genesis (Fowler et al. 1995; Mittlefehldt 1994; Shearer et al. 1997, 2010).

Tatahouine and MET 00424 represent special cases. The normalized REE abundances of Tatahouine increase very steeply from Sm to Lu (Fig. D5). This steep increase cannot be explained as originating in an orthopyroxene cumulate formed from magma with chondritic REE ratios (Fukuoka et al. 1977). This led to the hypothesis that the parent magma for Tatahouine was formed by remelting of an earlier generation of orthopyroxene cumulates followed by fractional crystallization to form a second generation cumulate, or that Tatahouine could be a melting residue of an early generation of orthopyroxene cumulates (Fukuoka et al. 1977). This hypothesis was reiterated by Mittlefehldt (1994), and extended by Barrat et al. (2008) to include MET 00424, the diogenite with the most extreme depletions in incompatible lithophile elements (Barrat et al. 2008, 2010; Mittlefehldt 2002).

Expanding on Fukuoka et al. (1977), Barrat et al. (2008) have concluded that rather than being cumulates from earlier in the crystallization sequence of a molten Vesta, diogenites are cumulates formed from magmas generated by remelting lower crustal cumulates of the initial magma ocean stage. This research group extended their interpretation by noting that the orthopyroxene fraction of some diogenites, prepared by acid leaching bulk rock samples to remove phosphates, has Eu/Eu* much lower than expected for orthopyroxene in equilibrium with a magma with chondritic REE ratios (Barrat et al. 2010). This led these authors to conclude that some diogenite parent magmas were contaminated by melts generated by remelting the basaltic (eucritic) crust, and therefore the diogenite parent magmas must be younger than the age of major crust formation on Vesta.

The crux of the argument is illustrated on a plot of Eu vs. Gd (Fig. D6) for the leached diogenite residues from Barrat et al. (2010). All diogenites plot below the CI ratio (dashed line) on this diagram and therefore have sub-chondritic Eu/Gd ratios. Many of the residues plot between the CI ratio line and the line for model orthopyroxene cumulates in equilibrium with melts having CI Eu/Gd ratios. The Eu and Gd partition coefficients used for this line are those from Barrat et al. (2007) that were used in modeling diogenite petrogenesis by Barrat et al. (2010). Diogenites that plot near the orthopyroxene cumulate line may have equilibrated with magma with chondritic Eu/Gd. Those that plot between the cumulate and CI ratio lines could represent cumulates with variable amounts of included trapped melt.

A large number of the diogenite residues plot below the cumulate line of Figure D6. If the Eu partition coefficient used is accurate for the conditions of diogenite

formation and diogenites are unmodified igneous cumulates, then those diogenites that plot below the cumulate line must have crystallized from magma with a sub-chondritic Eu/Gd ratio, as advocated by Barrat et al. (2010). For comparison, a model cumulate based on the Sr partition coefficient is shown. The partitioning behavior of Eu^{2+} will be very similar to that of Sr^{2+} (Drake and Weill 1975). Thus, the model cumulate line based on Sr is the absolute limit for orthopyroxene cumulates in equilibrium with magma with chondrite Eu/Gd under conditions so reducing that all Eu is divalent. Also shown on Figure 6 are our data for harzburgitic diogenite GRA 98108.

Barrat et al. (2010) show that a partial melt of basaltic eucrite crustal rock would have a subchondritic Eu/Gd ratio because the anatectic residue would be a mixture of low-Ca pyroxene and plagioclase. Europium is a compatible element in plagioclase. Mixing this crustal melt with a penultimate diogenite parent melt that has a chondritic Eu/Gd ratio would produce the ultimate diogenite parent melt with subchondritic Eu/Gd as suggested by Figure D6. The model of Barrat et al. (2010) is thus that diogenites crystallized from magmas produced by remelting early magma ocean cumulates, some of which were contaminated by partial melts of the eucritic crust of Vesta.

The crustal melt also has super-chondritic Gd/Lu and La/Sm that will be inversely correlated with Eu/Eu* (see Fig. 11 of Barrat et al. 2010). Thus, in a simple model of formation of diogenites from magmas mixed with crustal melts, one would expect that the derived ultramafic cumulates (harzburgites and orthopyroxenites) should express an inverse correlation between Eu/Eu* and Gd/Lu. In gross detail, this is what is observed (Fig. D7a). Excluding a few outliers for the moment, there is a good general trend of decreasing Eu/Eu* with increasing $(Gd/Lu)_{CI}$ that qualitatively matches expectations

from the Barrat et al. (2010) hypothesis. Several diogenites plot close to the orthopyroxene/melt D ratios (those with slightly lower $(Gd/Lu)_{CI}$ and similar Eu/Eu*). These are plausible cumulates from parent melts that were not contaminated by crustal melts. Because these melts plot close to the orthopyroxene/melt D ratios, their parent melts may have had chondritic-relative REE ratios, that is, they were not liquids produced by remelting magma ocean cumulates. The unlabeled points with higher $(Gd/Lu)_{CI}$ than the orthopyroxene partition coefficient are plausible cumulates from parent melts that had been contaminated by crustal melts. Based on their position in Figure D7a, LEW 88679 and GRA 98108 are consistent with an origin as cumulates derived from magmas contaminated by crustal melts.

As mentioned, Tatahouine is extremely depleted in LREE compared to HREE and is consistent with being a restite from orthopyroxenite cumulate melting, or a cumulate formed from magmas produced by remelting orthopyroxenitic cumulates (Fukuoka et al. 1977). The low $(Gd/Lu)_{CI}$ and EuEu* ratios for Tatahouine (Fig. D7a) can be modeled by this process. Contamination of the Tatahouine parent magma by crustal melts is not required to model the REE pattern of this diogenite.

Barrat et al. (2010) group MET 00425, MET 00436 and MIL 07001 into a compositional subtype of diogenites by virtue of their similar REE patterns, excluding their Eu/Eu*, but do not specifically address their genesis. Figure D7a indicates that these three diogenites, especially MIL 07001, have trace element characteristics that suggest they may be cumulates plus trapped melt, but that their parent magma did not assimilate crustal melts. MET 00425 is the most magnesian diogenite (Barrat et al. 2008;

Mittlefehldt 2002), and because of its high mg#, it cannot easily be fit into any generalized model for diogenite genesis.

The expected inverse relationship between Eu/Eu* and La/Sm is not observed, however (Fig. D7b). Many of those diogenites with the lowest Eu/Eu* and highest Gd/Lu (Fig. D7a) have among the lowest La/Sm, and if any relationship is present, it is an increase in Eu/Eu* with increasing La/Sm (Fig. D7b). Cumulates formed from contaminated magmas à la Barrat et al. (2010), regardless of whether they contain a trapped melt component, ought to exhibit a distribution on Figure D7b similar to that in Figure D7a. We find little compelling evidence that a substantial number of diogenites were formed from remelted cumulates, or that contamination of diogenitic precursor magmas by partial melts of the basaltic crust was a common process. Nevertheless, the very low Eu/Eu* for some leached diogenites is an anomaly that does not obviously fit in to the common model of formation of diogenites as cumulates from a Vestan magma ocean.

Mittlefehldt (1994) first demonstrated that the major element concentrations of diogenites are decoupled from their trace element concentrations. He further demonstrated that mineral equilibration temperatures for diogenites are several hundred degrees below plausible magmatic crystallization temperatures. Following Lambert and Simmons (1987), Mittlefehldt (1994) posited that the decoupling of Fe-Mg from Al, Sc, Ti and REE was due to differences in mean diffusion distance for Fe-Mg exchange compared to those for minor and trace elements. In this scenario, diffusion homogenizes the orthopyroxene mg# but leaves igneous-derived variation in incompatible lithophile elements (Al, etc.) largely unaffected.

Cherniak and Liang (2007) have studied REE diffusion in natural enstatite in air and in seal capsules buffered at iron-wüstite (IW). They found that diffusion of Gd did not change with oxygen fugacity, whereas Eu diffusion was more than an order of magnitude faster at IW than in air. Cherniak and Liang (2007) concluded that Eu^{2+} diffusion in pyroxene is faster than for Eu^{3+}. This suggests that a possible alternative to the Barrat et al. hypothesis for generating low Eu/Eu* in diogenite is that subsolidus diffusive exchange permitted equilibration of Eu^{2+} between orthopyroxene and accessory phases such as plagioclase or phosphate, while Eu^{3+} more closely retains its original igneous distribution. The leaching procedure of Barrat et al. (2010) must have removed much or all of the Eu-rich phase, which as they noted, implies that it is a phosphate.

One condition that must be met in order for this mechanism to work is that $D^{phos/opx}{}_{Eu}2+$ must increase with falling temperature. This will favor transport of Eu^{2+} out of orthopyroxene into the phosphate. We know of no experimental study of the effects of temperature on $D^{phos/opx}$, however it is plausible that this partition coefficient would have increased with falling temperature in diogenite plutons. Orthopyroxene/melt REE partition coefficients are directly correlated with D_{Ca} (e.g. Jones 1995). This is understandable because the larger Ca^{2+} ion distorts the pyroxene M2 site, making it more favorable for incorporation of the REE. At lower temperature, orthopyroxene can contain less Ca than at higher temperature (c.f. the two-pyroxene thermometer of Lindsley and Anderson 1983), implying that Eu^{2+} would also be excluded at lower T. In contrast, Ca phosphates are favorable hosts for REE. Merrilite (whitlockite)/melt partition coefficients are >1 for REE and Sr (Dickinson and Hess 1983), and Ca phosphates in

diogenites are highly enriched in REE (Domanik et al. 2004, 2005; Mittlefehldt 1994). It is thus very likely that with decreasing T, $D^{phos/opx}$ for Eu^{2+} will increase.

Figure D6 shows our analyses of GRA 98108 along with the leached diogenites of Barrat et al. (2010). Our samples were untreated by mineral acids and any phosphates they may have contained were included in the analyzed samples. The GRA 98108 sample analyzed by ICP-MS has a very low Eu/Eu*, and plots very near the orthopyroxene cumulate line using the Sr (as an analog for Eu^{2+}) partition coefficient. GRA 98108 contains a modest amount of olivine – 18.5 vol% in the thin section studied by Beck and McSween (2010) – but this will not greatly affect the ratio of Eu (or Sr) to Gd in the cumulate because of the very low partition coefficients for olivine (c.f. McKay 1986). GRA 98108 is plagioclase-bearing, but Beck and McSween (2010) measured only 0.3 vol% in their thin section. The bulk samples we have analyzed are low in plagioclase as indicated by the low Na and Al contents (Tables D6-8; Fig. D3). However, GRA 98108 is heterogeneous in its olivine and orthopyroxene distribution (see Fig. 1 of Righter 2001), and plagioclase may be heterogeneously distributed on the cm-scale. In the thin section studied here (,15), plagioclase is not uniformly distributed; instead it is concentrated along the margin between an olivine-rich region and an orthopyroxene-rich region. Thus, either under- or over-sampling of plagioclase relative to that of a true "bulk rock" sample could easily occur. Our INAA sample has higher Na and Eu contents than the ICP-MS samples (Tables D7, D8) indicating a greater plagioclase content in the former. The INAA sample plots in the region of cumulate plus trapped melt on Figure D6. (To plot the INAA sample, the Gd concentration was calculated by interpolation of the REE pattern.) Our GRA 98108 data are consistent with subsolidus diffusion of Eu^{2+}

from orthopyroxene to plagioclase as engendering the very low Eu/Gd ratio in the ICP-MS sample, which under-sampled plagioclase.

Barrat et al. (2010) considered the low Eu/Eu* of their leaching residues to be innate to the orthopyroxene cumulate and thus can be used to infer magma compositions. Following Treiman (1996), we consider the low Eu/Eu* of the leaching residues to represent orthopyroxene that equilibrated with Ca phosphate (and/or plagioclase) at low, subsolidus temperatures. In particular, our hypothesis is that because of the more rapid diffusion of Eu^{2+} relative to Eu^{3+} (Cherniak and Liang 2007), the Eu/Eu* of orthopyroxene was lowered by this mechanism. A corrolary is that the leaching residues cannot be used as a guide to diogenite parent magma compositions.

5.0 CONCLUSIONS

Two brecciated diogenites, ALH 85015 and PCA 02008, stand out has having higher contents of the major elements Al_2O_3 and CaO compared to most diogenites, and have higher incompatible trace lithophile element contents than typically observed for diogenites. These breccias also contain small amounts of basaltic (eucritic) debris. Mafic debris is also present in PCA 02017, a suggested pair of PCA 02008. Pyroxene compositions in mafic clasts in PCA 02017 have compositions similar to those of cumulate eucrites (mg# 54-55) and basaltic eucrites (mg# 35-39), but some are more ferroan than found in eucrites (mg# 28). These diogenites are polymict breccias, and the unusual compositional characteristics of them are due to contamination by mafic lithologies.

QUE 93009 is an unusual diogenite that has pyroxene compositions at the ferroan end of the diogenite range, contains coarse-grained norititc clasts, and has chromite grains with ilmenite exsolution lamellae. No basaltic material is present in this breccia. QUE 93009 is enriched in incompatible lithophile elements. QUE 93009 shares some petrologic and compositional characteristics with the Yamato Type B diogenites, although there are distinctions as well. QUE 93009 is possibly a transitional rock type between classic, magnesian diogenites and magnesian cumulate eucrites, such as the cumulate component of the Binda polymict cumulate eucrite.

LEW 88679 is anomalously depleted in the most highly incompatible elements (Nb, LREE, Ta, Th, U) relative to elements that are not as highly incompatible (Y, Zr, Yb, Lu, Hf) when compared to most diogenites. It is unlikely that this is caused by a lower trapped melt component in LEW 88679 compared to most diogenites. LEW 88679 is a dimict breccia composed of more magnesian harzburgite and more ferroan orthopyroxenite (Beck and McSween 2010). It is unlikely that the two components of LEW 88679 would both be atypically poor in trapped melt compared to most diogenites. A plausible explanation is that mobilization of the incompatible lithophile elements occurred after assembly of the breccia.

The very low Eu/Eu* ratios of diogenite orthopyroxenes (acid-washed bulk samples) has been cited as evidence that mixing of diogenite parent magmas with low-degree melts of the basaltic crust occurred (Barrat et al. 2010). We find that this interpretation is not compelling. Subsolidus equilibration has mobilized major elements in orthopyroxenes resulting in Fe-Mg exchange (Mittlefehldt 1994). This process may have caused exchange of Eu^{2+} over greater distances than for Sm, Eu^{3+} or Gd because of

the much higher diffusion coefficient of the former (Cherniak and Liang 2007). Exchange of Eu^{2+} between REE-poor orthopyroxene and REE-rich phosphate during equilibration on the parent asteroid, followed by laboratory dissolution of phosphates prior to analysis, would result in at residue with a Eu/Eu* much lower than that of the original cumulate. Remembering past cautions (Treiman 1996), we suggest that leached diogenite samples cannot be used to infer parent magma compositions or constrain the processes by which they were formed.

ACKNOWLEDGMENTS

We thank the National Science Foundation for funding the ANSMET collecting teams that brought back the Antarctic samples studied here, and the Meteorite Working Group, NASA-Johnson Space Center and the National Museum of Natural History (Smithsonian Institution) for allocation of the samples. We thank K. J. Domanik and M. J. Drake of the University of Arizona for providing the sample of Bilanga studied here. This work was funded through the NASA Cosmochemistry Program to DWM and Cosmochemistry grant NNG06GG36G to HYM.

REFERENCES

Barrat J. A., Gillet Ph., Lesourd M., Blichert-Toft J., and Poupeau G. R. 1999. The Tatahouine diogenite: mineralogical and chemical effects of sixty-three years of terrestrial residence. *Meteoritics & Planetary Science* 34:91–97.

Barrat J. A., Yamaguchi A., Greenwood R. C., Bohn M., Benoit M., and Franchi I. A. 2007. The Stannern trend eucrites: Contamination of main group eucritic magmas by crustal partial melts. *Geochimica et Cosmochimica Acta* 71:4108-4124.

Barrat J. A., Yamaguchi A., Benoit M., and Bohn M. 2008. Geochemistry of diogenites: still more diversity in their parental melts. *Meteoritics & Planetary Science* 43:1759–1775.

Barrat J.-A., Yamaguchi A., Zanda B., Bollinger C., and Bohn M. 2010. Relative chronology of crust formation on asteroid Vesta: Insights from the geochemistry of diogenites. *Geochimica et Cosmochimica Acta* 74:6218–6231.

Beck A. W., and McSween H. Y. 2010. Diogenites as polymict breccias composed of orthopyroxenite and harzburgite. *Meteoritics & Planetary Science* **45**:850-872, doi: 10.1111/j.1945-5100.2010.01061.x.

Beck A. W., McSween H. Y., Mittlefehldt D. W., and Lee C.-T. A. 2008. Fused bead analysis in diogenite meteorites (abstract# 1177). 40th Lunar and Planetary Science Conference. CD-ROM.

Beck A.W., Mittlefehldt D.W., McSween H.Y. Jr., Rumble D., Lee C.-T. A., and Bodnar R.J. 2011. MIL 03443, a Dunite from Asteroid 4 Vesta: Evidence for its Classification and Cumulate Origin. *Meteoritics & Planetary Science*, accepted.

Bédard J.H. 2007. Trace element partitioning coefficients between silicate melts and orthopyroxene: Parameterizations of D variations. *Chemical Geology* **244**:263–303.

Berkley J.L., and Boynton N.J. 1992. Minor/major element variation within and among diogenite and howardite orthopyroxenite groups. *Meteoritics* **27**:387-394.

Binzel R. P., and Xu S. 1993. Chips off asteroid 4 Vesta: Evidence for the parent body of basaltic achondrite meteorites. *Science* **260**:186-191.

Bowman L. E., Papike J. J., and Spilde M. N. 1999. Diogenites as asteroidal cumulates: Insights from spinel chemistry. *American Mineralogist* **84**:1020-1026.

Brown R. W. 1977. A sample fusion technique for whole rock analysis with the electron microprobe. *Geochimica et Cosmochimica Acta* **41**:435-438.

Cherniak D. J., and Liang Y. 2007. Rare earth element diffusion in natural enstatite. *Geochimica et Cosmochimica Acta* **71:**1324–1340.

Consolmagno G.J. 1979. REE patterns versus the origin of the basaltic achondrites. *Icarus* **40**:522-530.

Consolmagno G.J., and Drake M.J. 1977. Composition and evolution of the eucrite parent body: evidence from rare earth elements. *Geochimica et Cosmochimica Acta* **41**:1271-1282.

Delaney J.S., Takeda H., Prinz M., Nehru C.E., and Harlow G.E. 1983. The nomenclature of polymict basaltic achondrites. *Meteoritics* **18**:103-111.

Delaney J.S., Prinz M., and Takeda H. 1984. The polymict eucrites. Proceedings, 15th Lunar and Planetary Science Conference, Part 1, Journal of Geophysical Research, Supplement 89:C251-C288.

Dickinson J. E., and Hess P. C. 1983. Role of whitlockite and apatite in lunar felsites (abstract). 14th Lunar and Planetary Science Conference, 158-159.

Domanik K., Kolar S., Musselwhite D., and Drake M.J. 2004. Accessory silicate mineral assemblages in the Bilanga diogenite: A petrographic study. *Meteoritics & Planetary Science* **39**:567-579.

Domanik K. J., Sideras L. C., and Drake M.J. 2005. Olivine and Ca-phosphate in the diogenites Manegaon and Roda (abstract #2128). 36th Lunar and Planetary Science Conference. CD-ROM.

Drake M.J. 1979. Geochemical evolution of the eucrite parent body: Possible nature and evolution of asteroid 4 Vesta. In *Asteroids* ,edited by Gehrels T. Tucson: The University of Arizona Press. Pp. 765-782.

Duke M.B., and Silver L.T. 1967. Petrology of eucrites, howardites and mesosiderites. *Geochimica et Cosmochimica Acta* **31**:1637-1665.

Drake M.J., and Weill D.F. 1975. Partition of Sr, Ba, Ca, Y, Eu^{2+}, Eu^{3+}, and other REE between plagioclase feldspar and magmatic liquid: an experimental study. *Geochimica et Cosmochimica Acta* **39**:689-712.

Eggins S.M., Woodhead J.D., Kinsley L.P.J., Mortimer G.E., Sylvester P., McCulloch M.T., Hergt J.M., and Handler M.R. 1997. A simple method for the precise determinations of ≥40 trace elements in geological samples by ICPMS using enriched isotope internal standardisation. *Chemical Geology* **134**:311-326.

Fowler G.W., Papike J.J., Spilde M.N., and Shearer C.K. 1994. Diogenites as asteroidal cumulates: Insights from orthopyroxene major and minor element chemistry. *Geochimica et Cosmochimica Acta* **58**:3921-3929.

Fowler G.W., Shearer C.K., Papike J.J., and Layne G.D. 1995. Diogenites as asteroidal cumulates: Insights from orthopyroxene trace element chemistry. *Geochimica et Cosmochimica Acta* **59**:3071-3084.

Fukuoka T., Boynton W.V., Ma M.-S., and Schmitt R.A. 1977. Genesis of howardites, diogenites, and eucrites. Proceedings, 8th Lunar Science Conference. pp. 187-210.

Gooley R.C. (1972) Chemistry and mineralogy of the diogenites. Ph.D. dissertation, Arizona State University, Tempe, AZ, USA.

Greenwood R. C., Franchi I. A., Jambon A., and Buchanan P. C. 2005. Widespread magma oceans on asteroidal bodies in the early Solar System. *Nature* **435**:916-918.

Jones J.H. 1995. Experimental trace element partitioning. In *Rock Physics and Phase Relations. A Handbook of Physical Constants, AGU Reference Shelf 3*, edited by Ahrens T.J. Washington: The American Geophysical Union. Pp. 73-104.

Keil K. 2002. Geological history of asteroid 4 Vesta: The "smallest terrestrial planet." In *Asteroids III*, edited by Bottke W., Cellino A., Paolicchoi P., and Binzel R.P. Tucson: The University of Arizona Press. Pp. 573-584.

Lambert D. D., and Simmons E. C. 1987. Magma evolution in the Stillwater complex, Montana: I. Rare-earth element evidence for the formation of the ultramafic series. *American Journal of Science* **287**:1-32.

Lindsley D. H., and Anderson D. J. 1983. A two-pyroxene thermometer. Proceedings, 13th Lunar and Planetary Science Conference, Part 2, Journal of Geophysical Research, Supplement **88**:A887-A906.

Lindstrom D.J., and Korotev R.L. 1982. TEABAGS: computer programs for instrumental neutron activation analysis. *Journal of Radioanalytical Chemistry* **70**:439-458.

McCord T.B., Adams J.B., and Johnson T.V. 1970. Asteroid Vesta: Spectral reflectivity and compositional implications. *Science* **168**:1445-1447.

McKay G.A. 1986. Crystal/liquid partitioning of REE in basaltic systems: Extreme fractionation of REE in olivine. *Geochimica et Cosmochimica Acta* **50**:69-79.

McKay G., Wagstaff J., and Le L. 1990. REE distribution coefficients for pigeonite: Constraints on the origin of the mare basalt europium anomaly (abstract). 21st Lunar and Planetary Science Conference, 773-774.

McSween H., Mittlefehldt D., Beck A., Mayne R., and McCoy T. 2011. HED Meteorites and Their Relationship to the Geology of Vesta and the Dawn Mission. *Space Science Reviews*, doi:10.1007/s11214-010-9637-z.

Mittlefehldt D.W. 1979. Petrographic and chemical characterization of igneous lithic clasts from mesosiderites and howardites and comparison with eucrites and diogenites. *Geochimica et Cosmochimica Acta* **43**:1917-1935.

Mittlefehldt D.W. 1994. The genesis of diogenites and HED parent body petrogenesis. *Geochimica et Cosmochimica Acta* **58**:1537-1552.

Mittlefehldt D.W. 2000. Petrology and geochemistry of the Elephant Moraine A79002 diogenite; a genomict breccia containing a magnesian harzburgite component. *Meteoritics & Planetary Science* **35**:901-912.

Mittlefehldt D.W. 2002. Geochemistry of new, unusual diogenites and constraints on diogenite genesis (abstract). *Meteoritics & Planetary Science* **37**:A100.

Mittlefehldt D.W., and Lindstrom M.M. 1991. Generation of abnormal trace element abundances in Antarctic eucrites by weathering processes. *Geochimica et Cosmochimica Acta* **55**:77-87.

Mittlefehldt D.W., and Lindstrom M.M. 1993. Geochemistry and petrology of a suite of ten Yamato HED meteorites. *Antarctic Meteorite Research* **6**:268-292.

Mittlefehldt D.W., and Lindstrom M.M. 2001. Petrology and geochemistry of Patuxent Range 91501, an impact melt from the L chondrite parent body, and Lewis Cliff 88663, an L7 chondrite. *Meteoritics & Planetary Science* **36**:439-457.

Mittlefehldt D.W., and Lindstrom M.M. 2003. Geochemistry of eucrites: Genesis of basaltic eucrites, and Hf and Ta as petrogenetic indicators for altered antarctic eucrites. *Geochimica et Cosmochimica Acta* **67**:1911-1935.

Mittlefehldt D.W., Beck A.W., Lee C.-T.A., and McSween H.Y. Jr. 2009. Chemistry of diogenites and evolution of their parent asteroid (abstract #1038). 40th Lunar and Planetary Science Conference.

Papike J.J., Shearer C.K., Spilde M.N., and Karner J.M. 2000. Metamorphic diogenite Grosvenor Mountains 95555: Mineral chemistry of orthopyroxene and spinel and comparisons to the diogenite suite. *Meteoritics & Planetary Science* **35**:875-879.

Righter K. 2001. Petrography, mineralogy and petrology of two new HED meteorites: Diogenite GRA98108 and howardite GRA98030 (abstract #1765). 32nd Lunar and Planetary Science Conference.

Righter K., and Drake M. J. 1997. A magma ocean on Vesta: Core formation and petrogenesis of eucrites and diogenites. *Meteoritics & Planetary Science* **32**:929-944.

Ruzicka A., Snyder G. A., and Taylor L. A. 1997. Vesta as the howardite, eucrite and diogenite parent body: Implications for the size of a core and for large-scale differentiation. *Meteoritics & Planetary Science* **32**:825-840.

Sack R.O., Azeredo W.J., and Lipschutz M.E. 1991. Olivine diogenites: The mantle of the eucrite parent body. *Geochimica et Cosmochimica Acta* **55**:1111-1120.

Schwandt C.S., and McKay G.A. 1998. Rare earth element partition coefficients from enstatite/melt synthesis experiments. *Geochimica et Cosmochimica Acta* **62**:2845-2848.

Shearer C.K., Fowler G.W., and Papike J.J. 1997. Petrogenetic models for magmatism on the eucrite parent body: Evidence from orthopyroxene in diogenites. *Meteoritics & Planetary Science* **32**:877-889.

Shearer C. K., Burger P., and Papike J. J. 2010. Petrogenetic relationships between diogenites and olivine diogenites: Implications for magmatism on the HED parent body. *Geochimica et Cosmochimica Acta* **74**:4865-4880.

Stolper E. 1977. Experimental petrology of eucrite meteorites. *Geochimica et Cosmochimica Acta* **41**:587-611.

Takeda H., and Mori H. 1985. The diogenite-eucrite links and the crystallization history of a crust of their parent body. Proceedings, 15th Lunar and Planetary Science Conference, Part 2, Journal of Geophysical Research, Supplement **90**:C636-C648.

Takeda H., Miyamoto M., Ishii T., and Reid A.M. 1976. Characterization of crust formation on a parent body of achondrites and the moon by pyroxene crystallography and chemistry. Proceedings, 7th Lunar Science Conference. pp. 3535-3548.

Treiman A. H. 1996. The perils of partition: Difficulties in retrieving magma compositions from chemically equilibrated basaltic meteorites. *Geochimica et Cosmochimica Acta* **60**:147-155.

Warren P.H. 1985. Origin of howardites, diogenites and eucrites: A mass balance constraint. *Geochimica et Cosmochimica Acta* **49**:577-586.

Warren P.H. 1997. Magnesium oxide-iron oxide mass balance constraints and a more detailed model for the relationship between eucrites and diogenites. *Meteoritics & Planetary Science* **32**:945-963.

Warren P. H., Kallemeyn G. W., Huber H., Ulff-Møller F., and Choe W. 2009. Siderophile and other geochemical constraints on mixing relationships among HED-meteoritic breccias. *Geochimica et Cosmochimica Acta* **73**: 5918–5943.

Welten K.C., Caffee M.W., and Beck A.W. 2009. Cosmogenic radionuclides in three paired howardites and a polymict diogenite from Pecora Escarpment Icefield, Antarctica (abstract). *Meteoritics & Planetary Science* **44**:A216.

Appendix D

Table D1. Details of samples studied.

Meteorite	specific	mass received (mg)	type	remarks[†]
ALHA77256	,158	483	wr	olivine diogenite (1); harzburgitic diogenite (2)
ALH 85015	,7	383	wr	polymict diogenite (2)
Bilanga	UA1911,3f,3	644	wr	fall
EET 83246	,26	485	wr	polymict diogenite (2)
EET 83247	,20	40	opx	
EET 83247	,21	18	opx	
GRA 98108	,11	243	wr	harzburgitic diogenite (2)
GRA 98108	,22	540	wr	
GRO 95555	,10	527	wr	unbrecciated, metamorphic (3)
GRO 95555	,17	640	wr	
LAP 03979	,6	390	wr	polymict diogenite (2)
LAP 91900	,9	680	opx	
LAP 91900	,10	560	wr	
LAP 91900	,29	420	wr	
LEW 88008	,18	607	wr	polymict diogenite (2)
LEW 88679	,6	120	brec	polymict diogenite (2)
LEW 88679	,6		opx	
LEW 88679	,10	395	wr	
MET 00422	,6	1074	wr	
MET 00424	,10	1150	wr	
MET 00425	,6	1253	wr	
MET 00436	,9	1080	wr	
MET 00436	,13	840	wr	
MET 001060	,4	525	wr	
MET 01084	,8	368	wr	polymict diogenite (2)
MIL 03368	,10	613	wr	polymict diogenite (2)
PCA 91077	,4	311	wr	
PCA 02008	,6	540	wr	paired with PCA 02009 howardite (4); polymict diogenite (2)
QUE 93009	,8	270	opx	
QUE 93009	,8		wr	

[†]references:

1. Sack et al. (1991)
2. Beck and McSween (2010)
3. Papike et al. (2000)
4. Welten et al. (2009)

Table D2. Representative pyroxene compositions of diogenites determined by EMPA.

Meteorite	ALHA 77256	ALHA 77256	GRA 98108	GRA 98108	GRO 95555	LAP 91900	LEW 88011	LEW 88011	LEW 88011	LEW 88011	LEW 88011	LEW 88011
specific	,154	,155	,16	,16	,21	,9	,4	,4	,4	,4	,4	,4
SiO_2	54.2	52.4	54.6	52.8	54.4	54.2	54.5	53.9	53.7	53.2	52.9	53.4
TiO_2	0.114	0.281	0.155	0.263	0.064	0.056	0.104	0.130	0.222	0.228	0.414	0.348
Al_2O_3	0.794	1.617	0.862	1.344	0.565	0.588	0.923	1.026	1.005	0.939	1.124	1.087
Cr_2O_3	0.853	0.738	0.384	0.693	0.800	0.647	0.844	0.755	0.745	0.562	0.871	0.393
FeO	15.2	5.6	14.3	5.4	15.4	15.7	15.1	16.2	16.9	19.1	7.3	6.1
MnO	0.533	0.279	0.511	0.274	0.501	0.557	0.469	0.502	0.554	0.638	0.325	0.270
MgO	27.3	16.2	27.0	16.2	26.9	27.0	27.2	26.2	25.3	23.4	15.6	16.2
CaO	0.793	22.336	1.822	22.330	1.051	1.133	1.169	1.327	1.932	2.036	21.468	22.288
sum	99.787	99.451	99.634	99.304	99.681	99.881	100.309	100.040	100.358	100.103	100.002	100.086
						molar quantities						
Fe/Mn	28.1	20.0	27.6	19.6	30.3	27.9	31.7	31.8	30.1	29.5	22.3	22.2
Fe/Mg	0.312	0.196	0.296	0.188	0.322	0.327	0.311	0.346	0.374	0.457	0.264	0.211
mg#	76.2	83.6	77.2	84.2	75.7	75.4	76.3	74.3	72.8	68.6	79.1	82.6
Wo %	1.57	45.35	3.60	45.44	2.08	2.22	2.30	2.63	3.84	4.11	43.95	44.99
En %	75.04	45.70	74.38	45.93	74.09	73.68	74.52	72.33	69.97	65.80	44.34	45.44
Fs %	23.39	8.95	22.02	8.63	23.82	24.10	23.17	25.04	26.19	30.09	11.71	9.57
						atoms per 6 oxygens						
Si	1.9638	1.9414	1.9726	1.9545	1.9747	1.9668	1.9636	1.9582	1.9548	1.9625	1.9579	1.9649
Ti	0.0031	0.0078	0.0042	0.0073	0.0017	0.0015	0.0028	0.0036	0.0061	0.0063	0.0115	0.0096
Al	0.0339	0.0706	0.0367	0.0586	0.0242	0.0251	0.0392	0.0439	0.0431	0.0408	0.0491	0.0471
Cr	0.0244	0.0216	0.0110	0.0203	0.0229	0.0186	0.0240	0.0217	0.0215	0.0164	0.0255	0.0114
Fe	0.4591	0.1749	0.4314	0.1682	0.4672	0.4774	0.4537	0.4914	0.5143	0.5887	0.2272	0.1869
Mn	0.0164	0.0088	0.0157	0.0086	0.0154	0.0171	0.0143	0.0154	0.0171	0.0199	0.0102	0.0084
Mg	1.4726	0.8933	1.4571	0.8952	1.4530	1.4593	1.4592	1.4196	1.3738	1.2874	0.8598	0.8875
Ca	0.0308	0.8864	0.0706	0.8858	0.0409	0.0440	0.0451	0.0516	0.0754	0.0805	0.8522	0.8788

Table D2 (continued). Representative pyroxene compositions of diogenites determined by EMPA.

Meteorite	LEW 88679	LEW 88679	MET 001060	MET 00422	MET 00424	MET 00425	MET 00436	MET 00855	MET 01084	MET 01084
specific	,6	,5	,7	,9	,14	,10	,15	,6	,6	,6
SiO_2	54.1	54.1	55.7	54.1	53.9	56.0	54.0	54.7	54.9	54.1
TiO_2	0.193	0.178	0.058	0.043	0.019	0.027	0.021	0.029	0.177	0.250
Al_2O_3	1.230	1.141	0.436	0.487	0.274	0.421	0.249	0.304	0.935	0.616
Cr_2O_3	0.424	0.612	0.310	0.587	0.302	0.698	0.167	0.200	0.629	0.340
FeO	15.7	17.2	13.7	16.7	18.3	10.7	18.3	18.6	14.6	18.4
MnO	0.549	0.609	0.592	0.578	0.696	0.364	0.677	0.722	0.496	0.653
MgO	26.7	24.8	29.1	26.4	25.5	31.2	25.6	25.3	27.8	25.0
CaO	1.681	2.040	0.637	0.936	0.751	0.498	0.785	0.819	1.161	1.242
sum	100.577	100.680	100.533	99.831	99.742	99.908	99.799	100.674	100.698	100.601
					molar quantities					
Fe/Mn	28.2	27.9	22.9	28.5	26.0	29.0	26.7	25.5	29.1	27.9
Fe/Mg	0.330	0.390	0.264	0.354	0.404	0.193	0.402	0.413	0.296	0.414
mg#	75.2	71.9	79.1	73.9	71.3	83.9	71.3	70.8	77.2	70.7
Wo %	3.30	4.09	1.23	1.85	1.49	0.95	1.55	1.62	2.27	2.46
En %	72.72	69.00	78.13	72.51	70.19	83.06	70.21	69.63	75.44	68.98
Fs %	23.99	26.91	20.65	25.65	28.32	15.99	28.24	28.76	22.29	28.56
					atoms per 6 oxygens					
Si	1.9529	1.9648	1.9807	1.9717	1.9794	1.9776	1.9815	1.9882	1.9641	1.9720
Ti	0.0052	0.0049	0.0016	0.0012	0.0005	0.0007	0.0006	0.0008	0.0048	0.0068
Al	0.0523	0.0488	0.0183	0.0209	0.0119	0.0175	0.0108	0.0130	0.0394	0.0264
Cr	0.0121	0.0176	0.0087	0.0169	0.0088	0.0195	0.0048	0.0057	0.0178	0.0098
Fe	0.4726	0.5227	0.4082	0.5077	0.5629	0.3161	0.5623	0.5670	0.4373	0.5620
Mn	0.0168	0.0187	0.0178	0.0178	0.0217	0.0109	0.0211	0.0222	0.0150	0.0201
Mg	1.4328	1.3403	1.5447	1.4354	1.3951	1.6419	1.3981	1.3727	1.4798	1.3574
Ca	0.0650	0.0794	0.0243	0.0365	0.0295	0.0189	0.0309	0.0319	0.0445	0.0485

Table D2 (continued). Representative pyroxene compositions of diogenites determined by EMPA.

Meteorite	PCA 02017	PCA 02017	PCA 02017	PCA 02017	PCA 02017	PCA 02017	PCA 02017	PCA 02017	PCA 02017	QUE 93009	QUE 93009
specific	,4	,4	,4*	,4*	,4*	,4*	,4*	,4*	,4	,9	,9
SiO_2	55.2	54.2	51.4	53.1	51.3	49.3	48.1	48.7	52.5	52.9	54.1
TiO_2	0.099	0.091	0.338	0.007	0.508	0.493	0.686	0.796	0.003	0.299	0.214
Al_2O_3	0.793	0.733	0.682	0.567	1.069	1.051	0.963	1.285	0.824	0.978	0.382
Cr_2O_3	0.760	0.654	0.257	0.381	0.600	0.413	0.357	0.303	0.495	0.360	0.342
FeO	14.5	16.4	27.1	22.1	24.4	27.9	32.3	27.6	10.9	18.1	6.2
MnO	0.500	0.584	0.900	0.964	0.815	0.908	1.006	1.061	0.576	0.602	0.269
MgO	27.9	26.5	18.1	21.6	17.0	10.2	6.9	8.2	15.1	24.5	16.7
CaO	1.018	1.289	1.354	1.765	5.567	9.633	9.759	11.979	19.589	1.937	22.001
sum	100.770	100.451	100.131	100.484	101.259	99.898	100.071	99.924	99.987	99.676	100.208
					molar quantities						
Fe/Mn	28.6	27.8	29.7	22.6	29.6	30.3	31.7	25.7	18.7	29.6	22.8
Fe/Mg	0.291	0.347	0.842	0.574	0.808	1.533	2.614	1.886	0.406	0.414	0.209
mg#	77.5	74.2	54.3	63.5	55.3	39.5	27.7	34.7	71.1	70.7	82.7
Wo %	1.99	2.53	2.84	3.60	11.54	21.14	21.86	26.62	39.94	3.86	43.94
En %	75.91	72.34	52.74	61.24	48.94	31.13	21.62	25.43	42.72	68.01	46.36
Fs %	22.10	25.13	44.42	35.16	39.52	47.73	56.52	47.95	17.34	28.13	9.69
					atoms per 6 oxygens						
Si	1.9693	1.9617	1.9690	1.9784	1.9434	1.9549	1.9494	1.9433	1.9670	1.9518	1.9858
Ti	0.0027	0.0025	0.0097	0.0002	0.0145	0.0147	0.0209	0.0239	0.0001	0.0083	0.0059
Al	0.0334	0.0313	0.0308	0.0249	0.0478	0.0491	0.0460	0.0605	0.0364	0.0425	0.0165
Cr	0.0214	0.0187	0.0078	0.0112	0.0180	0.0130	0.0114	0.0096	0.0147	0.0105	0.0099
Fe	0.4330	0.4973	0.8686	0.6884	0.7744	0.9246	1.0957	0.9229	0.3417	0.5574	0.1908
Mn	0.0151	0.0179	0.0292	0.0304	0.0262	0.0305	0.0345	0.0359	0.0183	0.0188	0.0084
Mg	1.4869	1.4315	1.0312	1.1993	0.9589	0.6030	0.4192	0.4895	0.8419	1.3475	0.9127
Ca	0.0389	0.0500	0.0556	0.0705	0.2262	0.4095	0.4238	0.5123	0.7871	0.0766	0.8650

*Pyroxenes from mafic clasts.

Table D3. Representative chromite and ilmenite compositions determined by EMPA.

Meteorite	ALHA 77256	ALHA 77256	GRA 98108	GRA 98108	GRO 95555	LEW 88011	LEW 88011	LEW 88679	LEW 88679	MET 00422	MET 00422
specific	,155	,155	,16	,16	,21	,4	,4	,5	,5	,9	,9
TiO_2	0.751	0.752	1.129	1.232	0.688	2.196	1.347	1.272	0.856	0.435	0.381
SiO_2	0.000	0.014	0.000	0.017	0.001	0.016	0.050	0.009	0.036	0.000	0.000
Cr_2O_3	46.1	46.1	52.5	47.9	56.9	52.5	50.5	46.5	47.9	60.4	59.2
Al_2O_3	21.4	21.2	15.1	16.2	9.0	10.3	13.4	17.5	15.7	8.9	8.9
V_2O_3*	0.251	0.246	0.377	0.740	0.574	0.496	0.450	0.463	0.480	0.398	0.389
FeO†	26.2	25.5	25.9	29.3	27.7	31.1	30.5	30.6	30.9	28.7	29.7
MnO	0.410	0.410	0.447	0.570	0.711	0.468	0.456	0.570	0.594	0.482	0.500
MgO	6.10	6.67	5.76	4.81	4.58	2.88	3.21	4.05	3.68	2.69	2.12
CaO	0.022	0.053	0.020	0.056	0.005	0.007	0.012	0.018	0.084	0.001	0.014
sum	101.234	100.945	101.233	100.825	100.159	99.963	99.925	100.982	100.230	102.006	101.204
					molar quantities						
Fe/Mn	63.1	61.3	57.1	50.8	38.5	65.6	65.9	52.9	51.4	58.9	58.7
mg#	29.3	31.8	28.4	22.6	22.7	14.2	15.8	19.1	17.5	14.3	11.3
cr#	59.0	59.3	70.0	66.5	80.9	77.4	71.7	64.0	67.2	82.0	81.7
					atoms per 4 oxygens (chromite) or 3 oxygens (ilmenite)						
Ti	0.0180	0.0181	0.0279	0.0308	0.0179	0.0574	0.0347	0.0317	0.0217	0.0112	0.0099
Si	0.0000	0.0004	0.0000	0.0006	0.0000	0.0006	0.0017	0.0003	0.0012	0.0000	0.0000
Cr	1.1623	1.1642	1.3642	1.2582	1.5551	1.4429	1.3661	1.2179	1.2795	1.6336	1.6226
Al	0.8066	0.7982	0.5839	0.6334	0.3665	0.4213	0.5402	0.6847	0.6245	0.3577	0.3629
V	0.0064	0.0063	0.0099	0.0197	0.0159	0.0138	0.0124	0.0123	0.0130	0.0109	0.0108
Fe^{2+}	0.6992	0.6797	0.7114	0.8143	0.8012	0.9038	0.8717	0.8471	0.8732	0.8232	0.8611
Mn	0.0111	0.0111	0.0125	0.0160	0.0208	0.0138	0.0132	0.0160	0.0170	0.0140	0.0147
Mg	0.2900	0.3173	0.2825	0.2381	0.2357	0.1492	0.1638	0.1999	0.1854	0.1370	0.1094
Ca	0.0008	0.0018	0.0007	0.0020	0.0002	0.0003	0.0004	0.0006	0.0030	0.0000	0.0005

*Vanadium corrected for Ti K_β interference.
†All Fe as FeO.

Table D3 (continued). Representative chromite and ilmenite compositions determined by EMPA.

Meteorite	MET 00424	MET 00424	MET 00425	MET 00425	MET 00436	QUE 93009	QUE 93009	QUE 93009	QUE 93009
specific	,14	,14	,10	,10	,15	,9	,9	,9	,9
TiO_2	0.315	0.166	0.200	0.176	0.411	0.847	1.052	0.515	52.0
SiO_2	0.000	0.000	0.000	0.000	0.000	0.000	0.010	0.026	0.093
Cr_2O_3	64.0	65.6	65.3	63.0	61.9	59.4	54.9	54.7	1.23
Al_2O_3	5.7	3.7	5.7	6.9	7.3	8.7	9.1	9.4	0.066
V_2O_3	0.491	0.412	0.214	0.213	0.495	0.299	0.566	0.536	0.004
FeO_T	27.7	28.3	24.8	26.5	28.8	29.8	32.4	31.5	43.6
MnO	0.582	0.538	0.456	0.477	0.553	0.499	0.607	0.588	0.979
MgO	3.05	2.31	4.93	3.78	2.44	2.01	1.84	2.01	2.90
CaO	0.007	0.021	0.007	0.015	0.003	0.005	0.025	0.021	0.105
sum	101.845	101.047	101.607	101.061	101.902	101.560	100.500	99.296	100.977
				molar quantities					
Fe/Mn	46.9	52.0	53.6	54.9	51.4	59.1	52.7	52.9	44.0
mg#	16.4	12.7	26.2	20.2	13.1	10.7	9.20	10.2	10.6
cr#	88.2	92.2	88.5	86.1	85.0	82.2	80.1	79.7	92.6
				atoms per 4 oxygens (chromite) or 3 oxygens (ilmenite)					
Ti	0.0082	0.0044	0.0052	0.0046	0.0107	0.0220	0.0278	0.0137	0.9640
Si	0.0000	0.0000	0.0000	0.0000	0.0000	0.0000	0.0004	0.0009	0.0023
Cr	1.7558	1.8404	1.7720	1.7238	1.6911	1.6228	1.5242	1.5340	0.0240
Al	0.2339	0.1561	0.2307	0.2795	0.2983	0.3526	0.3781	0.3916	0.0019
V	0.0137	0.0117	0.0059	0.0059	0.0137	0.0083	0.0159	0.0153	0.0001
Fe^{2+}	0.8033	0.8400	0.7108	0.7677	0.8322	0.8622	0.9512	0.9347	0.8985
Mn	0.0171	0.0162	0.0133	0.0140	0.0162	0.0146	0.0180	0.0177	0.0204
Mg	0.1577	0.1218	0.2524	0.1948	0.1255	0.1035	0.0964	0.1063	0.1066
Ca	0.0003	0.0008	0.0003	0.0006	0.0001	0.0002	0.0009	0.0008	0.0028

*Vanadium corrected for Ti K_β interference.
†All Fe as FeO.

Table D4. Representative olivine compositions in diogenites determined by EMPA.

Meteorite	ALHA 77256	GRA 98108	LEW 88679	PCA 02017
specific	,155	,16	,5	,4
SiO_2	37.9	38.0	38.1	38.2
TiO_2	0.002	0.006	0.019	0.008
Al_2O_3	0.004	0.012	0.072	0.015
Cr_2O_3	0.014	0.022	0.023	0.026
FeO	25.1	24.4	25.6	24.2
MnO	0.530	0.529	0.530	0.554
MgO	36.5	36.6	36.3	37.8
CaO	0.055	0.053	0.043	0.133
sum	100.105	99.622	100.687	100.936
		molar quantities		
Fe/Mn	46.8	45.5	47.6	43.2
Fe/Mg	0.386	0.373	0.396	0.360
mg#	72.1	72.8	71.7	73.5
		atoms per 4 oxygens		
Si	0.9988	1.0025	1.0006	0.9942
Ti	0.0000	0.0001	0.0004	0.0002
Al	0.0001	0.0004	0.0022	0.0005
Cr	0.0003	0.0005	0.0005	0.0005
Fe	0.5540	0.5384	0.5614	0.5276
Mn	0.0118	0.0118	0.0118	0.0122
Mg	1.4343	1.4417	1.4195	1.4664
Ca	0.0016	0.0015	0.0012	0.0037

Table D5. Representative plagioclase compositions determined by EMPA.

Meteorite	GRA 98108	LEW 88011	LEW 88011	LEW 88011	LEW 88011	LEW 88011	LEW 88011	LEW 88679	MET 01084	PCA 02017	PCA 02017	QUE 93009	QUE 93009	QUE 93009
specific	,15	,4*	,4*	,4*	,4	,4	,4	,5	,6	,4	,4	,9	,9	,9
SiO_2	46.1	50.1	48.4	51.4	46.8	46.3	48.8	44.9	44.5	44.8	46.0	46.0	45.6	47.1
Al_2O_3	34.6	32.4	33.4	31.8	34.3	34.7	33.1	35.6	35.2	35.1	34.6	34.6	35.0	34.0
FeO	0.084	0.165	0.133	0.127	0.148	0.179	0.300	0.126	0.134	0.540	0.308	0.030	0.194	0.101
MgO	0.003	0.070	0.054	0.066	0.054	0.035	0.086	0.000	0.019	0.022	0.007	0.000	0.000	0.002
CaO	17.7	15.5	16.6	14.8	17.3	17.8	16.1	18.6	18.7	18.5	18.2	17.8	18.2	17.0
Na_2O	1.37	2.35	1.90	2.71	1.43	1.19	1.87	0.861	0.810	0.823	1.12	1.34	1.10	1.76
K_2O	0.088	0.151	0.068	0.201	0.066	0.045	0.107	0.010	0.031	0.044	0.064	0.037	0.033	0.062
sum	99.945	100.736	100.555	101.104	100.098	100.249	100.363	100.097	99.394	99.829	100.299	99.807	100.127	100.025
							molar quantities							
An	87.26	77.71	82.53	74.21	86.67	89.02	82.12	92.23	92.55	92.33	89.65	87.89	89.93	83.92
Ab	12.22	21.39	17.07	24.59	12.94	10.71	17.23	7.72	7.27	7.41	9.98	11.89	9.88	15.72
Or	0.52	0.90	0.40	1.20	0.39	0.27	0.65	0.06	0.18	0.26	0.38	0.22	0.19	0.36
							atoms per 8 oxygens							
Si	2.1212	2.2696	2.2054	2.3121	2.1453	2.1229	2.2232	2.0677	2.0667	2.0741	2.1141	2.1198	2.0982	2.1621
Al	1.8783	1.7274	1.7902	1.6862	1.8549	1.8762	1.7755	1.9340	1.9295	1.9143	1.8747	1.8785	1.9003	1.8373
Fe	0.0032	0.0063	0.0051	0.0048	0.0057	0.0069	0.0114	0.0049	0.0052	0.0209	0.0118	0.0012	0.0075	0.0039
Mg	0.0002	0.0047	0.0037	0.0044	0.0037	0.0024	0.0058	0.0000	0.0013	0.0015	0.0005	0.0000	0.0000	0.0001
Ca	0.8729	0.7510	0.8095	0.7133	0.8521	0.8765	0.7874	0.9201	0.9284	0.9197	0.8956	0.8808	0.8955	0.8358
Na	0.1223	0.2067	0.1674	0.2363	0.1272	0.1054	0.1652	0.0770	0.0730	0.0738	0.0997	0.1192	0.0984	0.1566
K	0.0052	0.0087	0.0040	0.0115	0.0039	0.0026	0.0062	0.0006	0.0018	0.0026	0.0038	0.0022	0.0019	0.0036

*Most heterogeneous grain; first column is the average composition, second is most calcic analysis, third is most sodic analysis.

Table D6. Major and minor element concentrations on fused beads determined by LA-ICP-MS.

Meteorite	ALH 85015	ALHA 77256	EET 83246	GRA 98108	LAP 03979	LEW 88008	LEW 88679	MIL 03368	PCA 02008
split	,7	,158	,26	,22	,6	,18	,10	,10	,6
mass (mg)	347	453	447	500	315	572	369	552	510
SiO_2	48.7	49.7	50.1	47.9	49.4	49.6	49.5	49.5	50.6
TiO_2	0.149	0.126	0.101	0.118	0.124	0.135	0.142	0.095	0.180
Al_2O_3	2.65	1.32	1.02	0.911	2.05	1.80	1.30	0.918	2.15
Cr_2O_3	1.03	0.907	0.985	0.626	0.961	1.03	0.565	1.03	0.906
FeO	17.9	15.8	17.1	17.3	17.3	17.9	17.2	16.6	15.1
MnO	0.571	0.547	0.556	0.557	0.549	0.626	0.565	0.546	0.522
MgO	25.7	28.7	27.2	31.0	25.7	25.1	27.6	28.2	27.7
CaO	2.84	1.42	1.43	1.37	2.37	2.38	1.71	1.55	2.35
Na_2O	0.066	0.006	0.021	0.019	0.062	0.038	0.012	0.019	0.066
Total	99.6	98.5	98.5	99.8	98.5	98.6	98.6	98.5	99.6

Table D7. Whole work and clast separate compositions determined by INAA.

Meteorite		Bilanga	EET 83247	EET 83247	EET 83247	GRA 98108	GRO 95555	GRO 95555	LAP 91900	LAP 91900	LAP 91900	LAP 91900
split		,3f,3	,20	,21	,16	,11	,10	,17	,9a	,9b	,10	,29
type		wr	opx	opx	wr[1]	wr	wr	wr	opx	opx	wr	wr
mass	mg	104.67	31.65	15.23	83.22	117.11	102.38	112.94	155.80	180.89	157.52	44.09
Na	µg g^{-1}	80	669	66	339	170	137	145	107	112	71	80
K	µg g^{-1}	111	357			38	34	11	29	69		
Ca	mg g^{-1}	6.5	6.3	4.7	13.6	6.6	8.2	9.5	7.4	7.8	7.9	6.4
Sc	µg g^{-1}	9.84	11.6	10.9	13.8	9.56	11.9	11.8	13.8	13.8	13.8	13.3
Cr	mg g^{-1}	6.04	6.28	4.47	8.35	3.59	7.01	7.08	5.27	5.31	5.29	4.99
Fe	mg g^{-1}	99	127	125	129	170	125	123	123	122	121	120
Co	µg g^{-1}	21.8	14	19.1	19.1	19.9	14.9	15.8	11.1	12.2	9.71	10.5
Ni	µg g^{-1}	24			50	29			13	17	15	
Se	ng g^{-1}		620	970	1200	790	320	280	190	220	160	
Br	ng g^{-1}	158			56							
La	ng g^{-1}	34.8	49	15	74	75.2	16	24	5.5	9.7	3.9	9.3
Ce	ng g^{-1}											
Sm	ng g^{-1}	68	15.8	15	78	83.8	17.1	24.8	18.6	20	20.7	20.1
Eu	ng g^{-1}	9			20	20		5.1	2.9		2.2	
Tb	ng g^{-1}	30	19		25	22		15	9	8	8	
Yb	ng g^{-1}	136	73	70	170	184	88	93	85	80	82	88
Lu	ng g^{-1}	23.1	13	11	28	29	20	17	15.5	14.9	16.8	19.5
Hf	ng g^{-1}	45			60	80			31	39		

Table D7 (continued). Whole work and clast separate compositions determined by INAA (continued).

Meteorite		LEW 88679	LEW 88679	MET 00422	MET 00424	MET 00425	MET 00436	MET 00436	MET 001060	PCA 91077	QUE 93009	QUE 93009
split		,6	,6	,6	,10	,6	,13	,9	,4	,4	,8a	,8b
type		opx	wr	wr	wr	wr	wr	wr	wr	wr[2]	clast[3]	wr[4]
mass	mg	65.18	46.51	103.82	107.25	97.19	100.45	101.31	141.07	160.29	40.48	125.24
Na	µg g^{-1}	107	189	23	29	59	28	22	8	96	365	877
K	µg g^{-1}					17					21	56
Ca	mg g^{-1}	11.4	12.2	5.3	4.2	4.4	4.1	4.9	3.15	9.4	17.9	26.4
Sc	µg g^{-1}	23	23	15.9	16.7	7.28	16.3	16.5	11.6	14.3	19.8	19.9
Cr	mg g^{-1}	4.57	4.26	6.19	7.47	5.15	12.75	15.99	11.43	5.77	5.76	5.53
Fe	mg g^{-1}	129	128	134	152	89	152	154	149	121	145	140
Co	µg g^{-1}	9.87	10.1	22.8	35.8	9.54	14.3	17.6	59	17	14.7	13.6
Ni	µg g^{-1}	19							47	36.3		
Se	ng g^{-1}	600	690		1300		1300	1000	3450	101		
Br	ng g^{-1}					38						
La	ng g^{-1}	8.6	16.4	3.3	5.3	15.4	9.4	5.7	27.5	13.3	465	1140
Ce	ng g^{-1}										2020	3600
Sm	ng g^{-1}	92.9	96	5.2	1.7	31	12.1	12		29.5	411	726
Eu	ng g^{-1}	13.7	28.8						2.7	4.5	59	165
Tb	ng g^{-1}	48	46							13.7	138	186
Yb	ng g^{-1}	387	391	41		85			29	152	721	816
Lu	ng g^{-1}	62	61	9		15.1	4.2	4.4	6.7	25.4	112	124
Hf	ng g^{-1}	119	122							19	320	573

[1]Data repeated from Mittlefehldt (1994); includes 2.8 ng g^{-1} Ir.
[2]Includes 0.84 ng g^{-1} Ir
[3]Includes 43 ng g^{-1} Ta
[4]Includes 18 µg g^{-1} Sr, 20 µg g^{-1} Zr, 69 ng g^{-1} Ta, 116 ng g^{-1} Th.

Table D8. Whole rock compositions determined by solution ICP-MS.

Meteorite		EET 83246	EET 83246	LAP 03979	LAP 03979	LEW 88008	LEW 88008	LEW 88679	LEW 88679	MET 01084	MET 01084
split		,26 (a)	,26 ©	,6 (a)	,6 ©	,18 (a)	,18 ©	,10 (a)	,10 ©	,8 (a)	,8 ©
type		dimict	dimict	dimict	dimict	dimict	dimict	dimict	dimict	dimict	dimict
mass	mg	68.58	67.80	64.44	60.00	65.14	62.74	67.11	49.10	69.34	59.68
Li	µg g^{-1}	4.56	3.65	1.99	1.89	2.19	1.97	1.66	0.836	2.86	2.54
Be	ng g^{-1}			30.4		36.9				36.5	
Na	µg g^{-1}	106	149	379	497	249	276	72.8	101	183	234
Al	mg g^{-1}	4.60	5.81	11.6	14.5	10.3	10.4	7.54	6.95	8.50	10.4
P	µg g^{-1}	4.98	5.72	18.8	23.1	10.1	13.7	6.82	9.42	32.4	34.7
K	µg g^{-1}		72.5			151	177		62.9		43.2
Ca	mg g^{-1}	9.82	9.90	18.0	19.1	18.1	15.9	13.0	12.1	12.8	12.7
Sc	µg g^{-1}	11.1	13.5	14.3	19	20.7	20.1	20.3	16	13.8	16.6
Ti	mg g^{-1}	0.640	0.641	0.819	0.981	0.855	0.858	0.950	0.908	1.01	1.07
V	µg g^{-1}	94.6	116	120	147	147	142	116	90.5	82.6	101
Cr	mg g^{-1}	5.92	5.90	6.38	7.62	7.53	5.85	3.05	3.32	4.21	3.99
Mn	mg g^{-1}	4.00	4.32	4.03	4.87	4.78	4.71	4.12	4.36	3.64	3.96
Fe	mg g^{-1}	109	1305	125	151	148	142	143	143	116	129
Co	µg g^{-1}	15.8	16.5	23.1	26.4	16.0	16.9	19.1	21.2	17.3	18.7
Ni	µg g^{-1}	28.5	34.5	137	168	31.1	36.9	31.3	38.2	49.9	62.6
Cu	µg g^{-1}	2.45	1.66	3.91	5.42	3.20	4.09	8.63	9.93	4.36	3.24
Zn	µg g^{-1}	5.86	4.51	4.22	5.63	2.54	5.95	6.16	5.99	4.60	5.58
Ga	µg g^{-1}	0.506	0.690	0.562	0.919	0.506	0.791	0.589	0.736	0.517	0.788
Ge	ng g^{-1}		150		217		210		248		168
Rb	ng g^{-1}	75.5	100	33.9	79.4	147	120	35.6	56.2	44.2	78.2
Sr	µg g^{-1}	1.63	1.51	6.78	7.49	3.64	3.61	1.30	1.33	4.26	4.03
Y	µg g^{-1}	1.23	1.17	1.91	2.11	1.95	2.00	2.52	1.94	3.11	3.24
Zr	µg g^{-1}	3.00	2.14	4.45	6.23	4.22	2.84	2.81	2.20	5.82	7.18
Nb	ng g^{-1}	127	114	288	281	165	132	54.6	50.2	339	349
Cs	ng g^{-1}	2.6	2.1	1.7	2.1	4.3	4.1	1.4		3.1	2.7
Ba	µg g^{-1}	0.635	0.495	1.55	1.60	1.50	1.46	0.128		1.47	1.22
La	ng g^{-1}	67.8	62.9	145	158	87.6	91.1	7.50	5.00	168	206
Ce	ng g^{-1}	212	198	379	412	501	519	32.0	24.1	475	540
Pr	ng g^{-1}	25.2	23.1	59.7	62.9	38.5	38.3	8.80	6.70	81.1	87.0
Nd	ng g^{-1}	140	124	316	332	217	214	84.6	63.3	470	487
Sm	ng g^{-1}	58.3	54.2	118	123	94.7	92.2	79.1	60.1	196	199
Eu	ng g^{-1}	7.8	8.5	45.7	54.6	18.8	22.3	7.8	9.5	34.4	38.7
Gd	ng g^{-1}	98.6	90.0	180	189	164	159	181	136	308	306
Tb	ng g^{-1}	20.3	18.3	35.1	37.8	33.2	33.7	40.1	30.1	59.2	59.8
Dy	ng g^{-1}	157	144	261	276	258	258	327	240	435	438
Ho	ng g^{-1}	41.9	38.6	66.1	70.9	68.9	67.4	86.5	65.6	108	109
Er	ng g^{-1}	143	134	217	229	226	224	293	217	338	341
Tm	ng g^{-1}	25.2	22.6	35.4	37.8	38.2	37.4	48.2	35.7	54.7	55.4
Yb	ng g^{-1}	166	162	233	258	277	263	329	250	354	366
Lu	ng g^{-1}	28.7	26.9	39.5	42.3	43.5	42.2	53.8	39.7	56.8	59.0
Hf	ng g^{-1}	88.8	57.2	116	154	106	80.2	97.9	77.0	183	185
Ta	ng g^{-1}	4.8	5.6	10.8	12.7	5.5	6.0	1.7	1.8	13.1	15.1
Tl	ng g^{-1}	7.7	7.4	0.6	0.6	65.4	69.4	6.7	7.2	2.3	2.2
Pb	ng g^{-1}	85.8	55.3	103	30.0	494	635		20.5	113	22.8
Th	ng g^{-1}	11.1	10.9	18.8	20.9	23.3	23.5	0.5	1.4	21.3	27.0
U	ng g^{-1}	2.6	2.7	6.3	5.7	10.6	10.8	1.4	1.5	7.8	8.1
Eu/Eu*		0.317	0.376	0.972	1.109	0.465	0.568	0.196	0.316	0.433	0.486
Ce/Ce*		1.211	1.226	0.962	0.976	2.036	2.075	0.811	0.828	0.957	0.953

Table D8 (continued). Whole rock compositions determined by solution ICP-MS.

Meteorite		MIL 03368	MIL 03368	ALHA 77256	ALHA 77256	GRA 98108	GRA 98108	ALH 85015	ALH 85015	PCA 02008	PCA 02008
split		,10 (a)	,10 ©	,158 (a)	,158 ©	,22 (b)	,22 ©	,7 (a)	,7 ©	,6 (b)	,6 ©
type		dimict	dimict	harzburgitic	harzburgitic	harzburgitic	harzburgitic	polymict	polymict	polymict	polymict
mass	mg	63.69	59.34	65.49	61.18	66.70	64.51	69.14	49.43	67.40	65.97
Li	µg g^{-1}	3.31	3.18	1.82	1.63	3.00	1.45	3.37	3.24	3.65	3.34
Be	ng g^{-1}			28.7				36.1		45.4	
Na	µg g^{-1}	133	165	80.5	38.2	101	130	431	508	433	467
Al	mg g^{-1}	4.27	5.60	6.28	8.14	4.24	4.11	14.5	16.5	11.8	13.3
P	µg g^{-1}	15.0	3.13	9.88	10.3	26.5	27.6	48.2	55.7	50.9	55.7
K	µg g^{-1}				47.2		58.4		56.4		45.3
Ca	mg g^{-1}	11.6	10.9	10.6	10.3	8.79	8.30	19.1	19.1	15.9	15.6
Sc	µg g^{-1}	10.9	13.7	15.7	18.9	14.4	11.3	14.5	16.1	14.9	15.9
Ti	mg g^{-1}	0.626	0.626	0.803	0.814	0.759	0.671	0.839	0.843	1.06	1.13
V	µg g^{-1}	144	172	122	149	143	137	116	122	98.7	105
Cr	mg g^{-1}	6.03	6.18	6.09	5.47	4.65	3.79	6.43	6.63	5.66	4.40
Mn	mg g^{-1}	3.77	4.26	3.91	4.13	3.82	4.00	4.02	4.39	3.75	3.96
Fe	mg g^{-1}	123	133	114	126	125	131	133	144	120	127
Co	µg g^{-1}	21.5	21.9	10.7	12.8	13.4	14.5	24.5	27.7	21.8	21.8
Ni	µg g^{-1}	11.2	12.2	9.92	12.6	17.4	19.7	130	979	118	144
Cu	µg g^{-1}	3.87	4.49	2.73	3.16	3.48	2.89	5.68	9.40	2.73	3.53
Zn	µg g^{-1}	13.3	3.88	8.30	4.88	5.19	3.77	6.24	5.91	6.37	5.51
Ga	µg g^{-1}	0.407	0.655	0.536	0.814	0.473	0.723	0.817	1.14	0.760	1.04
Ge	ng g^{-1}		170		190		205		280		209
Rb	ng g^{-1}	41.2	63.1	14.8	29.1	37.7	54.8	39.0	80.2	36.0	63.5
Sr	µg g^{-1}	0.396	0.299	0.674	0.341	0.405	0.319	11.0	10.7	11.1	8.66
Y	µg g^{-1}	1.00	1.04	1.84	1.88	2.43	2.06	2.22	2.29	3.71	3.87
Zr	µg g^{-1}	0.680	0.777	4.59	3.63	4.82	3.71	5.77	6.21	8.02	8.83
Nb	ng g^{-1}	62.3	49.9	335	329	205	189	426	402	534	588
Cs	ng g^{-1}	3.5	1.8	11.9		2.5	2.1	1.5	1.6	2.0	1.3
Ba	µg g^{-1}	0.0968		0.789		0.0839	0.0332	3.46	3.21	4.06	3.84
La	ng g^{-1}	19.6	15.5	110	136	50.9	43.8	279	289	471	521
Ce	ng g^{-1}	50.7	41.9	294	330	210	175	705	717	1170	1250
Pr	ng g^{-1}	8.5	9.1	40.3	43.5	44.4	38.4	107	106	179	192
Nd	ng g^{-1}	49.3	59.7	215	227	305	258	546	537	934	988
Sm	ng g^{-1}	28.0	27.8	84.5	84.6	155	129	182	175	309	321
Eu	ng g^{-1}	1.5	3.2	6.0	7.5	1.5	2.4	79.9	83.6	75.1	77.3
Gd	ng g^{-1}	60.2	61.6	144	145	244	206	255	245	428	448
Tb	ng g^{-1}	13.9	14.3	30.2	30.2	47.8	40.4	46.4	45.7	79.4	80.9
Dy	ng g^{-1}	119	121	238	236	338	288	326	319	536	546
Ho	ng g^{-1}	34.0	34.6	62.3	62.6	83.7	71.2	78.1	78.1	127	129
Er	ng g^{-1}	122	124	210	211	267	226	248	247	389	397
Tm	ng g^{-1}	21.7	21.5	34.2	34.9	42.9	36.6	39.8	40.1	60.3	59.9
Yb	ng g^{-1}	146	161	231	237	286	247	271	273	388	396
Lu	ng g^{-1}	26.7	27.5	38.4	39.0	46.8	39.9	43.5	43.2	61.4	61.5
Hf	ng g^{-1}	20.4	24.4	138	96.2	141	100	149	152	211	221
Ta	ng g^{-1}	0.9	1.9	8.2	8.3	8.6	8.9	18.4	20.6	25.7	28.8
Tl	ng g^{-1}	4.7	4.4	2.1	0.9	3.4	3.7	0.5	0.8	2.4	2.5
Pb	ng g^{-1}	36.6		75.9		24.7	94.1	32.0	75.6	308	103
Th	ng g^{-1}	3.9	2.3	14.2	16.2	16.6	10.0	36.4	34.6	57.7	61.4
U	ng g^{-1}	2.3	1.7	6.5	6.1	5.0	4.7	10.7	10.9	15.2	15.6
Eu/Eu*		0.111	0.233	0.168	0.209	0.024	0.046	1.151	1.253	0.641	0.633
Ce/Ce*		0.927	0.818	1.042	1.007	0.969	0.935	0.964	0.967	0.952	0.933

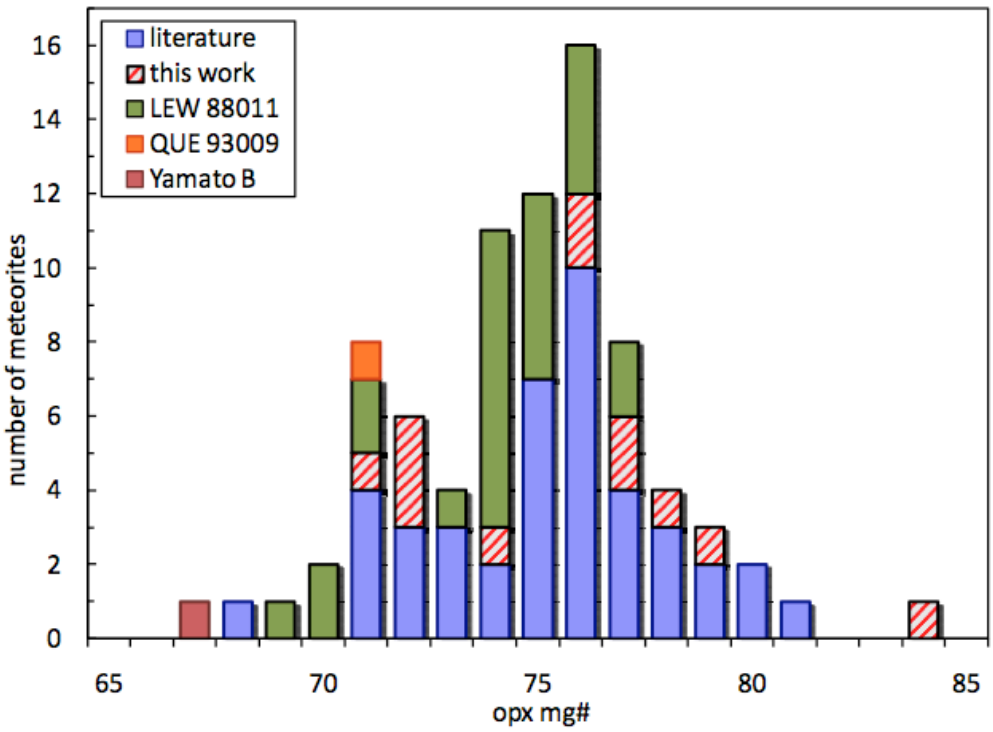


Figure D1. Histogram of orthopyroxene mg# for diogenites. Shown are average pyroxene compositions for individual meteorites except for LEW 88011 where grain averages are shown for this heterogeneous diogenite. Literature data are from: Beck and McSween (2010); Beck et al. (2011); Domanik et al. (2004); Fowler et al. (1994); Gooley (1972); Mittlefehldt (1994, 2000); Mittlefehldt and Lindstrom (1993).

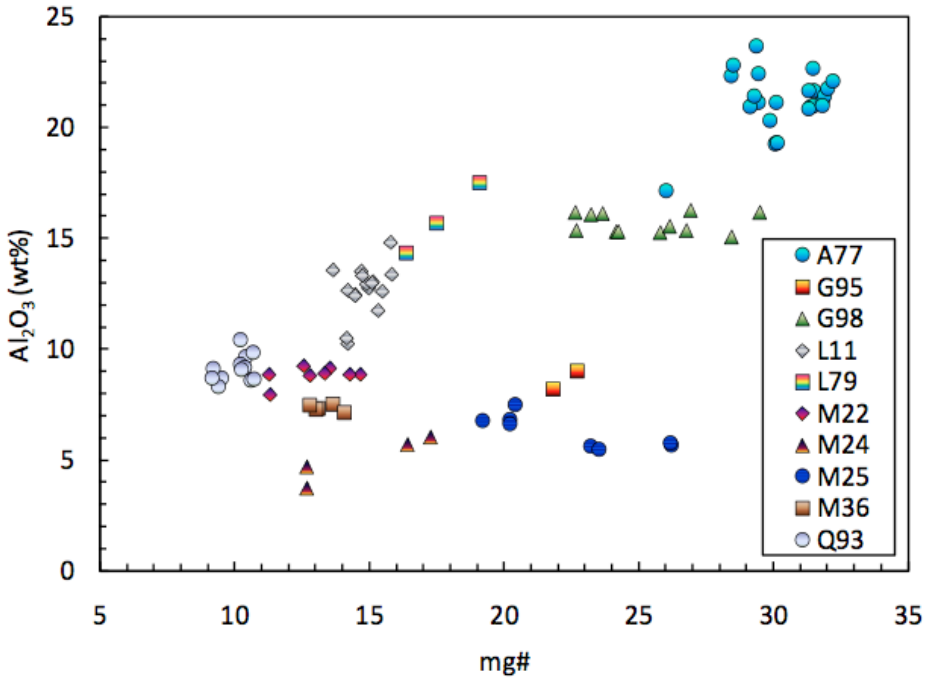


Figure D2. Al_2O_3 vs. mg# for chromites. Meteorite abbreviations are; A77 – ALHA77256, G95 – Grosvenor Mountains (GRO) 95555, G98 – GRA 98108, L11 – LEW 88011, L79 – LEW 88679, M22 – MET 00422, M24 – MET 00424, M25 – MET 00425, M36 – MET 00436, Q93 – QUE 93009.

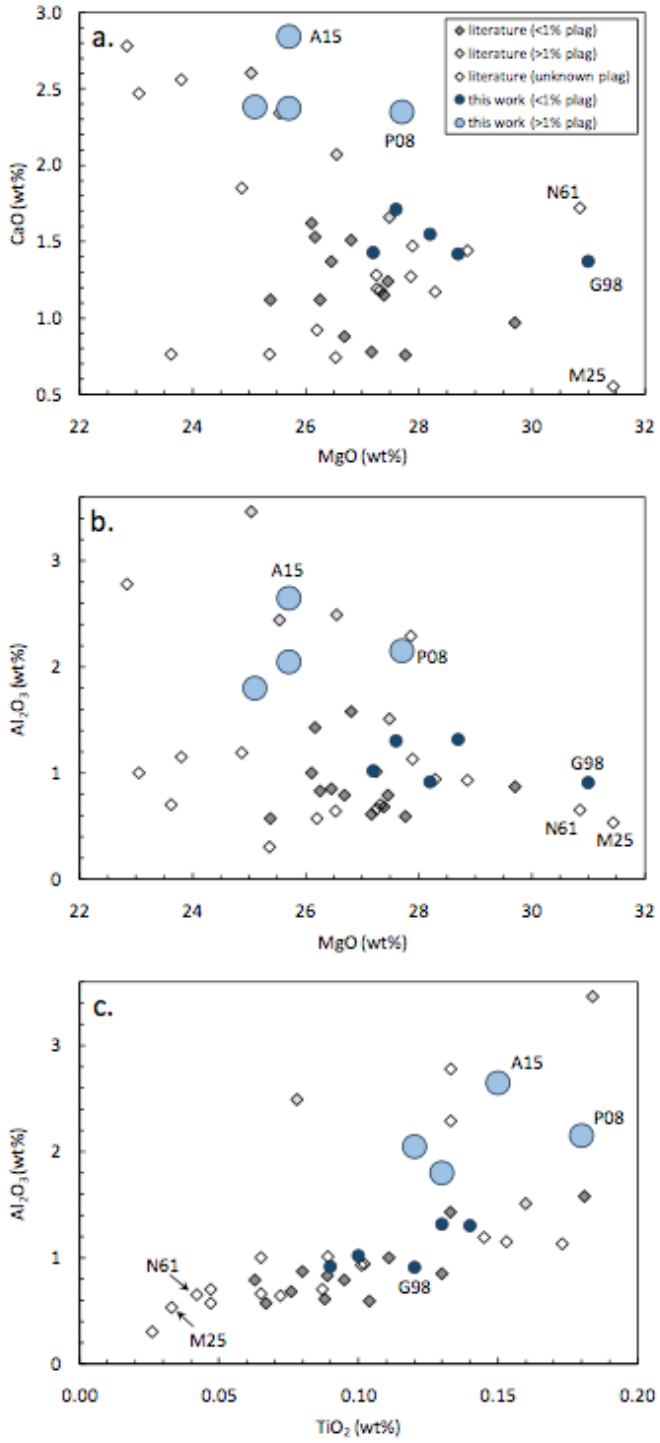


Figure D3. Major element compositions of diogenites determined by LA-ICP-MS of fused beads in this work compared to literature data on diogenites. Labeled samples are A15 – ALH 85015, G98 – GRA 98108 and P08 – PCA 02008 from this study and M25 – MET 00425 from Barrat et al. (2008) and N61 – NWA 1461 from Warren et al. (2009).

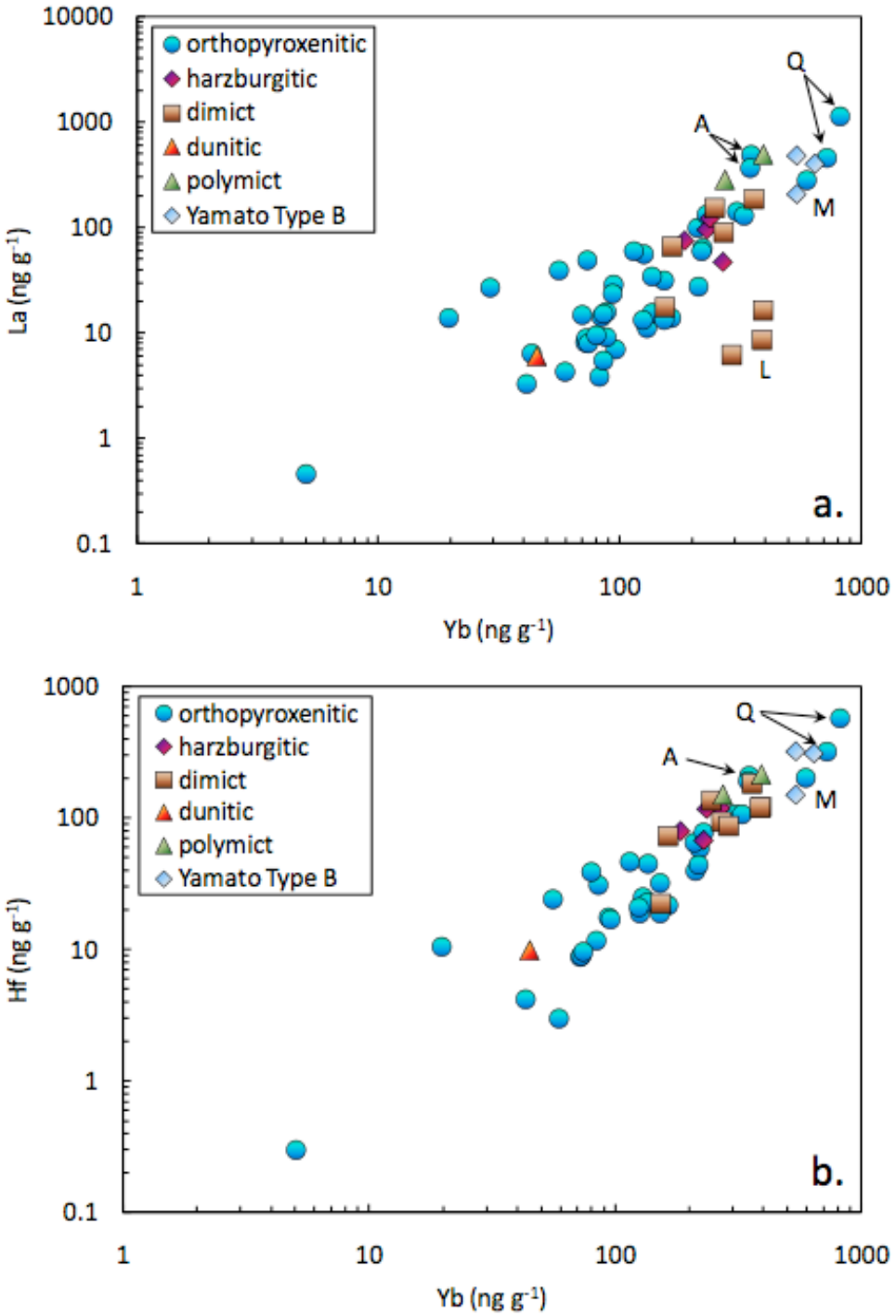


Figure D4. La vs. Yb and Hf vs. Yb for the diogenites studied here and literature analyses. Nomenclature modified from Beck and McSween (2010) (see text). Labeled diogenites are E – EET 83246, L – LEW 88679, 8 – LEW 88008 and Q – QUE 93009 from this work, and A – A-881838 and A-881839 and M – MIL 07001 from Barrat et al. (2010). Other literature data are from Barrat et al. (1999, 2008, 2010), Beck et al. (2011) and Mittlefehldt and Lindstrom (1993).

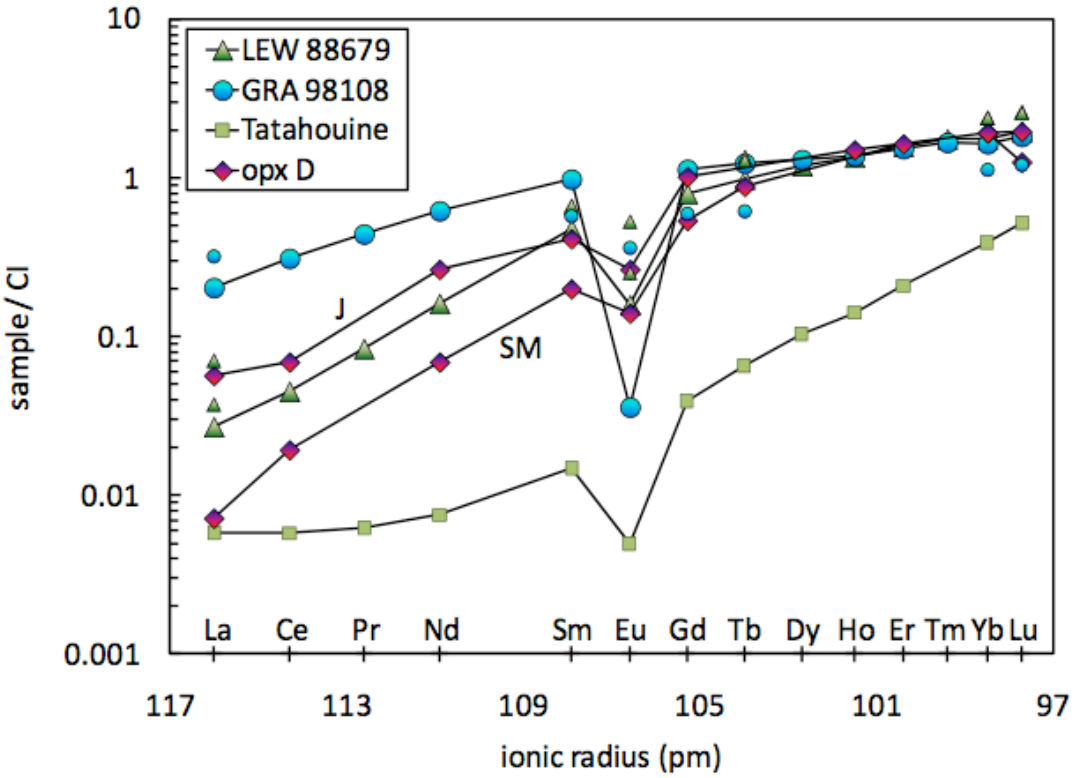


Figure D5. REE diagram for GRA 98108 and LEW 88679 compared to two orthopyroxene/melt distribution coefficient sets; J calculated after Jones (1995) and SM from Schwandt and McKay (1998). Smaller symbols (not joined by lines) are our INAA data; larger symbols are our ICP-MS data. Comparative data for Tatahouine from Barrat et al. (1999) are shown.

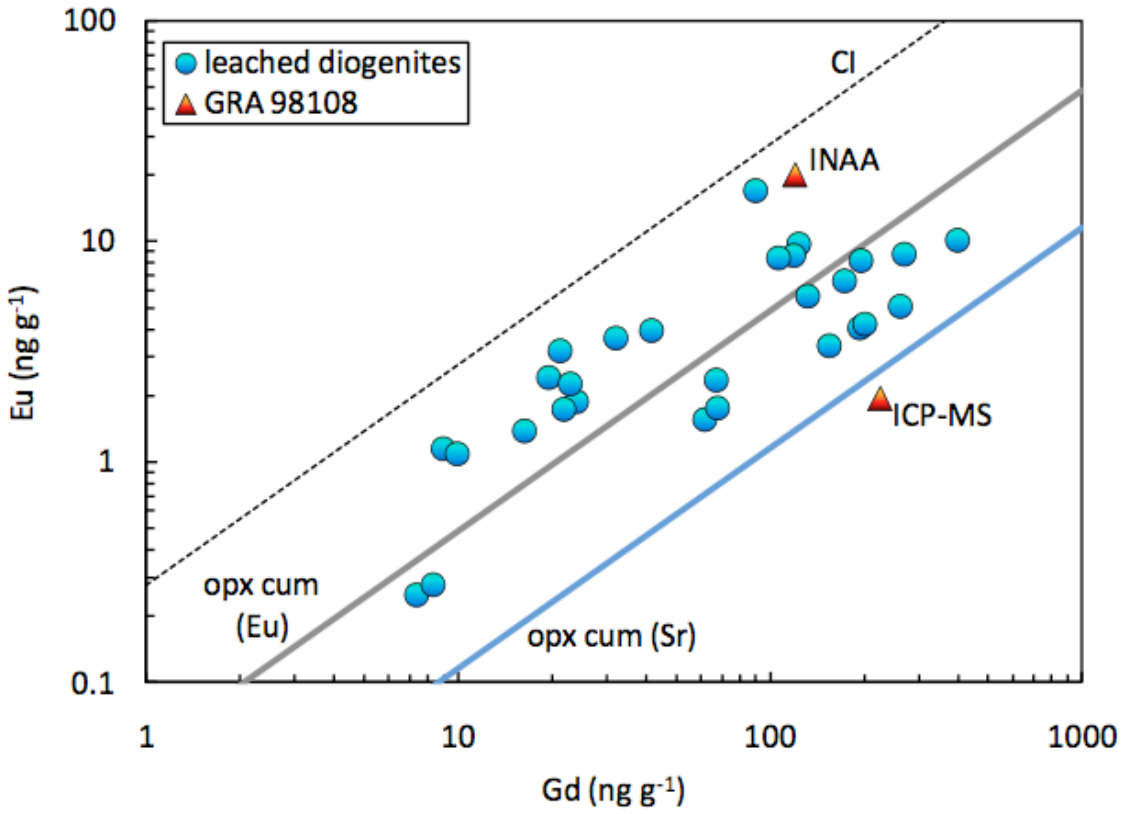


Figure D6. Eu vs. Gd for acid leached diogenites from Barrat et al. (2010) and (untreated) GRA 98108 from this study. Only falls and Antarctic diogenites are plotted. The line labeled opx cum (Eu) is the locus of orthopyroxene in equilibrium with melts with CI Eu/Gd ratios. The line labeled opx cum (Sr) is the locus of orthopyroxene in equilibrium with melts with CI Sr/Gd ratios. The partition coefficients used are from Barrat et al. (2007) and were used by Barrat et al. (2010) to model diogenite genesis. See text for discussion.

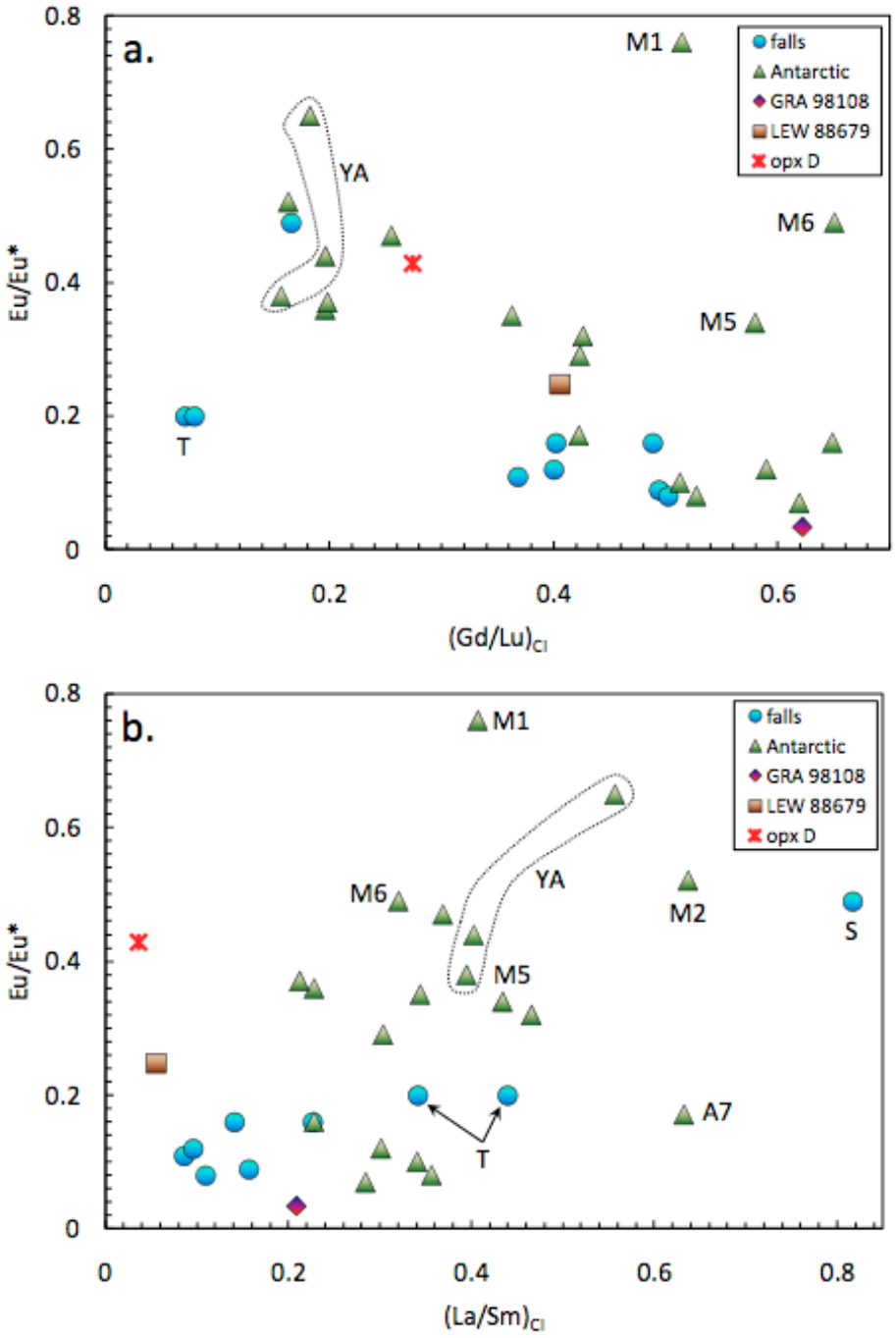


Figure D7. Eu/Eu* vs. Gd/Lu and Eu/Eu* vs. La/Sm for leached diogenites from Barrat et al. (2010) compared to unleached GRA 98108 and LEW 88679 from this study. Opx D is the orthopyroxene/melt partition coefficient set of Schwandt and McKay (1998). Labeled diogenites are A7 – ALHA77256, M1 – MIL 07001, M2 – MET 00422, M5 – MET 00425, M6 – MET 00436, S – Shalka, T – Tatahouine, YA – paired Yamato Type A diogenites Y-74013 and Y-74097.

Part 6
Petrologic and textural diversity in one of the largest samples of the Vestan regolith.

This part will be submitted for publication in Meteoritics and Planetary Science. Andrew Beck, Hap McSween, and Christina Viviano are authors. Andrew preformed all data analyses, except for EMP analyses on PCA 02015, section #4.

ABSTRACT

Mineral and textural variations are measured in six of the paired PCA 2002 howardites to discern and describe diversity in one of the largest single samples of the Vestan surface. Mineral compositions nearly span the entire range of known eucrite and diogenite compositions. Distinct, non-diogenite groups of Mg- and Fe-rich olivine grains are observed and are interpreted to be from chondritic contamination and impact melts, respectively. We analyzed a glass fragment with very high K concentration and hypothesize an origin from either impact melting of a quartz syenite or as a highly fractionated eucritic mesostasis. Impact melt breccia clasts comprise up to 30 vol.% of these samples. These clasts are very olivine-rich and likely formed from howardites rich in dunitic and harzburgitic diogenites. Finally, we present a method for mapping distributions of the wide variety of lithologies present in these howardites. We find that the PCA 02 howardites are primarily comprised of diogenitic material and demonstrate that eucritic material dominates the finer-grain sizes. This grain size fractionation has implications for interpretation of visible/near-infrared spectra of Vesta's surface from the Dawn spacecraft, as the eucritic material will disproportionately dominate a VIR spectrum of surface regolith.

1.0 INTRODUCTION

Howardites are fragmental and regolith breccias that primarily consist of eucrite and diogenite clasts. These breccias are formed by impact excavation and local mixing on or near the surface of Vesta (Bunch 1975). Howardites typically contain coarse fragments embedded in a fine-grained matrix (e.g. Delaney et al. 1984; Bunch 1975). Impact generated features (i.e. glass and impact-melt rocks) can also be found in howardites as a result of their formation mechanism. Ground-based telescopic observation suggests that much of the Vestan surface is covered in eucrite and howardite-like material (Gaffey 1997). Therefore, determining the nature and scale of petrologic variations within surface samples is essential in the geologic interpretation of Dawn mission spectroscopic data.

The primary instrument on Dawn that will be used to map the surface of Vesta is the visible and near-infrared spectrometer (VIR). The VIR instrument operates with a 0.25-5.05 micron spectral range and a spatial resolution of ~170 m/pixel (Russell et al., 2004). Grain size distribution is important to Dawn VIR data interpretation, as spectral absorptions in the spectral range covered by this instrument are dominated by volume scattering, where fine-grained textures promote multiple scattering and would relatively increase reflectance (Hapke 1993). In other words, if VIR is used to observe an area where a mixture of coarse and fine grains is present, the finer grained material will contribute disproportionately to the spectral signature. Therefore, it is important to understand grain size distribution of different lithologies expected to be on the surface of Vesta to interpret VIR data accurately.

Along with variance in textures, it is also important to determine localized compositional diversity expected in the Vestan regolith. This will add insights into

regolith maturity on Vesta and aid in the interpretation of VIR data as well. While lithologic distributions with respect to grain size have been studied for individual howardites (e.g. Fuhrman and Papike 1981; Labotka and Papike 1980), and in one case for a small group of paired howardites (Buchanan and Mittlefehldt 1993), variation has not been investigated within a group of paired samples that represent a volumetrically large sample of the Vestan regolith.

Collectively, the Pecora Escarpment Icefield (PCA) howardites, recovered in 2002, represent a ≥1m (diameter) piece of the Vestan surface (Welten et al. 2008). This is one of the largest, pre-atmospheric, howardite meteoroids that has been identified, and provides an appropriate sample set to investigate localized Vestan regolith variability. In this study we determine compositional and textural diversity within this group to ascertain a scale of heterogeneity for the surface, and to attempt to add insight into the distribution of eucrite and diogenite fragments in the howardites with respect to grain size.

2.0 METHODS

For this study, we selected six of the nine howardite samples recovered from the Pecora Escarpment Icefield in 2002 (McBride et al. 2005; 2004). The six samples are PCA 02: 009,12, 013,9, 014,6, 015,7, 018,4 and 019,4. For the majority of this paper will omit the "PCA 02" prefix and refer to the samples by collection number and section number. To examine smaller, centimeter-scale variations, we examined additional thin sections of 009,7, 013,6 and 015,4.

Chemical analyses were made using a Cameca SX-100 electron microprobe (EMP) at the University of Tennessee. Analytical conditions were: 20 kV, 30 nA, 2 μm

diameter beam for pyroxene, olivine, chromite, metal, and troilite; 15 kV, 10-20 nA, 8-10 μm diameter beam for plagioclase, glass, and phosphate. We analyzed impact melt clasts using a 50-100 μm diameter defocused beam to determine bulk composition. The counting time for major elements ranged from 20-40 s, and for minor elements it ranged from 60-80 s. Approximately 200 analyses were conducted for each sample. Only analyses that had significant oxide totals (98.5-101 wt.%) and acceptable stoichiometry were used.

One component of this work is to examine eucrite and diogenite grain size variation in these howardites. While cross-polarized images are able to display textural variations, they are limited in their ability to quantify compositional variations, which may be tied to textures (Fig. F1a). X-ray images, however, do show both textural and compositional variability. Typical x-ray image compilations can only represent 3 elemental concentrations at a time, as they are limited to a red-green-blue (RGB) display input. It is possible to add grayscale as a fourth component, but this result is non-unique as pixels with equivalent RGB elemental concentrations will also appear grayscale. These 3-component RGB x-ray maps are ideal for rocks like eucrites that contain a compositionally limited number of phases (*e.g.*, Mayne et al. 2009). Howardites comprise a wide range of minerals, sampled from an assortment of lithologies, and therefore variability is difficult to distinguish with only 3 elements (Fig. F1b). In an effort to depict textural variations in these howardites, we devised a method that combines 8 elemental x-ray maps into a single image and uses image processing software to discreetly map the distribution of specific phases, which correspond to typical HED components (Fig. F1c). Similar methods have been effectively utilized in other achondrites (e.g. Floss et al. 2007). A detailed explanation of how we developed this

method is given in Appendix E. The resulting lithologic distribution maps were also used to determine a mode for each thin section, which will also be reported.

3.0 RESULTS

3.1 Mineral compositions

Pyroxene and olivine

Pyroxene and olivine end member compositions are displayed in Figure F2. Diogenite pyroxene (En_{85-66}), cumulate eucrite pyroxene (En_{65-46}), and basaltic eucrite pyroxene (En_{45-33}) have been denoted by different colors, which are consistent with those used later in lithologic distribution maps. It is important to note that while the En_{65-46} and En_{45-33} ranges generally separate the cumulate and basaltic eucrite pyroxenes, there are some basaltic eucrites that contain pyroxene that falls in the cumulate eucrite range as defined here, and vice versa (Mayne et al. 2009; Mittlefehldt et al.1998). However, this is generally not the case and is not anticipated to affect results presented here. All of the PCA02 howardite samples contain pyroxenes from each HED sub-lithology (Fig. F2). Most samples display a continuum of compositions across all lithologies; however, both sections of 009 contain three discrete populations of pyroxene corresponding to the diogenite, cumulate eucrite, and basaltic eucrite fields. Most samples are dominated by pyroxenes with diogenitic compositions, except 013. Both sections of 013 have a majority of pyroxene compositions falling in the basaltic eucrite field. Clinopyroxene is also observed, typically as exsolved lamellae associated with En_{65-46} and En_{45-33} pyroxenes (cumulate eucrite and basaltic eucrite, respectively).

The majority of olivine compositions fall within those known for diogenites (Fo_{78-61}, Beck and McSween 2010; Shearer et al. 2010) (Fig. F2). However, all the

samples also contain olivine grains that are near Fo_{50}, which is much more Fe-rich than diogenite olivine. PCA 02015 contains the highest concentration of ~Fo_{50} olivine, and section #7 of that sample contains olivine down to Fo_{44}. Section ,7 of 013, section ,7 of 009, and section ,6 of 014 contain olivine in the Fo_{79-88} range, which are more Mg-rich than diogenitic olivine. In other howardites, both of these non-diogenite olivine compositions (Fo_{60-44} and Fo_{79-88}) have also been documented (Delaney et al. 1980; Fuhrman and Papike 1981), yet their origin remains unclear.

Plagioclase, silica and K-rich glass, opaques

Plagioclase compositions in all the PAC 02 howardites fall within the compositional range of eucrites (Fig. F3) (An_{96-75}, McSween et al. 2011). Samples 018, 019, and 015,7 have higher concentrations of calcic plagioclase, consisting of ~An_{90-96} plagioclase exclusively. The rest of the samples have a broader range of plagioclase composition. Glass is primarily silica-rich, ranging from 88.9 – 99.4 wt.% SiO_2, with the majority being in the ~97-99 wt.% SiO_2 range.

PCA 02014 contains one grain of K-rich glass (K_2O = 10.1[wt.%], along with P_2O_5 = 0.09, SiO_2 = 65.0, TiO_2 = 0.14, Al_2O_3 =19.3, MgO = 0.05, CaO = 2.71, MnO = 0.03, FeO = 0.45, Na_2O = 2.12). This grain is ~225 μm, angular, almost completely glass with the exception of one small crystal grain and is mantled by small (10 μm), ~Fo_{50} olivine (Fig. F4). Texturally this glass is similar to the phyric glass fragments described by Barrat et al. (2009a). Compositionally, the glass in PCA 02014 is similar to the "felsite glass" Barrat et al. (2009a) reported in Northwest Africa (NWA) 1769. The K-rich glass in PCA 02014 contains approximately 2 and 4 times the concentrations of K_2O and Na_2O, respectively, than the felsite glass in NWA 1664. Along with Na_2O and K_2O, the K-rich glass in PCA 02014 also contains significantly more P_2O_5 and Al_2O_3 than

glass in NWA 1664, and less TiO_2, MgO, CaO, and FeO. PCA 02014 K-rich glass is enclosed within a large impact melt breccia clast composed of olivine phenocrysts, plagioclase and pyroxene. The interpretation of these impact melt breccia clasts is addressed in section 3.2.1.

FeNi metal ranges from Ni-poor kamacite to taenite, with up to 54.2 wt.% Ni. Variation in FeNi metal observed in three of these samples (009,7, 013,6, 015,4; Beck et al. 2007) is consistent with the variation we observe in the rest of the group. The majority of the FeNi metal grains have Co/Ni compositions that are identical to those from iron meteorites or ordinary chondrites (Goldstein and Yakowitz 1971), likely indicating that they were intermixed through impact and brecciation of meteoritic debris on the Vestan surface (Hewins 1979). All sulfides in these samples are troilite. Spinels range from Cr_2O_3 = 58.5 (wt.%), TiO_2 = 0.63, Al_2O_3 = 6.70 (consistent with diogenitic chromite; Bowman et al. 1999), to Cr_2O_3 = 45.6, TiO_2 = 5.50 (consistent with ulvospinel in eucrites; Mayne et al. 2009). Ilmenite compositions also fall within the eucrite range, spanning from 0.70-3.2 wt.% MgO and 0.04-1.2 wt.% Cr_2O_3 (eucrites 0.3-5.2 wt.% MgO and <0.03-5.5 wt.% Cr_2O_3; Mayne et al. 2009).

3.2 Petrography

3.2.1 Classification of non-eucrite and non-diogenite material

Regolith breccia clasts

In PCA 02013,9 and PCA 02019 we observe clasts of what we interpret as regolith breccias. These clasts are dominated by basaltic eucrite crystal fragments (~75 μm) or eucrite clasts (~500 μm), where distinct crystal shapes and primary igneous grain boundaries can be (Fig. F5a). The matrix separating these eucritic clasts and fragments is too fine to resolve, but has high concentrations of opaques (Fig. F5b) and a slightly more

ferroan, less aluminous, bulk composition than typical eucrite (fine grained matrix SiO_2 = 48.6 [wt.%], Al_2O_3 = 15.6, MgO = 8.2, CaO = 10.7, FeO = 14.5, vs. approximate eucrite bulk chemistry SiO_2 = 48.6 [wt.%], Al_2O_3 = 12.2, MgO = 8.9, CaO = 10.4, FeO = 18.8; Kitts and Lodders 1998). The high concentration of siderophile elements suggests a regolith origin for these clasts, and the bulk composition of the fine material matching eucrite also suggests a regolith origin (Gaffey 1997). A single, ~1 mm, vitrophyric clast, with spherical opaques (some troilite), is also found in this regolith breccia clast (Fig F5c). We interpret this as either a single piece of lithified regolith soil, or a rapidly quenched impact melt of eucritic composition.

Impact melts

Each thin section contains clasts of olivine-phyric (0.2 – 1 mm, ~Fo_{75}) basaltic clasts, with a fine-grained groundmass (~10 μm) of olivine (~Fo_{50}) + pyroxene (~En_{65}) + plagioclase + opaques (mainly FeNi metal and sulfide). We interpret these clasts as impact melt breccia clasts (Fig. F6). The large, ~Fo_{75} olivine phenocrysts in these impact melt breccias are relic grains, which are zoned and in equilibrium with the matrix at their rim. The cores of these grains have diogenitic compositions (~Fo_{75}) while the rims do not (~Fo_{50}). Also present are partially absorbed lithic fragments composed of ~Fo_{75} olivine and ~En_{75} orthopyroxene, which are similar in texture and composition to the harzburgitic diogenites (Beck and McSween 2010). There are partially absorbed phenocrysts of En_{75} orthopyroxene, which are also diogenitic in composition. Like olivine phenocrysts, orthopyroxene phenocrysts are also zoned and in equilibrium with the melt matrix (Fig F6). In a few cases phenocrysts of plagioclase and eucritic pyroxene are observed, although these are uncommon. While the impact melt breccia clast shown in Figure F6 has 12 vol.% olivine, most of the other impact melt breccia clasts contain

much larger relic ~Fo_{75} olivine phenocrysts (e.g. Fig. F7a), and much higher concentrations of ~Fo_{50} olivine in the melt matrix (estimated ~30 vol.% Fo_{50} olivine, e.g. Fig. F7b). In most clasts, small ≤1-5 μm spherules of troilite and metal occur in the impact melt matrix (Fig. F7c).

We interpret these as impact melt breccia clasts, based on their textural and compositional properties (i.e. partially reabsorbed grains, fine-grained textures, high concentrations of siderophile elements). These indicators have been used to distinguish impact melt rocks in lunar samples (Lucey et al. 2006), and in another howardites (Hewins and Klein 1978). Furthermore, these clasts would be difficult to explain petrogenetically if interpreted as erupted eucritic basalts. The olivine-normative nature of these melts and high concentration of olivine phenocrysts would be inconsistent with the silica-normative, and generally less mafic, chemistry of other eucrites (McSween et al. 2011).

Chondritic fragment

A possible chondrule, displayed in Figure F8, was identified in PCA 02014. This is the only chondritic fragment observed in the nine sections. The chondrule is 400 μm, circular, and composed primarily of En_{65} orthopyroxene with small amounts of plagioclase, and spherules of metal and troilite. The orthopyroxene Fe/Mn is 33, which falls just outside the range for Vestan pyroxene (Fe/Mn 30 ±2, Papike et al. 2003). Plagioclase was too small to measure with the EMP. If this is in fact a chondrule, the chemistry and mineralogy of this fragment is consistent with a type IIB chondrule (McSween 1977). As mentioned above, much of the FeNi metal in these samples has non-HED Co/Ni compositions. This metal likely originated from the impact and mixing of chondritic, or possibly iron meteorite, material. Due to the presence of a chondrule in

these samples, we favor an ordinary chondrite origin for the metal as well, though both foreign sources could be possible contributors.

3.2.2 Lithologic distribution maps

Samples with two thin sections

We have separated the samples into two groups for the basis of discussion of the lithologic distribution maps. The first group, shown in Figure F9, consists of the samples where two thin sections of the same meteorite were mapped. We attempted to make maps of both sections of PCA 02015; however, one section (,4) contained too high a concentration of impact melt, which made it difficult to properly discern the other HED lithologies. Included in Figure F9 is a key and % mode histogram for each section. Between the two sections of PCA 02013, a large variation in lithologic abundance can be seen. Section ,6 is dominated by coarse diogenitic orthopyroxene and olivine (combined 62 vol.%, most $\geq$500 μm with some up to 5 mm), with lesser amounts of finer-grained basaltic and cumulate eucritic pyroxene, plagioclase and glass (34 vol.% combined, typically $\leq$75 μm). For the remainder of this discussion "diogenitic material" will refer to diogenite orthopyroxene + olivine, while "eucritic material" will refer to cumulate and basaltic eucrite pyroxene (low and high-Ca) + plagioclase + glass. Section ,6 of 013 also contains a 1 mm impact melt breccia clast with an enclosed harzburgitic diogenite fragment (013,6; Fig. F9). Section ,9 is composed of more eucritic material, has more equal proportions of grain sizes between eucrite and diogenite lithologies, and contains a large, 1.2 mm regolith breccia clast. Diogenitic material makes up a combined 34 vol.% of this sample, while eucrite material makes up a combined 59 vol.%. The grain sizes between components from the two lithologies are about the same, with the majority of diogenitic material being in the 120-200 μm range, and eucritic material slightly finer,

typically ranging from 50-125 μm (013,9; Fig. F9). A few diogenite and eucrite fragments are nearer to 800 μm in size.

The two sections from PCA 02009 are generally more similar than the two sections from PCA 02013. Both sections of 009 are dominated by large (≥2 mm) diogenitic orthopyroxenes (,7 = 69 vol.%, #12 = 89 vol.%), which are separated by a much finer-grained (generally ≤80 μm, with the majority being ~40 μm) matrix dominated by eucritic material (,7 = combined 25 vol.% and ,12 = combined 7 vol.%). A few, ~400 μm, eucrite mineral grains occur in 009,7. Olivine in 009,7 is small (80 μm), and spread throughout the eucrite-dominated matrix, except in impact melt breccia clasts, where olivine is slightly larger (150 μm). Section ,7 also contains a 125 μm phosphate grain, colored magenta, and on the right side of the map (009,7; Fig. F9). Section ,12 of 009 contains no impact melt breccia clasts, and olivine in this sample is mainly found in distinct olivine + orthopyroxene, harzburgitic diogenite clasts (009,12; Fig. F9).

Samples with one thin section

The lithologic distribution maps for the single-section samples are displayed in Figure F10. PCA 02018 contains the highest concentration of metal + sulfide in the entire group (8 vol.%). The breakdown of this metal is: ~80% kamacite (low-Ni), ~20% taentite (high-Ni). PCA 02018 has approximately equal proportions of diogenitic and eucritic material (~40 vol.%), but they vary in grain size. Diogenitic orthopyroxene and olivine are typically large, ≥400 μm grains, while eucrite pyroxene and plagioclase are smaller, ≤70 μm grains in the matrix. This sample also contains two elongated basaltic eucrite clasts, preserving igneous contact between enclosed phases. The clasts are 800 μm and 3.9 mm in their longest dimension, and are in the right middle and right side of the section, respectively. There are two clasts of harzburgitic diogenite in this section: a

1 mm grain in the middle, and a 400 μm grain enclosed in the impact melt breccia clast in the upper right (018,4; Fig. F10).

PCA 02014 has the second highest abundance of impact melt (20 vol.%), and in those clasts, large olivine phenocrysts can be observed (014,6; Fig. F10). These impact melt breccia clasts are quite large, measuring up to ~4 x 4 mm. Impact melt breccia clasts in this sample also contains multiple, ~250 μm, round pieces of metal + sulfide. All of the diogenitic and eucritic material is roughly proportional (diogenite material = 44 vol.% vs. eucrite material = 36 vol.%). However, the average grain size of diogenitic material is much larger, typically ranging from 400 μm to 1.1 mm, with a few ≥2 mm clasts, while most of the eucritic material is ≤ 70 μm (014,6; Fig. F10). There are three large (1-2 mm) cumulate eucrite clasts in this section, which occur in the top right, center and bottom middle. The K-rich glass, shown in Figure F4 and discussed in section 3.1, occurs at the top left edge of the 4 x 1 mm impact melt breccia clast that is on the left side of the map. It has not been distinguished from silica glass (blue) on the lithologic distribution map.

PCA 02015,7 contains the highest concentration of impact melt (28 vol.%), and like PCA 02014, has impact melt breccia clasts with large olivine phenocrysts and a few metal + sulfide blebs (015,6; Fig. F10). This sample consists of about 42 vol.% diogenitic material, and eucritic material only comprises 29 vol.% of the sample. As with previous samples, diogenitic material is much coarser (most grains are ≥200 μm, with the majority close to 600 μm), while eucrite grain fragments are smaller (typically ≤90 μm). A single 1 mm cumulate eucrite clasts occurs in the top portion of this section, while a ~800 μm basaltic eucrite clast is in the bottom left (015,6; Fig. F10). This sample contains two harzburgitic diogenite fragments. One is partially absorbed, approximately

1 mm, and enclosed in the larger impact melt breccia clast on the left half of the section. The other clast is elongated (1.2 mm) in the right center between two impact melt breccia clasts, and is composed of small, 40 μm olivine crystals.

PCA 02019 has the second highest concentration of diogenitic pyroxenes (74 vol.%), which are typically 1.5 mm with some mineral clasts up to 4 mm. Olivine (4 vol.%) occurs as 300 μm grains in the matrix, and can be found in high concentration on the left side of the sample in a 3 mm harzburgitic diogenite clast (019,3; Fig. F10). The majority of basaltic and cumulate eucrite pyroxene, plagioclase and silica (combined 17 vol.%) are ~100 μm and dispersed in the matrix between larger diogenite clasts and grains. Some eucrite clasts are as large as 1 mm. A 1.5 mm clast of lithified regolith can be found in the upper right portion of this sample. It contains crystal and lithic fragments of basaltic eucrite material. This is the same lithified regolith clast previously shown in Figure F5. Impact melt breccia clasts in 019 are ≤1 mm.

4.0 Discussion

4.1 Mineral compositions

Olivine

As described in section 3.1, two olivine compositional ranges in the PCA 02 howardites (Fo_{60-44} and Fo_{79-88}) fall outside of the diogenitic olivine range (Fo_{78-61}; Beck and McSween 2010; Shearer et al. 2010). It has been hypothesized that Mg-rich olivine in howardites, up to Fo_{96}, was derived from Mg-rich diogenitic lithology, yet to be observed in diogenite meteorites, and incorporated into howardite breccias (Delaney et al. 1980). This is a possibility for the Fo_{79-88} olivine we observe in the PCA 02 howardites. Another interpretation is that the Fo-rich olivine is exogenic and was incorporated into

howardites from the impact and mixing of chondritic olivine, which is typically $\geq Fo_{80}$ (Brearley and Jones 1998). The presence of chondritic fragments in one of the samples, the abundance of metal in these samples, and the Co/Ni compositions of the metal, all suggest high amounts of chondritic material in these breccias. This supports an interpretation that the $Fo_{79\text{-}88}$ olivine in these samples is also from chondritic contamination. Furthermore, if the $Fo_{79\text{-}88}$ grains were incorporated from the brecciation and mixing of a $>Fo_{80}$ diogenitic lithology, we would expect to find fragments of this lithology, or other phases from this lithology, in the sections examined here. We do not find any of these fragments. Finally, two recent studies involving olivine in diogenites, which examined 13 of 16 olivine-bearing diogenites in the Antarctic Meteorite collection, did not reveal any $\geq Fo_{80}$ olivine (Beck and McSween 2010; Shearer et al. 2010), further supporting an exogenic origin for Fo-rich olivines in howardites.

The other non-diogenitic olivine compositional range ($Fo_{60\text{-}44}$) likely has a more straightforward origin. We find these, relatively Fe-rich, olivines exclusively as ~10 μm grains in the impact melt matrix of the impact melt breccia clasts (Fig. F6). Large olivine phenocrysts in the impact melt breccia clasts are also typically zoned to $Fo_{60\text{-}44}$ compositions where they are in contact with the melt matrix. Because these are impact melts, the smaller $Fo_{60\text{-}44}$ olivines were not derived from a diogenitic lithology. Rather, these olivines were formed through impact melting of howardite material on the Vestan surface. It is likely that $Fo_{60\text{-}44}$ olivine found in other howardites (e.g. Delaney et al. 1980) crystallized from impact melts as well. Two of the three samples where $Fo_{60\text{-}44}$ olivine was reported by Delaney et al. (1980), Kapoeta and Malvern, contain significant portions of impact melt rock (20.6 and 20.0 vol.% respectively; Fuhrman and Papike

1981, Labotka and Papike 1980), possibly indicating that Fo_{60-44} olivine in those samples was generated via impact melting as well.

K-rich glass

The K-rich glass in PCA 02014 may have a similar origin to K-rich glasses identified in other howardites, although its composition is more extreme. Barrat et al. (2009a, 2009b) proposed that the K-rich glass fragments in NWA 1664 resulted from the impact melting of a K-rich terrane on Vesta. A normative mineral calculation of that glass indicates that the target rock may have been a monzongranite (Quartz:30, Alkali feldspar:35, Plagioclase:35) (Barrat et al. 2009a). It is possible that the K-rich glass observed in PCA 02014 was also produced by impact melting of a K-rich terrane on Vesta. The normative mineralogy of the glass in PCA 02014 is equivalent to a quartz syenite (Q:8, A:61, P:31), a more evolved lithology than monzogranite. If a quartz syenite were the target material for glass in PCA 02014, this would be evidence for the most evolved lithology yet discovered on Vesta. However, it is also possible that the small K-rich impact glasses in NWA 1664 and PCA 02014 are not representative of the K-rich target material, especially if that material is coarse-grained as presumably a granitic rock might be. For example, material forming NWA 1664 K-rich glass may have derived from a portion of the K-rich target containing disproportionately high amounts of plagioclase, while the original material for PCA 02014 K-rich glass was disproportionately enriched in alkali feldspar. In this case, the single K-rich lithology from which both lithologic fragments originated would have a composition between monzogranite and quartz syenite (i.e. monzonite). If in fact the glasses in NWA 1664 and PCA 02014 represent two distinct target lithologies, this would require either extreme

amounts of fractionation if both lithologies evolved from the same magma, or separate magmatic trends producing the two lithologies.

If the K-rich glass in PCA 02014 resulted from impact melting of a K-rich lithology, be it either quartz syenite or monzonite, we might expect to find shocked lithologic clasts or mineral fragments from that target in the nine thin sections we examined in this study. We do not find any such evidence, which makes an interpretation of these glasses as impact melts of granites problematic. However, the composition of the glass in PCA 02014 is also consistent with eucritic mesostasis, which would explain the lack of granitic fragments and mineral clasts in the PCA 02 howardites. Regardless of the origin of 014 glass, it represents the most highly evolved magmatic composition yet discovered in the HEDs.

Impact melt breccia clasts

Given the high abundance of olivine phenocrysts and harzburgitic lithic fragments, it would seem probable that the target rock for the PCA 02 impact melt clasts was a harzburgitic or dunitic diogenite. However, the chemistry of melt matrix cannot be attributed to the melting of olivine-rich diogenite lithologies alone. Given the lack of an olivine norite (olivine + orthopyroxene + plagioclase) in the HED suite, we propose that the target rock for these melt breccia clasts was a harzburgitic and/or dunitic diogenite-rich howardite (i.e. harzburgitic/dunitic diogenite + eucrite). This is supported by the presence of some partially absorbed eucritic crystal and lithic fragments in the impact melt breccias, suggesting they were components of the target rock as well. Because of its lower melting temperature, eucritic material would more readily melt and absorb into the impact melt relative to the ultramafic diogenitic lithologies, and thus be less abundant as phenocrysts and lithic fragments. To further test the hypothesis that the target rock was a

mixture of eucrite and olivine-rich diogenite (dunitic or harzburgitic diogenite), we examine the bulk compositions of impact melts on an HED mixing diagram modified after Usui and McSween (2007) (Fig. F11). A mixing of eucrite and either dunitic or harzburgitic diogenite best explains many of the impact melt clast compositions, supporting our hypothesis that the target rock was harzburgitic/dunitic diogenite-rich howardite.

It is important to note that, as previously stated, the eucrite portion of the howardite target rock likely preferentially melted during impact, relative to olivine-rich diogenite portion, and thus is overrepresented in the melt matrix compositions plotted in Figure F11. If we incorporate the un-absorbed olivine phenocrysts and lithic fragments of harzburgite into the bulk compositions plotted, the compositions would fall much closer to the dunitic and harzburgitic end members on that figure.

Identifying the occurrence of impact melts that incorporate dunitic and harzburgitic diogenite has significant implications for the geologic history of Vesta. First, this provides evidence that dunitic and harzburgitic diogenite lithologies are likely exposed in craters from the initial impact that excavated and mixed these lithologies with eucritic debris. After being combined and lithified, these lithologies would later be melted by subsequent impact. This conclusion is consistent with spectral interpretations used to hypothesize exposure of olivine-rich lithologies such as these on the surface of Vesta (Gaffey 1997). Secondly, these impact melts indicate that there may be large areas of the surface that contain olivine-rich basaltic material. As we describe in detail above, these are not primary eucritic basalts, but secondary impact melts. These interpretations will be tested through remotely sensed observations of terranes such as these by Dawn.

4.2 Lithologic distribution maps

Lithologic heterogeneity: Small and large-scale variation

Although our work was not singularly driven towards characterizing the scale of heterogeneity in howardite samples, several trends that may be useful for constraining regolith variability were revealed. By examining the variation in lithologic components between multiple sections of one sample, we can infer a relative scale of variation at an approximately centimeter scale. Between sections ,6 and ,9 of PCA 02013, the concentrations of diogenitic and eucritic material vary by a factor of 2. Section ,6 contains ~60% diogenite and 30% eucrite, whereas section ,9 contains ~30% diogenite and 60% eucrite. The two sections of PCA 02009 vary by similar amounts, with diogenitic and eucritic material changing in abundance by factors of ~0.3 and 3.5, respectively, between the two sections. Similar intra-sample variations also occur with the abundances of lithified regolith (013,6 = 0 vol.% vs. 013,9 = 5 vol.%) and impact melt (009,12 = 0 vol.% vs. 009,5 = 4 vol.%) in these two samples. These results suggest that within a centimeter-sized scale on the surface of Vesta where these samples originated, the amount of eucritic, diogenitic and secondary (regolith and impact melt) varied significantly.

Examining variation among the entire group of paired samples may constrain larger, meter-scale variation for the Vestan surface. Among the entire group of samples we see similar variations. Diogenitic material varies by a factor of ~2.5 across the 9 sections (34 to 89 vol.%), while eucritic material varies by a factor of ~4 (7 to 40 vol.%). Other phases and lithologies vary in similar proportions. Metal + sulfide range from <1 to 8 vol.%, and impact melt abundance ranges from <1 to 28 vol.%. Large variability indicates that the pre-atmospheric meteoroid was heterogeneous even at the meter scale.

The large and small-scale variations displayed here indicate that the region on Vesta where the PCA 02 howardites originated is immature. Given the ~170m/pixel footprint of VIR, Dawn will not be sensitive to meter-scale heterogeneity in the Vesta regolith.

Lithologic Grain size distribution: Implications for VIR

As seen in the lithologic distribution map of each sample, diogenitic material clearly dominates the coarser grain size fractions. Typically, diogenitic material is ≥500 μm, but in two samples it is much larger, nearer 1.5 mm. Individual mineral grains of eucritic material, however, are ≤70 μm in all samples. This variance in grain sizes between the lithologies is likely a combination of both primary and secondary processes (i.e. diogenites are coarser grained plutonic rocks vs. fine grained eucritic basalts, and eucrites were likely exposed at the surface longer that diogenites and therefore impacted a disproportionately higher number of times). The order-of-magnitude grain size difference between eucritic and diogenitic material could be problematic for VIR spectral interpretation. Our findings here suggest that eucritic components typically only make up ~30 vol.%, but dominate the fine grain size fraction of these howardites. Similar findings have been demonstrated in other howardites (e.g. Labotka and Papike 1980; Buchanan and Mittlefehldt 1993), suggesting this phenomenon may not be localized.

This particular lithologic grain size distribution has significant implications for visible and near infrared reflectance spectra from the Vestan regolith. Each time light passes between two grains, there is the possibility of scattering at the media interface. Therefore, as other authors have shown (*e.g.* Hapke 1993) the trend of decreasing grain size amplifies the reflectance of the sample. Consequently, this phenomenon will result in increasing the overall contribution of the fine-grained eucritic material (verses the coarser-grained diogenitic material) to a reflectance spectrum of the PCA 02 samples. In

other words, the eucritic material will disproportionately dominate a VIR spectrum of surface regolith, if the lithologic grain size distribution we observe here is ubiquitous.

Effects of grain size, as well as other factors, in the visible/near-infrared wavelength range complicate spectral deconvolution, or the estimation of modal abundances of natural surfaces that are mixtures of multiple phases (such as regolith). Therefore, characterizing possible regolith grain size variability in howardites can be used to help constrain different VIR data reduction techniques. Both the models of Hapke (1981, 1993) and Shkuratov et al. (1999) call for an average particle radius, or the distance light propagates through a particle before internal reflection. These parameters, and the derived grain sizes modeled by these two approaches, can be checked against the anticipated lithologic grain size distribution from this study.

5.0 CONCLUSIONS

1. The PCA 02 howardites contain silicate mineral compositions that span almost all known HED ranges, suggesting their sources on Vesta are diverse. The mineralogical diversity observed here is an indicative of an immature regolith. These samples also contain some unusual mineral compositions and lithologies.

2. Two groups of olivines have compositions outside those known for diogenites. One group (~Fo_{85}) that is more Mg-rich than diogenites is likely due to chondritic contamination. The other, more Fe-rich group (~Fo_{50}) crystallized from impact melts.

3. Olivine-rich impact melts comprise up to ~30 vol.% of these samples. The target rocks for these melts were likely howardite, composed of dunitic or harzburgitic diogenite and eucrite. These are the only impact melts identified in HEDs thus far that involve the

melting of olivine-rich lithologies on Vesta. These impact melts support the occurrence of olivine-rich lithologies exposed within craters on Vesta.

4. Glass, with 10.1 wt.% K_2O, was observed. This is the most K-rich HED glass yet reported. While this glass may be impact melted quartz syenite, an origin as eucrite mesostasis may be more probable.

5. Lithologic variation observed among this group of howardites suggests an immature regolith on Vesta. Eucritic material is fine-grained, while diogenitic material is very coarse. This will likely affect the interpretation of VIR spectra. These data might be used to test models that correctly estimate the proportions of these two lithologies in the Vestan regolith.

ACKNOWLEDGMENTS

The authors thank the MWG for allocating meteorite samples. This work was partially supported by NASA Cosmochemistry Grant NNG06GG36G to HYM.

REFERENCES

Barrat J. A., Bohn M., Gillet Ph., and Yamaguchi A. (2009a) Evidence for K-rich Terranes on Vesta from impact spherules. *Meteoritics & Planetary Science* **44**:359-374.

Barrat J. A., Yamaguchi A., Greenwood R. C., Bollinger C., Bohn M., and Franchi I. A. (2009b) Trace element geochemistry of K-rich impact spherules from howardites. *Geochimica et Cosmochimica Acts* **73**:5944-5958.

Barrat J. A., Yamaguchi A., Benoit M., and Bohn M. (2008). Geochemistry of diogenites: Still more diversity in their parental melts. *Meteoritics & Planetary Science* **43**:1759–1775.

Beck A. W. and McSween H. Y. (2010) Diogenites as polymict breccias composed of orthopyroxenite and harzburgite. *Meteoritics and Planetary Science* **45**:850-872.

Beck A. W., Mittlefehldt D. W., McSween H. Y., Rumble D., Lee C.-T. A., and Bodnar R. J. (2011) MIL 03443, a dunite from asteroid 4 Vesta: Evidence for its classification and cumulate origin. *Meteoritics & Planetary Science*, in press.

Beck A. W., Viviano C. E., Cheung K. K., and Taylor L. A. (2007) Geochemical variations among a trio of paired howardites: Do the pieces fit together? (abstract) Lunar and Planetary Science Conference XXXVIII, CD#1123.

Bohn M., Yamaguchi A., Jambon A., and Barrat J. A. (2011) Possible debris of highly evolved lithologies in howardites: Additionaly evidence of K-rich areas on 4-Vesta? (abstract). 74th Meteoritical Society Meeting, CD#5496.

Bowman L. E., Papike J. J., and Spilde M. N. (1999) Diogenites as asteroidal cumulates: Insights from spinel chemistry. *American Mineralogist* **84**:1020-1026.

Brearley A. J. and Jones R. H. (1998) Chondritic meteorites. In *Planetary Materials*, J. J. Papike, ed., *Reviews in Mineralogy and Geochemistry* **36**:3.1-3.398, Mineralogical Society of America, Chantilly VA.

Buchanan P. C. and Mittlefehldt D. W. (2003) Lithic components in the paired howardites EET 87503 and EET 87513: Characterization of the regolith of 4 Vesta. *Antarctic Meteorite Research* **16**:128-151.

Bunch T. E. (1975) Petrography and petrology of basaltic achondrite polymict breccias (howardites). *Proceedings of the Lunar and Planetary Science Conference VI*, **1**:469-492.

Delaney J. S., Nehru C. E., and Prinz M. (1980) Olivine clasts from mesosiderites and howardites: Clues to the nature of achondritic parent bodies. *Proceedings of the Lunar and Planetary Science Conference XI*, **2**:1073-1087.

Delaney J. S., Prinz M., and Takeda H. (1984) The polymict eucrites. *Proceedings of the Lunar and Planetary Science Conference XV*, **89**:C251-C288.

Desnoyers C. and Jerome D. Y. (1977) The Malvern howardite: A petrological and chemical discussion. *Geochimica et Cosmochimica Acta* **41**:81-86.

ENVI 4.2, ITT Visual Information Solutions (2006) Boulder, Colorado.

Floss C., Jolliff B. L., Benedix G. K., Stadermann F. J., and Reid J. (2007) Hammadah al Hamra 193: The first amphibole-bearing winonaite. *American Mineralogist* **92**:460-467.

Fuhrman M. and Papike J. J. (1981) Howardites and polymict eucrites: Regolith samples from the eucrite parent body. Petrology of Bholgati, Bununu, Kapoeta, and ALHA76005. *Proceedings of the Lunar and Planetary Science Conference XII*, **12**:1257-1279.

Gaffey M. J. (1997) Surface lithologic heterogeneity of asteroid 4Vesta. *Icarus* **127**:130-157.

Goldstein J. I. and Yakowitz H. (1971) Metallic inclusions and metal particles in the Apollo 12 lunar soil. *Proceedings of the Lunar and Planetary Science Conference II*, **1**:177-191.

Hewins R. H. (1979) The composition and origin of metal in howardites. *Geochimica et Cosmochimica Acta* **43**:1663-1673.

Hapke, B. (1981). Bidirectional reflectance spectroscopy. 1. Theory. J. Geophys. Res. 86, 3039–3054.

Hapke B. (1993) In *Introduction to the Theory of Reflectance and Emittance Spectroscopy*, Rycroft M. J. and Arvidson R. E., eds., Cambridge University Press, Cambridge, UK.

Hewins R. H. and Klein L. C. (1978) Provenance of metal and melt rock textures in the Malvern howardite. *Proceedings of the Lunar and Planetary Science Conference IX,* **1:**C251-C288.

Irving A. J., Kuehner S. M., Rumble D., Hupe A. C., and Hupe G. M. (2003) Olivine diogenite NWA 1459: Plumbing the depths of 4 Vesta (abstract). Lunar and Planetary Science Conference XXXIV, **CD#**1502.

Labotka T. C. and Papike J. J. (1980) Howardite: Samples of the regolith of the eucrite parent-body: Petrology of Frankfort, Pavlovka, Yurtuk, Malvern, and ALHA 77302. *Proceedings of the Lunar and Planetary Science Conference XI*, **1**:1103-1130.

Lucey P., Korotev R. L., Gillis J. J., Taylor L. A., Lawrence D., Campbell B. A., Elphic R., Feldman B., Hood L. L., Hunten D., Mendillo M., Noble S., Papike J. J., Reedy R., Lawson S., Prettyman T., Gasnault O., and Maurice S. (2006) Understanding the lunar surface space-Moon interactions. In *New Views of the Moon*, Jolliff B. L., Wieczorek M.

A., Shearer C.K., and Neal C. R., eds., *Reviews in Mineralogy and Geochemistry* **60**:2.83-2.219, Mineralogical Society of America, Chantilly VA.

Kitts K. and Lodders K. (1998) Survey and evaluation of the eucrite bulk compositions. *Meteoritics and Planetary Science* **33**:A197-A213.

Mayne R. G., McSween H. Y., McCoy T. J. and Gale A. (2009) Petrology of the unbrecciated eucrites. *Geochimica et Cosmochimica Acta* **73**:794-819.

McBride K., Corrigan C., and McCoy T. J. (2005). *Antarctic Meteorite Newsletter* **28**(1):19.

McBride K., McCoy T. J., and Welzenbach L. (2004). *Antarctic Meteorite Newsletter* **27**(1):19.

McSween H. Y. (1977) Chemical and petrographic constraints on origin of chondrules and inclusions in carbonaceous chondrites. *Geochimica et Cosmochimica Acta* **41**:1843-1860.

McSween H., Mittlefehldt D., Beck A., Mayne R., and McCoy T. (2011) HED meteorites and their relationship to the geology of Vesta and the Dawn mission. *Space Science Reviews*, doi:10.1007/s11214-010-9637-z.

Metzler K. and Stöffler D. (1987) Polymict impact breccias on the eucrite parent body: I. Lithic clasts in some eucrites and howardites (abstract). Lunar and Planetary Science Conference. XVII, 641–642.

Metzler K., Bobe K. D., Palme H., Spettel B., and Stoffler D. (1995) Thermal and impact metamorphism on the HED parent asteroid. *Planetary Space Science* **43**:499-525.

Metzler K. and Stoffler D. (1995) Impact melt rock and granulites from the HED asteroid (abstract). *Meteoritics* **30**:547.

Mittlefehldt D. W., McCoy T. J., Goodrich C. A. and Kracher A. (1998) Non-chondritic meteorites from asteroidal bodies. In Planetary Materials, Papike J. J. ed., *Reviews in Mineralogy and Geochemistry* **36**:4.1-4.195, Mineralogical Society of America, Chantilly VA.

Mittlefehldt D. W., Beck A. W., Lee C-T. A., McSween H. Y., Buchanan P. C., and Burbine T. (2011). Compositional constraints on the genesis of diogenites. *Meteoritics and Planetary Science* submitted.

Papike J. J., Karner J. M. and Shearer C. K. (2003) Determination of planetary basalt parentage: A simple technique using the electron microprobe. *American Mineralogist* **88:**469-472.

Pun A., Keil K., Taylor G. J., and Wieler R. (1998) The Kapoeta howardite: Implicaions for the regolith evolution of the howardite-eucrite-diogenites parent body. *Meteoritics and Planetary Science* **33**:835=851.

Russell C., Coradini A., Christensen U., De Sanctis M., Feldman W., Jaumann R., Keller H., Konopliv A., McCord T., McFadden L., McSween H., Mottola S., Neukum G., Pieters C., Prettyman T., Raymond C., Smith D., Sykes M., Williams B., Wise J., and Zuber M. (2004) Dawn: A journey in space and time. *Planetary and Space Science* **52**:465-489.

Shearer C. K., Burger P., and Papike J. J. (2010) Petrogenetic relationships between diogenites and olivine diogenites: Implications for magmatism on the HED parent body. *Geochimica et Cosmochimica Acta* **74**:4865-4880.

Shkuratov, Y., Starukhina L., Hoffmann H., and Arnold G. (1999) A model of spectral albedo of particulate surfaces: Implications for optical properties of the Moon. *Icarus* **137**, 235–246.

Usui T. and McSween H. Y. (2007) Geochemistry of 4 Vesta based on HED meteorites: prospective study for the interpretation of gamma ray and neutron spectra for the Dawn mission. *Meteoritics and Planetary Science* **42:**255-269.

Welten K.C., Caffee M.W., and Beck A.W. (2009) Cosmogenic radionuclides in three paired howardites and a polymict diogenites from Pecora Escarpment Icefield, Antarctica (abstract). *Meteoritics and Planetary Science* **44**:A216.

Appendix E

X-RAY MAP METHODS

To create lithologic distribution maps, we first acquired 8 elemental x-ray images of sample on the electron microprobe. The eight elements measured were Mg, Al, Si, K, Ca, Ti, Cr, and Fe. We used a 2 μm beam set at 20 kV and 30 nA, an 8 μm step size and 50 ms counting times for each element. A 16 bit image range was necessary to preserve each ~0-2000 counts possible in each elemental x-ray image. Each of the 8 element x-ray maps of a given sample was mosaicked and stacked into a single image cube using the image-processing software Environment for Visualizing Images software (ENVI 4.2), where each element represents a single band of the cube. Background epoxy and cracks in the thin section were masked using a threshold of counts below 340 for all elements. We then produced an images mask to remove all background epoxy and cracks in the thin section.

The next step in the process involved making a region of interest (ROI) for each of the typical phases we wished to distinguish. In all, 13 ROIs were defined: olivine, En_{65}-$_{85}$ (diogenite pyroxene), En_{65-45} (cumulate eucrite pyroxene), En_{45-33} (basaltic eucrite pyroxene), plagioclase, clinopyroxene, silica, chromite, ilmenite, FeNi metal, sulfide, phosphate, impact melt glass, and lithified regolith. This is a robust list of all phases expected in an HED meteorite (Mittlefehldt et al. 1998) and all were measured through detailed spot analysis in our samples. To create each ROI, we chose a select number of grains with a known compositional range (from our EMP data) that fell within our 13 classifications. For example, for the cumulate eucrite pyroxene ROI, we chose several pyroxene grains with compositions between En_{65-45}, taking care to select a uniform distribution of En values within our range. Plagioclase, silica, clinopyroxene, the opaque phases, phosphate, lithified regolith and impact melt were relatively homogeneous in

composition within each sample, and therefore we did not need to take care in selecting a uniform distribution of compositions, as we did with pyroxene.

After creating the ROIs, we applied a minimum distance supervised classification technique (ENVI 4.2) to classify each pixel in our image cube as one of the 13 classifications derived from our ROIs. The minimum distance classification calculates the Euclidean distance of each unknown pixel to the center of each ROI class. Pixels are classified to the closest ROI class, unless they fall outside the defined standard deviations for each class, in which case they are 'unclassified'. We assigned different maximum values for the standard deviation from the mean of each ROI to produce results that mostly closely resembled observations of these samples in thin section. They were olivine=12, En_{65-85}=15, En_{65-45}=5.5, En_{45-33}=11, plagioclase=13.5, clinopyroxene=7, silica=14, chromite=8, ilmenite=8, metal=10, sulfide=10, phosphate=10, lithified regolith=2.5, and impact melt glass =2.5. The minimum distance used for lithified regolith and impact melt are particularly low, as the technique would misclassify many pixels from the very fine-grained parts of the matrix as either one of these two ROIs. It is likely that the pixels in the very fine-grained parts of the matrix are sampling <5 μm fragments of pyroxene + plagioclase, too small to be distinguished by our 8 μm step size. Therefore we set the maximum standard deviation from the mean for these ROIs to leave these pixels unclassified, while retaining the correct classification of the larger pieces of impact melt and regolith we observed in thin section. In one case, PCA 02013 section ,9, fusion crust was misclassified as impact melt, as seen in Figure F9.

Each sample had ≤ ~10% unclassified pixels. As stated above, we believe a large amount of the unclassified pixels are very fine grains in the matrix that were too small to be resolved by the 8 μm step size. The matrix is observed to be an approximately even

mixture of pyroxene + plagioclase, using the EMP 2 μm beam size; therefore, we believe the calculated modes of these samples are not significantly different from what we have calculated using this technique. Modal calculation of each phase using ENVI 4.2 reports the number of pixels in each classification, which we then normalized to 100% and used to calculate a mode.

Appendix F

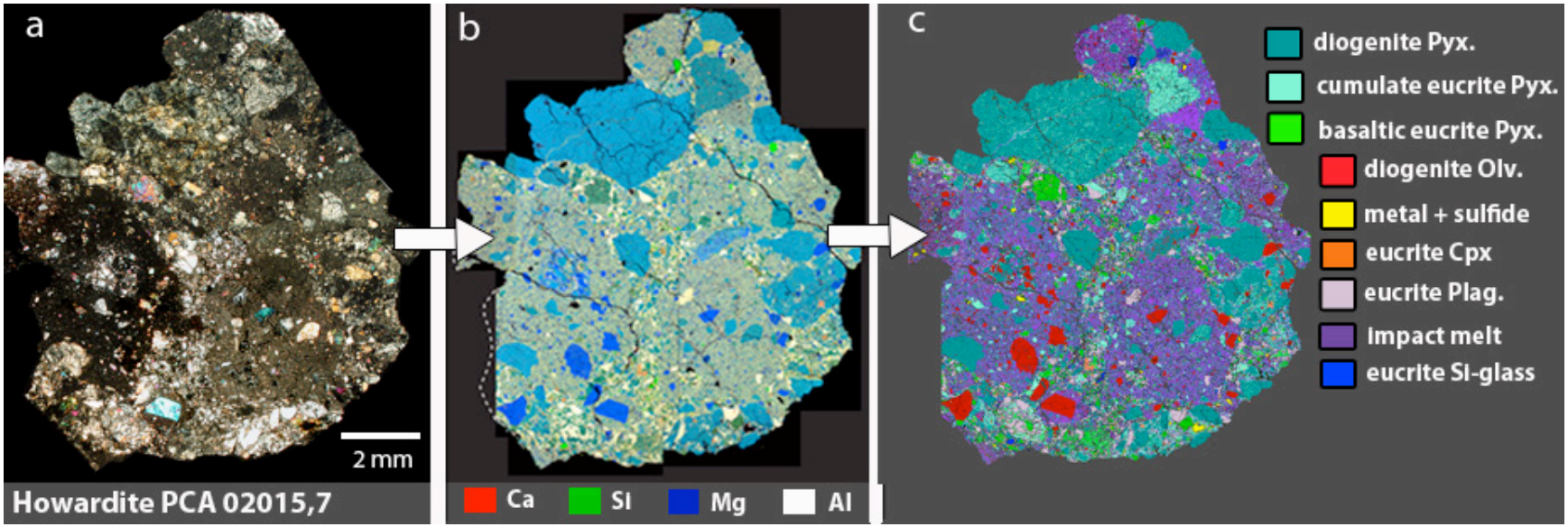


Figure F1. (a) Cross-polarized image of howardite PCA 02015, (b) typical composite x-ray map of 4 elements, (c) composite x-ray map of 8 elements, where minerals belonging to specific HED lithologies have been grouped, and denoted by different colors.

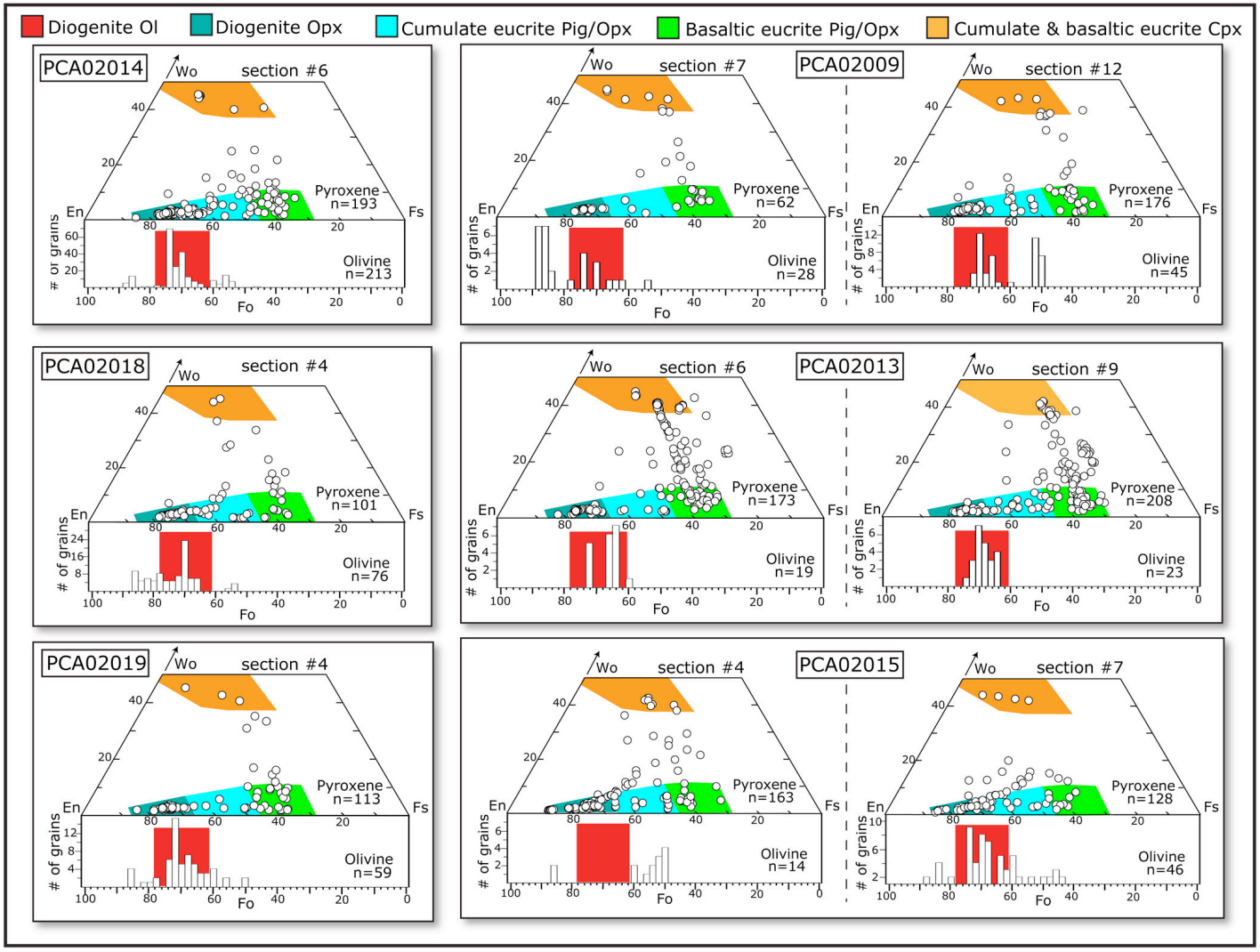


Figure F2. Pyroxene and olivine compositions in the PCA02 howardites. Each pyroxene quadrilateral/olivine histogram combination plot represents one thin section. Multiple thin sections from a single sample have been grouped. Diogenite and eucrite ranges (colored) from Mittlefehldt et al. forthcoming, Beck and McSween (2010), Shearer et al. (2010), Mayne et al. (2009), and Mittlefehldt et al. (1998).

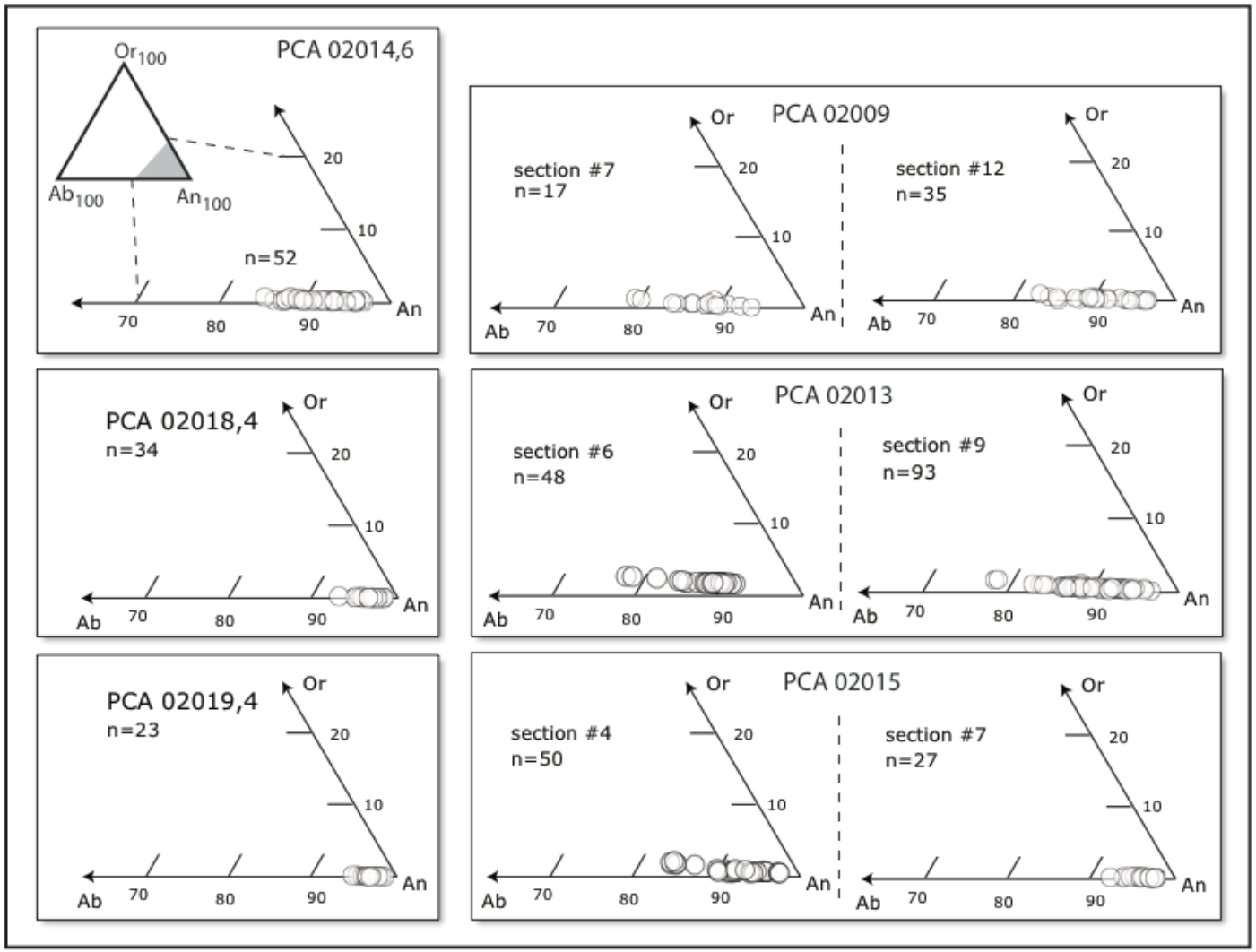


Figure F3. Plagioclase compositions for six paired howardites. Each plot represents a different thin section and multiple thin sections from a single sample have been grouped. All measurements fall within the range of plagioclase found in cumulate and basaltic eucrites.

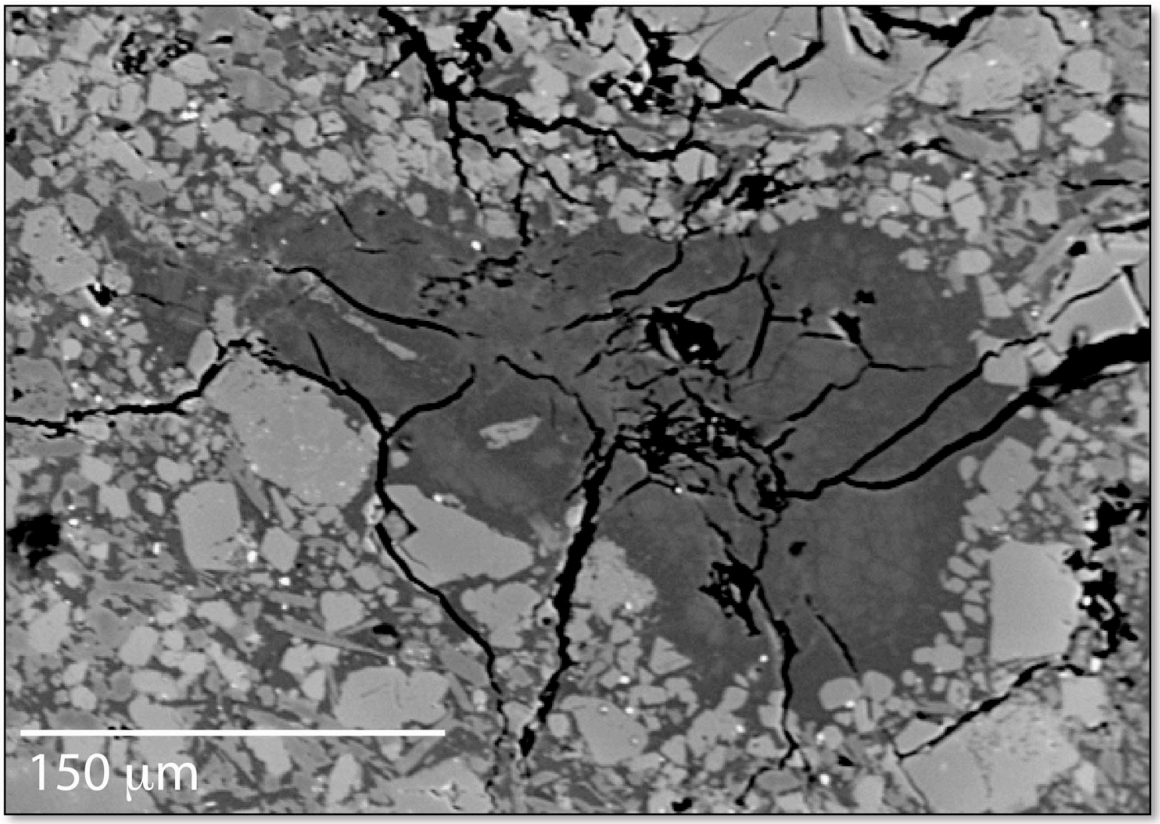


Figure F4. BSE image of K-rich (K_2O = 10.1 wt.%) glass in howardite PCA 02014,6. This grain is almost completely glass, though one small crystal inclusion can be seen. The elongated crystal on the left side of the glass is an embayment, not an inclusion. This glass is in contained an impact melt breccia clast, dominated by olivine (Fo_{50}) phenocrysts, which can be seen concentrated around the rim of the glass.

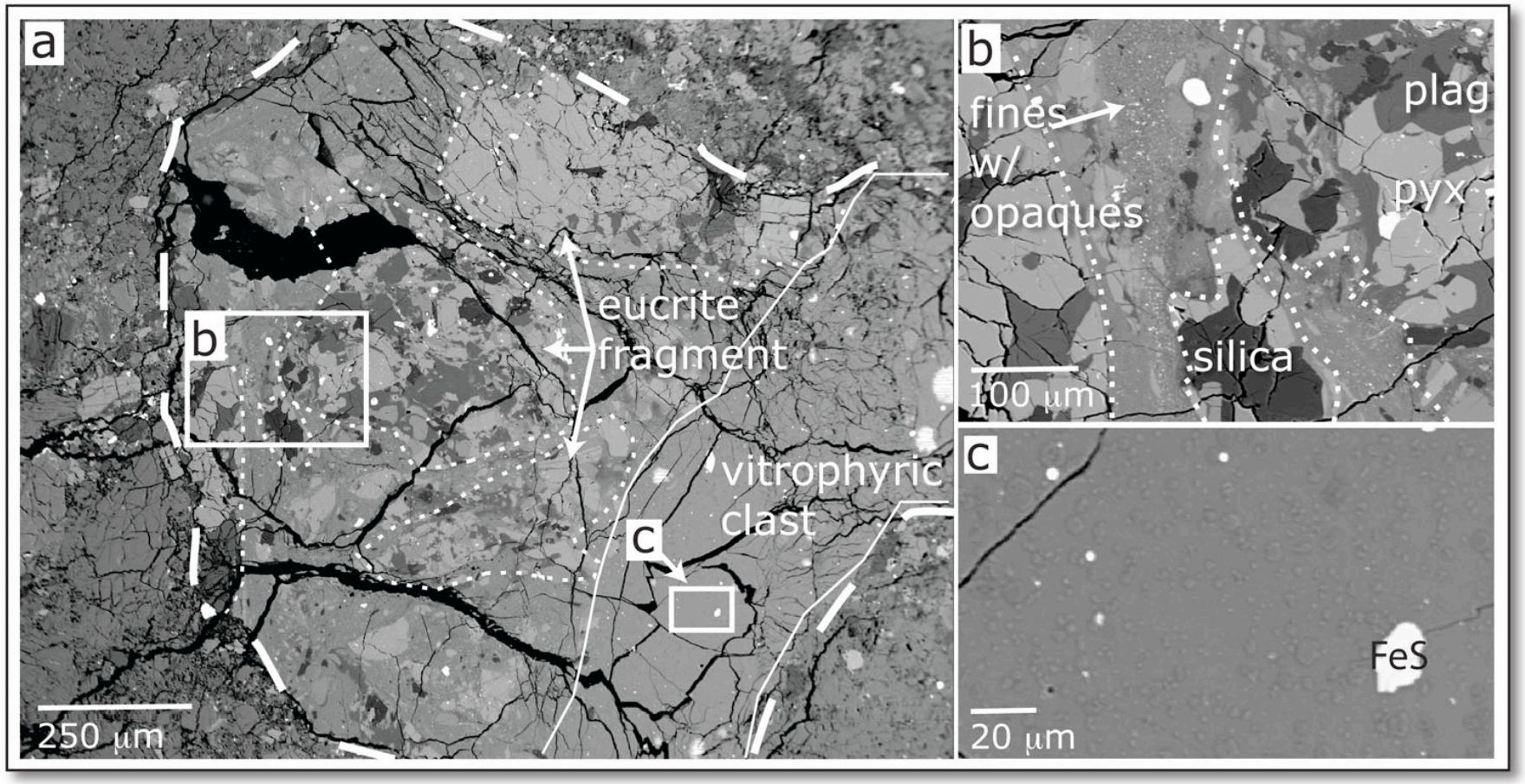


Figure F5. BSE image of a lithified regolith clast in PCA 02019,4. (a) This clast is comprised of eucritic fragments, containing plagioclase + pyroxene + silica, (b) which are separated by a fine-grained matrix with high concentrations of opaques that is interpreted as regolith material. (c) This clast also contains a fragment which is vitrophyric and contains opaques. This fragment is approximately eucritic in composition, and is likely either a quickly quenched impact melt, or solid piece of lithified regolith.

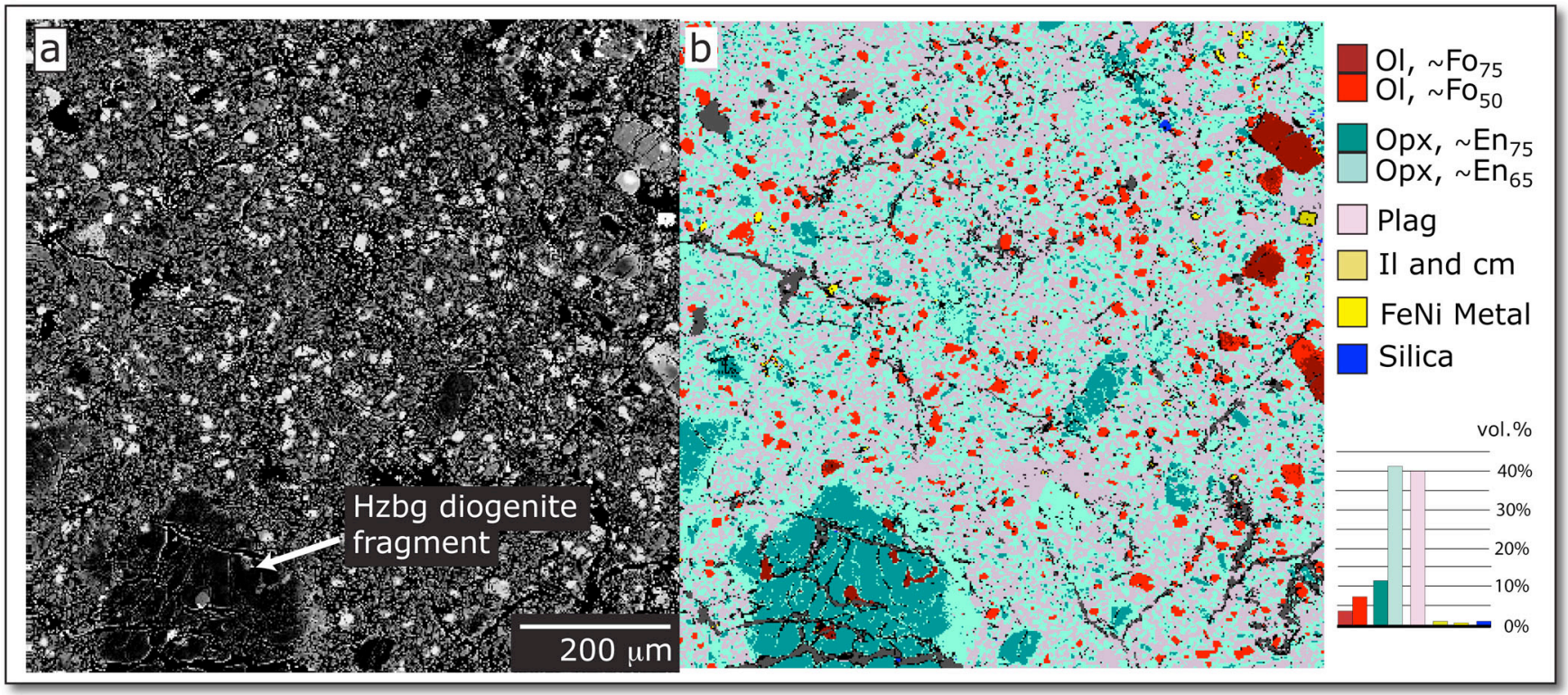


Figure F6. Impact melt breccia clast in PCA 02015. (a) BSE image, (b) and false color lithologic distribution map of the same area. The actual impact melt is predominantly En_{65} Opx and plagioclase, along with phenocrysts of Fo_{50} olivine. Relic lithic clasts of harzburgitic (Hzbg) diogenite and relic phenocrysts of diogenitic Fo_{75} olivine, and En_{75} Opx can also be seen. These phenocrysts have equilibrated with the impact melt, as seen by their Fe-enrichment from core to rim. Note that the BSE image in (a) was taken under different conditions than those shown in Figs F4, 5 and 7, causing common phases to have different shades of gray.

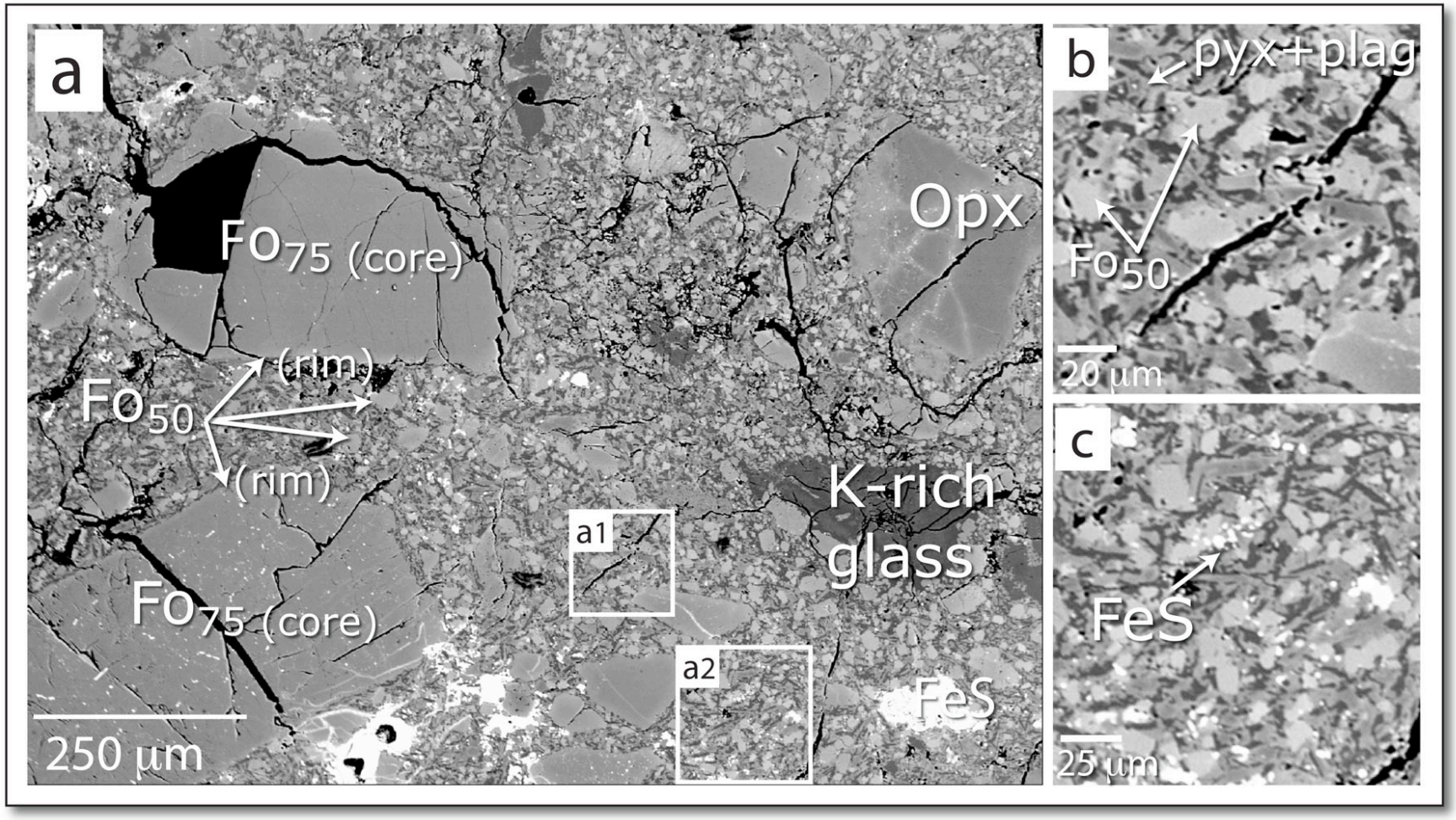


Figure F7. BSE images of an impact melt breccia clast in the howardite PCA 02014,6. (a) Clasts are composed of large phenocrysts of ~Fo_{75} relic olivine, zoned to ~Fo_{50} at rims. Larger relic Opx phenocrysts also occur, and one K-rich glass (close magnification in Fig. F4) also observed. (b) Impact melt matrix composed mainly of Fo_{50} olivine, with lesser amounts of pyroxene and plagioclase. c) Some impact melt also has high concentrations of sulfide and or metal spherules.

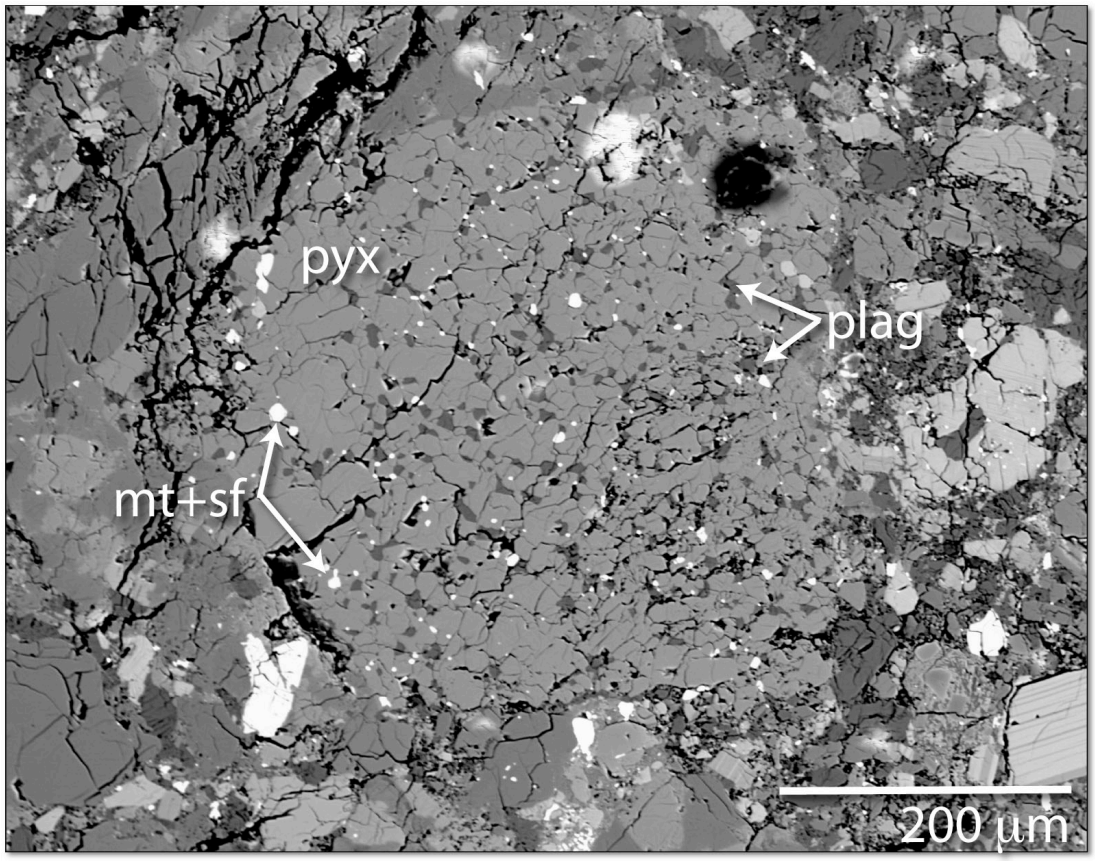


Figure F8. A possible type IIB chondrule in PCA 02014, comprised primarily of pyroxene (Wo_2 En_{64} Fs_{34}), with small amounts of interstitial plagioclase, metal (mt), and sulfide (sf).

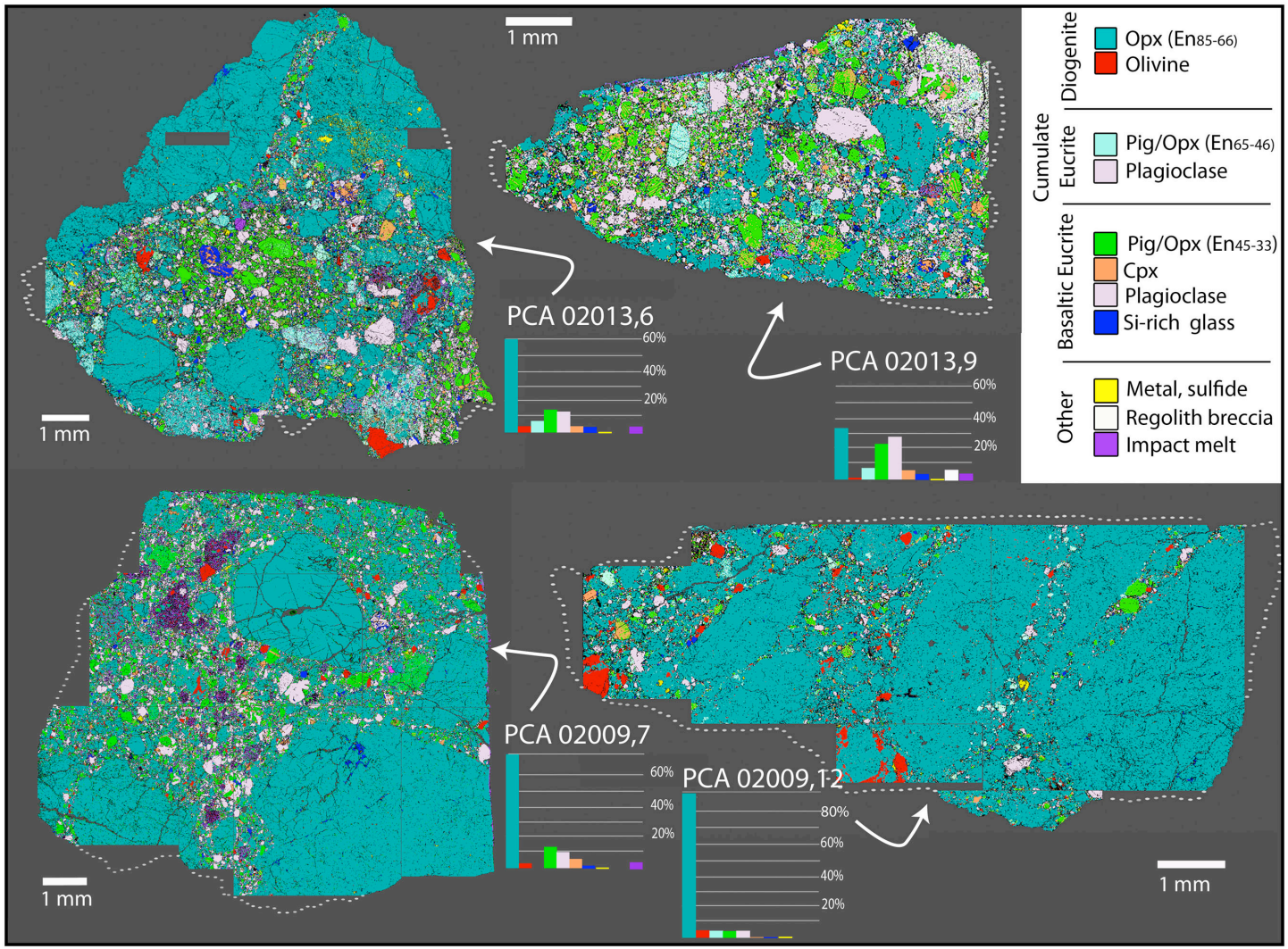


Figure F9. False color lithologic distribution maps of two howardites. Two thin sections from each meteorite are shown. Colors represent minerals from different HED lithologies (see inset key). Relative phase distributions are shown on histograms associated with each map.

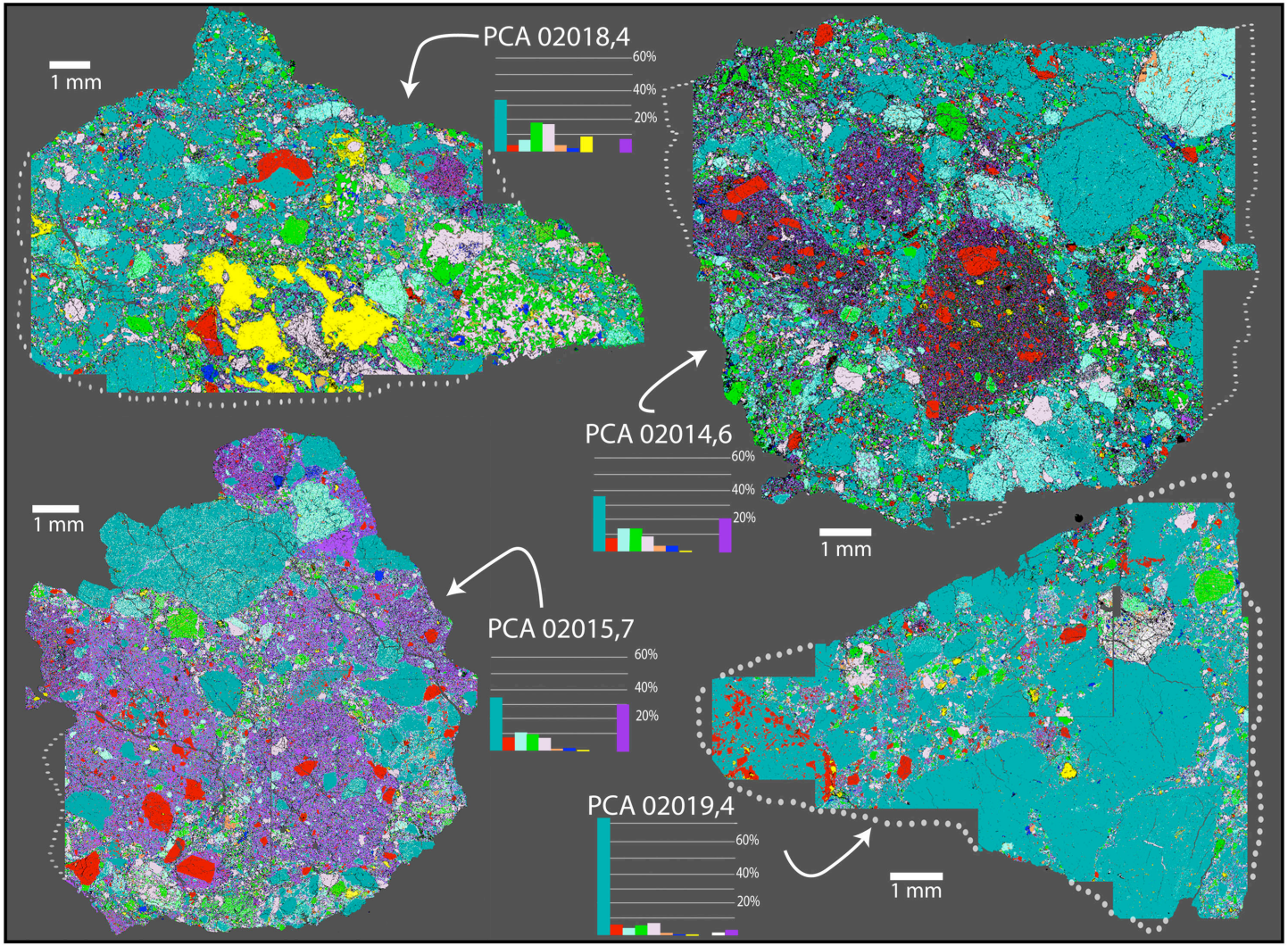


Figure F10. False color lithologic distribution maps for the remaining howardites. Each color represents a mineral from a different HED lithology (see inset key, Fig. F9). Relative phase distributions are shown on histograms associated with each map.

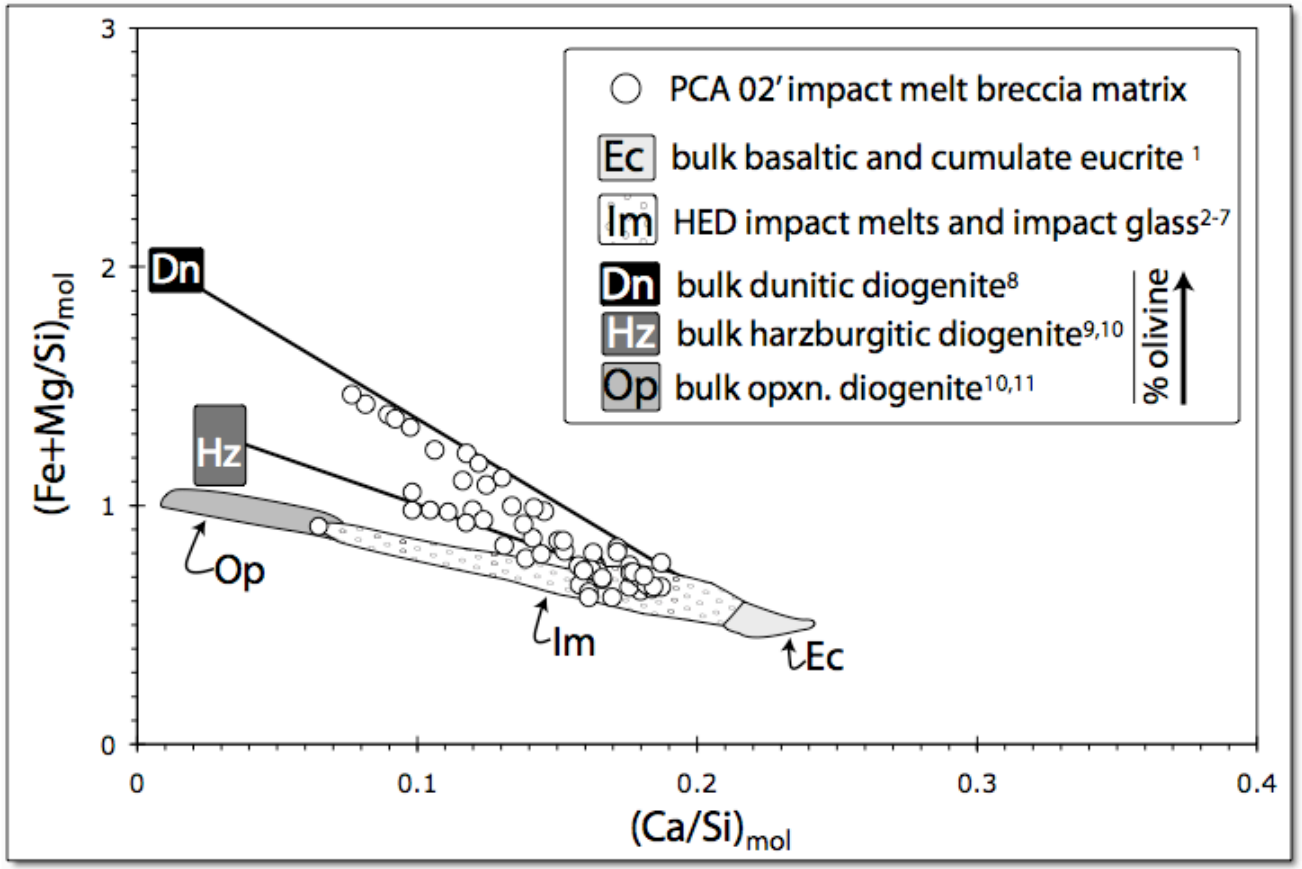


Figure F11. Bulk compositions of matrix in PCA 02 impact melt breccia clasts compared to bulk eucrite and diogenite compositions, modified from Usui and McSween (2007). Separate diogenite lithologies are distinguished and connected to eucrite bulk compositions via tie-lines. Previously published HED impact melt matrix and impact glass compositions are also plotted, and completely overlay the tie-line between eucrite and orthopyroxenitic (opxn.) diogenite. Most impact melt matrix compositions in the PCA 02 howardites suggest mixing of eucritic and harzburgitic or dunitic material. [1]Kitts and Lodders (1998); [2] Desnoyers and Jerome (1977); [3]Metzler and Stoffler (1987,1995); [4]Metzler et al. (1995); [5]Pun et al. (1998); [6]Buchanan and Mittlefehldt (2003); [7]Barrat et al. (2009a); [8]Beck et al. (2011); [9]Irving et al. (2003); [10]Mittlefehldt et al. forthcoming; [11]Barrat et al. (2008).

Part 7
Conclusion

In part 2 we show that diogenite breccias containing olivine are composed of two distinct lithologies. One lithology is harzburgitic (olivine + magnesian orthopyroxene) while the other is orthopyroxenitic (ferroan orthopyroxene-only). The former are represented by the olivine-rich diogenites, and the latter represent 'normal' orthopyroxenite diogenites. Both lithologies likely originated in multiple plutons through fractional crystallization. Minor element patterns suggest that these plutons had varying source compositions. In this work we a new classification scheme for diogenites reflecting the two lithologies that were identified, and breccia mixtures of them. The discovery of two distinct diogenitic lithologies suggests that Dawn spacecraft may observe stratigraphic variation in larger craters that expose diogenitic plutons.

In part 3 we examine the mineralogy, petrology and bulk chemistry of anomalous dunite breccia MIL 03443. Similarities in oxygen isotopes, silicate compositions, and geochemistry between MIL 03343 and the diogenites strongly support its grouping with the HEDs. We also present findings that suggest a cumulate origin for akin to the diogenites for this meteorite, not a mantle restite. The classification of a HED dunite supports spectral interpretations of the Vestan surface which identify olivine-rich lithologies.

Part 4 further test the hypothesis formulated in part 1, that olivine-bearing diogenitic breccias are composed of two distinct lithologies by examining trace element variation. In situ trace element concentrations confirm that the majority of the dimict samples are in fact are composed of harzburgite and orthopyroxenite lithologies. The

majority of trace element variation between the two lithologies can be explained by pyroxene fractionation. Decreases in Eu and HREE concentrations from harzburgite to orthopyroxenite, however, are likely due to either plagioclase crystallization in the orthopyroxenite lithology, or harzburgite equilibration with HREE-rich trapped melt.

Part 5 examines the variation in bulk chemistry of a wide sampling of diogenites in order to further constrain petrogenesis of this group on Vesta. The bulk chemistries of some samples can be best explained by the incorporation of eucritic debris upon brecciation. One sample has highly evolved bulk compositions and may belong to a to transitional lithology between diogenites and cumulate eucrites. We also assess the hypothesis that very low Eu/Eu* in diogenites is evidence for mixing of diogenite parent magmas with basaltic crust, and do not find this evidence compelling. We find that subsolidus equilibration may have caused exchange of Eu^{2+} between REE-poor orthopyroxene and REE-rich phosphate. This, followed by laboratory dissolution of phosphates prior to analysis, would result in at residual orthopyroxene with a Eu/Eu* much lower than that of the original cumulate.

In part 6 we investigate petrologic and textural heterogeneity in six of the PCA 02 howardites, one of the largest pieces of the Vestan surface. We find significant textural and compositional variation among the group, suggesting a relatively immature regolith on Vesta. Ultramafic impact melt breccia clasts were also observed, and likely formed from the melting of harzburgitic or diogenitic diogenite-rich howardite material. We also find the most K-rich glass yet to be discovered in an HED. This glass may have formed

from the impact melting of highly evolved granites on Vesta, but may also be eucrite mesostasis. Finally, we observed a dominance of eucritic material in the finer grain sizes, while diogenitic material is very coarse. This will likely affect the ability of VIR to correctly measure the proportions of these two lithologies in the Vestan regolith.

VITA

Andrew William Beck was born on September 1st, 1981 in Dayton Ohio. He spent his childhood in Granville, Ohio where he attended Granville High School. He spent his summers between a family farm in Dayton Ohio, and a summer camp in northern Michigan. Interacting with nature in both of these locations played a crucial role in eventually leading him to the field of geology.

After graduating high school, Andrew attended St. Bonaventure University in Olean, New York for two years. He then transferred to Albion College in Albion, Michigan where he graduated cum laude with a Bachelor of the Arts in Philosophy and a minor in Geology in 2004. For the next two years, Andrew worked for the Albion College Geology Department as a technician. At this position, he maintained a rock preparation facility and also assisted in teaching both in the laboratory setting and in the field. Andrew also continued taking geology courses, and in 2006, had taken the course load equivalent to a BA in Geology.

Andrew entered the Earth and Planetary Sciences graduate program at the University of Tennessee, Knoxville, in the fall of 2006. Over the next five years he took courses in geology, math, physics and chemistry at UT in pursuit of a Doctor of Philosophy degree in Geology. He also taught many laboratory courses at UT, ranging from Introductory Geology to Petrogenesis of Crystalline Rocks, and was fortunate to have the opportunity to teach a Field Methods course for Albion College in 2008. Along with teaching and taking classes, he also conducted the research, which culminated in this document. He expects to be awarded his Doctor of Philosophy degree in August of 2011.